

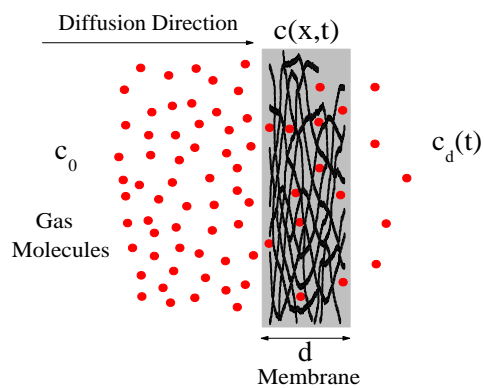


ΠΟΛΥΤΕΧΝΕΙΟ ΚΡΗΤΗΣ
ΓΕΝΙΚΟ ΤΜΗΜΑ

The Use of Nano-Particles for the Development of Enhanced Gas Barrier Polymeric Coatings

Μελέτη της διαπερατότητας αερίων σε πολυμερή ενισχυμένα με τεμαχίδια νανομετρικών διαστάσεων

Γεώργιος Α. Χουδαλάκης



ΔΙΔΑΚΤΟΡΙΚΗ ΔΙΑΤΡΙΒΗ

ΠΟΛΥΤΕΧΝΕΙΟ ΚΡΗΤΗΣ



Μελέτη της διαπερατότητας αερίων σε πολυμερή ενισχυμένα με τεμαχίδια νανομετρικών διαστάσεων

*The Use of Nano-Particles for the Development of
Enhanced Gas Barrier Polymeric Coatings*

Γεώργιος Α. Χουδαλάκης
Φυσικός, MSc

Διατριβή υποβληθήσα στα πλαίσια των απαιτήσεων για την
απόκτηση του Διδακτορικού τίτλου του Πολυτεχνείου Κρήτης

4 Φεβρουαρίου, 2013

ΔΙΔΑΚΤΟΡΙΚΗ ΔΙΑΤΡΙΒΗ

ISBN:

Γεώργιος Α. Χουδαλάκης,
αρ. φ. μητρώου: 2006040144
e-mail: gchoudalakis@isc.tuc.gr

Η διατριβή εγκρίθηκε από την ακόλουθη επταμελή συμβουλευτική επιτροπή:

1. Αλέξανδρος Δ. Γκότσης, αναπλ. καθηγητής Πολυτεχνείου Κρήτης, Επιβλέπων
2. Ευάγγελος Διαμαντόπουλος, καθηγητής Πολυτεχνείου Κρήτης
3. Παγώνα Μαραβελλάκη, επικ. καθηγήτρια Πολυτεχνείου Κρήτης
4. Κωνσταντίνος Προβιδάκης, καθηγητής Πολυτεχνείου Κρήτης
5. Μιχάλης Κονσολάκης, επικ. καθηγητής Πολυτεχνείου Κρήτης
6. Κωνσταντίνος Κομνίτσας, καθηγητής Πολυτεχνείου Κρήτης
7. Ιωάννης Γεντεκάκης, καθηγητής Πολυτεχνείου Κρήτης

στις 21 Ιανουαρίου, 2013

Εικόνα εξωφύλλου:

Diffusion process through a polymer-clay nanocomposite material.

ΔΙΕΥΘΥΝΣΗ ΕΡΓΑΣΤΗΡΙΟΥ:**ΠΟΛΥΤΕΧΝΕΙΟ ΚΡΗΤΗΣ, ΓΕΝΙΚΟ ΤΜΗΜΑ
ΕΡΓΑΣΤΗΡΙΟ ΜΗΧΑΝΙΚΗΣ ΤΩΝ ΥΛΙΚΩΝ**

Κτήριο Επιστημών, Πανεπιστημιούπολη, Κουνουπιδιανά, 73100 Χανιά
τηλ. 2821037259
fax. 2821037672
e-mail: gotsis@science.tuc.gr

DECLARATION

I hereby declare that the work presented here has been my independent work and has been performed during the course of my post-graduate studies at the Department of Sciences, Technical University of Crete, Chania.

All contributions drawn from external sources have been acknowledged with due reference to the literature.

ΔΗΛΩΣΗ

Δηλώνω υπεύθυνα ότι η παρούσα διατριβή είναι προϊόν ανεξάρτητης εργασίας μου που διεξήχθη κατά τις μεταπυχιακές μου σπουδές στο Γενικό τμήμα του Πολυτεχνείου Κρήτης, στα Χανιά,

Για ό,τι δεδομένα ή πληροφορίες χρησιμοποιήσα που προέρχονται από εξωτερικές πηγές έχουν δοθεί οι αρμόζουσες αναγνωρίσεις και αναφορές.

Γεώργιος Α. Χουδαλάκης

Foreword: Low permeability nanocomposite materials and coatings – Outline of this thesis

Low permeability nanocomposite materials can be used in a variety of applications, especially in liquid and food packaging. Generally, polymers present many advantages in comparison with conventional glass containers, such as, e.g., low weight and mechanical strength [Esfandiari et al., 2008]. The cost of the packaging materials represents 17% of the total cost of goods produced. This means that there is a potential for savings through source reduction. For example, there is a general trend to move from glass to lighter plastic bottles. This trend includes the replacement of glass also for sensitive beverages, such as beer and carbonated drinks, where one tries to keep the gas in the bottle, and fruit juice, where one wants to prevent the diffusion of oxygen into the beverage container. The benefits of replacing the glass include cost saving, weight reduction and reduced breakage [Lange and Wyser, 2003].

Polyethylene (PE), Polypropylene (PP) and poly(ethylene terephthalate) (PET) are widely used in bottles and containers. However, their limited barrier properties to oxygen make them inappropriate for products requiring long shelf life. A better solution may be offered by the recently developed polymer/clay nanocomposites. For example, polyester nanocomposites offer superior barrier properties to oxygen and high transparency and are suitable for use in the manufacture of closed containers [Barbee and Matayabas, 2000]. Nanoplatelets reinforced blends are used for barrier properties to oxygen and to organic solvents, as they also offer high mechanical properties [Frounchi et al., 2006; Myung-Ho and Ho, 2006]. Materials for hydrogen storage tanks is another area of applications for organoclay compositions [Jang Bor, 2006]. The use of the microbial barrier properties of the organoclays in polymers has been studied by [Wang et al., 2006].

Some of the desired barrier performances can be achieved by multiple layered structures. However the placing of the oxygen barrier films between two water vapour barrier layers is costly. Thus, there is a demand for oxygen barriers that retain their properties in the presence of water. One additional issue is the increasing demand for transparency where a combination of good barrier properties with (packaged) product visibility is required. Obviously, aluminum and metallised coatings are unable to pro-

vide this combination. Polymer/clay nanocomposites have better chances to be transparent and show good barrier properties.

Most of the commercial applications of polymer/clay nanocomposites use polar polymers, such as nylon and ethylene vinyl acetate. Highly polar polymers, such as those containing hydroxyl groups, are excellent gas barriers but poor water barriers. Non polar hydrocarbon polymers, such as polyethylene, have excellent water barrier properties but poor gas barrier properties. In order to be a truly good barrier material the polymer must have [Salame and Steingiser, 1977]:

- Some degree of polarity
- High chain stiffness
- Close chain-to-chain packing
- Some bonding or attraction between chains
- High glass transition temperature

In practice it has been found that only liquid crystalline polymers and ethylene vinyl alcohol materials among the polymers used in packaging can reach the highest demands for gas barrier properties [Hanika et al., 2003]. Some indicative values for the desirable oxygen permeation rate for food packaging are between 0.1 and 100 cm³/(m²day bar), while for gas storage tanks they are below 0.1 cm³/(m²day bar).

Another possible application for polymer nanocomposites is the area of flexible displays. Electronic devices like OLEDs (Organic Light Emitting Devices) demand high barrier properties. For an OLED lifetime to be > 10000 h the requirements are 10⁻⁶ g/m²day for water vapour transmission rate (WVTR) and 10⁻⁵ cm³/m²day for Oxygen. Flexible displays are extremely sensitive to water vapour and oxygen, which bring about their degradation. The degradation problem can be dealt with by sealing the devices in an inert atmosphere. Therefore, encapsulation of the devices and isolation of the active materials from the atmosphere are very important to prolong the lifetime of flexible devices [Choi et al., 2008].

Another area of research on this subject is the development of coatings incorporating nano-platelets. While this is mostly done to improve the mechanical properties (e.g. “chipping” of automobile paint) [Nobel, 2007; Nobel et al., 2007b,a], the improvement of the barrier properties has not gone unnoticed. Polymeric nanocomposite coatings are alternative inexpensive oxygen barrier materials [Venkata and Kattimuttathu, 2005]. Such anticorrosive coatings can be used on zinc-steel plates for automobiles [Chul and Jun, 2007]. Asphalt nanocomposite based coatings can be useful for materials for building components such as shingles [Vinay and Brian, 2007].

Synthetic polymer coatings have been widely used in the treatment of construction materials of historical monuments for conservation of such structures. Among the various properties [Sadat-Shojaei and Ershad-Langroudi, 2009] like optical transparency, high compatibility with the surface, stability against weathering and UV irradiation, the protective coating must be capable to stop the pollution gases, like sulphur dioxide, and also the water entry. Hybrid polymers are certainly among the most promising

challenges in the fields of packaging, flexible displays and protective coatings in the near future.

The current thesis examines the utilisation of nano-platelets with different aspect ratios for the development of polymeric nanocoatings with exceptional gas barrier properties. A nanocomposite is defined as a composite material in which at least one dimension of at least one component is in the nanometer size scale (<100 nm). The research work included two parts. The first was the development of a polymeric nanocoating under environmentally friendly and practical applicability conditions. For this purpose, a commercial aqueous resin emulsion was used in combination with various types of hydrophilic nanoparticles.

The solution method for coating fabrication was chosen also because other techniques, such as Chemical Vapor Deposition(CVD), generally operate at temperatures 300-500°C, much higher than the softening and melting temperatures of most polymers (125-250°C). Additionally, for layered silicates such as the clays, the low cost and well-established alkyl ammonium cation surface modifiers are thermally unstable above 200°C [Morgan, 2012]. The decomposition of this organic treatment causes the clay to return to organophobic status, which leads to polymer de-intercalation in the clay galleries and subsequent phase separation. With sufficient thermal decomposition, the well-constructed nanocomposite will return to a microcomposite structure and all nanocomposite benefits will be lost.

While the common procedure of mixing the two components is achieved after the surface of the particles has been chemically treated for compatibility, an alternative way was also tested in this study. The idea in the present work was to exploit the presence of the third component of the coating, which is the suspension medium/solvent (water). During the film formation process, the solvent evaporates and the curing reactions take place. Before the evaporation or in the initial stages there is no direct interactions between the hydrophobic polymer and the hydrophilic particles. By a proper choice of the solvent and controlling its evaporation rate, entrapment of the nanoparticles among the resin droplets may be achieved, resulting in a well exfoliated nanocomposite.

The second part of this research was the study of the gas transport properties of the nanocomposite films and their relation with the free volume characteristics of the polymer matrix. Since most commercially available permeation devices are able to measure only the gas transmission rate (permeability), a permeation cell was designed and an experimental apparatus was made capable to measure the three gas transport coefficients (permeability, diffusion, solubility).

The improved gas barrier properties of the polymer nanocoating is based on the fact that the dispersed crystalline layers of the clay act as obstacles to the diffusion of the gas molecules through the coating. In order to by pass them, the gas molecules are forced to follow more complicated/tortuous paths elongating their diffusion length. This elongation will be more effective when the exfoliation degree, the surface area and the volume fraction of the clay are higher. Also, the orientation of the inorganic layers to the diffusion direction affects the tortuosity and therefore the final gas barrier performance of the coating.

Since the free volume of the polymer matrix is one of the most important parameters that determines the transport properties of the composite, the measurement of the free volume and its correlation with the three transport coefficients was aspired. The

incorporation of the inorganic particles in the polymer matrix can cause various effects on the polymer free volume and this inevitably influences the gas barrier properties of the material.

Contents

Foreword: Low permeability nanocomposite materials and coatings – Outline of this thesis	iii
ACKNOWLEDGEMENTS	xi
Nomenclature	xii
Σύνοψη (στα Ελληνικά)	1
1 Nanocomposites	27
1.1 Introduction	27
1.2 Waterborne acrylic resin coatings	31
2 Mass Transport Principles	33
2.1 Gas permeation	33
2.1.1 Gas Permeation in Rubbery Polymers	34
2.1.2 Glassy Polymers	35
2.2 Measurements of the transport coefficients	37
2.2.1 Permeation Cell Procedure	37
2.2.2 Sorption/Desorption Experiments	39
3 Permeability Models	43
3.1 Regular arrangement of parallel nano-platelets	44
3.2 Random spatial positioning of parallel plates	47
3.3 Arrangement of the plates at angles $\theta \neq 90^\circ$ to the main diffusion direction	50
3.4 Influence of particle aggregation	51
3.5 Influence of the interfacial regions	52
3.6 Model validation	53
4 Transport Coefficients and Free Volume	57
4.1 Free Volume	58
4.2 Effects of Nanoparticles	61
4.3 Solubility and Free Volume	62
4.4 Diffusion and Free Volume	63
4.5 Permeability and Free Volume	66

5	Measurement of free volume	69
5.1	PALS	69
5.1.1	Doppler broadening of the annihilation line	73
5.2	Nanocomposites	74
6	Laponite nanocomposites	77
6.1	Experimental	77
6.1.1	Sample preparation	77
6.1.2	Measurements	78
6.2	Results and Discussion	80
6.2.1	X-ray diffraction patterns	80
6.2.2	PALS results	81
6.2.3	Effect of particle content on the free volume	83
6.2.4	Permeability measurements	85
6.3	Conclusions	86
7	Bentonite nanocomposites	89
7.1	Experimental	89
7.1.1	Sample preparation	89
7.1.2	Measurements	91
7.2	Results	91
7.2.1	X-ray Diffraction	92
7.2.2	Transport Coefficients	94
7.3	Discussion	94
7.3.1	The stability of the aqueous suspensions	94
7.3.2	Coating film formation	96
7.3.3	Transport properties	99
7.4	Conclusions	100
8	Hectorite nanocomposites	101
8.1	Li-Hectorites	101
8.2	X-ray results	102
8.3	Transport properties	104
8.3.1	Low-energy or no ultrasonication treatment	104
8.3.2	High-energy ultrasonication treatment	108
8.4	Discussion	108
8.5	Conclusions	112
9	Organo-modified montmorillonite	115
9.1	Sample preparation and characteristics	115
9.2	Solubility parameters and surface tensions	119
9.3	The state of particle deagglomeration	121
9.4	Transport Properties	127
9.5	Conclusions	130
10	General Conclusions and Recommendations	135

Bibliography	151
A δ and γ Calculations	153
A.1 Solubility Parameter	153
A.2 Surface Tension	154
B Sample codes and solvent characteristics	159
C Permeation Measurements	163
C.1 Test measurements	163
C.2 Nanocomposites	164
Index	188
Epilogue	191

ACKNOWLEDGEMENTS

I would like to thank my supervisor prof. Alexandros Gotsis for his continuous support and encouragement during the PhD elaboration. His free scientific perception, far away from intractability, and his optimistic confrontation were the driving forces for my objective and the motivation I needed in order to accomplish the laborious requirements of a PhD project. Most important of all, his entrustment to my face from the offering till the end of the PhD was an honour to me.

I would like to thank prof. Stephen J. Picken and Dr. Henk Schut from the Technical University of Delft for their great hospitality and help during my staying at the Interfaculty Reactor Institute for the PALS measurements. Also, many thanks to Dr. Louise Nobel for the supply of the acrylic resin emulsion.

I deeply thank prof. Josef Breu for his invitation and excellent hospitality at the University of Bayreuth in Germany. His high level scientific team and work was an important experience for me. Also many thanks to Dr. Daniel Kunz for his support and for the supply of the hectorite powder.

I am grateful to prof. Dionysios Mantzavinos of the Environmental Engineering Department for the ultrasound device. Also I thank prof. Georgios Kostakis of the Mineral Resources Engineering Department for the X-ray measurements and Ms. Maria Stratigaki for conducting the PALS measurements of the hectorite samples.

I would like to deeply thank prof. Spiridon Anastasiadis, prof. Dimitrios Vlasopoulos, Dr. Emmanuel Stratakis and Mr. Lampros Papoutsakis of the University of Heraklion and Foundation of Research and Technology (F.O.R.T.H.) for the X-ray and TGA measurements and for the supply of the organo-modified montmorillonite powders. Their hospitality and willingness to help are the most obvious examples that explain why these research foundations are considered to be the best in Greece.

Finally, I thank all seven members of the advisory committee for their thoughtful comments on this dissertation.

Nomenclature

A	surface area, m ² εμβαδόν
A_H	Hamaker constant, = $\pi^2 C \rho_1 \rho_2$ ρ_i : atom number densities of the two interacting bodies; C : interaction constant σταθερά του Hamaker
B	bulk modulus, Pa μέτρο ελαστικότητας μάζας
C	constant (≈ 0.0018) used to evaluate the free volume in eq. 5.5, nm ⁻³ σταθερά στην εξ. 17
C'_H	Langmuir capacity, mol/m ³ χωρητικότητα κατά Langmuir
C_D	concentration of sorbed gas, mol/m ³ συγκέντρωση του προσροφημένου αερίου
C_H	concentration of Langmuir population, mol/m ³ συγκέντρωση κατά Langmuir
D	diffusion coefficient, m ² /s συντελεστής διάχυσης
D_0	diffusion coefficient of the matrix, m ² /s συντελεστής διάχυσης της μήτρας
D_s	diffusion coefficient of the interfacial region, m ² /s συντελεστής διάχυσης περιοχής διεπιφάνειας
E	energy of the positron beam, keV ενέργεια της δέσμης ποζιτρονίων
E	energy, J ενέργεια

E_p	activation energy for permeation, J/mol ενέργεια ενεργοποίησης για τη διαπερατότητα
I	scattering intensity ένταση σκέδασης
I_1	para-positronium annihilation intensity ένταση εξαύλωσης παρα-ποζιτρονίων
I_2	positron direct annihilation intensity ένταση κατ' ευθείαν εξαύλωσης ποζιτρονίων
I_3	ortho-positronium annihilation intensity ένταση εξαύλωσης ορθο-ποζιτρονίων
I_i	intensity of positron annihilation in mode i ένταση εξαύλωσης ποζιτρονίων σύμφωνα με την i -οστή διαδικασία εξαύλωσης
J	mass flux, mol/(m ² s) ροή μάζας
L/W	aspect ratio, length over thickness λόγος διαστάσεων, μήκος προς πάχος
M_t, M_{eq}	mass uptake of the membrane at times t and at equilibrium ροφημένη μάζα στην μεμβράνη σε χρόνο t και στην ισορροπία
$N(t)$	positron lifetime spectrum φάσμα χρόνου ζωής ποζιτρονίων
P	permeability, mol/(m Pa s) συντελεστής διαπερατότητας
P'	parachor, (m ³ /mol) × (mJ/m ²) ^{1/4} παρα-χώρος
$P(q)$	scattering form factor παράγοντας μορφής σκέδασης
R	free volume hole radius, Å ακτίνα οπής ελεύθερου όγκου
R_c	minimum radius of free volume hole for detection via PALS, Å ελάχιστη ακτίνα οπής ελεύθερου όγκου μετρήσιμη με PALS
S	sorption coefficient (solubility), mol/(m ³ Pa) συντελεστής (ρόφησης) διαλυτότητας
S'	orientation parameter παράμετρος προσανατολισμού

$S(q)$	scattering structure factor παράγοντας δομής σκέδασης
S_1, W	Doppler broadening parameters παράμετροι φαινομένου Doppler
T	temperature, °C θερμοκρασία
T_g	glass transition temperature, °C θερμοκρασία υαλώδους μετάπτωσης
T_m	melting point / temperature, °C θερμοκρασία/σημείο τήξης
U	interaction energy, J ενέργεια αλληλεπιδράσεων
U	interaction energy ενέργεια αλληλεπιδράσεων
U_A	van der Waals attraction energy ελκτική ενέργεια van der Waals
U_R	repulsion energy απωθητική ενέργεια
U_{int}	interfacial energy, J/m ² διεπιφανειακή ενέργεια
U_{surf}	energy per unit area, eq. 1.1, J/m ² ενέργεια ανά μονάδα επιφάνειας
V	volume, m ³ όγκος
V_f	free volume Å ³ ελεύθερος όγκος
V_f	volume of reinforcing phase, m ³ όγκος ενισχυτικής φάσης
V_g	specific volume at gas phase, m ³ /kg ειδικός όγκος στην αέρια φάση
V_h	volume of a free volume hole, Å ³ όγκος οπής ελεύθερου όγκου
V_l	specific volume at liquid phase, m ³ /kg ειδικός όγκος στην υγρή φάση
V_m	molar volume, m ³ /mol μοριακός όγκος

V_p	molar volume of gas, m ³ /mol μοριακός όγκος αερίου
V_s	volume of the interfacial region, m ³ όγκος περιοχής διεπιφάνειας
W	platelet thickness, μm πάχος πλακιδίου
Z_0	positron mean implantation depth, Å βάθος εμφύτευσης ποζιτρονίου
ΔG^M	Gibbs free energy of mixing, J/m ³ ελεύθερη ενέργεια ανάμιξης του Gibbs
ΔH^M	enthalpy of mixing, J/m ³ ενθαλπία ανάμιξης
ΔS^M	entropy of mixing, J/m ³ K εντροπία ανάμιξης
α	aspect ratio λόγος διαστάσεων
α	plasticisation power
α_T	thermal expansion coefficient συντελεστής θερμικής διαστολής
$\alpha_{A/B}$	membrane selectivity επιλεκτικότητα της μεμβράνης
β^+	positron ποζιτρόνιο
δ	solubility parameter, MPa ^{1/2} παράμετρος διαλυτότητας
δ_D	dispersive contribution to the solubility parameter, MPa ^{1/2} συνεισφορά διασποράς στην παράμετρο διαλυτότητας
δ_H	hydrogen bonding contribution to the solubility parameter, MPa ^{1/2} συνεισφορά δεσμών υδρογόνου στην παράμετρο διαλυτότητας
δ_P	polar contribution to the solubility parameter, MPa ^{1/2} πολική συνεισφορά στην παράμετρο διαλυτότητας
ℓ, ℓ'	diffusion lengths (eq. 3.3), μm μήκη διαδρομών διάχυσης
γ	surface/interfacial tension, J/m ² (δι)επιφανειακή τάση

λ	X-ray wavelength (nm) μήκος κύματος ακτίνων Χ
\mathbf{r}	position vector διάνυσμα θέσης
ν_e	electron neutrino νετρίνο ηλεκτρονίου
ϕ	volume fraction κλάσμα όγκου
ρ	density, kg/m ³ πυκνότητα
σ	width of the Gaussian distribution εύρος της κατανομής κατά Gauss
τ	tortuosity δαιδαλώδες (πολυπλοκότητα)
τ_1	para-positronium lifetime (s) μέσος χρόνος ζωής παρα-ποζιτρονίων
τ_2	positron lifetime (s) μέσος χρόνος ζωής ποζιτρονίων
τ_3	ortho-positronium lifetime (s) μέσος χρόνος ζωής ορθο-ποζιτρονίου
τ_i	lifetime for positron annihilation in mode i (s) μέσος χρόνος ζωής για εξαύλωση ποζιτρονίων σύμφωνα με την i -οστή διαδικάσια εξαύλωσης
θ	diffraction angle (°) γωνία περίθλασης
\widetilde{D}_0	proportionality (diffusion) coefficient in eq. 4.8, m ² /s συντελεστής αναλογίας για τον συντελεστή διάχυσης στην εξ. 4.8
b	hole affinity constant in eq. 2.10 σταθερά συνάφειας για την οπή στην εξ. 2.10
c	concentration, mol/m ³ συγκέντρωση
c	velocity of light, m/s ταχύτητα του φωτός
c_d	concentration at the low end of the membrane, mol/m ³ συγκέντρωση στη κατάντη πλευρά της μεμβράνης

d	membrane thickness, mm πάχος μεμβράνης
d, d_{001}	distance between (001) planes, Å απόσταση ανάμεσα στα (001) επίπεδα
e^+	positron ποζιτρόνιο
e^-	electron ηλεκτρόνιο
f_V	fractional free volume κλάσμα ελεύθερου όγκου
k_D	Henry's coefficient of solubility, mol/(m ³ Pa) συντελεστής διαλυτότητας κατά Henry
m	size of scattering object μέγεθος του σκεδάζοντος αντικειμένου
m, m_0	mass, kg μάζα
n	diffraction peak order τάξη κορυφής περίθλασης
p	(partial) pressure, Pa (μερική) πίεση
q	scattering vector διάνυσμα σκέδασης
t	time, s χρόνος
t_L	time to steady state, s χρόνος μέχρι τη σταθερή κατάσταση
u^*	critical size of free volume hole for diffusion, Å ³ κρίσιμος όγκος οπής για διάχυση
u_f	mean hole free volume, Å ³ μέσος όγκος οπών
u_s	volume of penetrant molecule, Å ³ όγκος διαχεόμενου μορίου
w	weight fraction κλάσμα βάρους

x, y, z	spatial coordinates χωρικές συντεταγμένες
<i>o-Ps</i>	ortho-positronium όρθο-ποζιτρόνιο
<i>p-Ps</i>	para-positronium πάρα-ποζιτρόνιο
2M2HT	dimethyl, dihydrogenated tallow, quaternary ammonium
2MBHT	dimethyl, benzyl, hydrogenated tallow, quaternary ammonium
AFV	accessible free volume fraction κλάσμα προσβάσιμου ελεύθερου όγκου
BE	Hydrophilic bentonite υδρόφιλος μπεντονίτης
BT	bentonite μπεντονίτης
C10A	natural MMT modified with 2MBHT φυσικός MMT τροποποιημένος με 2MBHT
C20A	natural MMT modified with 2M2HT φυσικός MMT τροποποιημένος με 2M2HT
C30B	natural MMT modified with MT2EtOH φυσικός MMT τροποποιημένος με MT2EtOH
C93A	natural MMT modified with M2HT φυσικός MMT τροποποιημένος με M2HT
CEC	cation exchange capacity ικανότητα ανταλλαγής κατιόντων
CED	cohesive energy density, J/mol πυκνότητα συνεκτικής ενέργειας
DLVO	Derjaguin-Landau-Verwey-Overbeek theory
DSC	Differential Scanning Calorimetry Διαφορική θερμιδομετρία σάρωσης
EDL	electrical double layer διπλή ηλεκτρική στοιβάδα
FFV	fractional free volume κλάσμα ελεύθερου όγκου
M2HT	methyl, dihydrogenated tallow ammonium

MMT Montmorillonite
μοντμοριλλονίτης

MT2EtOH methyl, tallow, bis-2-hydroxyethyl, quaternary ammonium

OLED organic light emitting diode
οργανική φωτοδίοδος

OMBE montmorillonite organically modified with octadecylamine
μοντμοριλλονίτης (MMT) τροποποιημένος με οκταδεσυλαμίνη

OMMT Organo-modified montmorillonite
οργανικά τροποποιημένος μοντμοριλλονίτης

PALS Positron annihilation lifetime spectroscopy
φασματοσκοπία χρόνου ζωής εξασθλωσης ποζιτρονίων

SEM scanning electron microscopy
ηλεκτρονική μικροσκοπία σάρωσης

TEM transmission electron microscopy
ηλεκτρονική μικροσκοπία διέλευσης

WVTR water vapour transmission rate, g/m²day
ρυθμός διαπερατότητας υδρατμού

XRD X-Ray Diffraction
Περιθλασμετρία ακτίνων Χ

OTR oxygen transmission rate, g/m²day
ρυθμός διαπερατότητας οξυγόνου

Σύνοψη

Εισαγωγή

Σε πληθώρα εφαρμογών είναι απαραίτητη η προστασία των προϊόντων (π.χ. τρόφιμα, ηλεκτρονικές συσκευές) από ανεπιθύμητα αέρια που προκαλούν μείωση της διάρκειας χρήσης τους όπως για παράδειγμα το οξυγόνο και οι υδρατμοί. Επομένως υπάρχει η ανάγκη για προστατευτικές επικαλύψεις απέναντι σε αυτούς τους εισβολείς που θα αυξήσουν το χρόνο χρήσης των προϊόντων. Τα υλικά που χρησιμοποιούνται συχνά για επικαλύψεις είναι τα πολυμερή, κυρίως λόγω του χαμηλού τους κόστους και βάρους, αλλά και της υψηλής τους ευκαμψίας. Το γυαλί και το αλουμίνιο είναι οι πιο συνηθισμένες μη πολυμερικές επικαλύψεις (συσκευασίες) για πολλά προϊόντα όπως, π.χ., οιθόνες ή αναψυκτικά.

Το υψηλό τους κόστος σε συνδυασμό με την απουσία των κατά περίπτωση επιθυμητών ιδιοτήτων (ευκαμψία, αντοχή) δημιουργεί την ανάγκη εύρεσης εναλλακτικών υλικών. Χαρακτηριστικό παράδειγμα είναι η επόμενη γενιά οιθονών, οι λεγόμενες εύκαμπτες οιθόνες, στις οποίες δεν είναι δυνατόν να χρησιμοποιηθεί το γυαλί. Άλλα και σε άλλες εφαρμογές που χρησιμοποιούνται πολυμερή, όπως για παράδειγμα χρώματα, βερνίκια κ.λπ., υπάρχει η ανάγκη τόσο για περαιτέρω μείωση του κόστους όσο και του περιορισμού της χρήσης οργανικών διαλυτών που συνήθως περιέχουν.

Όμως τα περισσότερα πολυμερή (εκτός των υγροκρυσταλλικών) παρουσιάζουν σχετικά υψηλή διαπερατότητα σε αέρια και υδρατμούς. Άρα η χρήση τους ως εναλλακτικών υλικών επικάλυψης δεν είναι δυνατή υπό τις παρούσες συνθήκες. Επιβάλλεται επομένως η βελτίωση των ιδιοτήτων φραγής τους. Αυτό είναι δυνατόν να επιτευχθεί με τη χρήση νανοσωματιδίων, όπως ισχυρίζεται και αποδεικνύει η παρούσα διατριβή. Παρόλο που η μελέτη βασίζεται σε πολυμερική ρητίνη κατάλληλη για χρήση ανάλογη αυτής των βερνικιών, αρκετά από τα συμπεράσματα είναι γενικότερα και αφορούν και άλλες κατηγορίες πολυμερών.

Η κεντρική ιδέα για τη μείωση της διαπερατότητας αερίων με τη χρήση νανοσωματιδίων σε πολυμερή, στηρίζεται στην αύξηση του μήκους διάχυσης των μορίων του αερίου κατά τη διέλευσή τους διαμέσου της επικάλυψης. Αυτό οφείλεται στο γεγονός ότι τα κρυσταλλικά νανοσωματιδία παρουσιάζουν σημαντικά μειωμένη διαπερατότητα σε σχέση με την άμορφη πολυμερική μήτρα και έτσι λειτουργούν ως φράγματα στα διαχεόμενα μόρια του αερίου, επιμηκύνοντας σημαντικά το μήκος της διαδρομής τους. Η επιμήκυνση της διαδρομής αυτής μονολεκτικά αναφέρεται ως δαιδαλώδες ή παράγοντας δαιδαλώδους. Είναι προφανές ότι όσο περισσότερο δαιδαλώδης είναι η διαδρομή

(διάχυση) των μορίων του αερίου τόσο μεγαλύτερη θα είναι και η μείωση στη διαπερατότητα.

Γίνεται λοιπόν σαφές ότι όσο καλύτερη είναι η διασπορά των νανοσωματιδίων στην πολυμερική μήτρα τόσο αποτελεσματικότερος θα είναι ο παράγοντας δαιδαλώδους. Επίσης, σε αυτό θα συνεισφέρουν το κλάσμα όγκου των νανοσωματιδίων, ο προσανατολισμός τους σε σχέση με τη διεύθυνση διάχυσης και το μέγεθός της επιφάνειάς τους. Το θέμα που προκύπτει, και που αποτελεί μια μεγάλη πρόκληση, είναι με ποιόν τρόπο θα γίνει η διασπορά των νανοσωματιδίων στην πολυμερική μήτρα, αφού τα δύο αυτά συστατικά είναι τις περισσότερες φορές ασύνβατα μεταξύ τους.

Η πιο συνηθισμένη διαδικασία που ακολουθείται στην περίπτωση αυτή είναι η συμβατοποίηση των δύο συστατικών μέσω της οργανικής τροποποίησης των υδρόφιλων νανοσωματιδίων με κατάλληλες επιφανειοδραστικές ενώσεις. Παρόλο που η οργανική τροποποίηση βελτιώνει το βαθμό αλληλεπίδρασης ανάμεσα στα σωματίδια και το πολυμερές, ωστόσο ο βαθμός διασποράς των σωματιδίων παραμένει σχετικά χαμηλός στα περισσότερα συστήματα που έχουν έως τώρα μελετηθεί με αποτέλεσμα η βελτίωση των ιδιοτήτων φραγής να είναι περιορισμένη.

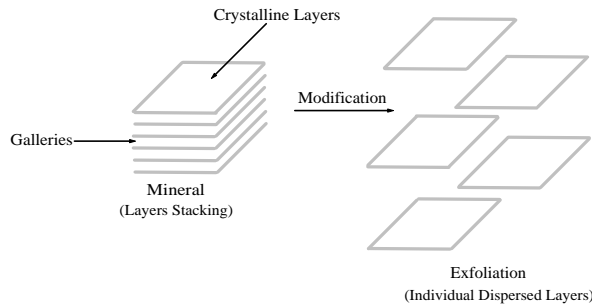
Στην παρούσα διατριβή μελετήθηκε η δυνατότητα βελτίωσης των ιδιοτήτων φραγής επικαλύψεων ακρυλικής ρητίνης με τη χρήση διαφόρων τύπων νανοσωματιδίων τόσο ως προς το μέγεθος και το σχήμα τους όσο και ως προς το είδος του οργανικού τροποποιητή. Για τα σωματίδια χωρίς επιφανειακή τροποποίηση (υδρόφιλα) επιχειρήθηκε η ενσωμάτωση τους στην πολυμερική μήτρα μέσω της διαδικασίας παγιδευσής τους ανάμεσα στα σταγονίδια της ρητίνης και παρεμπόδισης της επανασυσσωμάτωσής τους κατά τη διαδικασία σχηματισμού της επικάλυψης. Η μέθοδος αυτή παρουσιάζει επιτυχία για χαμηλά κλάσματα όγκου των νανοσωματιδίων (1 – 2%) αλλά δεν λειτουργεί επαρκώς για υψηλότερες συγκεντρώσεις.

Πέρα όμως από το βαθμό διασποράς των σωματιδίων, ένας άλλος πολύ σημαντικός παράγοντας για τη βελτίωση ή μη των ιδιοτήτων φραγής της νανοσύνθετης επικάλυψης είναι και ο ελεύθερος όγκος της πολυμερικής μήτρας μέσω του οποίου πραγματοποιείται η διάχυση των μορίων του αερίου. Για το λόγο αυτό διερευνώνται οι επιπτώσεις της μεταβολής του ελεύθερου όγκου που προκαλούνται από την εισαγωγή των ανόργανων νανοσωματιδίων στην οργανική μήτρα στις ιδιότητες φραγής της επικάλυψης. Τα σωματίδια με χαμηλό λόγο διαστάσεων αυξάνουν τον ελεύθερο όγκο, αντισταθμίζοντας τη μείωση από τον παράγοντα δαιδαλώδους, καταστρέφοντας έτσι τις ιδιότητες φραγής του επιστρώματος.

Από την άλλη, σωματίδια με υψηλό λόγο διαστάσεων και, κατά συνέπεια, υψηλό παράγοντα δαιδαλώδους, βελτιώνουν σημαντικά τις ιδιότητες φραγής ακόμα και σε σχετικά μικρά κλάσματα όγκου, όπως πραγματοποιήθηκε στην παρούσα διατριβή σε επικαλύψεις με νανοσωματίδια εκτορίτη, όπου η μείωση στη διαπερατότητα φτάνει τη μια τάξη μεγέθους. Το αποτέλεσμα αυτό αποτελεί μια από τις σημαντικότερες βελτιώσεις που έχουν παρατηρηθεί, κυρίως όσον αφορά επικαλύψεις που παρασκευάζονται με τη μέθοδο της ανάμιξης αιωρημάτων.

Πολυμερή Ενισχυμένα με Φυλλόμορφα Νανοσωματίδια

Τα νανοσύνθετα πολυμερή είναι υβριδικά συστήματα αποτελούμενα από μια πολυμερική μήτρα μέσα στην οποία είναι διασπαρμένα ανόργανα σωματίδια, μια διάσταση



Σχήμα 1: Διαχωρισμός των κρυσταλλικών επιπέδων του αρχικού συσσωματώματος.

των οποίων είναι σε νανομετρική κλίμακα. Μια κατηγορία τέτοιων νανοσωματιδίων είναι τα φυλλόμορφα πυριτικά, τα οποία αποτελούνται από λεπτούς και πλατιούς κρυστάλλους σε σχήμα φύλλων (επιπέδων) διαταγμένους παράλληλα ο ένας στον άλλο. Το πάχος κάθε κρυστάλλου είναι 1 nm ενώ οι όλες τους διαστάσεις κυμαίνονται από 30 nm έως 1000 nm. Στην αρχική τους μορφή, τα φυλλόμορφα ορυκτά, αποτελούνται από συσσωματώματα εκατοντάδων τέτοιων παράλληλων κρυσταλλικών επιπέδων σε μικρή απόσταση μεταξύ τους (~1 nm), τα οποία συγκρατούνται με ελκτικές δυνάμεις Van der Waals.

Για τη δημιουργία ενός νανοσύνθετου υλικού, πρέπει τα επίπεδα αυτά (πλακίδια) να διαχωριστούν μεταξύ τους (Σχ. 1). Αυτό είναι δυνατόν να επιτευχθεί μόνο αν εξασθενήσουν οι ελκτικές δυνάμεις που τα συγκρατούν. Στην αρχική τους μορφή, τα σωματίδια είναι υδρόφιλα και επομένως διογκώνονται στο νερό. Αυτό σημαίνει ότι οι αποστάσεις μεταξύ των παράλληλων επιπέδων αυξάνονται λόγω της αντικατάστασης των αρχικών δεσμών από ασθενέστερους δεσμούς υδρογόνου.

Υπό την επίδραση υπέρηχων στο υδατικό αιώρημα, δίνεται η απαιτούμενη ενέργεια στα πλακίδια ώστε να υπερνικηθούν οι εξασθενημένες δυνάμεις που τα συγκρατούν και να διαχωρισθούν. Το διασπαρμένο αυτό αιώρημα νανοσωματιδίων μπορεί να αναμιχθεί με κάποιο υδρόφιλο πολυμερές (π.χ. πολυβινυλική αλκοόλη) και να προκύψει τελικά ένα νανοσύνθετο υλικό.

Επειδή, όμως, τα περισσότερα πολυμερή είναι υδρόφιβα, η απ' ευθείας ανάμιξή τους με το υδατικό αιώρημα των νανοσωματιδίων δεν είναι δυνατή. Έτσι, είναι απαραίτητη μια συμβατοποίηση ανάμεσα στα υδρόφιλα σωματίδια και στο υδρόφιβο πολυμερές. Οι επιφάνειες των πλακιδίων περιέχουν κατιόντα Na^+ τα οποία μπορούν να αντικατασταθούν από οργανικά κατιόντα (π.χ. κατιόντα αλκυλαμμώνιου) που περιέχουν αλιφατικές αλυσίδες υδρογονανθράκων με τουλάχιστον 12 άτομα άνθρακα. Με απλά λόγια, τα κατιόντα αυτά αποτελούνται από δυο άκρα, το ένα εκ των οποίων είναι πολικό και αντικαθιστά το κατιόν Na^+ στην επιφάνεια του πλακιδίου, ενώ το άλλο άκρο είναι υδρόφιβο και επομένως συμβατό με το πολυμερές.

Με τη διαδικασία αυτή, η οποία ονομάζεται οργανική τροποποίηση, επιτυγχάνονται δύο πράγματα: Πρώτον η αντικατάσταση των κατιόντων Na^+ από τα μεγαλύτερα κα-

τιόντα αλκυλαμμωνίου αυξάνει την απόσταση μεταξύ των παράλληλων κρυσταλλικών επιπέδων εξασθενίζοντας τις ελκτικές δυνάμεις, και δεύτερον συμβατοποιεί το ανόργανο με το οργανικό συστατικό καθιστώντας τα αναμίξιμα.

Η συμβατοποίηση των δυο συστατικών είναι μεν επιθυμητή, δεν εγγυάται όμως τη δημιουργία του νανοσύνθετου υλικού. Και αυτό γιατί εξαρτάται από διάφορους παράγοντες όπως ο βαθμός αλληλεπίδρασης των δυο συστατικών, το κλάσμα όγκου των σωματιδίων, το μέγεθος των πολυμερικών αλυσίδων (η απόσταση των άκρων της αλυσίδας) σε σχέση με το λόγο διαστάσεων των σωματιδίων κ.λπ. Αν η αλληλεπίδραση είναι ισχυρή, τότε οι πολυμερικές αλυσίδες θα εισχωρήσουν στο διάστημα ανάμεσα στα πλακίδια βοηθώντας το διαχωρισμό τους. Αν αυτό δεν συμβεί, τότε ο διαχωρισμός των σωματιδίων δεν θα επιτευχθεί και έτσι θα παραμείνουν στο τελικό υλικό με τη μορφή συσσωματωμάτων.

Η ικανότητα των πολυμερικών αλυσίδων να διαβρέξουν πλήρως τα ανόργανα σωματίδια εξαρτάται, πέρα από το βαθμό αλληλεπίδρασής τους, από το μέγεθος των αλυσίδων και το κλάσμα όγκου των σωματιδίων. Είναι προφανές ότι από ένα κλάσμα όγκου και μετά οι πολυμερικές αλυσίδες δεν μπορούν να διαβρέξουν πλέον τα σωματίδια λόγω της εξαιρετικά μεγάλης τους επιφάνειας και επομένως ο σχηματισμός του νανοσύνθετου είναι αδύνατος. Αυτό συμβαίνει για κλάσματα όγκου μεγαλύτερα του 10% αλλά σε πολλές περιπτώσεις αυτό κλάσμα είναι αρκετά μικρότερο.

Υπάρχουν διάφορες μορφολογίες, ανάλογα με το βαθμό διαχωρισμού των σωματιδίων, που παρατηρούνται συνήθως. Αυτές είναι:

- Κροκιδωμένη ή συσσωματωμένη (flocculated)
- Διογκωμένη, ή μορφολογία παρεμβολής (intercalated)
- Αποφυλλωμένη σε κάποια διάταξη (ordered-exfoliated)
- Αποφυλλωμένη χωρίς κάποια διάταξη (disordered-exfoliated)

Στην μορφολογία παρεμβολής, υπάρχει μια διόγκωση του συσσωματώματος εξαιτίας της μερικής διείσδυσης των πολυμερικών αλυσίδων στα διάκενα ανάμεσα στα κρυσταλλικά επίπεδα. Τα συσσωματώματα αυτά ανιχνεύονται με τις ακτίνες X και μπορεί να εκτιμηθεί η απόσταση μεταξύ των επιπέδων. Στην κροκιδωμένη μορφολογία, υπάρχουν αλληλεπιδράσεις επιπέδου-επιπέδου ή επιπέδου-άκρου μεταξύ των σωματιδίων, δηλαδή, το συσσωμάτωμα αποτελεί ένα συνονθύλευμα συνδεδεμένων σωματιδίων. Οι άλλες δύο μορφολογίες αντιστοιχούν σε πλήρη διαχωρισμό των σωματιδίων, αλλά στην μεν πρώτη υπάρχει ένας προσανατολισμός των επιφανειών των πλακιδίων, ενώ η άλλη αντιστοιχεί σε μια τυχαίου προσανατολισμού διευθέτηση των νανοπλακιδίων

Τα νανοσύνθετα πολυμερή παρουσιάζουν μεγάλο επιστημονικό και τεχνολογικό ενδιαφέρον. Οι μεγάλη ειδική επιφάνεια των διαχωρισμένων νανοπλακιδίων (της τάξης των $750 \text{ m}^2/\text{g}$) διευκολύνουν τη μεταφορά τάσεων από τη μήτρα στην ενισχυτική φάση και εμποδίζουν τη διάδοση ρωγμών βελτιώνοντας σημαντικά τις μηχανικές τους ιδιότητες. Από την άλλη, ο μεγάλος λόγος διαστάσεων (μήκος/πάχος) των πλακιδίων βελτιώνει σημαντικά τις ιδιότητες φραγής αερίων των υλικών αυτών αφού τα κρυσταλλικά σωματίδια παρουσιάζουν πολύ χαμηλή διαπερατότητα σε σχέση με τη μήτρα, λειτουργώντας έτσι ως φράγματα στη διάχυση των μορίων του αερίου μέσα από το υλικό.

Επικαλύψεις υδατικών γαλακτωμάτων ακρυλικής ρητίνης

Κάθε μοντέρνο επίστρωμα (coating) είναι ένα σύνθετο μίγμα που αποτελείται από διάφορα συστατικά. Τα βασικότερα είναι η ρητίνη (το πολυμερές) και ο διαλύτης. Συνήθως υπάρχουν και άλλα συστατικά όπως χρωστικές, πλαστικοποιητές, επιφανειοδραστικά κ.ά. που ονομάζονται πρόσθετα. Τα ακρυλικά πολυμερή που χρησιμοποιούνται στα επιστρώματα, είναι συνήθως εστέρες του ακρυλικού και του μεθακρυλικού οξείος, οι οποίοι πολυμερίζονται μέσω του μηχανισμού των ελευθέρων ριζών.

Οι θερμοσκληρυνόμενες ακρυλικές ρητίνες περιέχουν ομάδες όπως καρβοξύλια και υδροξύλια, τα οποία μπορούν να αντιδράσουν με κάποιο άλλο πολυμερές ή μονομερές όπως π.χ. τη μελαμίνη, σχηματίζοντας ένα δικτυωμένο πλέγμα πολυμερικών αλυσίδων. Η διαδικασία αυτή ονομάζεται δικτύωση και αποτελεί τη σημαντικότερη χημική διεργασία σχηματισμού του φιλμ.

Η ακρυλική ρητίνη περιέχει υδρόφιλες ομάδες. Με την προσθήκη του νερού, τα υδρόφοβα τμήματα των μονομερών συγκεντρώνονται μαζί σχηματίζοντας σταγονίδια. Τα μη πολικά τμήματα βρίσκονται στο κέντρο ενώ τα πολικά στην περιφέρεια των σταγονιδίων αυτών. Έτσι, σχηματίζεται ένα αιώρημα που αποτελείται από τα διασπαρμένα σταγονίδια της ρητίνης και τη συνεχή φάση που είναι το νερό. Για να διασφαλιστεί η σταθερότητα του αιωρήματος αυτού, έχουν προστεθεί επιφανειοδραστικές ουσίες, οι οποίες εμποδίζουν τα σταγονίδια να ενωθούν μεταξύ τους.

Ο σχηματισμός του φιλμ του επιστρώματος κατά την εναπόθεση του αιωρήματος πάνω σε μια επιφάνεια, περιλαμβάνει διάφορες αλληλεπικαλυπτόμενες φυσικοχημικές διαδικασίες. Αρχικά, λόγω της εξάτμισης του διαλύτη λαμβάνει χώρα μια μείωση του όγκου η οποία εξαναγκάζει τα σωματίδια της ρητίνης να έρθουν ολοένα και περισσότερο κοντά μεταξύ τους. Οταν οι απωστικές δυνάμεις ανάμεσα στα σωματίδια υπερνικηθούν, τότε αυτά θα έρθουν σε άμεση επαφή και θα ξεκινήσει η συνένωσή τους. Λόγω τριχοειδών δυνάμεων, τα σταγονίδια αρχίζουν να παραμορφώνονται ενώ ταυτόχρονα ξεκινούν οι αντιδράσεις πολυμερισμού και δικτύωσης μέχρις ότου δημιουργηθεί ένα συνεχές και ομοιόμορφο φιλμ.

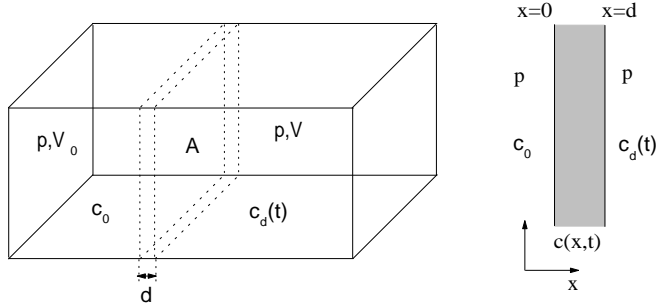
Φαινόμενα μεταφοράς μάζας

Η διαπερατότητα αερίων μέσα από πολυμερική μεμβράνη είναι μια σύνθετη διαδικασία που περιλαμβάνει την προσρόφηση των μορίων του αερίου στην μεμβράνη, η οποία εκφράζεται μέσω του συντελεστή διαλυτότητας, και τη διάχυση τους μέσα από τη μεμβράνη, η οποία εκφράζεται μέσω του συντελεστή διάχυσης. Ο συντελεστής διαπερατότητας είναι το γινόμενο των δύο προηγούμενων δηλαδή:

$$P = D \cdot S , \quad (1)$$

όπου D ($\text{m}^2 \text{s}^{-1}$) ο συντελεστής διάχυσης, S ($\text{mol m}^{-3} \text{Pa}^{-1}$) ο συντελεστής διαλυτότητας και P ($\text{mol m}^{-1} \text{Pa}^{-1} \text{s}^{-1}$) ο συντελεστής διαπερατότητας. Γενικά, η διαδικασία μεταφοράς μάζας περιγράφεται από το νόμο Fick, σύμφωνα με τον οποίο η ροή μάζας διαμέσου της πολυμερικής μεμβράνης καθορίζεται από τη βαθμίδα συγκέντρωσης των μορίων του αερίου:

$$J(\mathbf{r}, t) = -D \nabla c(\mathbf{r}, t), \quad (2)$$



Σχήμα 2: Σχηματική αναπαράσταση του κελιού διαπερατότητας. Η μεμβράνη πάχους d και επιφάνειας A χωρίζει το κελί σε δύο τμήματα. Το αέριο εισάγεται στο αριστερό τμήμα, όγκου V_0 , υπό πίεση 1 atm. Η συγκέντρωση του αερίου που διαπερνά τη μεμβράνη $c_d(t)$ καταγράφεται (στο δεξιό τμήμα) σαν συνάρτηση του χρόνου.

Η παραπάνω εξίσωση σε μια διάσταση και σε συνδυασμό με την εξίσωση συνέχειας, αλλά και με την προϋπόθεση ότι ο συντελεστής διάχυσης είναι ανεξάρτητος της συγκέντρωσης, γίνεται:

$$\frac{\partial c(x, t)}{\partial t} = D \frac{\partial^2 c(x, t)}{\partial x^2} \quad (3)$$

Η διαφορική αυτή εξίσωση μπορεί να λυθεί αναλυτικά με κατάλληλες οριακές συνθήκες. Σε μια μεμβράνη πάχους d , το αποτέλεσμα είναι:

$$c(x, t) = Sp \left[1 - \frac{x}{d} - \frac{2}{\pi} \sum_{m=1}^{\infty} \frac{1}{m} \sin \frac{m\pi x}{d} \exp \left(-\frac{m^2 \pi^2 D t}{d^2} \right) \right]. \quad (4)$$

Η λύση αυτή στην ουσία δίνει τη συγκέντρωση του αερίου μέσα στη μεμβράνη συναρτήσει του χρόνου. Επειδή όμως αυτό που ενδιαφέρει είναι η συγκέντρωση ή η ροή του αερίου που διαπερνά τη μεμβράνη, θέτοντας $x = d$ στην εξ. 4 και αντικαθιστώντας στην εξ. 2 προκύπτει:

$$J(t) = \frac{DSp}{d} \left[1 + \sum_{m=1}^{\infty} 2 \cos m\pi \cdot \exp \left(-\frac{m^2 \pi^2 D t}{d^2} \right) \right]. \quad (5)$$

Η συγκέντρωση του αερίου $c_d(t)$ που διαπερνά τη μεμβράνη βρίσκεται αντικαθιστώντας την εξ. 5 στην $J(t) = dc/Adt$ και ολοκληρώνοντας από 0 ως t :

$$c_d(t) = \frac{ADSp}{Vd} \left[t - \frac{d^2}{6D} - \frac{2d^2}{\pi^2 D} \cdot \sum_{m=1}^{\infty} (-1)^m \frac{\exp(-m^2 \pi^2 D t / d^2)}{m^2} \right]. \quad (6)$$

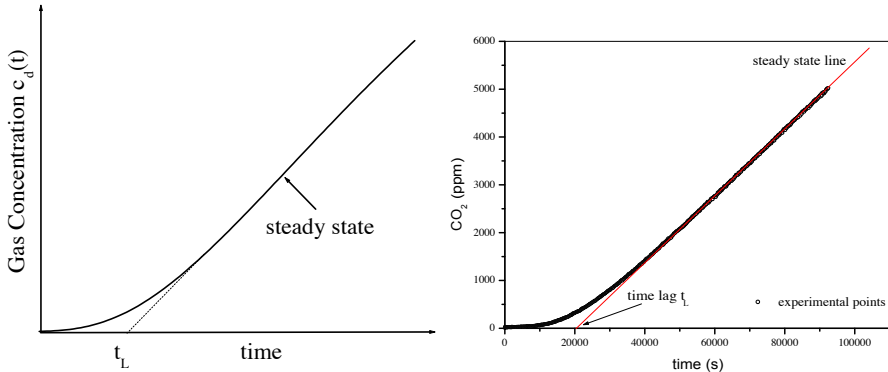


Figure 3: (a) Θεωρητική καμπύλη της συγκέντρωσης του αερίου που διαπερνά τη μεμβράνη συναρτήσει του χρόνου εξ. 6. Το γραμμικό τμήμα είναι η ευθεία σταθερής κατάστασης. (b) Πειραματική καμπύλη μεμβράνης από νανοσύνθετο πολυμερές μετρημένο στο κελί διαπερατότητας.

Για αρκετά μεγάλους χρόνους (σταθερή κατάσταση) η εξ. 6 απλοποιείται στην

$$c_d(t) = \frac{ADSp}{Vd}(t - t_L) \quad (7)$$

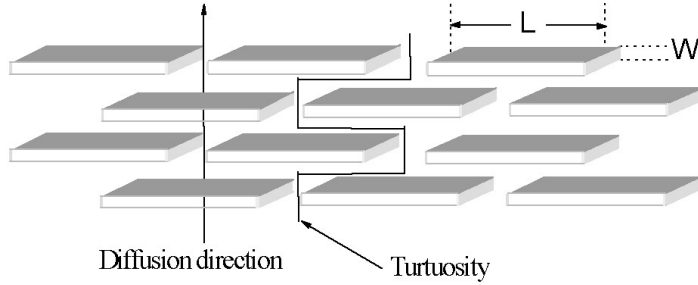
$$\text{όπου} \quad t_L = \frac{d^2}{6D}. \quad (8)$$

Ο χαρακτηριστικός χρόνος t_L είναι ο χρόνος που απαιτείται προκειμένου το σύστημα να φτάσει σε κατάσταση σταθερής ροής. Επομένως από την καμπύλη $c_d(t)$ (Σχ. 3), για αρκετά μεγάλους χρόνους ώστε να αποκατασταθεί σταθερή ροή, ο χρόνος t_L μπορεί να υπολογιστεί και από εκεί ο συντελεστής διάχυσης. Η κλίση της ευθείας δίνει το συντελεστή διαπερατότητας και από την εξ. 1 υπολογίζεται ο συντελεστής διαλυτότητας.

Η συγκέντρωση $c_d(t)$ μπορεί να καταγραφεί πειραματικά με τη χρήση ενός αισθητήρα αερίου ή, εναλλακτικά, με ένα μανόμετρο διαφορικής πίεσης υψηλής ακρίβειας. Επίσης υπάρχει η δυνατότητα να χρησιμοποιηθούν άλλες τεχνικές μέτρησης, όπως η βαρυτομετρική, στην οποία μετράται η αύξηση μάζας της μεμβράνης συναρτήσει του χρόνου με τη βοήθεια ζυγού ακριβείας (πείραμα προσρόφησης). Αντίστροφα, εάν η μεμβράνη έχει προσροφήσει το μέγιστο ποσό αερίου που μπορεί, τότε είναι δυνατόν να μετρηθεί βαρυτομετρικά η μάζα του αερίου που εκροφάται από τη μεμβράνη συναρτήσει του χρόνου (πείραμα εκρόφησης).

Μοντέλα διαπερατότητας αερίων σε ενισχυμένα με νανοσωματίδια πολυμερή

Στα ενισχυμένα με νανοπλακίδια πολυμερή, η διασπαρμένη φάση αποτελείται από ανόργανα κρυσταλλικά επίπεδα. Η διαπερατότητα των μορίων του αερίου μέσα από την κρυσταλλική φάση είναι μια τάξη μεγέθους χαμηλότερη από την αντίστοιχη μέσα



Σχήμα 4: Η ιδανική περίπτωση ορθογωνίων διεσπαρμένων πλακιδίων σε περιοδική διάταξη με τις επιφάνειες τους κάθετες στη διεύθυνση διάχυσης.

από την άμορφη φάση του πολυμερούς. Έτσι, τα νανοσωματίδια μπορούν να θεωρηθούν ως φράγματα στη διάχυση των μορίων του αερίου. Κατά τη διαδικασία διάχυσης επομένως, τα μόρια του αερίου προσπαθούν να παρακάμψουν τα μη διαπερατά ανόργανα σωματίδια αυξάνοντας έτσι το μήκος διάχυσης τους μέσα στο υλικό.

Επομένως η διαπερατότητα θα εξαρτάται από τρεις βασικούς παράγοντες: Το κλάσμα όγκου των σωματιδίων, το λόγο διαστάσεων τους και τον προσανατολισμό των επιφανειών τους σε σχέση με τη διεύθυνση διάχυσης.

Σε πρώτη προσέγγιση, θα θεωρηθεί ότι οι ιδιότητες της μήτρας δεν μεταβάλλονται με την προσθήκη των νανοσωματιδίων. Επίσης θα θεωρηθεί ότι ο συντελεστής διαλυτότητας του νανοσύνθετου θα είναι μειωμένος σε σχέση με αυτόν της μήτρας κατά το κλάσμα όγκου ϕ των σωματιδίων:

$$S_{composite} = S_{matrix}(1 - \phi), \quad (9)$$

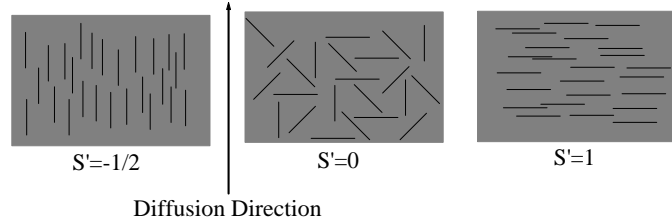
Επειδή το κλάσμα όγκου των σωματιδίων είναι πολύ μικρό, η επίδρασή τους στο συντελεστή διαλυτότητας είναι πολύ μικρή. Επομένως, η βελτίωση των ιδιοτήτων φράγματος θα οφείλεται κυρίως στη μείωση του συντελεστή διάχυσης εξαιτίας του δαιδαλώδους ή πολυπλοκότητας (tortuosity – αλεπάλληλες στροφές που τα μόρια του αερίου πρέπει να υποστούν προκειμένου να παρακάμψουν τα νανοσωματίδια) που δημιουργεί η παρουσία των νανοπλακιδίων.

Ο παράγοντας πολυπλοκότητας τ ορίζεται ως

$$\tau \equiv \frac{\ell'}{\ell}, \quad (10)$$

όπου ℓ' είναι το μήκος διάχυσης παρουσία των νανοσωματιδίων και ℓ το μήκος διάχυσης της μήτρας. Επομένως, αναμένεται ότι ο συντελεστής διάχυσης του νανοσύνθετου θα είναι μειωμένος σε σχέση με αυτόν του καθαρού πολυμερούς κατά τον παράγοντα πολυπλοκότητας:

$$D_{composite} = \frac{D_{matrix}}{\tau}, \quad (11)$$



Σχήμα 5: Τιμές της παραμέτρου τάξης S' για τρεις διαφορετικούς προσανατολισμούς των σωματιδίων.

Ο παράγοντας τ υπολογίστηκε πρώτη φορά από τον Nielsen με γεωμετρικό τρόπο. Για την ιδανική περίπτωση του Σχήμα 4 είναι:

$$\tau = 1 + \frac{L}{2W}\phi, \quad (12)$$

όπου L το μήκος της μεγάλης επιφάνειας των πλακιδίων και W το πάχος τους. Ο λόγος $\alpha = L/W$ είναι ο λόγος διαστάσεων των σωματιδίων. Συνδυάζοντας τις εξ. 1, 9, 11, 12 προκύπτει για τη διαπερατότητα η σχέση:

$$\frac{P_{composite}}{P_{matrix}} = \frac{1 - \phi}{1 + \frac{\alpha}{2}\phi}, \quad (13)$$

Το μοντέλο αυτό προσαρμόζεται ικανοποιητικά με τις πειραματικές μετρήσεις για ρεαλιστικές τιμές του λόγου διαστάσεων. Πρέπει να σημειωθεί ότι ο ακριβής λόγος διαστάσεων είναι δύσκολο να προσδιοριστεί πειραματικά γιαντό λαμβάνεται συνήθως ως ελεύθερη παράμετρος. Επίσης το κλάσμα όγκου των σωματιδίων δεν μπορεί στην πράξη να ξεπεράσει το 10%. Γίνεται λοιπόν σαφές ότι η βελτίωση των ιδιοτήτων φραγής εξαρτάται κυρίως από το λόγο διαστάσεων του ενισχυτικού μέσου, ο οποίος με τη σειρά του καθορίζεται από το βαθμό διαχωρισμού των αρχικών φυλλοπυριτικών συσσωματωμάτων.

Υπάρχουν αρκετά άλλα μοντέλα στη βιβλιογραφία τα οποία παρόλο που έχουν διαφορετική αφετηρία καταλήγουν σε παρόμοιο αποτέλεσμα με αυτό της εξ. 13. Μια γενίκευση του μοντέλου του Nielsen είναι αυτό που προτάθηκε από τον Bharadwaj και το οποίο λαμβάνει υπ' όψιν του και τον προσανατολισμό των σωματιδίων, μέσω της παραμέτρου τάξης S' οι τιμές της οποίας φαίνονται στο Σχ. 5

$$\frac{P_{composite}}{P_{matrix}} = \frac{1 - \phi}{1 + \frac{\alpha}{2} \left(S' + \frac{1}{2} \right) \phi}. \quad (14)$$

Συντελεστές Μεταφοράς και Ελεύθερος Όγκος

Τα παραπάνω μοντέλα έχουν βασιστεί στην υπόθεση ότι η προσθήκη των σωματιδίων δεν αλλάζει τις ιδιότητες της πολυμερικής μήτρας. Όμως αυτό δεν είναι πάντα αληθές διότι τα σωματίδια μπορεί να επηρεάζουν τις φυσικές ιδιότητες του πολυμερούς και, πιο συγκεκριμένα, τις ιδιότητες του ελεύθερου όγκου στο πολυμερές. Είναι προφανές ότι η διαδικασία μεταφοράς μάζας λαμβάνει χώρα μέσα από τον ελεύθερο όγκο της άμορφης μήτρας. Συνεπώς, οποιαδήποτε μεταβολή του ελεύθερου όγκου θα επηρεάσει άμεσα τους συντελεστές αυτούς.

Ελεύθερος όγκος είναι ο χώρος που δεν είναι δυνατόν να καταληφθεί από τις πολυμερικές αλυσίδες (κύριες ή πλευρικές). Για τα υαλώδη πολυμερή, δηλαδή αυτά που βρίσκονται σε θερμοκρασία κάτω από τη θερμοκρασία υαλώδους μετάπτωσης, $T < T_g$, ο ελεύθερος όγκος μπορεί να θεωρηθεί στατικός, αφού οι θερμικές κινήσεις των αλυσίδων είναι σημαντικά περιορισμένες. Δηλαδή οι κενές θέσεις (οπές) βρίσκονται σε συγκεκριμένη θέση και έχουν συγκεκριμένο μέγεθος και σχήμα.

Στα ελαστομερή, όμως, δηλαδή αυτά τα οποία ευρίσκονται σε θερμοκρασία $T > T_g$, οι οπές δεν έχουν τίποτα σταθερό, ούτε θέση, ούτε μέγεθος, ούτε σχήμα, και αυτό γιατί οι πολυμερικές τους αλυσίδες είναι ευκίνητες και μπορούν να κινούνται συνεχώς και ακανόνιστα λόγω θερμικών διεγέρσεων.

Η διαδικασία της προσρόφησης των μορίων του αερίου, θα εξαρτάται αφενός από τις αλληλεπιδράσεις μεταξύ των μορίων του αερίου και του πολυμερούς και αφετέρου από τη διαθεσιμότητα ελεύθερου όγκου. Επομένως ο συντελεστής διαλυτότητας είναι μια θερμοδυναμική παράμετρος που καθορίζεται από το βαθμό συνάφειας αερίου-πολυμερούς και από τον ελεύθερο όγκο.

Από την άλλη, η διαδικασία της διάχυσης λαμβάνει χώρα μέσω αλμάτων των μορίων του αερίου σε γειτονικές ελεύθερες οπές. Επομένως ο συντελεστής διάχυσης αντανακλά την ευκινησία με την οποία κινούνται τα μόρια του αερίου μέσα στον ελεύθερο όγκο του πολυμερούς. Συνεπώς, είναι ένας κινητικός παράγοντας ο οποίος, όμως, δεν καθορίζεται από το συνολικό ελεύθερο όγκο, όπως ο συντελεστής διαλυτότητας, αλλά από τον προσβάσιμο ελεύθερο όγκο. Δηλαδή, εξαρτάται ισχυρά από τη διευθέτηση των στοιχείων του ελεύθερου όγκου στο χώρο (κυρίως για τα υαλώδη πολυμερή), από την κατανομή των μεγεθών των στοιχείων του ελεύθερου όγκου και από την τυχόν ύπαρξη διασυνδεδεμένων μεταξύ τους οπών οι οποίες δημιουργούν κανάλια μεταφοράς μάζας.

Γίνεται λοιπόν σαφές ότι αν η προσθήκη των νανοσωματιδίων στην πολυμερική μήτρα επηρεάζει τις ιδιότητες του ελεύθερου όγκου της, τότε θα επηρεαστούν άμεσα και οι συντελεστές μεταφοράς. Μάλιστα, η επίδρασή των σωματιδίων μπορεί να είναι τέτοια ώστε τελικά να λειτουργήσουν ακόμα και καταστρεπτικά στις ιδιότητες φραγής του νανοσύνθετου.

Κάποιες από τις κύριες επιπτώσεις της προσθήκης των ανόργανων σωματιδίων στον ελεύθερο όγκο του πολυμερούς είναι:

Δημιουργία διεπιφανειών: Λόγω της μεγάλης τους επιφάνειας, τα νανοσωματίδια δημιουργούν εκτεταμένες διεπιφάνειες με την οργανική μήτρα. Οι διεπιφάνειες αυτές δημιουργούν επιπλέον κενούς χώρους και συνεισφέρουν στην αύξηση του συνολικού ελεύθερου όγκου.

Ακινητοποίηση των πλευρικών αλυσίδων: Η ακινητοποίηση τμημάτων των πολυμερικών αλυσίδων αυξάνει τον ελεύθερο όγκο. Η επίδραση της μπορεί να είναι ισχυρή, ειδικά στα ελαστομερή, ή λιγότερο εμφανής, π.χ., στα υαλώδη πολυμερή.

Παρεμπόδιση της κανονικής διευθέτησης των αλυσίδων: Τα σωματίδια καταλαμβάνουν περιοχές όπου κανονικά θα τοποθετούνταν τμήματα της πολυμερικής αλυσίδας καλύπτοντας τον κενό χώρο.

Αλλαγές στην κατανομή μεγεθών των στοιχείων του ελεύθερου όγκου: Η αλλαγές στην κατανομή μεγεθών των οπών του ελεύθερου όγκου μπορεί να έχει δραματικές επιπτώσεις, κυρίως στα υαλώδη πολυμερή. Και αυτό γιατί αλλάζοντας την κατανομή αυτή, η ευκινησία των μορίων του αερίου επηρεάζεται σημαντικά και, επομένως, και ο συντελεστής διάχυσης.

Μέτρηση του ελεύθερου όγκου - εξαῦλωση ποζιτρονίων

Ένας ακριβής και άμεσος τρόπος πειραματικού υπολογισμού του ελεύθερου όγκου είναι η φασματοσκοπία του χρόνου ζωής των ποζιτρονίων. Τα ποζιτρόνια δημιουργούνται από ραδιενέργεια ^{22}Na , το οποίο μεταστοιχειώνεται σε ^{22}Ne με την ταυτόχρονη εκπομπή ενός e^+ και ενός φωτονίου γ ενέργειας 1.28 MeV. Τα ποζιτρόνια που εκπέμπονται από τέτοιες πηγές έχουν μια ενεργειακή κατανομή 0–540 keV και αποκαλούνται «γρήγορα» ποζιτρόνια. Αυτά έχουν αρκετά μεγάλο βάθος διείσδυσης και χρησιμοποιούνται για μετρήσεις του εσωτερικού των δειγμάτων. Κατά την είσοδό τους στο υλικό η ενέργεια τους μειώνεται σημαντικά λόγω των ανελαστικών συγκρούσεών τους με τα ιόντα του μέσου. Φτάνοντας σε θερμικές ενέργειες ~ 0.027 eV, το ποζιτρόνιο διαχέεται στο υλικό (μήκος διάχυσης ~ 100 nm) πριν παγιδευτεί σε κάποια οπή του ελεύθερου όγκου.

Το ποζιτρόνιο είναι το αντισωμάτιο του ηλεκτρονίου και θα εξαῦλωθεί κατά τη σύγκρουσή του με ένα ηλεκτρόνιο δημιουργώντας φωτόνια καθορισμένης ενέργειας, όπως προβλέπεται από την εξίσωση μάζας-ενέργειας του Einstein, $E = m_0c^2$. Όταν τα δύο σωμάτια εξαῦλώνονται στο κενό, η εξαῦλωση μπορεί να λάβει χώρα με τρεις διαφορετικές διαδικασίες. Η πρώτη είναι η άμεση εξαῦλωση η οποία έχει σαν αποτέλεσμα τη δημιουργία δύο φωτονίων με ενέργειες 511 keV που εκπέμπονται σε αντίθετες κατευθύνσεις ως προς το κέντρο μάζας του συστήματος. Οι άλλες δύο διαδικασίες περιλαμβάνουν τη δημιουργία ενός προσωρινού ζ -εύγονου μεταξύ των δύο σωματίων που ονομάζεται «άτομο» ποζιτρονίου και συμβολίζεται ως Ps . Η ενέργεια σύνδεσης αυτού του ατόμου είναι ~ 6.8 eV και η ακτίνα του 1.06 Å. Ανάλογα με την κατάσταση σπin των δύο σωματίων, μπορεί να υπάρξουν δύο είδη Ps : Το $p - Ps$ το οποίο αντιστοιχεί σε αντιπαράλληλα σπin και το $o - Ps$ που αντιστοιχεί σε παράλληλα σπin. Στο κενό, η εξαῦλωση αυτών των ατόμων γίνεται σε χρόνους 0.125 ns για το $p - Ps$ και 140 ns για το $o - Ps$.

Όταν τα ποζιτρόνια εγχέονται σε ένα υλικό, ανάλογες διαδικασίες εξαῦλωσης λαμβάνουν χώρα. Στην περίπτωση αυτή ο σχηματισμός του Ps γίνεται μόνο σε περιοχές χαμηλής ηλεκτρονιακής πυκνότητας όπως οι οπές του ελεύθερου όγκου. Αν δεν υπάρχουν τέτοιες περιοχές, τότε η εξαῦλωση θα πραγματοποιηθεί με την άμεση διαδικασία. Οι χρόνοι ζωής των ελεύθερων και των $p - Ps$ ποζιτρονίων είναι οι ίδιοι όπως και στην

περίπτωση του κενού, αλλά ο χρόνος ζωής του $o - Ps$ μειώνεται σημαντικά από τα 140 ns στα 2–5 ns.

Η μείωση του χρόνου ζωής του $o - Ps$ οφείλεται σε μια διαδικασία που χαρακτηρίζεται ως “pick-off” αντίδραση και στην οποία το ηλεκτρόνιο με το παράλληλο σπίν ανταλλάσσεται με ένα ηλεκτρόνιο αντιπαράλληλου σπίν από το τοίχωμα της οπής. Η μείωση αυτή εξαρτάται από την αλληλεπικάλυψη των κυματοσυναρτήσεων ανάμεσα στο $o - Ps$ και το ηλεκτρονικό νέφος γύρω από την οπή. Σε υλικά με μικρά κενά, η επικάλυψη είναι ισχυρή και η μείωση του χρόνου ζωής είναι μεγάλη.

Ο πειραματικά μετρούμενος χρόνος ζωής του ποζιτρονίου είναι η διαφορά ανάμεσα στην ανίχνευση του 1.28 MeV γ φωτονίου και των 511 KeV φωτονίων. Στα πολυμερή το φάσμα των χρόνων ζωής μπορεί να αναλυθεί σε τρεις συνιστώσες, εξ. 15:

$$F(t) = \sum_{i=1}^3 \frac{I_i}{\tau_i} \exp\left(-\frac{t}{\tau_i}\right), \quad (15)$$

όπου I_i είναι η ένταση και τ_i ο αντίστοιχος χρόνος ζωής της i -οστης διαδικασίας εξαύλωσης. Η πρώτη διαδικασία (I_1, τ_1) έχει χρόνο ζωής $\tau_1 \sim 0.125$ ns και προέρχεται από στην εξαύλωση του $p - Ps$, η δεύτερη (I_2, τ_2) με χρόνο ζωής $\tau_2 \sim 0.4$ ns οφείλεται στην άμεση εξαύλωση των ελεύθερων ποζιτρονίων, και η τρίτη (I_3, τ_3) είναι η pick-off εξαύλωση του $o - Ps$ με χρόνο ζωής από 1 έως 5 ns.

Ο χρόνος ζωής του $o - Ps$ σχετίζεται άμεσα με το μέγεθος της οπής και σύμφωνα με το μοντέλο Tao-Eldrup είναι:

$$\tau_3 = \frac{1}{2} \left[1 - \frac{R}{R + \Delta R} + \frac{\sin \frac{2\pi R}{R + \Delta R}}{2\pi} \right]^{-1}, \quad (16)$$

όπου R η ακτίνα της οπής (θεωρώντας την σφαιρική) και $\Delta R \sim 0.1656$ nm το πάχος του ηλεκτρονιακού νέφους γύρω από την οπή το οποίο θεωρείται ομοιόμορφο. Η αντίστοιχη ένταση I_3 συνδέεται με την πιθανότητα σχηματισμού του $o - Ps$ στις οπές του ελεύθερου όγκου και επομένως αντανακλά τον αριθμό τους. Έτσι ο κλασματικός ελεύθερος όγκος ($FFV = V_f/V$) θα είναι:

$$FFV = CV_h I_3, \quad (17)$$

όπου C μια σταθερά που εξαρτάται από το πολυμερές και V_h ο όγκος κάθε οπής.

Αποτελέσματα και Συζήτηση

Η ακρυλική ρητίνη που χρησιμοποιήθηκε, είναι ένα εμπορικό ακρυλικό γαλάκτωμα σε νερό της Nuplex® με το κωδικό όνομα Setalux 6768®, πυκνότητας $\rho_{resin} = 1.04$ g/cm³, η οποία περιέχει και τον δικτυωτή της και, επομένως, δικτυώνεται μόνη της σε κατάλληλες περιβαλλοντικές συνθήκες. Η διασπορά των ανόργανων σωματιδίων πραγματοποιήθηκε επίσης σε νερό υπό συνθήκες υψηλής διάτμησης και υπερήχων. Για τα οργανικά τροποποιημένα σωματίδια η διασπορά έλαβε χώρα σε αιθανόλη και ακετόνη.

Τα δείγματα που χρησιμοποιήθηκαν για τις μετρήσεις ακτίνων X και διαπερατότητας παρασκευάστηκαν σε υποστρώματα φίλτρων υαλονήματος. Οι διάμετροι των δειγμάτων ήταν 25 mm για τα δείγματα ακτίνων X και 55 mm για τα δείγματα διαπερατότητας, το δε πάχος τους ήταν < 1 mm. Τα φίλτρα υαλονήματος είναι άμορφα και δεν έχουν σημαντική συνεισφορά στις μετρήσεις ακτίνων X. Επίσης είναι πορώδη. Επομένως η διαπερατότητά τους είναι αμελητέα σε σχέση με αυτή του δείγματος.

Οι μετρήσεις ακτίνων X πραγματοποιήθηκαν κυρίως στο περιθλασμέτρο του Πολυτεχνείου Κρήτης με ακτινοβολία CuK_{α} και μήκος κύματος $\lambda = 1.5406 \text{ \AA}$. Μετρήσεις ακτίνων X πραγματοποιήθηκαν επίσης και στο Ίδρυμα Τεχνολογίας και Έρευνας (ITE) στο Ηράκλειο, καθώς και στο Τμήμα Χημείας του Πανεπιστημίου Bayreuth της Γερμανίας με την ίδια ακτινοβολία και μήκος κύματος.

Οι μετρήσεις του ελεύθερου όγκου πραγματοποιήθηκαν στο Διατμηματικό Ινστιτούτο του Αντιδραστήρα του Πολυτεχνείου του Delft της Ολλανδίας, καθώς και στο Πανεπιστήμιο Halle της Γερμανίας. Οι μετρήσεις έλαβαν χώρα σε θερμοκρασία περιβάλλοντος με τη βοήθεια ραδιενεργού πηγής ποζιτρονίων ^{22}Na . Τα δείγματα δεν βρίσκονταν πάνω σε υπόστρωμα και το πάχος τους ήταν περίπου 2 mm ώστε να εξασφαλιστεί ότι τα ποζιτρόνια θα παραμείνουν στο εσωτερικό του δείγματος χωρίς να το διαπεράσουν. Τα φάσματα αναλύθηκαν στα τρία συστατικά τους με τη βοήθεια των προγραμμάτων Positronfit® και LT®.

Οι μετρήσεις των συντελεστών μεταφοράς πραγματοποιήθηκαν σε κελί με τη βοήθεια αισθητήρα διοξειδίου του άνθρακα της Vaisala® με κλίμακα μέτρησης 0-5000 ppm. Ο μέσος χρόνος μέτρησης κάθε δείγματος ήταν περίπου 48 h.

Επικαλύψεις ακρυλικής ρητίνης με νανοσωματίδια λαπονίτη

Τα σωματίδια λαπονίτη είναι νανο-δισκία διαμέτρου 20-30 nm και πάχους 1 nm. Μικρή ποσότητα φωσφονικού εστέρα ($PNP9$, Akzo Nobel) προστέθηκε για τη βελτίωση της συμβατότητας μεταξύ των σωματιδίων και της ακρυλικής ρητίνης. Προετοιμάστηκαν δείγματα με περιεκτικότητες 0, 0.5, 2 και 4.5 w/w% δισκίων λαπονίτη. Τα κλάσματα μάζας ταυτοποιήθηκαν με θερμο-βαρυτομετρικές μετρήσεις (TGA).

Η μορφολογία του νανοσύνθετου ελέγχθηκε με περιθλασμετρία ακτίνων X στην περιοχή $2^\circ < 2\theta < 10^\circ$. Οι ακτίνες X μπορούν να ανιχνεύσουν την ύπαρξη συσσωματωμάτων από την παρουσία της κορυφής στο περιθλασγραμμα που οφείλεται στα κρυσταλλικά επίπεδα (001). Η γωνιακή μετατόπιση της κορυφής προς χαμηλότερες τιμές υποδηλώνει αύξηση της απόστασης των κρυσταλλικών επιπέδων, και αντιστρόφως, σύμφωνα με το νόμο του Bragg:

$$2d_{001} \sin \theta = n\lambda \quad (18)$$

όπου d_{001} η απόσταση των παραλλήλων και ισαπεχόντων κρυσταλλικών επιπέδων (001), 2θ η γωνιακή θέση της κορυφής, λ το μήκος κύματος των ακτίνων X και $n = 1$ η τάξη της περίθλασης.

Πέρα από την ύπαρξη και τη γωνιακή θέση της κορυφής, ένα άλλο χαρακτηριστικό του περιθλασγράμματος είναι η διεύρυνση της κορυφής. Όσο περισσότερα είναι τα κρυσταλλικά επίπεδα στο συσσωμάτωμα, τόσο πιο οξεία είναι η κορυφή που αντιστοιχεί στην ανάκλαση (001) και αντιστρόφως. Επομένως η διεύρυνση της κορυφής υπο-

δηλώνει ότι ο παράγοντας συσσωμάτωσης ελαττώνεται, άρα ένα μέρος των κρυσταλλικών επιπέδων έχει διαχωριστεί από το συσσωμάτωμα. Προφανώς αν το συσσωμάτωμα διαχωριστεί πλήρως τότε η κορυφή εξαφανίζεται από το περιθλασσιγραμμα και αυτό αποτελεί μια ισχυρή ένδειξη επιτυχούς δημιουργίας του νανοσύνθετου υλικού.

Η απουσία κορυφής στο περιθλασσιγραμμα δεν εγγυάται τον πλήρη διαχωρισμό των κρυσταλλικών επιπέδων. Σε κάποιες περιπτώσεις δεν ανιχνεύεται κορυφή αλλά το σύστημα εξακολουθεί να περιέχει συσσωματώματα. Αυτό συμβαίνει είτε επειδή οι εντάσεις των περιθλάμενων ακτίνων X είναι πολύ ασθενείς λόγω του χαμηλού παράγοντα συσσωμάτωσης είτε λόγω της άτακτης (τυχαίας) διευθέτησής τους μέσα στην πολυμερική μήτρα. Αυτή η κατάσταση αντιστοιχεί στην κροκιδωμένη μορφολογία που αναφέρθηκε παραπάνω, στην οποία τα κρυσταλλικά επίπεδα αποτελούν ένα συνονθύλευμα επιπέδων συνδεδεμένων μεταξύ τους με τυχαίο τρόπο. Αυτό το συνονθύλευμα δεν μπορεί να δώσει ανάκλαση Bragg, αλλά αυτό δε σημαίνει ότι τα σωματίδια είναι διαχωρισμένα μεταξύ τους.

Ο παράγοντας συσσωμάτωσης μπορεί να εκτιμηθεί από την περιοχή χαμηλών γωνιών του περιθλασσιγράμματος. Γενικά, η σκεδαζόμενη ένταση I για μικρές γωνίες ($2^\circ < 2\theta < 3^\circ$) συνδέεται με το μέσο μέγεθος των συσσωματωμάτων, και ακολουθεί μια συμπεριφορά $I \sim q^m$ όπου $q = 4\pi \sin \theta / \lambda$ είναι το κυματάνυσμα σκέδασης και m το μέσο μέγεθος των σκεδαζόμενων αντικειμένων. Για πλήρως διαχωρισμένα αντικείμενα η τιμή του m πλησιάζει το -2. Από το διάγραμμα (ευθεία) του $\log I$ συναρτήσει του $\log q$ ο εκθέτης m μπορεί να υπολογιστεί από την κλίση της ευθείας.

Τα XRD διαγράμματα των διαφόρων δειγμάτων παρουσιάζονται στα αντίστοιχα κεφάλαια στο αγγλικό κείμενο (6 έως και 9). Στο διάγραμμα του Σχημ. 6.3, σελ. 81, π.χ., φαίνονται τα περιθλασσιγράμματα για τα δείγματα που περιέχουν δισκία λαπονίτη. Παρόλο που υπάρχει απουσία κορυφής και σε πρώτη προσέγγιση το σύστημα φαίνεται να έχει υψηλό βαθμό διασποράς, ωστόσο είναι εμφανής μια εξάρτηση της σχεδιαζόμενης έντασης στην περιοχή των μικρών γωνιών, από την περιεκτικότητα των σωματιδίων. Πράγματι, οι τιμές του παράγοντα m αυξάνονται συναρτήσει του κλάσματος όγκου των νανοσωματιδίων (Σχημ. 6.4, σελ. 82) γεγονός που υποδηλώνει ότι ο βαθμός διαχωρισμού τους στη μήτρα δεν είναι πλήρης ιδίως για το δείγμα με την υψηλότερη περιεκτικότητα ($m = -2.67$).

Προκειμένου να ελεγχθεί αν η προσθήκη των νανοσωματιδίων λαπονίτη επηρεάζει τις ιδιότητες ελεύθερου όγκου της μήτρας, πραγματοποιήθηκαν μετρήσεις με τη μέθοδο PALS τα αποτελέσματα της οποίας δίνονται στο Σχ. 6.5. Ο χρόνος ζωής τ_3 για την καθαρή ρητίνη είναι 2.175 ns ο οποίος αντιστοιχεί σε ακτίνα οπής 3 Å με βάση την εξ. 16. Η αντίστοιχη ένταση είναι 25.24% και ο κλασματικός ελεύθερος όγκος προκύπτει 5.16% σύμφωνα με την εξ. 17.

Ο χρόνος ζωής του $\sigma - Ps$ παραμένει σχεδόν σταθερός συναρτήσει του κλάσματος όγκου των σωματιδίων (Σχημ. 6.5, σελ. 83). Αυτό σημαίνει ότι το μέσο μέγεθος των οπών του ελεύθερου όγκου δεν μεταβάλλεται. Ανάλογη είναι και η εικόνα που παρουσιάζει η ένταση I_3 η οποία είναι ανάλογη του αριθμού των οπών του ελεύθερου όγκου. Επομένως, εκ πρώτης όψεως τα σωματίδια δεν φαίνεται να επιδρούν στις φυσικές ιδιότητες του πολυμερούς.

Στο Σχ. 6 φαίνονται τα αποτελέσματα των μετρήσεων των συντελεστών μεταφοράς. Τόσο ο συντελεστής διάχυσης όσο και ο συντελεστής διαπερατότητας αυξάνονται συναρτήσει του κλάσματος όγκου των σωματιδίων. Δηλαδή οι ιδιότητες φραγής του

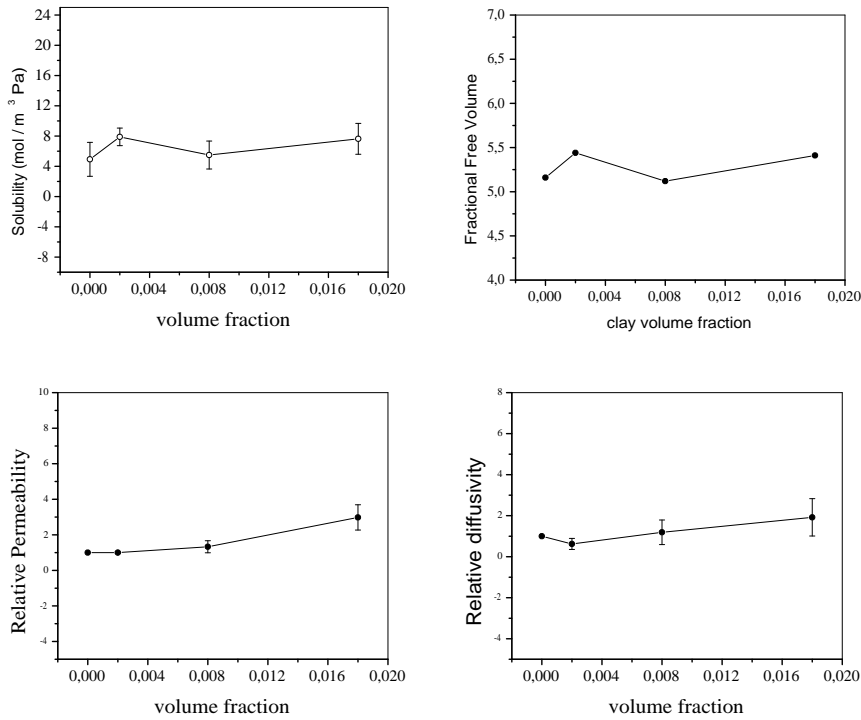


Figure 6: Συντελεστής διαλυτότητας (S), κλασματικός ελεύθερος όγκος (FFV), σχετική διαπερατότητα (P_{comp}/P_{matrix}) και σχετική διαχυτότητα (D_{comp}/D_{matrix}) συναρτήσει του κλάσματος όγκου των νανοσωματιδίων.

αρχικού πολυμερούς έχουν ελαττωθεί αντί να αυξάνονται όπως θα αναμενόταν με βάση τον παράγοντα πολυπλοκότητας που τα σωματίδια δημιουργούν. Το γεγονός αυτό σε συνδυασμό με τα αποτελέσματα των μετρήσεων του ελεύθερου όγκου (ο οποίος δεν φαίνεται να έχει αυξηθεί) έρχονται προς το παρόν σε αντίφαση.

Αν και ο συνολικός ελεύθερος όγκος παραμένει σταθερός, η κατανομή των μεγεθών των οπών του ελεύθερου όγκου μπορεί να αλλάζει από την παρουσία των σωματιδίων. Η αλλαγή στην κατανομή δε συνεπάγεται απαραίτητα και μεταβολή του συνολικού ελεύθερου, αφού για τον ίδιο όγκο είναι δυνατόν να αντιστοιχούν περισσότερες από μια κατανομές μεγεθών. Όπως αναφέρθηκε στα προηγούμενα, η αλλαγή στην κατανομή αυτή μπορεί να προκαλέσει δραστικές μεταβολές στο συντελεστή διάχυσης και κατ' επέκταση στο συντελεστή διαπερατότητας.

Από την άλλη, ο συντελεστής διαλυτότητας είναι σχεδόν σταθερός, και το αξιοσημείωτο είναι ότι η συμπεριφορά του ακολουθεί αυτή του κλασματικού ελεύθερου όγκου ($FFV \sim \tau_3 I_3$), Σχ. 6. Όπως αναφέρθηκε, ο συντελεστής διαλυτότητας αντανακλά το συνολικό ελεύθερο όγκο, επομένως οι δύο ανεξάρτητες μετρήσεις παρουσιάζουν την ίδια συμπεριφορά. Η ταύτιση αυτή επιβεβαιώνει την ακρίβεια της μεθόδου των ποζ-

τρονίων στη μέτρηση του ελευθέρου όγκου.

Επικαλύψεις Ακρυλικής Ρητίνης με Νανοσωματίδια Μπεντονίτη

Τα σωματίδια μπεντονίτη έχουν σχήμα ορθογωνίων πλακιδίων μήκους 300-500 nm και πάχους 1 nm. Ο σχηματισμός του νανοσύνθετου επιχειρήθηκε χωρίς χημική τροποποίηση των σωματιδίων και βασίστηκε στην εξής ιδέα: Τα υδρόφιλα σωματίδια και η οργανική μήτρα δεν είναι συμβατά μεταξύ τους. Όμως, κατά τη διαδικασία σχηματισμού του φιλμ, είναι δυνατόν υπό κάποιες συνθήκες να επιτευχθεί παγίδευση των σωματιδίων ανάμεσα στα σταγονίδια της ρητίνης εμποδίζοντας έτσι την επανασυσσωμάτωσή τους.

Κατά την εξάτμιση του διαλύτη, το ιξώδες αυξάνεται και ο ελεύθερος όγκος μειώνεται. Η επανασυσσωμάτωση των πλακιδίων λαμβάνει χώρα μέσω της διάχυσης τους η οποία εξαρτάται κυρίως από το μέγεθος τους, τη συγκέντρωσή τους και τον ελεύθερο όγκο. Αν η διάχυση τους εμποδίστει, τότε τα σωματίδια θα παραμείνουν διασπαρμένα και κατά το τελικό στάδιο σχηματισμού του φιλμ.

Οσο υπάρχει νερό, οι απωστικές δυνάμεις ανάμεσα στα σωματίδια υπερτερούν. Αν η συγκόλληση των σωματιδίων της ρητίνης γίνει με γρηγορότερο ρυθμό από το ρυθμό διάχυσης των νανοσωματιδίων, τότε αυτό θα έχει ως αποτέλεσμα την παγίδευσή τους. Αυτό είναι δυνατόν, μιας και η εμβέλεια των ελεκτικών δυνάμεων ανάμεσα στα σωματίδια της ρητίνης είναι μεγαλύτερη από την αντίστοιχη μεταξύ των νανοσωματιδίων. Αν το νερό εξατμιστεί γρήγορα, τότε οι απωστικές δυνάμεις καταστρέφονται και η επανασυσσωμάτωση θα λάβει χώρα πριν την παγίδευση των σωματιδίων.

Επομένως, η επιθυμητές συνθήκες είναι ένας σχετικά αργός ρυθμός εξάτμισης του διαλύτη και ένας σχετικά υψηλός ρυθμός της αντίδρασης δικτύωσης. Αν επιδιωχθεί αύξηση της ταχύτητας της αντίδρασης μέσω αύξησης της θερμοκρασίας, αυτό αναπόφευκτα θα επηρεάσει και το ρυθμό εξάτμισης του διαλύτη οδηγώντας σε λιγότερο ικανοποιητικά αποτελέσματα, όπως φαίνεται και στο Σχ. 7.3, σελ. 93. Η κορυφή περίθλασης για τα δείγματα που δικτυώθηκαν στους 80°C είναι περισσότερο εμφανής σε σχέση με αυτή στους 20°C. Για περιεκτικότητες πάνω από 2 vol%, η διαδικασία της παγίδευσης των νανοσωματιδίων δεν είναι πλέον εφικτή αφού οι αποστάσεις μεταξύ τους είναι πολύ μικρές και η επανασύνδεσή τους δεν μπορεί να εμποδιστεί.

Στο Σχ. 7 φαίνονται ο σχετικός συντελεστής διαπερατότητας, ο σχετικός συντελεστής διαχυτότητας και ο συντελεστής διαλυτότητας συναρτήσει του κλάσματος όγκου των σωματιδίων μπεντονίτη. Σε αντίθεση με την περίπτωση του λαπονίτη, τα νανοπλακίδια μπεντονίτη δημιουργούν ένα δαιδαλώδες δίκτυο που αυξάνει σημαντικά το μήκος διάχυσης της τάξης του 40% για 1.3 vol% σωματίδια μπεντονίτη. Η προσαρμογή της εξ. 11 του μοντέλου Nielsen δίνει για το λόγο διαστάσεων των σωματιδίων ($\alpha = L/W$) την τιμή 130, η οποία βρίσκεται μέσα στο διάστημα τιμών που υπολογίστηκε από την περιθλασμετρία ακτίνων X στην περιοχή των μικρών γωνιών (δηλ. $105 < \alpha < 177$).

Από την άλλη, ο συντελεστής διαλυτότητας παρουσιάζει μια αύξηση της τάξης του 20% πιθανότατα λόγω της συνεισφοράς στον ελεύθερο όγκο των διεπιφανειών των δυο συστατικών. Η επίδραση των σωματιδίων στην ακινητοποίηση των πλευρικών τμημάτων των μακροαλυσίδων του πολυμερούς δεν είναι σημαντική μιας και αυτό βρίσκεται στην υαλώδη κατάσταση. Η αλλαγή της κατανομής των μεγεθών των στοιχείων του

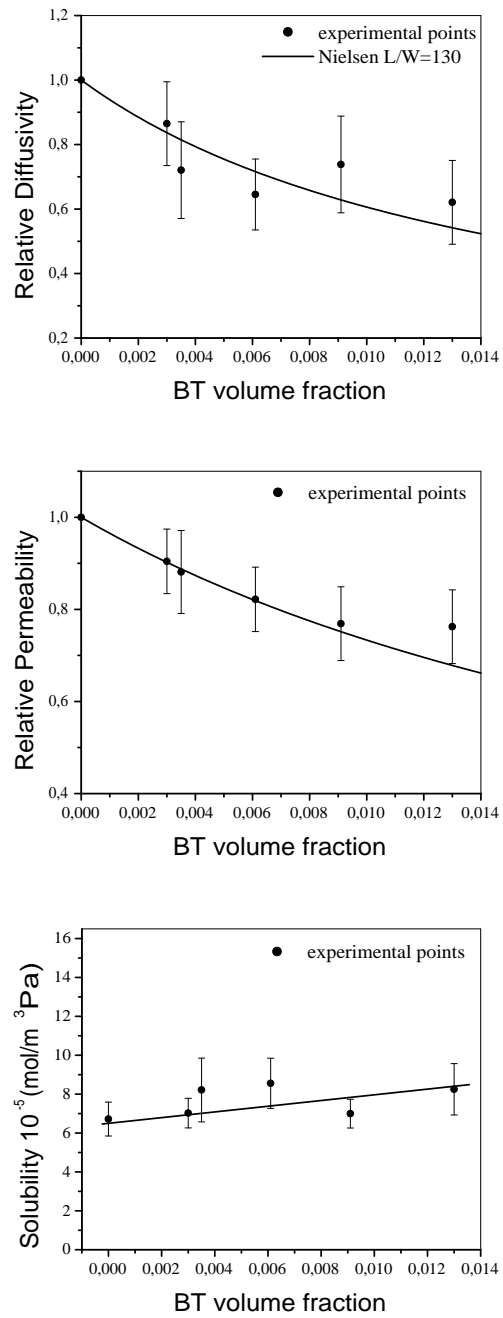


Figure 7: Συντελεστές μεταφοράς μάζας για το νανοσύνθετο ακρυλική ρητίνη/μπεντονίτης συναρτήσει του κλάσματος όγκου των νανοσωματιδίων.

ελεύθερου όγκου, όμως, θα επηρεάσει το συντελεστή διάχυσης και όχι το συντελεστή διαλυτότητας.

Επομένως, η ύπαρξη των διεπιφανειών φαίνεται να είναι η πιο λογική ερμηνεία για την αύξηση του συντελεστή διαλυτότητας. Μπορεί η παγίδευση των νανοσωματιδίων να εμποδίζει την επανασυσσωμάτωσή τους, δημιουργεί όμως χαμηλής πυκνότητας διεπιφάνεις λόγω της ασυμβατότητας των δύο συστατικών. Οι περιοχές αυτές, συνεισφέρουν στην προσρόφηση των μορίων του αερίου γύρω από τα σωματίδια αυξάνοντας έτσι το συντελεστή διαλυτότητας. Η έκταση των διεπιφανειών αυξάνεται όσο αυξάνεται η συγκέντρωση των νανοσωματιδίων. Αυτό περιορίζει τη βελτίωση των ιδιοτήτων φραγής και έτσι ο συντελεστής διαπερατότητας μειώνεται περίπου κατά 25%.

Επικαλύψεις ακρυλικής ρητίνης με νανοσωματίδια εκτορίτη

Η αύξηση του λόγου διαστάσεων των νανοσωματιδίων μπορεί να γίνει κυρίως αν αυξηθεί η παράλληλη διάστασή τους, αφού το πάχος τους δεν μπορεί να είναι μικρότερο του 1 nm. Κάτω από συγκεκριμένες συνθήκες αυτό μπορεί να επιτευχθεί και πραγματοποιήθηκε στο εργαστήριο ανόργανης χημείας του πανεπιστημίου του Bayreuth της Γερμανίας από την ομάδα του καθ. Joseph Breu. Εκεί κατάφεραν να φτιάξουν νανοσωματίδια εκτορίτη με λόγους διαστάσεων της τάξης του 10000. Είναι προφανές ότι η διασπορά των σωματιδίων αυτών στην οργανική μήτρα θα μπορεί να προκαλέσει σημαντική βελτίωση των ιδιοτήτων φραγής του τελικού νανοσύνθετου υλικού.

Στην παρούσα διατριβή παρασκευάστηκαν τρεις σειρές δειγμάτων ακρυλικής ρητίνης/εκτορίτη με διαφορετικές διαδικασίες. Στην πρώτη διαδικασία τα σωματίδια εισήχθησαν στο γαλάκτωμα της ρητίνης με απλή ανάμιξη χωρίς χρήση υπέρηχων ή ισχυρή διατμητική ροή, στη δεύτερη χρησιμοποιήθηκε μπάνιο υπερήχων ενώ στη τρίτη χρησιμοποιήθηκαν ισχυρή διάτμηση και ένα ηχόδιο υπερήχων, το οποίο είναι κατά πολύ ισχυρότερο από το λουτρό υπερήχων.

Όπως διαπιστώθηκε από τα περιθλαστιγράμματα ακτίνων X (Σχ. 8.1, σελ. 103), στην πρώτη περίπτωση υπάρχει μια μικρή διόγκωση των κρυσταλλικών συσσωματωμάτων η οποία εμφανίζεται ως μια μικρή γωνιακή μετατόπιση της γωνίας περίθλασης σε σχέση με αυτή των αρχικών συσσωματωμάτων εκτορίτη. Ανάλογη είναι η εικόνα και στην περίπτωση των δειγμάτων που προετοιμάστηκαν στο λουτρό υπερήχων με τη διαφορά ότι παρατηρείται μια διεύρυνση των κορυφών Bragg που σημαίνει ότι υπάρχει ένα υψηλότερο ποσοστό διεσπαρμένων/διαχωρισμένων κρυσταλλικών επιπέδων. Επομένως το λουτρό υπερήχων έχει μια ασθενή επίδραση στο βαθμό αποφύλλωσης των συσσωματωμάτων διότι η μεταφερόμενη ενέργεια των κυμάτων στα συσσωματώματα δεν είναι αποτελεσματική με αυτό τον τρόπο. Αντίθετα, όταν χρησιμοποιείται ηχόδιο υπερήχων, οι κορυφές Bragg εξαφανίζονται από το περιθλασίγραμμα γεγονός που αποτελεί ισχυρή ένδειξη πλήρους αποφύλλωσης των αρχικών συσσωματωμάτων εκτορίτη.

Ανεξάρτητα από το βαθμό αποφύλλωσης τους, όλα τα δείγματα με ενίσχυση εκτορίτη παρουσίασαν βελτιωμένες ιδιότητες φραγής σε σχέση με την καθαρή οργανική μήτρα, γεγονός που οφείλεται στις τεράστιες διαστάσεις των επιφανειών των σωματίδιων εκτορίτη (Σχ. 8.2, σελ. 105). Για κλάσματα όγκου μικρότερα του 1%, η μείωση της διαπερατότητας είναι της τάξης του 30%, κυρίως λόγω της αρνητικής συνεισφοράς του συντελεστή διαλυτότητας, ο οποίος αυξάνεται κατά 10–25%, που οφείλεται στις διεπιφάνεις μεταξύ των δύο συστατικών. Για κλάσματα όγκου μεγαλύτερα από 1%,

υπάρχει περαιτέρω μείωση της διαπερατότητας που φθάνει μέχρι και μια τάξη μεγέθους για το αποφυλλωμένο δείγμα με 3.7 vol% εκτορίτη (Σχ. 8.4, 107).

Η συμπεριφορά της σχετικής διαχυτότητας παρουσιάζει μια δυαδικότητα σχετικά με τα μοντέλα διαπερατότητας. Στην περιοχή των χαμηλών κλασμάτων όγκου, το μοντέλο του Nielsen προσαρμόζεται ικανοποιητικά στα πειραματικά αποτελέσματα για όλα τα δείγματα. Στην περιοχή των υψηλών κλασμάτων όγκου (> 1 vol%), όμως, το μοντέλο αυτό υποεκτιμά την επίδραση των σωματιδίων στις ιδιότητες φραγής. Αντίθετα, το μοντέλο του Cussler φαίνεται να προσεγγίζει καλύτερα την περιοχή αυτή, ενώ το μοντέλο του Lape αποτελεί μια ενδιάμεση περίπτωση των δύο προηγούμενων.

Από την άλλη, τα μοντέλα σχετικής διαπερατότητας δεν μπορούν να δώσουν αξιόπιστα αποτελέσματα όσον αφορά το λόγο διαστάσεων των σωματιδίων, αφού βασίζονται στην υπόθεση ότι ο συντελεστής διαλυτότητας θα πρέπει να είναι σταθερός ή να μειώνεται με την προσθήκη των κρυσταλλικών σωματιδίων, πράγμα που τις περισσότερες φορές δεν ισχύει, όπως φαίνεται και στα πειραματικά αποτελέσματα, κυρίως για την περιοχή χαμηλών κλασμάτων όγκου. Για τα υψηλότερα κλάσματα όγκου, ο συντελεστής διαλυτότητας είναι σχεδόν σταθερός, οπότε, για την περιοχή αυτή, η προσαρμογή των μοντέλων διαπερατότητας είναι εφικτή.

Ο λόγος διαστάσεων που προκύπτει από την προσαρμογή των μοντέλων (100–400) είναι, παρόλα αυτά, αρκετά χαμηλότερος από αυτόν που θα αναμένονταν με βάση τις τεράστιες παράλληλες διαστάσεις των επιφανειών των σωματιδίων. Πιθανή αιτία για το φαινόμενο αυτό είναι η καμπύλωση των επιφανειών των σωματιδίων, η οποία μειώνει δραστικά τον ενεργό λόγο διαστάσεών τους. Η καμπύλωση αυτή οφείλεται στις δυνάμεις που αναπτύσσονται μεταξύ της υδρόφοβης οργανικής μήτρας και των εύκαμπτων υδρόφιλων ανόργανων σωματιδίων. Προφανώς, όσο μεγαλύτερος είναι ο βαθμός αποφύλλωσης των συσσωματωμάτων, τόσο μεγαλύτερη ευκαμψία θα παρουσιάζουν και, συνεπώς, τόσο μεγαλύτερη θα είναι η καμπύλωσή τους. Στο φαινόμενο αυτό οφείλεται τόσο η αύξηση του συντελεστή διαλυτότητας στην περιοχή των χαμηλών κλασμάτων όγκου, όσο και ο μειωμένος σε σχέση με τον αναμενόμενο βαθμός πολυπλοκότητας.

Όπως έχει αναφερθεί στα προηγούμενα, οι ιδιότητες φραγής εξαρτώνται άμεσα από τις ιδιότητες του ελευθέρου όγκου της οργανικής μήτρας. Κατά τη διαδικασία σχηματισμού του φιλμ ένα μέρος της ποσότητας του διαλύτη παραμένει παγιδευμένο στο εσωτερικό της μεμβράνης. Αυτό δημιουργεί έναν επιπλέον ελεύθερο όγκο, διότι ο χώρος που καταλαμβάνουν τα παγιδευμένα μόρια του διαλύτη θα είχε πιθανώς καλυφθεί από τις πολυμερικές αλυσίδες αν δεν υπήρχαν τα μόρια αυτά κατά τη διαδικασία της δικτύωσης.

Προκειμένου να μελετηθεί η επίδραση του επιπλέον αυτού ελεύθερου όγκου στους συντελεστές μεταφοράς μάζας, δύο μεμβράνες θερμάνθηκαν σε θερμοκρασίες πάνω από τη θερμοκρασία υαλώδους μετάπτωσης της ρητίνης για 24 ώρες ώστε να απομακρυνθεί η παγιδευμένη ποσότητα του διαλύτη, και έπειτα μετρήθηκαν ξανά στο κελί διαπερατότητας (Σχ. 8.5, σελ. 109). Η μεταβολή του βάρους της μεμβράνης κατά τη διαδικασία της θέρμανσης ήταν περίπου 3% και για τα δύο δείγματα. Η αύξηση των συντελεστών διάχυσης και διαπερατότητας και για τα δύο δείγματα ήταν περίπου 40% ενώ ο συντελεστής διαλυτότητας δεν παρουσίασε σημαντική μεταβολή.

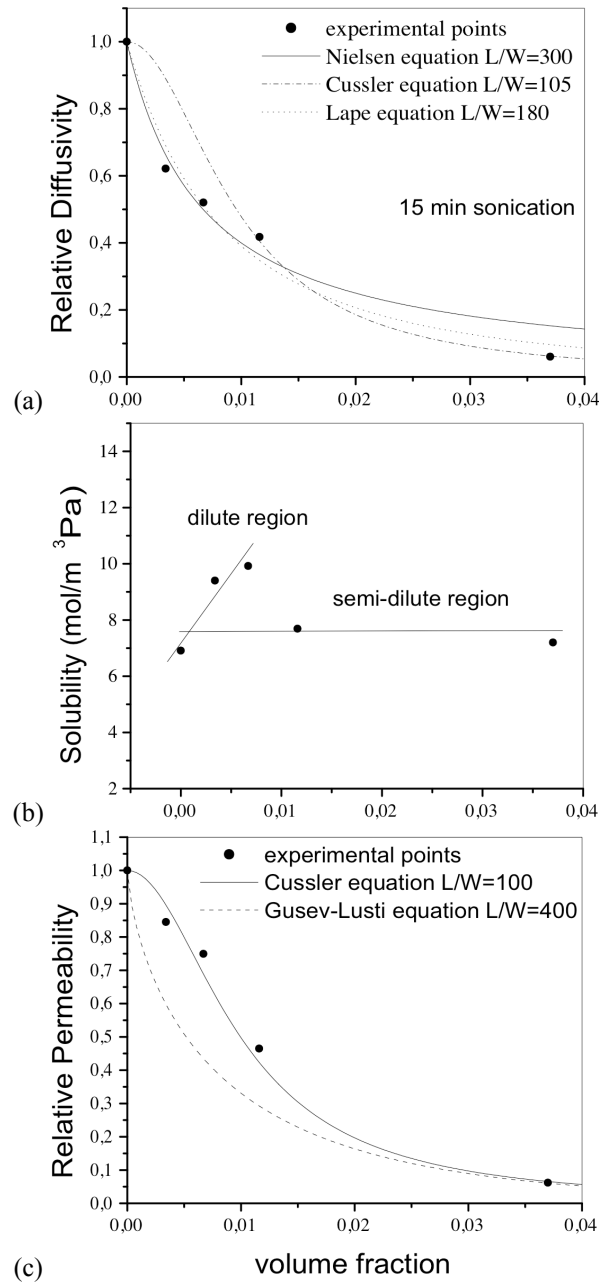


Figure 8: Συντελεστές μεταφοράς μάζας για το νανοσύνθετο ακρυλική ρητίνη/εκτορίτης συναρτήσει του κλάσματος όγκου των νανοσωματιδίων.

Επικαλύψεις ακρυλικής ρητίνης με οργανικά τροποποιημένα νανοσωματίδια μοντμορίλλονίτη

Η βελτίωση της συμβατότητας μεταξύ της οργανικής μήτρας και των ανόργανων κρυσταλλικών νανοσωματιδίων, απαιτεί τη χρήση οργανικών τροποποιητών οι οποίοι αντικαθιστούν τα κατιόντα Na^+ στην επιφάνεια των σωματιδίων μειώνοντας το επιφανειακό τους φορτίο και την επιφανειακή τους τάση. Η αντικατάσταση αυτή, εξασθενεί τις ελκτικές δυνάμεις ανάμεσα στα κρυσταλλικά επίπεδα αυξάνοντας έτσι την απόσταση μεταξύ τους.

Προφανώς, η διασπορά των τροποποιημένων σωματιδίων δεν μπορεί να λάβει χώρα κατ' ευθείαν στο νερό, αλλά πρώτα σε κάποιον οργανικό διαλύτη. Η επιλογή του διαλύτη δεν είναι απλή υπόθεση διότι πρέπει να πληρεί 3 προϋποθέσεις:

- Οι παράμετροι διαλυτότητας του διαλύτη και του οργανικού τροποποιητή των σωματιδίων πρέπει να είναι παραπλήσιες, διότι σε διαφορετική περίπτωση η προσθήκη των σωματιδίων στον διαλύτη θα δημιουργήσει γέλη (διαχωρισμός φάσεων).
- Η επιφανειακή τάση του διαλύτη πρέπει να είναι μεγαλύτερη ή ίση με αυτή των σωματιδίων ώστε να υπάρξει πλήρης διαβροχή και άρα πλήρης διαχωρισμός τους υπό την επίδραση των υπερήχων.
- Επειδή το αιώρημα των διεσπαρμένων σωματιδίων θα προστεθεί στο υδατικό γαλάκτωμα της ακρυλικής ρητίνης, θα πρέπει ο οργανικός διαλύτης να είναι αναμίξιμος με το νερό.

Γίνεται σαφές από τα παραπάνω, ότι η εύρεση διαλύτη που να ικανοποιεί και τις τρεις προϋποθέσεις είναι σχεδόν αδύνατη. Η αιθανόλη και η ακετόνη είναι δύο διαλύτες που ικανοποιούν τα κριτήρια της παραμέτρου διαλυτότητας και της αναμιξιμότητας με το νερό αλλά η επιφανειακή τους τάση είναι μικρότερη από αυτή των σωματιδίων. Έτσι η διασπορά των σωματιδίων σε αυτούς τους διαλύτες είναι δύσκολη ακόμα και υπό την επίδραση ισχυρής διάτμησης και υπερήχων.

Η ακετόνη έχει υψηλότερη διπολική ροπή από την αιθανόλη αλλά μικρότερη ικανότητα σχηματισμού δεσμών υδρογόνου. Γιαυτό είναι και λιγότερο αναμιξιμη με το νερό. Από την άλλη, παρουσιάζει χαμηλότερο σημείο βρασμού και είναι περισσότερο πτητική από την αιθανόλη, γεγονός που δημιουργεί προβλήματα στον σχηματισμό του φίλμ (δημιουργία φυσαλίδων και πόρων) κατά τη διάρκεια της δικτύωσης. Αυτές οι ατέλειες καθιστούν τη μέτρηση των συντελεστών μεταφοράς στο κελί διαπερατότητας για αυτά τα δείγματα αδύνατη.

Έξι διαφορετικού τύπου τροποποιημένα σωματίδια δοκιμάστηκαν στην αιθανόλη, και έξι νανοσύνθετα παρασκευάστηκαν με παραπλήσιες περιεκτικότητες σωματιδίων. Τα αποτελέσματα της περιθλασμετρίας ακτίνων X (Σχ. 9.3, σελ. 125) έδειξαν (001) ανάκλαση Bragg για τα τρία εκ των δειγμάτων, ενώ για τα υπόλοιπα δεν υπήρξε ένδειξη κορυφής, οπότε ο βαθμός διασποράς των σωματιδίων σε αυτά αναμένεται να είναι ικανοποιητικός.

Με βάση τα αποτελέσματα αυτά, πέντε διαφορετικές συγκεντρώσεις για κάθε τύπο νανοσωματιδίων από τους τρεις παραπάνω παρασκευάστηκαν και ελέγχηκε με μεγαλύτερη λεπτομέρεια τόσο η μορφολογία τους όσο και οι ιδιότητες φραγής τους. Στην

περίπτωση του τροποποιημένου μπεντονίτη, το περιθλαστήραμμα ακτίνων X δείχνει ικανοποιητικό βαθμό διασποράς, παρατηρείται όμως μια πολύ ασθενής κορυφή για $2\theta \approx 6.2^\circ$ που αντιστοιχεί σε αυτή των μη τροποποιημένων σωματιδίων μπεντονίτη (Σχ. 9.4, σελ. 126). Το γεγονός αυτό σημαίνει ότι η αιθανόλη αντιδρά με τον οργανικό τροποποιητή. Έτσι, εξουδετερώνοντας τον τροποποιητή, τα απογυμνωμένα σωματίδια επανασυσσωματώνονται στις αρχικές τους αποστάσεις.

Αλλά ας δούμε με μεγαλύτερη λεπτομέρεια τι ακριβώς συμβαίνει: Το αρχικό αιώρημα των σωματιδίων στον διαλύτη, μετά την επίδραση της υψηλής διάτμησης και των υπερήχων, περιέχει ένα μικρό ποσοστό διεσπαρμένων νανοπλακιδίων και ένα μεγαλύτερο ποσοστό συσσωματωμάτων. Αυτό συμβαίνει διότι η επιφανειακή τάση του διαλύτη είναι μικρότερη από αυτή των σωματιδίων με αποτέλεσμα η διασπορά τους να μην είναι πλήρης. Επομένως, η αιθανόλη θα αντιδράσει και θα εξουδετερώσει τον τροποποιητή των διεσπαρμένων σωματιδίων αφήνοντας ανέπαφο αυτόν των συσσωματωμάτων αφού δεν μπορεί να εισχωρήσει ανάμεσα στα κενά των κρυσταλλικών επιπέδων.

Όταν το αιώρημα αυτό αναμιχθεί με εκείνο της ακρυλικής ρητίνης, τα σωματίδια που ήταν αρχικά διασπαρμένα και δεν περιέχουν πλέον οργανικό τροποποιητή θα επανασυσσωματωθούν, ενώ τα συσσωματώματα που περιέχουν τον τροποποιητή είναι συμβατά με τη ρητίνη και αλληλεπιδρούν ισχυρά με αυτή. Η ρητίνη εισχωρεί ανάμεσα στα κρυσταλλικά επίπεδα του συσσωματώματος βοηθώντας το διαχωρισμό τους. Έτσι, γίνεται μια αντιστροφή της αρχικής κατάστασης, δηλαδή το μεγαλύτερο ποσοστό των αρχικά μη διεσπαρμένων σωματιδίων διασπείρεται και το αρχικά μικρό ποσοστό των διεσπαρμένων σωματιδίων επανασυσσωματώνονται. Να σημειωθεί εδώ ότι η διαδικασία της παγίδευσης των σωματιδίων, που αναφέρθηκε στα προηγούμενα, δεν είναι ιδιαίτερα αποτελεσματική σε αυτή την περίπτωση, διότι το μίγμα αιθανόλης/νερού είναι πολύ πιο πτητικό από το νερό και εξατμίζεται με πολύ πιο γρήγορο ρυθμό.

Ανάλογη είναι και η εικόνα που παρατηρείται για την περίπτωση των οργανικά τροποποιημένων σωματιδίων μοντμορίλλονίτη (C25A και C93A). Στις μικρές συγκεντρώσεις δεν παρουσιάζεται κορυφή περίθλασης ενώ για τις μεγαλύτερες αρχίζει να εμφανίζεται για το μεν C25A για $2\theta = 5^\circ$ ενώ για το C93A για $2\theta = 4^\circ$. Εδώ η γωνιακή μετατόπιση της κορυφής περίθλασης δεν είναι στις 6.2° όπως για τον οργανικό τροποποιημένο μπεντονίτη, γεγονός που υποδηλώνει ότι η επίδραση της αιθανόλης στους τροποποιητές αυτούς είναι λιγότερο ισχυρή. Ειδικότερα για τον C93A ουσιαστικά δεν υπάρχει μετατόπιση και η κορυφή εμφανίζεται σχεδόν στην ίδια περιοχή με αυτή των αρχικά τροποποιημένων σωματιδίων.

Ο βαθμός διασποράς των σωματιδίων C25A και C93A αναμένεται υψηλότερος σε σχέση με τους υπόλοιπους επειδή παρουσιάζουν τις μεγαλύτερες αρχικές αποστάσεις κρυσταλλικών επιπέδων. Επομένως οι ιδιότητες φραγής τους θα είναι περισσότερο βελτιωμένες σε σχέση με αυτές του οργανικά τροποποιημένου μπεντονίτη. Πράγματι (Σχ. 9.6 και 9.7), οι σχετικοί συντελεστές διάχυσης για τους C25A και C93A ακολουθούν το μοντέλο της διαδαλώδους διαδρομής για την τιμή του λόγου διαστάσεων $L/W = 200$ και παρουσιάζουν μια συνολική μείωση της τάξης του 30% για μόλις 0.6 vol % σωματίδια.

Όμως, η αύξηση του συντελεστή διαλυτότητας κατά 30-40% περιορίζει τη μείωση του συντελεστή διαπερατότητας στο 15-20%. Η συμπεριφορά του συντελεστή διαλυτότητας υποδηλώνει αφενός τη δημιουργία ελεύθερου όγκου στις περιοχές των

διεπιφανειών και αφετέρου την αλληλεπίδραση μεταξύ των μορίων του διοξειδίου του άνθρακα με τον οργανικό τροποποιητή, ο οποίος λειτουργεί ως κέντρο προσρόφησης των μορίων του αερίου.

Τα δείγματα με τον οργανικά τροποποιημένο μπεντονίτη, από την άλλη, δείχνουν μια λίγο διαφορετική εικόνα, κυρίως όσον αφορά το συντελεστή διάχυσης (Σχ. 9.5, σελ. 128). Η σχετική μείωση του συντελεστή διάχυσης, αποκλίνει από το μοντέλο της δαιδαλώδους διαδρομής και παρουσιάζει μια γραμμική συμπεριφορά. Αυτό σημαίνει ότι ο παράγοντας πολυπλοκότητας των σωματιδίων είναι λιγότερο ισχυρός σε σχέση με τα προηγούμενα δείγματα των C25A και C93A, γεγονός που οφείλεται στο χαμηλότερο βαθμό διαχωρισμού των σωματιδίων. Όπως και στα προηγούμενα δείγματα, έτσι και εδώ ο συντελεστής διαλυτότητας παρουσιάζει σημαντική αύξηση της τάξης του 40%. Αυτό, σε συνδυασμό με τον χαμηλό βαθμό πολυπλοκότητας, οδηγεί τον συντελεστή διαπερατότητας να παραμένει σχεδόν σταθερός.

Συμπεράσματα

Στην παρούσα διατριβή μελετήθηκε η επίδραση στα μορφολογικά χαρακτηριστικά, τον ελεύθερο όγκο και τις ιδιότητες μεταφοράς μάζας, της προσθήκης ανόργανων ανισομετρικών κρυσταλλικών σωματιδίων στην οργανική μήτρα ακρυλικών νανοσύνθετων επικαλύψεων. Το σχήμα, το μέγεθος, το κλάσμα όγκου, ο τύπος του οργανικού τροποποιητή των ανόργανων σωματιδίων, καθώς και οι επιδράσεις των διαλυτών και οι θερμοδυναμικές αλληλεπιδράσεις μεταξύ των δύο συστατικών ελέγχθηκαν και αναλύθηκαν κυρίως με τρεις πειραματικές τεχνικές, όπως η περιθλασμετρία ακτίνων X, η φασματοσκοπία του χρόνου ζωής των ποζιτρονίων και η μέθοδος του κελίου διαπερατότητας.

Η προσθήκη σωματιδίων χαμηλών διαστάσεων στην οργανική μήτρα (λαπονίτης) προκαλεί σημαντικές μεταβολές στις ιδιότητες του ελεύθερου όγκου της και, σε συνδυασμό με το χαμηλό βαθμό πολυπλοκότητας που αυτά δημιουργούν, δεν βελτιώνουν τις ιδιότητες φραγής του τελικού νανοσύνθετου υλικού, αλλά, αντιθέτως, μπορούν να τις καταστρέψουν. Από την άλλη, η προσθήκη σωματιδίων με σημαντικά μεγαλύτερο λόγο διαστάσεων (μπεντονίτης) βελτιώνει τις ιδιότητες φραγής, όχι όμως σε σημαντικό βαθμό λόγω της αρνητικής συνεισφοράς των διεπιφανειών, αλλά και του γεγονότος ότι η διασπορά του στην οργανική μήτρα δεν μπορεί να ξεπεράσει το 2% κατ' όγκο, εξαιτίας της ισχυρής τάσης επανασυσσωμάτωσης των υδρόφιλων κρυσταλλικών επιπέδων.

Αντίθετα, τα υδρόφιλα σωματίδια εκτορίτη, λόγω των ιδιαίτερα υψηλών παράλληλων διαστάσεων, αλλά και του γεγονότος ότι είναι δυνατόν να διασπαρούν σε μεγαλύτερα κλάσματα όγκου στην οργανική μήτρα λόγω της αποτελεσματικότερης παγίδευσής τους, μπορούν να βελτιώσουν τις ιδιότητες φραγής της νανοσύνθετης επικαλυψης κατά, τουλάχιστον, μια τάξη μεγέθους. Από την άλλη, η χρήση οργανικά τροποποιημένων ανόργανων σωματιδίων δε φαίνεται να βελτιώνει σημαντικά τις ιδιότητες φραγής, κυρίως λόγω της χαμηλού βαθμού αποφύλλωσης των κρυσταλλικών επιπέδων στον οργανικό διαλύτη, αλλά και στη σημαντική αύξηση του συντελεστή διαλυτότητας, εξαιτίας του οργανικού τροποποιητή.

Προκειμένου να βελτιστοποιηθούν οι ιδιότητες φραγής των νανοσύνθετων επικαλύψεων, πέρα από το λόγο διαστάσεων και το κλάσμα όγκου της ανόργανης ενίσχυσης,

Θα πρέπει να αποφευχθούν τα ακόλουθα: Η καμπύλωση των κρυσταλλικών επιπέδων, η ύπαρξη συνάφειας μεταξύ του υπό εξέταση αερίου και του οργανικού τροποποιητή, οι εκτεταμένου όγκου και χαμηλής πυκνότητας διεπιφάνειες μεταξύ των δύο συστατικών και ο επιπλέον ελεύθερος όγκος που προέρχεται από τα παγιδευμένα μόρια του διαλύτη κατά τη διαδικασία σχηματισμού του φιλμ.

Περιεχόμενα Αγγλικού κειμένου

Τα επόμενα κεφάλαια (Αγγλικό κείμενο) περιέχουν:

Κεφάλαιο 1: Εισαγωγή στα νανοσύνθετα πολυμερή που περιλαμβάνει τα χαρακτηριστικά της ενισχυτικής φάσης, τις πιθανές μορφολογίες των νανοσύνθετων πολυμερών και μια γενική περιγραφή του υδατικού γαλακτώματος της ακρυλικής ρητίνης που χρησιμοποιήθηκε.

Κεφάλαιο 2: Περιγράφονται οι βασικές αρχές των φαινομένων μεταφοράς μάζας για τα ελαστομερή και τα υαλώδη πολυμερή. Παρουσιάζονται επίσης οι δύο βασικές μέθοδοι για τη μέτρηση των συντελεστών μεταφοράς μάζας (διάχυση, διαλυτότητα, διαπερατότητα) που είναι η μέτρηση στο κελί διαπερατότητας και τα πειράματα προσρόφησης/εκρόφησης.

Κεφάλαιο 3: Αναφέρεται η βασική ιδέα στην οποία στηρίζεται η βελτίωση των ιδιοτήτων φραγής των νανοσύνθετων πολυμερών και παρουσιάζονται τα μοντέλα διαπερατότητας που έχουν προταθεί για τα υλικά αυτά. Γίνεται επίσης σύγκριση και πειραματική επαλήθευση των μοντέλων αυτών.

Κεφάλαιο 4: Αναλύεται η έννοια του ελεύθερου όγκου στα πολυμερή και περιγράφεται η εξάρτησή του από τη θερμοκρασία και το είδος του πολυμερούς (υαλώδες, ελαστομερές). Αναφέρονται οι πιθανές επιδράσεις που προκαλεί η εισαγωγή των νανοσωματιδίων στον ελεύθερο όγκο της πολυμερικής μήτρας. Επίσης γίνεται μια συσχέτιση ανάμεσα στους συντελεστές μεταφοράς μάζας και τον ελεύθερο όγκο η οποία επαληθεύεται και με πειραματικά δεδομένα από τη βιβλιογραφία.

Κεφάλαιο 5: Περιγράφονται οι βασικές αρχές της μεθόδου μέτρησης του ελεύθερου όγκου που είναι η φασματοσκοπία του χρόνου ζωής των ποζίτρονίων. Επίσης αναφέρονται πειραματικά αποτελέσματα μετρήσεων του ελεύθερου όγκου σε νανοσύνθετα πολυμερή από τη βιβλιογραφία.

Κεφάλαιο 6: Στο κεφάλαιο αυτό μελετώνται τα χαρακτηριστικά διαπερατότητας της νανοσύνθετης επικάλυψης που περιέχει διασπαρμένα νανο-δισκία λαπονίτη. Οι επιδράσεις των νανοσωματιδίων στον ελεύθερο όγκο της πολυμερικής μήτρας εξετάζονται με τη μέθοδο της φασματοσκοπίας εξαφάνισης των ποζίτρονίων και με μετρήσεις των συντελεστών μεταφοράς στο κελί διαπερατότητας.

Κεφάλαιο 7: Διερευνάται η προσθήκη υδρόφιλων νανοπλακιδίων μπεντονίτη στην

πολυμερική επικάλυψη με στόχο τη βελτίωση των ιδιοτήτων φραγής του τελικού νανοσύνθετου επιστρώματος. Αναλύεται η διαδικασία σχηματισμού της νανοεπικάλυψης και ο μηχανισμός παγίδευσης των νανοσωματιδίων ανάμεσα στα σταγονίδια της ρητίνης κατά τη διάρκεια εξάτμισης του διαλύτη. Επίσης συζητώνται οι προκύπτουσες ιδιότητες φραγής με βάση τις μετρήσεις των συντελεστών μεταφοράς στο κελίο διαπρατότητας.

Κεφάλαιο 8: Μελετώνται οι επιπτώσεις της προσθήκης υδρόφιλων νανοπλακιδίων εκτορίτη πολύ μεγάλου λόγου διαστάσεων στις ιδιότητες φραγής της νανοσύνθετης επικάλυψης. Ελέγχονται και συγκρίνονται διάφορες διαδικασίες προετοιμασίας των δειγμάτων και μετράται ο ελεύθερος όγκος και οι συντελεστές μεταφοράς μάζας. Επίσης γίνεται μια πειραματική επαλήθευση/έλεγχος των μοντέλων διαπερατότητας.

Κεφάλαιο 9: Μελετάται η διασπορά διάφορων τύπων οργανικά τροποποιημένων μοντμορίλλονιτών σε οργανικούς διαλύτες συμβάτοντάς με το νερό και η ανάμιξή τους με το υδατικό γαλάκτωμα της ακρυλικής ρητίνης. Διερευνώνται οι διάφορες αλληλεπιδράσεις ανάμεσα στα συστατικά και συσχετίζονται με τις προκύπτουσες μορφολογίες καθώς και τις ιδιότητες φραγής των τελικών νανοσύνθετων επικαλύψεων.

Chapter 1

Polymer/clay nanocomposites

1.1 Introduction: Nanocomposites with phyllosilicate reinforcement and polymeric matrix

Nanocomposites materials are two phase systems that consist of a polymeric matrix and dispersed inorganic particles of nanometer scale. The most common inorganic particles belong to the family of 2:1 phyllosilicates. Their crystal structure (Fig. 1.1) [Ray and Okamoto, 2003] consists of an aluminium or magnesium hydroxide octahedral sheet sandwiched between two silicon oxide tetrahedral sheets. The layer thickness of each platelet is around 1nm, and their lateral dimensions may vary from 30 nm to several microns.

The isomorphic substitution of the tetrahedral or octahedral cations, e.g. the substitution of Al^{3+} with Mg^{2+} or Fe^{2+} with Li^{1+} , generates negative charges that are counterbalanced by alkali and alkaline earth cations located inside the galleries. In the case of tetrahedral substitution, the negative charge is located on the surface of the silicate layers and, thus, the polymer matrices can interact more readily with tetrahedral than with octahedral substituted material.

The capacity to substitute the cations (cation exchange capacity, CEC) of the clay ranges between 0.5 to 2 meq/g [Duran et al., 2000]. The CEC value determines the number of cationic surfactants that can be intercalated into the galleries by ion exchange. The layers are located on top of each other like the pages of a book (Fig. 1.2). Van der Waals gaps are created between the layers, called galleries. According to the Derjaguin-Landau-Verwey-Overbeek (DLVO) theory [Duran et al., 2000] the energy, per unit area, between two basal planes of the particles is given by the relation

$$U_{surf} = -\frac{A}{12\pi d^2} \quad (1.1)$$

where d is their face-to-face distance and A is the Hamaker constant (typical values of the order of $10^{-20} J$). The force keeping the platelets together is given by the first derivative of the above energy, $\partial U / \partial d$, and decays as d^{-3} .

In order to achieve the dispersion of the individual layers, these forces must be

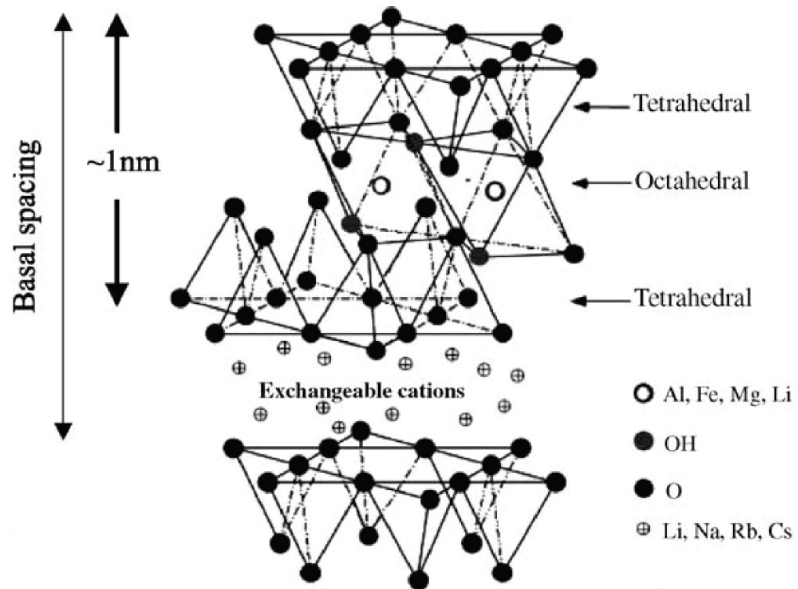


Figure 1.1: The crystal structure of the phyllosilicates [Ray and Okamoto, 2003].

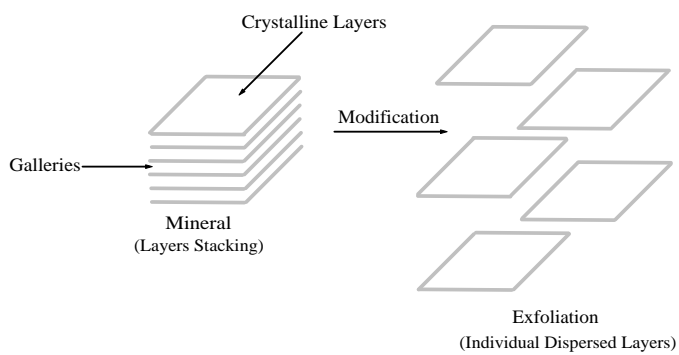


Figure 1.2: Delamination of the primary mineral particles into individual nano-layers. The layers are located on top of each other like the pages of a book. The Van der Waals gaps between the layers, are called galleries.



Figure 1.3: Schematic of an alkylammonium cation [Holmberg et al., 2002].

weakened, e.g. by substituting the Na^+ , K^+ or Ca^{2+} cations between the layers with larger cations, e.g. cations employing large organic tails. The primary phyllosilicate particulates usually contain Na^+ or K^+ ions and are hydrophilic. The Na^+ clay swells in water because the cations are diluted (replaced by weaker hydrogen bridges) and the attractive van der Waals forces between the galleries are weakened. Complete wetting of the clay surfaces by the water, thus, results in expansion of the inter-layer distance (swelling). When ultrasonic waves hit the suspension, the expanded particulates absorb the ultrasonic energy, and the individual crystalline layers exfoliate. By mixing this finely dispersed suspension with a hydrophilic polymer and extracting the water, an exfoliated polymer nanocomposite can be obtained [Strawhecker and Manias, 2000].

However, polymers and inorganic particles are mostly incompatible and produce composites with aggregated nanoparticles. This failure is due to the weak entropy of mixing and the particle-particle attractions or van der Waals forces. Even when there is relative miscibility between the polymer and the inorganic phase, the simple mixing of polymer and layered silicates rarely result in a nanocomposite. Various factors, related to the clay volume fraction, the large surface areas, the molecular weight of the monomers, the radius of gyration of the polymer, the strength of the interactions between the different phases and the kinetics are of importance. The degree of wettability of the clay layer surfaces by the polymer molecules and the morphology of the nano-composite depend strongly on all these factors.

To render the layered silicates compatible with non-polar polymers one must convert the hydrophilic silicate surface to organophilic. This can be achieved by ion exchange reactions with cationic surfactants including primary, secondary, tertiary, and quaternary alkylammonium cations or phosphonium cations which contain various substituents. At least one of these substituents must be a long carbon chain of 12 carbon atoms or more, in order to make the clay mineral compatible with the polymer [Usuki et al., 2005; Lagaly, 1986; Yoon et al., 2007]. Organic molecules may interact with clay particles in several ways: the molecules may be adsorbed on clay surface by ion-dipole forces, by dispersion forces or by hydrogen bonding.

The alkylammonium cations lower the surface energy of the inorganic reinforcement, improve the wetting characteristics of the polymer matrix, and result in larger inter-layer spacing (swelling). Additionally, the alkylammonium cations can provide functional groups that react with the polymer matrix or, in some cases, can initiate the polymerisation of monomers to form the polymer in-situ [Yano et al., 1993].

The objectives of the modification process are (i) the reduction of the electrostatic forces (swelling) and (ii) the compatibilisation of the filler with the matrix. The latter determines the degree of interaction between the two phases, which is crucial for the final nanocomposite morphology. The most common morphologies obtained in nanocomposites consist of intercalated, flocculated and exfoliated clay particles dispersed

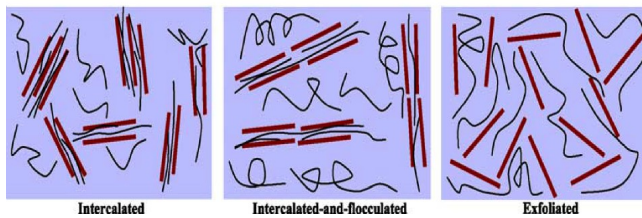


Figure 1.4: Schematic representation of three types of polymer/clay nanocomposites [Ray and Okamoto, 2003].

in the polymeric matrix (Fig. 1.4).

Intercalation refers to partial separation of the individual crystalline layers, increased relative to the separation in the clay powder, while the stacks of the platelets remain (face to face association). In the flocculated state there is an edge to edge or edge to face association of the particles. Exfoliation corresponds to complete delamination of the phyllosilicate particulates and dispersion of the individual layers. This state can be divided in the ordered exfoliated state, in which there is a parallel orientation of the particles with respect to each other and in the disordered exfoliated state in which there is no orientation.

The exfoliation of the clay particles results in the creation of a very large area of new surface (interface), A . The formation of this interface costs energy:

$$U_{int} = \left(\gamma - T \frac{d\gamma}{dT} \right) A \quad (1.2)$$

where the first term, γ , is the interfacial energy of the organic / inorganic interface and the second term represents the interface entropy. If the interface formation is energetically favourable, the polymer chains will wet the dispersed inorganic clays generating an exfoliated nanocomposite.

Obviously, the higher the surface area and the volume fraction of the inorganic layers the more organic phase is required to saturate the particles and prevent them from re-agglomeration or phase separation. Consequently, in effective polymer clay nanocomposites the maximum dispersible volume fraction of the clay usually does not exceed 10 vol%; for many systems this fraction is much lower.

The three most common methods that are used for the preparation of a polymer-nanocomposite are:

1. intercalation in a suitable monomer and subsequent in situ polymerisation that leads to exfoliation
2. intercalation of polymer from solution and exfoliation
3. polymer melt intercalation and exfoliation

Recent reviews of the methods that are used for the synthesis of polymer-clay nanocomposites can be found in [Usuki et al., 2005; Nguyen and Baird, 2006].

The nanocomposites have become an area of intensive research activity. The first reason for this development is their excellent mechanical properties. The complete dispersion of clay nanolayers in a polymer optimises the number of available reinforcing elements that carry an applied load and deflect the evolving cracks. The coupling between the large surface area of the clay and the polymer matrix facilitates the stress transfer to the reinforcing phase allowing for the improvement of the tensile stress and toughness [LeBaron et al., 1999; Powell and Beall, 2006; Jordan et al., 2005].

The second major advantage of the nanocomposites is their enhanced barrier properties. In their exfoliated state, the inorganic nanoparticles have very high aspect ratios of width/thickness, in the order of 50 – 1000. The impermeable crystalline clay layers create tortuous paths for diffusion inside the matrix, hindering the transport of gas molecules and, thus, they reduce the permeability of the material. It is reported that gas permeability through polymer films can be reduced further even with small nanoclay loadings. The relevant research on polymer-clay nanocomposite concerns mostly oxygen, carbon dioxide and nitrogen barrier films, a.o., for packaging food, carbonated drinks [Hatzigrigoriou and Papaspyrides, 2011; Sorrentino et al., 2007] and flexible electronics [Priolo et al., 2010]. Other applications include gas tanks and protective coatings that could be used for the protection from atmospheric pollution gasses (e.g. SO_3), flame retardant materials etc.[Sadat-Shojaei and Ershad-Langroudi, 2009].

However, the permeability reduction may sometimes be limited or even reversed in nano-clay/polymer composites because of possible free volume enhancement in the polymer matrix caused by the incorporated particles. The large interfacial regions and the polymer side-chain immobilisation are two effects that may influence the free volume properties of the polymer and, thus, the rate of the gas transport process through the nanocomposite [Choudalakis and Gotsis, 2012].

1.2 Waterborne acrylic resin coatings

Coating is a liquid material that is applied to a substrate resulting in a dry film. It is a complex mixture consisting of various ingredients. The most important are the binder (resin) and the volatile component (solvent). The other components are called additives. Acrylic polymers, which are used as coating binders, are comprised mainly of esters of acrylic and methacrylic acid that are polymerised by additional polymerisation, usually using a free radical mechanism.

Thermosetting acrylic resins contain functional groups, such as carboxyl or hydroxyl, that are capable of reacting with another polymeric or monomeric multi-functional material (i.e. melamine, epoxy, isocyanate, etc.) to produce a crosslinked network.

The waterborne colloidal polymer suspension consists of an acrylic resin that contains hydrophilic groups. By the addition of water, the non-polar segments of various monomers associate with each other to form colloidal aggregates (droplets). The non-polar parts of the monomers are in the interior of aggregates while the polar groups reside on their periphery. These droplets are dispersed in the continuous phase (water). The stability of the dispersion is ensured by stabilisers (surfactants) on the surface of the particles (droplets) which prevent their coagulation. The particles usually have

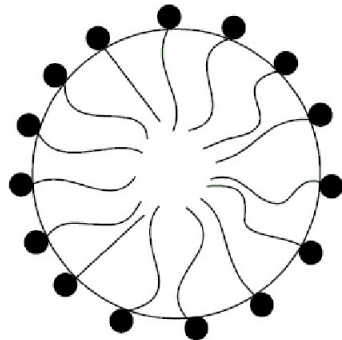


Figure 1.5: Schematic representation of a stabilised colloidal droplet [Holmberg et al., 2002].

diameters of about 30-500 nm.

In thermosetting resin coatings the film formation process occur via a physicochemical drying. After application of the resin dispersion, a volume reduction occurs as the result of water evaporation. As the solvent evaporates, the resin droplets are brought closer and closer until the repulsive forces are overcome, and there is a direct contact between the droplets which they start to coalesce. Then the particles are forced to deform due to capillary forces until a coherent film is obtained. At the same time the resin undergoes a change in chemical characteristics. A cross-linking agent is added (or it exists) to the resin, which enters into the polymerisation reaction and becomes a part of the final product.

Chapter 2

Mass Transport Principles

2.1 Gas permeation

The transport of gases through a polymer membrane is a complex process which involves sorption, diffusion and permeation. The transport behaviour is generally classified into three categories [Chen et al., 2001]:

- When the diffusion rate is much less than the sorption rate and sorption equilibrium is rapidly established, then the permeation is Fickian. The gas transport, then, follows the solution-diffusion mechanism.
- When the diffusion rate is very rapid compared with the sorption rate, the permeation process is sorption-controlled and is called “anomalous”.
- When the diffusion and sorption rates are comparable, then the transport is characterised as non-Fickian. This occurs in the case of liquid penetrants and glassy polymer membranes and it is the most complicated of the three.

In general, the transport process is described by Fick’s first law, in which the gas flux through a polymer membrane, J , is driven by the concentration gradient of absorbed molecules in the polymer matrix.

$$J(\mathbf{r}, t) = -D \nabla c(\mathbf{r}, t), \quad (2.1)$$

where D is the diffusion coefficient. The above equation in one dimension becomes:

$$J(x, t) = -D \frac{\partial c(x, t)}{\partial t}, \quad (2.2)$$

which, in combination with the continuity equation, gives:

$$\frac{\partial c(x, t)}{\partial t} = \frac{\partial}{\partial x} \left(D \frac{\partial c(x, t)}{\partial x} \right). \quad (2.3)$$

If the diffusion coefficient is independent of the concentration, then:

$$\frac{\partial c(x, t)}{\partial t} = D \frac{\partial^2 c(x, t)}{\partial^2 x}, \quad (2.4)$$

which is often referred to as Fick's second law.

Concentration dependent diffusion coefficient is often observed for many gas penetrants and is usually expressed as [Tortora et al., 2002]:

$$D(c) = D_0 e^{\alpha c}, \quad (2.5)$$

where D_0 is the zero-concentration diffusivity and α is the “plasticisation power” which accounts for the effectiveness of the penetrant to plasticise the matrix.

2.1.1 Gas Permeation in Rubbery Polymers

The transport of gases through a rubbery polymer membrane is based on the solution-diffusion mechanism: sorption of gas molecules on the surface of the membrane; diffusion through it; and, finally, desorption of gas from the other surface of the membrane.

The sorption behaviour is described by Henry's law

$$C_D = k_D \cdot p \quad (2.6)$$

where C_D is the concentration of sorbed gas, k_D is Henry's coefficient or Henry's solubility and p is the partial pressure of the gas. This represents the gas molecules that exist in the dissolved state (between the polymer chains) and is related to the fluctuating fraction of the free volume of the polymer [Manninen et al., 2005; Bohning et al., 2005]. The subscript D denotes the dissolved state.

Eq. 2.4 can be solved analytically for a flat membrane of thickness d separating two finite volumes, as in the cell in Fig. 2.1. The following initial and boundary conditions apply [Choudalakis and Gotsis, 2009]:

$t = 0$ The entire cell is initially under vacuum. The gas is introduced suddenly at $t = 0$ into the volume V_0 at pressure P_0 ; thus $c(x; t = 0) = 0$.

$t > 0$ The compartment V_0 is kept at constant pressure, P_0 . The solubility of the gas in the membrane is the ratio of its concentration to the external gas pressure, when these two phases are in equilibrium. The surface of the membrane that is exposed to the gas under pressure P_0 will absorb or dissolve the gas, until the concentration of dissolved gas reaches the saturation value, c_0 , given by Henry's equation; thus $c(x = 0; t) = c_0 = S \cdot P_0$.

The boundary value of c at the surface of the membrane on the side of volume V is considered to be zero: $c(x = d; t) = 0$.

The solution of the differential eq. 2.4 represents the concentration of the gas inside the membrane as a function of depth and time:

$$c(x, t) = Sp \left[1 - \frac{x}{d} - \frac{2}{\pi} \sum_{m=1}^{\infty} \frac{1}{m} \sin \frac{m\pi x}{d} \exp \left(-\frac{m^2 \pi^2 D t}{d^2} \right) \right]. \quad (2.7)$$

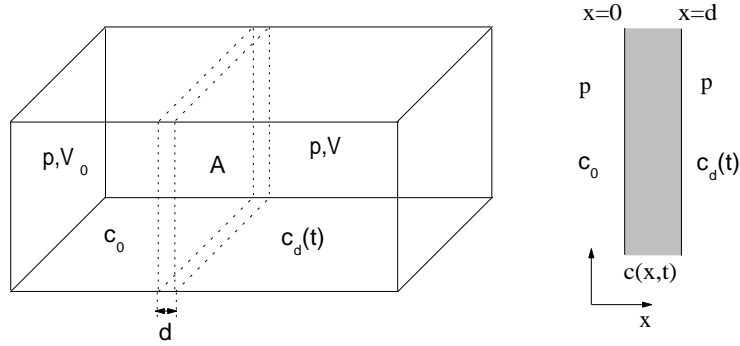


Figure 2.1: Schematic representation of the permeation cell. The gas diffuses through the membrane separating the two chambers [Rogers et al., 1954; Choudalakis and Gotsis, 2009].

The flux of the gas that permeates the membrane is obtained if we set $x = d$ in eq. 2.7 and then substitute in eq. 2.2. The result is:

$$J(t) = \frac{DSp}{d} \left[1 + \sum_{m=1}^{\infty} 2 \cos m\pi \cdot \exp \left(-\frac{m^2 \pi^2 D t}{d^2} \right) \right]. \quad (2.8)$$

2.1.2 Glassy Polymers

For sorption in a glassy polymer membrane, the sorbed penetrant concentration is the sum of Henry's population (C_D) and Langmuir's population (C_H)

$$C = C_D + C_H \quad (2.9)$$

The second term represents the adsorption of gas molecules into the free volume holes in the glassy polymer and is given by the relation:

$$C_H = \frac{C'_H bp}{1 + bp}. \quad (2.10)$$

Here C'_H is the Langmuir capacity and represents the amount of gas that the glassy polymer can accommodate into its unrelaxed free volume (excess free volume). This capacity is strongly temperature dependent, Fig. 2.2, and is given by:

$$C'_H = \left(\frac{V_g - V_l}{V_g} \right) \frac{22400}{V_p}. \quad (2.11)$$

V_g and V_l are the specific volumes in the glassy and the liquid (rubbery) states, Fig. 2.2, and V_p is the molar volume of sorbent gas (in ml) [Tsujita, 2003]. The parameter b in

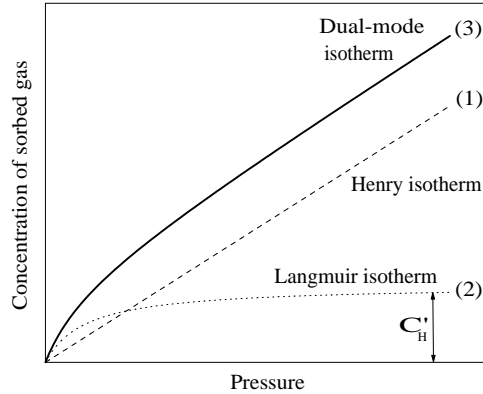


Figure 2.2: The three sorption isotherms.

eq. 2.10 is the hole affinity constant and characterises the tendency of a given penetrant to sorb into the excess unrelaxed volume in the non equilibrium matrix [Fu et al., 2007].

This sorption is characterised by a model which is the combination of two isotherms, a Henry-type for matrix absorption and a Langmuir-type for site sorption. The solubility coefficient in this case becomes:

$$S = k_D + \frac{C'_H b}{1 + bp}. \quad (2.12)$$

The gas transport behaviour in glassy polymers is described, thus, by the dual mobility model, which assigns two different diffusivities to the molecules absorbed by the two different mechanisms:

$$J = -D_D \frac{dC_D}{dx} - D_H \frac{dC_H}{dx}, \quad (2.13)$$

where the first term represents the flux due to Henry's law population while the second is due to Langmuir population. The permeability coefficient can be written in the form of:

$$P = k_D D_D + D_H \frac{bC'_H}{1 + bp}. \quad (2.14)$$

Rearranging the terms of eq. 2.14, this becomes:

$$P = k_D D_D \left(1 + \frac{FK}{1 + bp} \right), \quad (2.15)$$

where $F = D_H/D_D$ and $K = bC'_H/k_D$.

The ideal selectivity of a membrane between gasses A and B is the ratio of their gas permeabilities:

$$\alpha_{A/B} = \left(\frac{D_A}{D_B} \right) \times \left(\frac{S_A}{S_B} \right). \quad (2.16)$$

Solubility selectivity is determined by the relative affinity between the gases and the polymeric matrix, while diffusion selectivity depends on the size difference between the molecules of the gases and the minimum average free volume hole size of the polymer.

2.2 Measurements of the transport coefficients

2.2.1 Permeation Cell Procedure

The transport coefficients can be measured using the Permeation Cell Method, or a gravimetric technique in sorption/desorption experiments. In the first case one can use an arrangement such as shown in Fig. 2.1. A membrane of thickness d and area A , separates the cell into two compartments. The gas is introduced in the left compartment (Fig. 2.1) at concentration c_0 under constant pressure p . The concentration of the gas at the other side of the membrane, c_d , is monitored as a function of time.

By integrating eq. 2.8 from time 0 to t , and since $J(t) = dc/Adt$, with A the area of the membrane, one obtains the concentration, $c_d(t)$ (in mol/m³):

$$c_d(t) = \frac{ADSp}{Vd} \left[t - \frac{d^2}{6D} - \frac{2d^2}{\pi^2 D} \cdot \sum_{m=1}^{\infty} (-1)^m \frac{\exp(-m^2 \pi^2 D t / d^2)}{m^2} \right]. \quad (2.17)$$

For long times eq. 2.17 becomes:

$$c_d(t) = \frac{ADSp}{Vd} (t - t_L) \quad (2.18)$$

$$\text{with } t_L = \frac{d^2}{6D}. \quad (2.19)$$

The characteristic time, t_L , is a measure of the time that is required to establish a constant flow through the membrane. The permeability coefficient, P (in mol Pa⁻¹m⁻¹s⁻¹), is the product of the diffusion coefficient, D (in m²/s), and the sorption coefficient or solubility, S (in mol m⁻³Pa⁻¹):

$$P = D \cdot S. \quad (2.20)$$

By plotting c_d vs. t for sufficiently long times to reach a linear response, we can determine the time lag t_L , as shown in Fig. 2.3, and then the diffusion coefficient D from eq. 2.20. The slope of the steady state line gives the product $D \cdot S$, i.e. the permeability coefficient.

The concentration of the gas that permeates the membrane, $c_d(t)$, is recorded as a function of time using a gas sensor or a differential pressure gauge at the right compartment of the cell. In order to prevent external driving forces on the diffusion process the pressure in both chambers is initially set to be the same.

In spite of the simplicity of the calculations, the above method has practical difficulties because t_L is very large in many cases. Indeed, the diffusion coefficient for small gas molecules in most polymers is about $10^{-6} - 10^{-9}$ cm²/s. For polyethylene or polystyrene the diffusion coefficient is about 10^{-8} cm²/s and a membrane of that

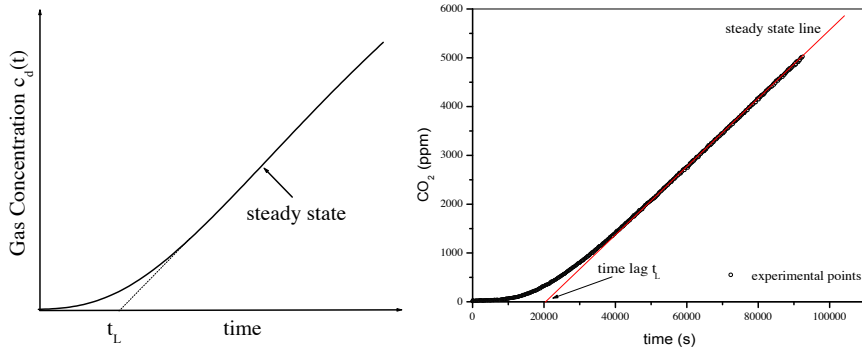


Figure 2.3: (a) The theoretical curve of the concentration of the gas that permeates the membrane as a function of time based on eq. 2.17. The linear part is the steady state line. (b) Experimental curve for a nanocomposite membrane measured by the permeation cell procedure.

polymers with 1 mm thickness requires approximately two days to reach steady state. An alternative solution for eq. 2.2 was proposed by Holstein [Rogers et al., 1954]:

$$J(t) = 2SP_0 \cdot \sqrt{\frac{D}{\pi t}} \sum_{m=1}^{\infty} \exp \left[-\frac{d^2}{4Dt} (2m+1)^2 \right]. \quad (2.21)$$

For short times eq. 2.21 can be approximated by ignoring all but the first term of the sequence. Multiplying then with $t^{1/2}$ and taking the logarithm on both sides one gets:

$$\ln \{t^{1/2} \cdot J(t)\} = \ln \left[2SP_0 \left(\frac{D}{\pi} \right)^{1/2} \right] - \frac{d^2}{4Dt}. \quad (2.22)$$

Plotting the left hand side of eq. 2.22 against the reciprocal time we obtain a straight line. The diffusion coefficient can be calculated from the slope of this line ($-d^2/4D$).

Equilibrium permeation rates follow the classical Arrhenius temperature dependence [Salame and Steingiser, 1977]

$$P = P_0 \exp(-E_p/RT). \quad (2.23)$$

where P_0 is a constant for a given penetrant/polymer pair, E_p is the activation energy ranging generally from 8 to 20 kCal, R is the gas constant and T is the temperature. Around room temperature, the permeability increases by 30-50% for every 5 °C rise.

Permeation rates are normally given on a per unit thickness basis. For all polymers P varies as t^{-x} where in the ideal case $x = 1$. Extrapolation and prediction of thicker or thinner films than those measured can be erroneous if the permeation versus thickness slope deviates from a value of 1. In most cases, however, x varies between 0.8 and 1.2 [Salame and Steingiser, 1977]. Therefore a 2 mm film will have a permeability rate anywhere from 40-60% the value for a 1 mm film.

Some possible reasons for such behaviour are given by Shishatskii et al. [1996]:

- Pore flow through defects of the skin layers of membranes can affect the permeation rates. These effects become progressively less important as the thickness of the film is increased.
- If the more permeable phase becomes continuous in a size scale of the membrane thickness, a transmitting channel across the membrane can be formed, which will strongly affect the permeation rate. On the other hand, the length of the diffusion pathways within the membrane can be different in films with different thickness.
- The glassy polymers are not in equilibrium state. Therefore, the rate that they were cooled from the rubbery state may influence their current properties, e.g. the free volume.

The free volume and intrinsic permeation rates are different in thin films from those in the bulk. The density of amorphous polymer films increases when their thickness is reduced. This is caused by the diffusion of excess free volume elements to the film surface during the process of film formation.

For constant T and P , and for long enough measuring times (up to a few days), all changes in the polymer matrix will have taken place, even for the long relaxation times. These relaxations are initiated by the local concentration of the sorbed penetrant molecules. The steady state quantities P , D and S , may represent the gas transport in the quasi-equilibrium of the steady state.

In contrast, for permeation experiments in glassy polymers the measuring time is in general too short (some minutes up to few hours) for the equilibration of the polymer matrix after uptake of the penetrant molecules. Because of the reduced chain mobility below T_g , one obtains only an apparent or effective diffusion coefficient D_{eff} in the experiment. This coefficient depends, in general, on concentration and is usually not independent of the measuring time [Heuchel et al., 2004].

It should be noted that in the case of a glassy polymer membrane the permeation cell procedure gives, in fact, the effective transport coefficients, which include the contributions of both Henry and Langmuir populations.

2.2.2 Sorption/Desorption Experiments

On the other hand, sorption/desorption experiments are used to measure both the diffusion coefficient and the solubility and, therefrom, the permeability (eq. 2.20). In the simplest form of a sorption experiment, the membrane remains initially under vacuum and the gas is introduced and maintained at constant pressure. The gas is dissolved and diffuses into the membrane. The weight gain is estimated with a balance. The fractional mass uptake is reported as a function of time. Assuming a flat membrane of thickness d and uniform concentration of the gas in the membrane there are two possible solutions for eq. 2.4 [Neogi, 1996]:

$$\frac{M_t}{M_{\text{eq}}} = 8 \sqrt{\frac{Dt}{d^2}} \left[\frac{1}{\sqrt{\pi}} + 2 \sum_{m=0}^{\infty} (-1)^m \operatorname{erfc} \left(\frac{md}{4(Dt)^{1/2}} \right) \right], \quad (2.24)$$

$$\frac{M_t}{M_{\text{eq}}} = 1 - \frac{8}{\pi^2} \sum_{m=0}^{\infty} \frac{1}{(2m+1)^2} \cdot \exp \left[-\frac{D(2m+1)^2 \pi^2 t}{d^2} \right], \quad (2.25)$$

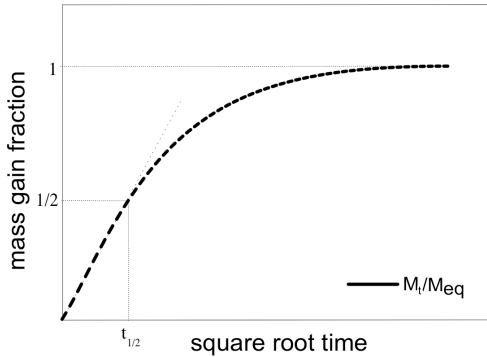


Figure 2.4: Plot of M_t/M_{eq} as a function of \sqrt{t}/d . The characteristic time $t_{1/2}$ is the half time for sorption and corresponds to the initial linear part of the curve.

where M_t and M_{eq} are the mass uptakes at times t and at equilibrium, and erfc is the error function integral.

Eq. 2.24 converges rapidly for short times and can be approximated then by:

$$\frac{M_t}{M_{eq}} = \frac{8}{\pi^{1/2}} \left(\frac{Dt}{d^2} \right)^{1/2}. \quad (2.26)$$

By plotting M_t/M_{eq} against \sqrt{t}/d we obtain a straight line until $t_{1/2}$, the half life time, when $M_t/M_{eq} = 1/2$ (Fig. 2.4). The diffusion coefficient is calculated from the slope of this line.

Alternatively, eq. 2.25 converges rapidly for long times. Keeping, then, only the first term and taking the logarithms on both sides, one obtains a straight line in the form:

$$\ln \left(1 - \frac{M_t}{M_{eq}} \right) = \ln \left(\frac{8}{\pi^2} \right) - \frac{\pi^2 D t}{d^2}. \quad (2.27)$$

By plotting the right hand side against t we can calculate D from the slope of this line.

Applying these methods, the diffusion coefficient can be determined in isothermal and isobaric sorption/desorption experiments. These methods present, however, an uncertainty in the time interval over which they are valid. A more detailed description of methods that are used to extract the diffusion coefficients from gravimetric data is presented in [Ballik, 1996; Wong et al., 1998].

Generally, the diffusion mechanism follows the following equation:

$$\frac{M_t}{M_{eq}} = K t^n, \quad (2.28)$$

where K depends on the structural features of the polymer and n determines the diffusion mechanism [Jacob et al., 2008]. When $n = 1/2$ the transport is Fickian, as it was

found previously, while $n = 1$ corresponds to the non-Fickian transport, in which the diffusion rate is rapid compared to the relaxation processes. The case $0.5 < n < 1$ is the anomalous transport behaviour and corresponds to the situation where the diffusion rate is comparable to the polymer relaxation. The values of K and n can be determined by plotting $\log(M_t/M_{eq})$ vs. $\log t$:

$$\log \frac{M_t}{M_{eq}} = \log K + n \log t. \quad (2.29)$$

The solubility coefficient is found by measuring the concentration of the soluble gas as a function of pressure $c = f(p)$ at constant temperature. By fitting these curves with eq. 2.10 the parameters k_D, b, C'_H can be extracted. Alternatively, it is possible to deduce the solubility by the relation [Thomas et al., 2011]:

$$S = \frac{M_{eq}}{M_p}, \quad (2.30)$$

where M_{eq} is the mass of the gas sorbed at equilibrium and M_p is the mass of the polymer. The solubility is then expressed as (g of sorbed gas)/(g of polymer)

Chapter 3

Permeability Models in Polymer Clay Nanocomposites

*Part of this chapter has been published in the European Polymer Journal, **45** (2009) 967–984 under the title "Permeability of polymer/clay nanocomposites: A review" (G. Choudalakis and A.D. Gotsis).*

In polymer clay nanocomposite the dispersed phase consists of inorganic crystalline layers. The gas molecules permeability in these crystals is orders of magnitude lower than that in the amorphous polymer matrix. It is obvious therefore, that the nanoplatelets could act as barriers to the diffusion of gas molecules through the nanocomposite membrane. That is, the gas molecules should follow a tortuous path around the platelets as they diffuse through the membrane. This effect is called tortuosity and is the key factor controlling the permeation characteristics of the nano-composites. Thus, in most theoretical treatises the nanocomposite is considered to consist of a permeable phase (polymer matrix) in which non-permeable nanoplatelets are dispersed. There are three main factors that influence the permeability of a nanocomposite: The volume fraction of the nanoplatelets; their orientation relative to the diffusion direction; and their aspect ratio.

It is generally accepted that the transport mechanism within the polymer matrix follows Fick's law, and that the matrix maintains the same properties and characteristics as the neat polymer. Therefore, a small decrease of the solubility is expected in the nanocomposite due to the reduced polymer matrix volume, as well as a decrease in diffusion due to the more tortuous path for the diffusing molecules.

The reduction of the diffusion coefficient is higher than that of the solubility coefficient. Indeed, the volume fraction of nanoplatelets is low and, thus, the reduction of the matrix volume is small. The major factor, then, is the tortuosity, which is connected directly to the shape and the degree of dispersion of the nanoplatelets.

The degree of dispersion of the nanoplatelets is determined by the degree of delamination (exfoliation) of the clay. The fully delaminated (exfoliated) nanocomposite presents much higher values for the tortuosity factor in the material and the aspect

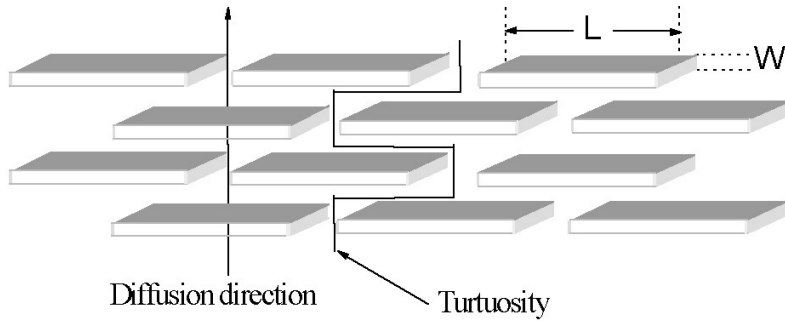


Figure 3.1: The ideal case of rectangular nano-platelets dispersed in a periodical arrangement perpendicular to the diffusion direction.

ratio of the clay particles in comparison with the partially delaminated (intercalated) nanocomposite and it is much more effective to be used in barrier membranes for gasses.

The terms *intercalated* and *exfoliated* layered silicate nanocomposites are often used to describe two extreme states of silicate layer organisation in the composite morphology. Intercalation implies the insertion of polymer chains in the galleries of the initial layered tactoids. This leads to a longitudinal expansion (swelling) of the galleries. Exfoliation implies complete destruction of the initial layer stacking order and homogeneous dispersion of the layers in the polymer matrix.

Several models have been developed in order to describe the mass transfer within the nanocomposites. Most models assume that the platelets have a regular and uniform shape (rectangular, sanidic or circular) and form a regular array in space. They are either parallel to each other or have a distribution of orientations with an average orientation angle to the main direction of diffusion of the gas molecules. Some of these models are outlined in the following.

3.1 Regular arrangement of parallel nano-platelets

One of the first attempts to describe the permeability of membranes, where a second phase is dispersed in a regular arrangement, was made by **Barrer and Petropoulos [1961]**. These authors calculated the diffusion through a regular array of parallelepipeds of a second phase dispersed in a matrix with a different diffusion coefficient. When this approach is applied in the case of dispersed impermeable thin plates, the change of the permeability is found to be proportional to the fractional cross section (slit) that is available for the diffusant to move forward and depends on the tortuosity of the path.

A simple permeability model for a regular arrangement of platelets has been proposed by **Nielsen [1967]** and is presented in Fig. 3.1. The nanoparticles are evenly dispersed and considered to be rectangular platelets with finite width, L , and thickness, W . Their orientation is perpendicular to the diffusion direction.

The solubility coefficient of this nanocomposite is:

$$S_{\text{composite}} = S_{\text{matrix}}(1 - \phi), \quad (3.1)$$

where S_{matrix} is the solubility coefficient of the neat polymer, and ϕ is the volume fraction of the nanoplatelets that are dispersed in the matrix. In this approximation the solubility does not depend on the morphological features of the phases.

The platelets act as impermeable barriers to the diffusing molecules forcing them to follow longer and more tortuous paths in order to diffuse through the nanocomposite. The diffusion coefficient, $D_{\text{composite}}$, is influenced by the tortuosity, τ :

$$D_{\text{composite}} = \frac{D_{\text{matrix}}}{\tau}, \quad (3.2)$$

where D_{matrix} is the diffusion coefficient of the matrix. The factor τ depends on the aspect ratio, the shape and the orientation of the nanoplatelets, and it is defined as

$$\tau \equiv \frac{\ell'}{\ell} \quad (3.3)$$

where ℓ' is the distance that a solute must travel to diffuse through the membrane when nanoplatelets are present and ℓ is the membrane thickness. From eq. 2.20, 3.1 and 3.2:

$$\frac{P_{\text{composite}}}{P_{\text{matrix}}} = \frac{1 - \phi}{\tau}. \quad (3.4)$$

The prolonged diffusion length ℓ' is estimated as follows: Each nanoplatelet contributes to the enhancement of the diffusion length by $L/2$ on the average. If $\langle N \rangle$ is the mean number of nanoplatelets that a solute encounters as it diffuses through the membrane, then:

$$\ell' = \ell + \langle N \rangle \frac{L}{2}. \quad (3.5)$$

Since $\langle N \rangle = \ell\phi/W$, the factor τ becomes:

$$\tau = 1 + \frac{L}{2W}\phi. \quad (3.6)$$

Eq. 3.4, then, gives:

$$\frac{P_{\text{composite}}}{P_{\text{matrix}}} = \frac{1 - \phi}{1 + \frac{\alpha}{2}\phi}, \quad (3.7)$$

where $\alpha = L/W$ is the aspect ratio of the nanoplatelets. This equation shows that the permeability of the nanocomposite decreases with the increase of ϕ and a . In practise however, the limit for the validity of the model is $\phi \leq 10\%$, because the particles have a tendency to aggregate which increases with ϕ .

The diffusion through a membrane simulated as a single multi-perforated lamina was studied by **Wakeham and Mason [1979]**. These authors found that the resistance to diffusion through such a membrane had one contribution from the need of the diffusant to enter the constriction into the pore/slit, and one contribution due to the length of the

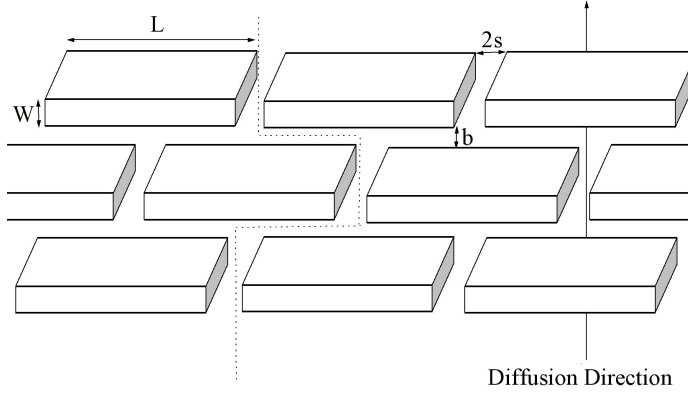


Figure 3.2: The 2D diffusion case. Rectangular dispersed nano-platelets in a periodical arrangement perpendicular to the diffusion direction. Some characteristic dimensions are shown.

pore. This approach was extended by Cussler et al. [1988] to multiple layers of parallel platelets of infinite third dimension (2D diffusion), separated by slits. The result was:

$$\frac{P_{\text{composite}}}{P_{\text{matrix}}} = \left(1 + \frac{LW}{2s(W+b)} + \frac{L^2}{4b(W+b)} + \frac{2b}{l} \ln \left(\frac{L}{4s} \right) \right)^{-1}, \quad (3.8)$$

where, l is the thickness of the membrane, and the other dimensions are shown in Fig. 3.2. In this arrangement, $LW/2[(L/2+s)(W+b)] = \phi$ is the volume fraction of the platelets, $L/2W = \alpha$ is the particle aspect ratio and $s/W = \sigma$ is the slit aspect ratio. Cussler et al. [1988] neglected the second term of eq. 3.8, since it is much smaller, and, for narrow slits ($\sigma \ll 1$), suggested the following simpler expression for the enhancement of the barrier properties of the membrane:

$$\frac{P_{\text{composite}}}{P_{\text{matrix}}} = \left(1 + \frac{\alpha^2 \phi^2}{1 - \phi} \right)^{-1}. \quad (3.9)$$

This model predicts a faster reduction of the relative permeability at small values of ϕ [Cussler et al., 1988] than the model of Nielsen (eq. 3.7), which needs either higher volume fraction or higher aspect ratio for the same reduction. This can be attributed to the different regions over which the above models are applicable.

Two more variations of eq. 3.8 were given by Falla et al. [1996] based on Aris [1986] and Wakeham and Mason [1979]:

$$\frac{P_{\text{composite}}}{P_{\text{matrix}}} = \left(1 + \frac{\alpha^2 \phi^2}{1 - \phi} + \frac{\alpha \phi}{\sigma} + \frac{4\alpha \phi}{\pi(1 - \phi)} \ln \left[\frac{\pi \alpha^2 \phi}{\sigma(1 - \phi)} \right] \right)^{-1} \quad (3.10)$$

$$\frac{P_{\text{composite}}}{P_{\text{matrix}}} = \left(1 + \frac{\alpha^2 \phi^2}{1 - \phi} + \frac{\alpha \phi}{\sigma} + 2(1 - \phi) \ln \left[\frac{1 - \phi}{2\sigma \phi} \right] \right)^{-1} \quad (3.11)$$

The second term of these equations which involves α^2 reflects the contribution of the tortuous path of the diffusant through the crystalline plates. The third term is due to the resistance to diffusion of the slits and depends on their aspect ratio, $\sigma = W/2s$. The last term represents the constriction from the wide space between the plates into the narrow slits and it should depend on the constriction ratio, α/σ , as it is the case in eq. 3.10. This term was derived from arguments presented by Aris [1986] for eq. 3.10 and Wakeham and Mason [1979] for eq. 3.9.

Hexagonal flakes arranged in regular parallel arrays were examined by Moggridge et al. [2003]. The same arguments as for eq. 3.8 were used and the reduction in permeability was found to be:

$$\frac{P_{\text{composite}}}{P_{\text{matrix}}} = \left(1 + \frac{2}{27} \frac{\alpha^2 \phi^2}{1 - \phi}\right)^{-1} \quad (3.12)$$

The difference, due to the specific platelet shape, is reflected by the coefficient (2/27) which reduces the effectiveness of the barrier.

3.2 Random spatial positioning of parallel plates

For the case of slits formed between randomly positioned parallel platelets of infinite third dimension Cussler et al. [1988] suggested the following expression for the permeability:

$$\frac{P_{\text{composite}}}{P_{\text{matrix}}} = \left(1 + \frac{\mu' \alpha^2 \phi^2}{1 - \phi}\right)^{-1}, \quad (3.13)$$

where μ' is a combined geometrical factor, characterising also the randomness of the porous media [Aris, 1986].

In a similar case, Lape et al. [2004] considered rectangular nanoplatelets of the same aspect ratio arranged randomly but parallel to each other and perpendicular to the diffusion direction. The reduction of the permeability in the nanoplatelet reinforced membrane is given by the product of the reduced area and the increased path length.

$$\frac{P_{\text{composite}}}{P_{\text{matrix}}} = \left(\frac{A_f}{A_0}\right) \cdot \left(\frac{\ell}{\ell'}\right) \quad (3.14)$$

The distance that the solute molecule diffuses through the nanocomposite, becomes in this case:

$$\ell' = \ell + \langle N \rangle \langle d \rangle. \quad (3.15)$$

which is the same as in eq. 3.5, except that the parameter $L/2$ is replaced by $\langle d \rangle$, the average distance the solute must travel to reach the edge of platelet. Using simple statistical considerations $\langle d \rangle$ can be estimated assuming that the molecule hits the platelet at a random point along its length and that the resistance to mass transfer is proportional to the length of the path traveled. Thus ℓ' becomes:

$$\ell' = \left(1 + \frac{1}{3} \alpha \phi\right) \ell. \quad (3.16)$$

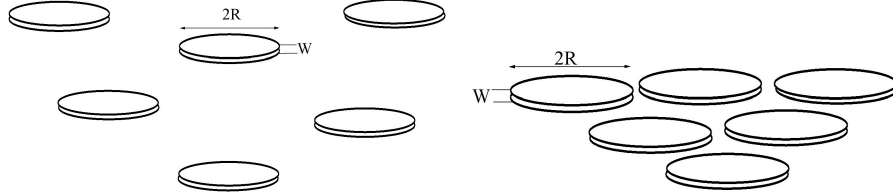


Figure 3.3: The dilute regime where the distances of the disks exceed R . The semi-dilute regime where the disks are overlapped.

Equation 3.13 differs from eq. 3.5 by a factor $2/3$, which is ascribed to the randomness of the positions of the nanplatelets.

The area available for diffusion, A_f , can be determined by dividing the volume available for diffusion by the distance traveled to cross the membrane:

$$\frac{A_f}{A_0} = \frac{(V_m - V_f)/\ell'}{V_m/\ell}, \quad (3.17)$$

where V_m is the total volume of the membrane and V_f is the volume of all platelets. The relative permeability then becomes:

$$\frac{P_{composite}}{P_{matrix}} = \frac{1 - \phi}{(1 + \frac{\alpha}{3}\phi)^2}. \quad (3.18)$$

The case where the nanplatelets are circular disks with radius R , thickness W and aspect ratio $\alpha = R/W$ (Fig. 3.3) was examined by [Fredrickson and Bicerano \[1999\]](#) using multiple scattering theory. When, the disks were spaced by an average distance exceeding R (dilute regime), then the diffusion coefficient is given by:

$$\frac{D_{composite}}{D_{matrix}} = \frac{1}{1 + \kappa\alpha\phi}, \quad (3.19)$$

where $\kappa = \pi / \ln \alpha$. This case corresponds to low values of the volume fraction and the aspect ratio of the nanplatelets ($\alpha\phi \ll 1$), and presents a form similar to Nielsen's equation (eq. 3.7). For low values of ϕ but high values of α ($\alpha\phi \gg 1$), the disks are overlapping (semi-dilute regime) and the relation becomes:

$$\frac{D_{composite}}{D_{matrix}} = \frac{1}{1 + \mu\alpha^2\phi^2}, \quad (3.20)$$

where $\mu = \pi^2 / 16\ln^2 \alpha$. This equation has a similar form with the equation of Cussler (eq. 3.9).

In a different approach, [Gusev and Lusti \[2001\]](#) developed a 3-D computational model for a random array of parallel circular disks. This model is based on the solution of the Laplace equation for the local chemical potential:

$$\nabla P(\mathbf{r}) \cdot \nabla \mu = 0 \quad (3.21)$$

with a space dependent local permeability coefficient. The latter is assumed to have a value of zero inside the platelets and be equal to P_{matrix} anywhere else. The proposed expression for the global permeability becomes:

$$\frac{P_{composite}}{P_{matrix}} = \exp \left[- \left(\frac{\alpha \phi}{x_0} \right)^\beta \right]. \quad (3.22)$$

The parameters β and x_0 are usually evaluated by fitting experimental data [Gusev and Lusti, 2001]. The values of $\beta = 0.71$ and $x_0 = 3.47$ were used by Picard et al. [2007] in order to obtain similar results as with the model of Nielsen (eq. 3.7) for the diffusion of several gasses in nylon-6/montmorillonite composites.

All the models above assume nanoplatelets of uniform size. If, instead, the platelets have a continuous distribution of sizes, $g(R)$, e.g. a Gaussian distribution of average size \bar{R} and standard deviation σ' :

$$g(R) = \frac{1}{\sqrt{2\pi}\sigma'} \exp \left(-\frac{(R - \bar{R})^2}{2\sigma'^2} \right), \quad (3.23)$$

and constant thickness, W , then the mean number of nanoplatelets of size $2R$ encountered by the solute becomes [Lape et al., 2004]:

$$\langle N(R) \rangle = \frac{\phi \ell}{W} \cdot \frac{g(R) R dR}{\int_0^\infty g(R) R dR}. \quad (3.24)$$

This gives:

$$\frac{P_{composite}}{P_{matrix}} = \frac{1 - \phi}{1 + \frac{2}{3} \frac{\phi}{W \bar{R}} (\bar{R}^2 + \sigma'^2)}. \quad (3.25)$$

If one compares this case with the case of nanoplatelets with a uniform size $R = \bar{R}$, then:

$$\frac{P_{uni}}{P_{polydisp}} \approx \left[1 + \left(\frac{\sigma'}{\bar{R}} \right)^2 \right]^2. \quad (3.26)$$

Increasing the polydispersity of the size distribution increases the standard deviation and reduces the permeability. Thus the barrier properties of the nanoplatelets with polydispersed sizes are better than these of monodispersed sizes of the same mean.

Picard et al. [2007] modified the model of Lape et al. [2004] (eq. 3.16) taking into account also the polydispersity in the thickness of the particles:

$$\frac{P_{composite}}{P_{matrix}} = \frac{1 - \phi}{\left[1 + \frac{1}{3} \phi \frac{\sum n_i \left(\frac{w_i}{t_i} \right)^2}{\sum n_i \frac{w_i}{t_i}} \right]^2}, \quad (3.27)$$

where w_i and t_i are the width and the thicknesses of the i fractions of the platelets. This model [Picard et al., 2007] is more appropriate for the cases of high loading of the impermeable phase, where there is a distribution in the values of the aspect ratio, due to the presence of agglomerates.

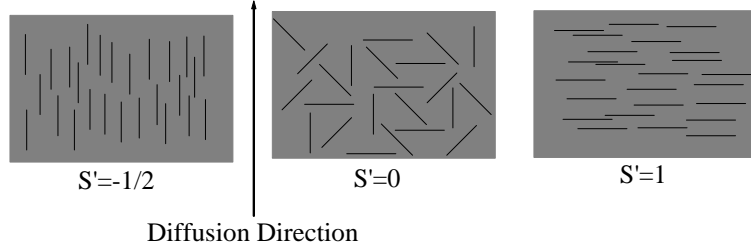


Figure 3.4: Values of the order parameter S' for three orientations of the particles [Bharadwaj, 2001].

3.3 Arrangement of the plates at angles $\theta \neq 90^\circ$ to the main diffusion direction

The tortuosity, τ , is the highest when the nanoplatelets are aligned perpendicular to the diffusion direction. For other orientation angles Nielsen's equation should be modified accordingly.

For non-uniform orientation of the platelets an order parameter, S' , is introduced to quantify the degree of their orientation around the diffusion direction [Bharadwaj, 2001]:

$$S' = \frac{1}{2} \langle 3 \cos^2 \theta - 1 \rangle, \quad (3.28)$$

where θ is the angle between the diffusion direction and the unit vector normal to the surface of a platelet. The average is taken over all platelets with all possible orientations. When all platelets are parallel to the direction of diffusion ($\theta = 0$), then the order parameter is $S' = -1/2$. When $\theta = \pi/2$, the orientation of the platelets is perpendicular to the diffusion direction and $S' = 1$. For random orientation $S' = 0$ (Fig. 3.4).

For non-uniform orientation Nielsen's equation takes the following form [Bharadwaj, 2001]:

$$\frac{P_{composite}}{P_{matrix}} = \frac{1 - \phi}{1 + \frac{\alpha}{2} \frac{2}{3} \left(S' + \frac{1}{2} \right) \phi}. \quad (3.29)$$

Obviously, the case $S' = 1$ corresponds to the maximisation of the tortuosity factor and, therefore, to the greatest reduction of the permeability. The term $\frac{2}{3}(S' + 1/2)$ ($= \langle \cos^2 \theta \rangle$, from eq. 3.29) takes the value $1/3$ for $S' = 0$. The predictions are then similar to the ones of the models of Lape et al. [2004] and Fredrickson and Bicerano [1999] for random spatial positioning of clay layers.

An empirical relation for the prediction of the permeability in nanocomposites with randomly (3D) oriented platelets has been proposed by Maksimov et al. [2008] in the form of:

$$P_{composite} = \frac{1}{3} (P_{\parallel} + 2P_{matrix}(1 - \phi)), \quad (3.30)$$

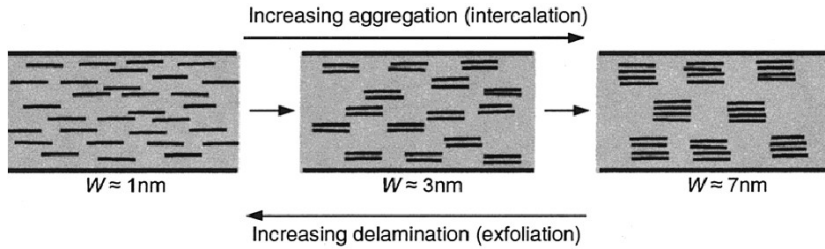


Figure 3.5: Degrees of delamination of clay layers [Bharadwaj, 2001].

where P_{\parallel} is the permeability of the nanocomposite as given by the model of Nielsen for oriented platelets. The second term corresponds to the permeability of the composites with platelets oriented parallel to the diffusion direction and it is assumed to be equal to the permeability of the matrix corrected for its volume fraction.

3.4 Influence of particle aggregation

A crucial factor that affects the permeation properties of the nanocomposite is the aggregation of silicate layers. This leads to a decrease of the aspect ratio of nanoparticles. Manninen et al. [2005] indicated that the processing method used to prepare the nanocomposites may result in agglomeration of the organoclay layers. These agglomerates may cause the formation of large scale holes (pores) in the matrix, which can act as low resistance pathways for gas transport within the nanocomposite. In such a case the diffusion becomes mostly of the Knudsen flux type.

For high clay contents, it is difficult to keep a high degree of platelet dispersion and avoid the presence of intercalated structures. Nazarenko et al. [2007] modified Nielsen's equation to take into account the case of stacks of layers (aggregates) dispersed homogeneously in the polymer matrix and oriented perpendicular to the diffusion direction. The proposed expression for the reduction in permeability is:

$$\frac{P_{\text{composite}}}{P_{\text{matrix}}} = \frac{1 - \phi}{1 + \frac{\alpha}{2N}\phi}, \quad (3.31)$$

where N is the number of layers in the layer stack, Fig. 3.5. Obviously, the value $N = 1$ corresponds to complete layer delamination (exfoliation). Again, the larger the degree of stacking, i.e. the higher the value of N , the less efficient is the enhancement of the barrier properties.

One observes that eq. 3.29 and eq. 3.31 have similar forms. The former accounts for the orientation of the platelets, while the latter for their degree of stacking. By combining these two equations we can obtain a single equation that might predict the change in permeability as a function of the volume fraction, the geometry, the orientation and

the degree of stacking of the nano-platelets:

$$\frac{P_{\text{composite}}}{P_{\text{matrix}}} = \frac{1 - \phi}{1 + \frac{\alpha}{3N} (S' + \frac{1}{2}) \phi}. \quad (3.32)$$

In a different approach, Bhattacharya et al. [2011] introduced a dimensionless corrective function, ψ , to accommodate the shape and aggregation effects of the particles, instead of the aspect ratio, and modified eq. 3.22 eq. 3.18 as:

$$\frac{P_{\text{composite}}}{P_{\text{matrix}}} = \exp \left[- \left(\frac{\psi \phi}{x_0} \right)^\beta \right] \quad (3.33)$$

$$\frac{P_{\text{composite}}}{P_{\text{matrix}}} = \frac{1 - \phi}{\left(1 + \frac{\psi}{3} \phi \right)^2} \quad (3.34)$$

with $\psi = \rho \cdot \zeta \cdot \xi \cdot \phi$, where ρ is the filler density, ζ is the specific surface area, ξ is the correlation length between the nanoparticles (which can be determined by statistically analysing TEM micrographs and is at least 100 nm for most nanocomposites) and ϕ is the filler volume fraction.

3.5 Influence of the interfacial regions

In many cases, the permeability of the nanocomposite is affected by the existence of interfacial regions between the matrix and the inorganic particles. Such domains will affect mainly the solubility coefficient but in some cases they may also enhance the diffusion coefficient. The interfaces are caused either by the surfactant that is used for the modification of the particles or/and are due to the formation of voids between the different phases.

The relative diffusion coefficient in such cases has been expressed by Sorrentino et al. [2006] as:

$$\frac{D_{\text{composite}}}{D_{\text{matrix}}} = \frac{a'}{\tau}, \quad (3.35)$$

where a' is a factor that quantifies the effect of the interfacial regions:

$$a' = 1 + \beta' \phi, \quad (3.36)$$

with the parameter β' given by:

$$\beta' = \frac{V_s}{V_f} \cdot \frac{D_s}{D_0} - \frac{V_s + V_f}{V_f}. \quad (3.37)$$

D_s , V_s are the diffusion coefficient and the volume of the interfaces, D_0 is the diffusion coefficient for the neat polymer and V_f is the volume of the nanoplatelets. If V_s/V_f is negligible, then $\beta' = -1$ and $a' = 1 - \phi$. However, the parameters D_s , V_s are not easily measurable. The value of the parameter β' has a strong effect on the diffusivity for all concentrations of the impermeable phase.

The overall transport properties of the nanocomposites are, thus, affected by the presence of interfacial regions. To quantify this effect, Xiao et al. [2010] developed a multi-scale hierarchical numerical model and defined a polymer-nanoparticle interaction strength parameter. For high values of this parameter, they showed that the polymer density next to the interface increases, indicating that the enhancement of the barrier properties there are due also to the decrease of the free volume. For large gas molecules Pryamitsyn et al. [2011] showed that the polymer-particle interactions are less important than the tortuosity effect. The mass transport properties, therefore, can be determined by the segmental dynamics of the matrix.

3.6 Experimental and numerical validation of models

A common feature in all the models that were presented here is the dependence of the permeation properties of the nanocomposite on the volume fraction and the aspect ratio of the reinforcing inorganic phase. In fact, the predictions of all the models are similar. When used in the reverse way, i.e. to predict the aspect ratio from the measured permeation properties, however, these models give different results. Some such predicted results for a number of the above described methods has been tabulated by Picard et al. [2007] as applied in a nylon-6/montmorillonite system.

The comparison of the models that have been presented so far is not straightforward because the definition of the aspect ratio of the platelets is not common in all the models. Some authors define this ratio as the half width to thickness ratio, while others as the width to thickness ratio. Adopting the latter as the typical definition of the aspect ratio, some of the models should be modified accordingly. In the model proposed by Fredrickson-Bicerano (eqs. 3.19 and 3.20), where the platelets are considered to be circular disks, the relation between the disk aspect ratio and a rectangular platelet aspect ratio can be derived by comparing the area of the disk (πR^2) to the area of a rectangular platelet (L^2). Thus, $\alpha_{disk} = \alpha / \sqrt{\pi}$ in this model. The coefficients κ and μ should also be modified accordingly.

When all the models are compared, it can be concluded that (relatively) large volume fractions or large aspect ratios are needed for a significant reduction of the permeability. The predictions for the trend of this reduction of the several models differ mainly in the area of low volume fractions and aspect ratios. The best way to compare the predictions of the models, then, is to use the product $\alpha\phi$ as the significant parameter of the membrane.

The models of Nielsen (eq. 3.7) and of Fredrickson-Bicerano (eq. 3.19) predict a stronger effectiveness of the platelets in reducing the permeability. In semi-dilute systems and for intermediate aspect ratios, $\alpha \sim 100$, the model of Fredrickson-Bicerano (eq. 3.20) seems to underestimate the barrier properties, while Cussler's model overestimates them. For higher aspect ratios Gusev's model predicts almost zero permeability for $\alpha\phi > 30$. As this product goes to higher values (e.g. $\alpha\phi > 60$) the absolute values of the permeability predicted by all the models become very low, in the range of 1-3% of the value of the unfilled polymer.

From a practical point of view, complete exfoliation is difficult to be achieved at high clay fractions and the actual aspect ratios are much lower than what is needed for

efficient enhancement of the barrier properties. For intermediate loadings, and looking at the comparisons with the available experimental data, it seems that the simple model of Nielsen is adequate to describe the reduction of the relative permeability in most cases.

The average aspect ratio of the particles is difficult to be determined experimentally. It has been observed that during the preparation of the nanocomposites the obtained aspect ratio depends on the volume fraction. In chlorobutyl/montmorillonite nanocomposites, e.g., the obtained aspect ratio decreases with increasing ϕ , using either modified or non-modified particles [Sridhar and Tripathy, 2006]. Obviously, increasing ϕ results in a reduction of the degree of delamination and, consequently, in the reduction of the final particle aspect ratio.

The decrease of the relative permeability is attributed in all models mainly to the inorganic phase. If their aspect ratio and volume fraction are the same, the particles will induce the same relative reduction of the permeability in any matrix they are dispersed, provided that the same degree of delamination is obtained. Further, if there are no special interactions between the solute gas and the particles, the relative enhancement of the barrier properties is not affected by the kind of the gas that is used [Yeh et al., 2006; Jacquelet et al., 2006]. In other words, according to the models, the improvement of the barrier properties of the material are determined solely by the dispersed inorganic phase.

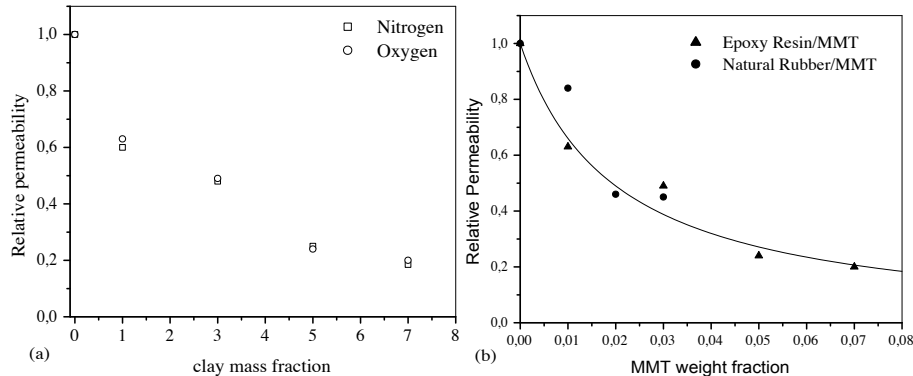


Figure 3.6: (a) Relative permeability as a function of clay mass fraction for an epoxy resin/MMT system for two different gases [Yeh et al., 2006]. (b) Oxygen relative permeability as a function of clay mass fraction for the same particles dispersed in different matrices [Zhong et al., 2007].

Fig. 3.7 gives the predictions of eq. 3.7 for some published data, with the corresponding values of α for best fit. The figure shows that the model of Nielsen (eq. 3.7) gives reasonable predictions for most experimental data, such as Polypropylene/EPDM/MMT [Frounchi et al., 2006], Ethylene Vinyl Acetate/MMT [Zhong et al., 2007], Butyl Rubber/Vermiculite composites [Takashi et al., 2006], Polyethylene/MMT [Jacquelet et al., 2006], Polystyrene/MMT [Nazarenko et al., 2007], Nylon6/MMT [Picard et al.,

2007]. Each fitting curve requires a different value of the aspect ratio. In fig. 3.7 a value of $\alpha = 400$ for the vermiculite particles seems logical as these particles have greater aspect ratio than montmorillonite.

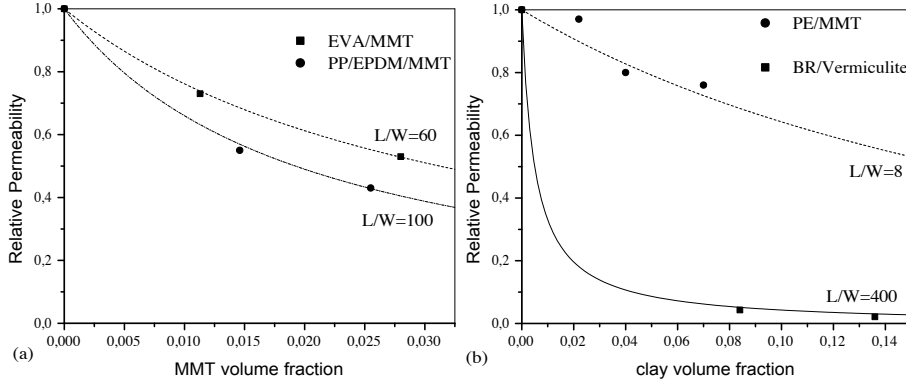


Figure 3.7: (a) Oxygen relative permeability as a function of clay volume fraction for an Ethylene Vinyl Acetate/MMT and Polypropylene/EPDM/MMT nanocomposites and the fitted model of Nielsen.(b) Carbon dioxide relative permeability as a function of clay volume fraction for a Polyethylene/MMT and Butyl Rubber/Vermiculite nanocomposite. The curves are the Nielsen equation fittings for the selected values of aspect ratio.

On the other hand, the permeability of water vapour in montmorillonite / styrene-acrylate copolymers was found by Maksimov et al. [2008] to follow Nielsen's model (eq. 3.7) at low weight fractions for $\alpha = 210$. At $\phi > 0.03$ incomplete exfoliation and decrease of the particle aspect ratio of the montmorillonite lead to a reduction of the efficiency of the barrier properties. Assuming that Nielsen's model holds at $\phi = 0.07$ (wt), an average stacking index of 1.8 can be calculated from the data of [Maksimov et al., 2008] using eq. 3.31.

Comparisons of the results of equations 3.10 and 3.11 with Monte Carlo calculations for the diffusion through membranes containing impermeable flakes were conducted by Falla et al. [1996] and Swannack et al. [2005]. Both papers reported rather good agreement between the theoretical and the simulation results, verifying the tortuous paths around the flakes and the effects of the constrictions into the slits and the diffusion through them. Falla et al. [1996] showed that eq. 3.10 is in general more sensitive to changes in the flake arrangement that will influence the diffusion mechanism, and can predict the resulting changes in the permeability of the membrane more accurately. Swannack et al. [2005] indicated the need for 3D calculations and showed that eq. 3.10 over-predicts the barrier effect of the membrane in this case, as the transverse slits are omitted.

Chapter 4

Transport Coefficients and Free Volume

Part of this chapter has been published in Current Opinion in Colloid and Interface Science, 17 (2012) 132–140, under the title "Free volume and mass transport in polymer nanocomposites" (G. Choudalakis and A.D. Gotsis).

The arguments in the previous chapter were based on the idea that the incorporation of the particles does not affect the physical characteristics of the matrix. However, this is not always the case, since the inorganic phase often alters the free volume properties of the polymer in which it is dispersed. Consequently, the transport properties of the nanocomposite may also change in a similar way, reflecting the specific impact of the nano-layers on the polymer free volume.

Gas permeation in a membrane is a complex process and has two main stages: Initially the gas molecules are adsorbed on the surface of the membrane, and then they diffuse through the membrane. During adsorption, the gas molecules are positioned in the free volume holes of the polymer that are created by Brownian motions of the chains or by thermal perturbations. The diffusion process occurs by jumps through neighbouring holes.

Thus, it depends on the number and the size of these holes (static free volume) and on the frequency of the jumps (dynamic free volume). The static free volume is independent of thermal motions of the macromolecules and is related to the gas solubility, while the dynamic free volume originates from the segmental motions of the polymer chains and is related to the gas diffusivity. Thus, the diffusion coefficient is a kinetic factor that reflects the mobility of the gas molecules in the polymeric phase, while the solubility coefficient, S , is a thermodynamic factor related to the interactions between the polymer and the gas molecules.

4.1 Free Volume

The term “free volume” in a polymer refers to the volume of the mass that is not actually occupied by the molecules themselves. This is really the room that the parts of the chains have to move around. The concept of the free volume is not uniquely defined. Various definitions are often used, such as hole, configurational, fluctuation and excess free volume [Choudalakis and Gotsis, 2012]:

Hole free volume: Even if the polymer chains were perfectly aligned, there would be free space between them. This is called “hole free volume”.

Configurational free volume: Due to the insufficient chain packing an additional free space is created.

Fluctuations free volume: The polymer chains or side chains are not fixed but can move (rotate, vibrate etc.) randomly due to their thermal activation. These motions of the side chains, generate transient gaps, which create an extra free volume that is called “fluctuation free volume”.

Excess free volume: At temperatures below T_g , the polymer has a specific volume greater than what it would have had if it had been allowed to cool slowly under equilibrium conditions. This difference between the equilibrium free volume and the actual volume under a given quenched condition is called “excess free volume”.

As time passes, the polymer molecules will try to rearrange themselves to approach the equilibrium density of the material, thus eliminating the excess free volume.

The sum of the hole free volume and the configurational free volume is often stated as static free volume, while the fluctuation free volume is called dynamic free volume. The excess free volume may be static or dynamic depending on the time scale of the relaxation processes. The ratio of static to dynamic excess free volume is thought to be greater than 1 and it depends on temperature.

The static free volume can, therefore, be defined as:

$$V_f = V - V_0 , \quad (4.1)$$

where $V = 1/\rho$ is the specific volume of the polymer and V_0 is the volume occupied by the atoms of the polymer chains at 0K. This volume is often calculated by the empirical relation:

$$V_0 = 1.3V_w , \quad (4.2)$$

where the coefficient 1.3 is assumed to apply for all groups and structures and may sometimes result in a faulty interpretation; V_w is the volume calculated using the group contribution method [Bondi, 1964] that employs the Van der Waals volume of the groups contained in the polymer repeat unit.

$$V_0 = 1.3 \sum_{i=1}^N (V_w)_i , \quad (4.3)$$

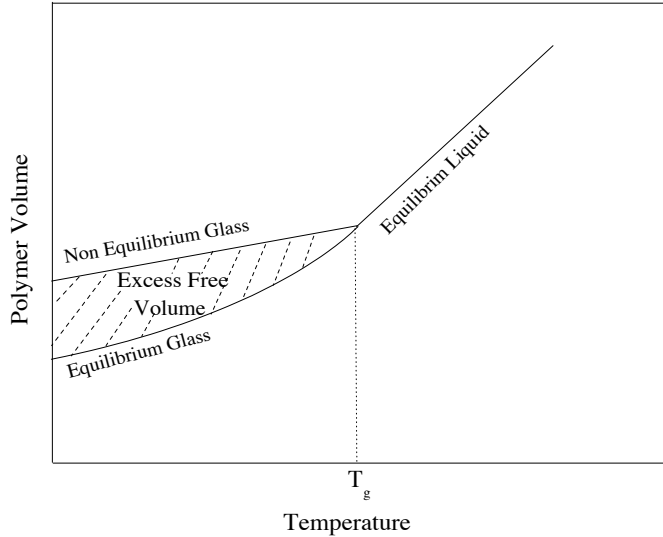


Figure 4.1: Definition of the excess free volume [Hiltner et al., 2005].

where N is total number of groups into which the repeat unit structure of the polymer is divided.

The fractional free volume (FFV) is defined as:

$$FFV = \frac{V_f}{V} . \quad (4.4)$$

In general, the polymer free volume can be assumed to consist of holes, the size, shape and position of which vary with time. Around the glass transition temperature, T_g , the polymer undergoes a dramatic transformation, as the degrees of freedom of the molecular chains and the resulting mobility change considerably and abruptly. From macroscopic point of view, the T_g can be considered as an index of the polymer backbone segmental mobility. At $T < T_g$ the segments motion is almost frozen and thermal expansion of free volume is almost impossible. In this case we can assume that the size, shape and the position of the free volume holes remain constant (have very long relaxation times) and, therefore, a definite time-averaged size distribution of holes is established. Assuming spherical in shape holes the distribution of hole sizes, $F(V_h)$ is given by a Gaussian function:

$$F(V_h) = \frac{N}{\sigma\sqrt{2\pi}} \exp\left[-\frac{(V_h - V_0)^2}{2\sigma^2}\right] , \quad (4.5)$$

where N is total number of the holes and σ is the width of the Gaussian distribution given by

$$\sigma = \sqrt{\frac{\bar{V}_h RT_g}{B}} . \quad (4.6)$$

Here B is the bulk modulus at T_g and \bar{V}_h is the average hole size [Arnold, 2010].

It has been found that high T_g polymers often consist of inflexible chains (for example polymers containing aromatic structures in their backbones) and are limited in their chain mobility, while low T_g polymers have, in general, more flexible chains and present higher segmental mobility. The higher the T_g the greater the polymer chain stiffness and the broader the distribution of hole sizes, since the available variety of chain conformations is further restricted. A very nice and representative description has been given by Hensema et al. [1993]:

An amorphous matrix of rigid polymer molecules can be compared to a heap of random strands of uncooked spaghetti, requiring substantially more free volume than flexible polymers, comparable to cooked spaghetti, which can pack into a much tighter form. This difference in packing density will result in a different free volume and in its distribution. Flexible polymers will be able to achieve a narrow distribution, while rigid polymers will lack this possibility since these polymers are limited in achieving the same variety of conformations, resulting in a broader free volume distribution, through which the number of larger holes is substantially increased.

Amorphous polymers in the rubbery state have high chain mobility and short relaxation times. Above T_g a liquid-like motion of much longer segments of the backbone chain can take place. This motion is directly related to the increase in free volume caused by the thermal expansion of the system.

$$FFV = (FFV)_{T_g} + (T - T_g) \alpha_T \quad (4.7)$$

where α_T is the thermal expansion coefficient for free volume. According to the WLF theory $(FFV)_{T_g} = 0.025$ and $\alpha_T = 4.8 \times 10^{-4}$ 1/K for many polymers [Fujita and Kishimoto, 1958; Jean, 1990].

Moreover, the position of the free volume holes changes with time owing to the non-harmonic oscillation of the polymer chains. That is, the holes can move freely inside the polymer, as no energy change is required for their redistribution [Consolati et al., 1996]. While the activity of main chain segmental motion in the rubbery state results in the enlargement of free volume holes, the question remains on what happens to the number of these holes.

At a given temperature the number of holes remains unchanged, while their size, shape and position varies with time. As the temperature increases the number of holes increases too, which means that additional free volume sites are created. It is interesting to note that the increase of the number of holes is induced by thermal activation (Brownian segmental motion) and not by an orientational effect. For example, Xie et al. [1995] measured the hole size and the number of the holes under mechanical deformation and observed that, while the size of the holes was sensitive to the applied stresses, the number of the holes remained unaffected.

Crosslinking does not contribute to changing the free volume size of the polymer in the glassy state, since the macromolecular motions are frozen (vitrified). However, crosslinking can decrease the size of free volume in the rubbery state, as it confines

the mobility of chain segments. Obviously, the more free and mobile the polymer network (e.g. linear polymers), the more effective is the reduction of free volume caused by cross-linking. On the other hand, in a rigid network structure (e.g. thermosetting polymer) the influence of crosslinking is expected to be smaller.

4.2 Effects of Nanoparticles on Polymer Free Volume

The incorporation of the inorganic nano-filters into the polymer matrix, will inevitably change the morphological features of the organic matrix and, consequently the free volume properties of the primary polymer. The following effects are expected in the nano-composite [Choudalakis and Gotsis, 2012]:

Interfacial regions: Because of their large surface area the inorganic particles create interfacial regions with the organic polymer. These regions are numerous and have finite thickness because of the weak interaction/miscibility between the inorganic reinforcement and the organic polymer and the need for compatibilisation. The interfacial adhesion between the two compatibilised components leads to the formation of an interfacial layer, which is helpful for the stress transfer between the nanoparticles and the matrix. These regions, however, may contribute to the enhancement of the overall free volume, especially when the interaction is weak [Paranchos et al., 2007; Wang et al., 2005].

Interstitial cavities in the filler agglomerates: In the case that the exfoliation is not complete, there will be stacks of nano-layers (intercalated morphology) inside the polymer. The interlayer spacing of these stacks varies from 2 to 5 nm, so it is expected that they contribute to the overall free volume of the composite. If the insertion/penetration of polymer chains in the galleries of these stacks is partial or incomplete, this extra free volume is in layers rather than in spherical holes.

However, experimental results of Na-MMT powder showed that the *FFV* was only 1.2% [Wang et al., 2004]. There is some uncertainty in these results, since the interlayer distances in this clay are very small: (i) *Ps* formation may have been hindered by the negative charges on the clay particle surfaces; and (ii) the penetration of the positrons may be limited by the presence of the cations in the galleries. In organomodified clays the *FFV* is expected to be much greater. [Becker et al., 2003].

Chain segmental motion immobilisation: The randomly distributed filler particles may restrict the chain segmental motion and reduce the chain mobility and the amount of free volume. Such effects are common to both PN and PCN. Due to their high surface area, nano-clays are expected to be more effective in immobilisation because they act as bridges over polymer chains, limiting their capability to change their conformation.

Insufficient chain packing: The filler nano-particles can confine the polymer chains and disrupt their packing. The free volume can be enhanced due to this inefficient packing or due to the increase of the distances between polymer segments [Merkel et al., 2003].

Changes of the free volume hole size distribution: The nano-particles may alter the free volume hole size distribution. Winberg et al. [2005a] observed broader distribution in the PTMSP/silica nanocomposite than in the unfilled polymer. Similar results have been reported by Choudalakis et al. [2011] in acrylic resin/laponite nanocomposites.

Changes of the crystallinity of the matrix: The incorporation of nano-particles often changes the crystallinity of the matrix polymer. The particles perturb the polymer chain packing and can reduce the crystallinity in the polymer, alleviating, thus, some of the decrease in chain mobility that accompanies crystallisation. Inevitably, this enhances the free volume. On the other hand, the nanofillers may also act as nucleating agents, increasing the degree of crystallinity and reducing the free volume. The net result will depend on the crystallisation characteristics of the matrix and its interaction with nucleation agents.

Changes of the crosslinking density of the matrix: Adding nano-particles in a thermosetting polymer can have two opposite effects. The particles may serve as crosslinkers, which increases the cross-link density and decreases the polymer mobility and the free volume. Or they may hinder the cross-linking reaction and enhance the free volume. The net effect depends on the chemistry of the crosslinking reaction, the possible catalytic action of the nano-particles and the interfacial properties of the system.

All the above effects of the nanoparticles on the polymer free volume coexist in any nanocomposite system. The question usually is which of them are dominant. This is determined primarily from the degree of interaction between the two components, the volume fraction of the filler and the geometrical features of the particles. Often the dominant factor, which is the interaction, cannot be predicted and usually has to be decided instinctively.

4.3 Solubility and Free Volume

Generally speaking, relations between solubility and free volume are not always obvious, since the way penetrants dissolve in the polymer depends on the total pressure, the affinity between gas and polymer and the temperature. However, for a specific gas-polymer system, these conditions are identical so only the free volume changes, due to the particles, affecting the solubility coefficient. During adsorption, the gas molecules are positioned in the free volume holes of the polymer that are created by Brownian motions of the chains or by thermal perturbations.

Henry's sorption in rubbery polymers cannot be directly associated to the existing free volume hole structure because the penetrants are dissolved in the matrix in a similar mode to the one that occurs in liquids. Thus, Henry's constant depends on the facility of the gas molecule to penetrate in the space between the chains [Garcia et al., 2006]. If we consider the case of holes that are large enough to accommodate gas molecules inside the polymer, then the solubility coefficient should reflect directly the number of

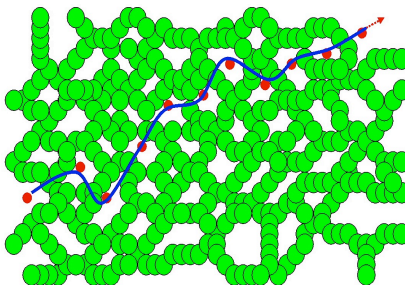


Figure 4.2: Schematic representation of the diffusion process of a gas molecule through a polymer.

the free volume holes and remain unaffected by their sizes. In an opposite case, the value of k_d increases with the increasing hole size, as well.

On the other hand, Langmuir's sorption is principally governed by the available free volume. Consequently the variation in the solubility is attributed mostly to C'_H , which is determined by the difference $V_g - V_l$. This, in turn, is influenced by the glass transition temperature. Therefore, higher T_g polymers generally exhibit higher solubility coefficients. It can be said that the FFV is related to the solubility because it corresponds to the free space in the polymer matrix, where the gas molecules can locate [Garcia et al., 2006].

The connection between the solubility coefficient and the number of free volume holes has been verified experimentally by Choudalakis et al. [2011] in an acrylic resin/laponite nanocomposite. The free volume in a material can be measured by Positron Annihilation Life Time Spectroscopy (PALS). In this method the intensity of the peak corresponding to the lifetime of the ortho-positronium in the material, I_3 , corresponds to the total free volume fraction, [Pethrick, 1997]. The value of I_3 was measured as a function of laponite particles loading in acrylic resin nano-composites and found to have an identical trend with the solubility coefficient, which was measured separately in a permeation cell [Choudalakis et al., 2011].

4.4 Diffusion and Free Volume

In contrast to the solubility, diffusion is a kinetic process which depends on the mobility of gas molecules in the polymer matrix. At temperatures below T_g , the polymer backbone is considered to be in a frozen state, segmental chain motions are drastically reduced, as compared to the rubbery state, the number of free volume holes is fixed and no hole redistribution is likely. Gas transport is, therefore, assumed to take place via fixed (pre-existing) holes [Hensema et al., 1993].

A gas molecule must “find its way” from hole to hole along pathways involving only minor segmental rearrangements. This means that the magnitude of the diffusivity depends largely on the number of holes with an appropriate size, able to accommodate a diffusing gas molecule.

A diffusing molecule can migrate if it can find a nearby hole large enough to jump into it, that is, larger than a critical size v^* . The probability for such a process is proportional to $\exp(-\gamma v^*/v_f)$ where v_f is the mean hole free volume per molecule, γ is an overlap factor between 0 and 1, which accounts for the fact that the same free volume may be available to more than one diffusing molecules. The diffusion coefficient can be written as [Thran and Faupel, 1999]:

$$D = \widetilde{D}_0 \exp(-E^*/kT) \exp(-\gamma \xi v^*/v_f). \quad (4.8)$$

where $\xi = v_s^*/v^*$; and v_s^* is the critical volume of the penetrant. The activation energy E^* needed for the diffusion of trapped molecules from one hole to another is related to the molecule “jumping length”. The proportionality coefficient \widetilde{D}_0 is related to the size and shape of the permeant and is given by the relation

$$\widetilde{D}_0 = \frac{RT\sigma^2}{M^{1/2}}, \quad (4.9)$$

where σ is the Lennard-Jones size parameter and M is the molecular weight of the permeant [Thran and Faupel, 1999].

The amount of free volume alone does not provide information about the possible connectivity of the holes. When free volume elements are added randomly to a system, the percolation threshold will be reached at some point. Then a connected pathway will exist from one side of the system to the other. Since glassy polymers consist of randomly placed free volume elements, this percolation threshold exists and has been determined by Greenfield and Theodorou [Greenfield and Theodorou, 1993] via molecular simulations. Therefore, as the FFV in the polymer increases, the holes become interconnected above the percolation threshold, and provide, thus, a flow-through path for the permeating gas. This has been commonly identified with a pore-flow diffusion process.

Diffusivity is better correlated to the accessible (for a given gas) free volume fraction (AFV). The percolation threshold is found to be in the range of 2 – 4% AFV for conventional glassy polymers. This range is equivalent to 25 – 31% FFV [Thornton et al., 2009]. This picture adequately describes the diffusion process in some high free volume glassy polymers.

In the rubbery state the picture of fixed holes needs to be replaced, since the polymer chains are mobile and the free volume holes are governed by a dynamic variation about their size, shape and position. The gas molecules are able to diffuse within the fluctuating interstitial free volume with greater mobility compared to the glassy state. That is to say, polymers with a stiff backbone have a large jumping step, whereas flexible chains have a smaller one [Thran and Faupel, 1999]. Equation 4.8 can be written in this case in the following form:

$$D = ART \exp(-B/FFV), \quad (4.10)$$

where the parameter B is equal to $\gamma \frac{v_s^*}{v^*}$. The factor $\exp(-E^*/kT)$ is neglected since no energy for diffusional jumping is required. The parameter A is related to the size and shape of the permeant and replaces the term $\sigma^2/M^{1/2}$ of eq. 4.4. It seems that the

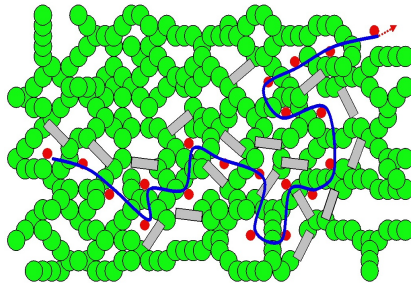


Figure 4.3: Schematic representation of the diffusion process of a gas molecule through a polymer/clay nanocomposite.

factor B depends not only on the type of gas but also on the polymer since v^* is the minimal free volume hole size required for the penetrant diffusion.

The size of the diffusing molecule has a smaller influence if the polymer is in the rubbery state than in a rigid glassy membrane, where the hole size distribution is frozen [Michaels and Bixler, 1961]. The glassy polymers seem to be more suitable to be used as gas separation membranes.

While a correlation between $\ln D$ and $1/FFV$ of the type of eq. 4.10 has been verified for various glassy polymers [Choudalakis and Gotsis, 2012; Hensema et al., 1993; Thran and Faupel, 1999] the values of parameters A and B show a significant variance. A linear fit of all the data gives $A = 4 \cdot 10^{-6} \text{ cm}^2/\text{s}$ and $B = 0.97$. In Polycarbonates Jean et al. [1995] reported $A = 39 \cdot 10^{-8} \text{ cm}^2/\text{s}$, $B = 0.297$ for CO_2 . The variance is due to the fact that the parameter B depends on the polymer and not only to the type of gas. Some indicative values of these parameters in rubbery polymers are $A = 7.4 \cdot 10^{-5} \text{ cm}^2/\text{s}$, $B = 0.1336$ for CO_2 in polyurethanes [Wang et al., 2003] and $A = 3.7 \cdot 10^{-8} \text{ cm}^2/\text{s}$, $B = 0.035$ for O_2 in NR and XSBR elastomers [Stephen et al., 2006].

In polymer nanocomposite systems, there is an additional feature that strongly affects the gas diffusion process: the tortuosity. In the case of nanocomposites eq. 4.10 should be modified to account for the tortuosity effect.

$$D = \frac{A'}{\tau} \exp(-B/FFV). \quad (4.11)$$

Thus, the variation of the diffusion coefficient in a polymer nanocomposite depends on the fractional free volume and tortuosity factor. These two parameters can be either in accordance or competitive. The final increase or decrease of the diffusion coefficient upon adding nanoclay depends on which of the two is dominant.

The curve of $\ln D$ vs. $1/FFV$ of some PVA-PA6/MMT nanocomposites [Cui et al., 2009] was linear for $1/FFV < 15$. That is, relations of the type of eq. 4.10 are valid in this case only when the fractional free volume is more than 6.7%. For smaller FFV the curve is not linear, showing a saturation with increasing $1/FFV$. Similar results were obtained in SBR/Rectorite nanocomposite where eq. 4.3 holds mainly for $FFV > 3.33\%$ [Wang et al., 2005]. This suggests that when the FFV is relatively high

it overcomes the influence of the tortuosity factor and the diffusion coefficient will be determined by the free volume variations.

There is also the case where the free volume consists of a network of large holes connected by channel-like holes. Diffusing molecules may now move with little friction within the network. Large variations in the size or in the number of larger holes have small effect on the free volume network, whereas a small decrease in the size of smaller holes may destroy the connectivity of the channel network. In this case the mobility of diffusing molecules may become strongly hindered [Consolati et al., 1996]. This means that a broader distribution of free volume holes can result in higher values of the gas diffusion coefficient than a narrow distribution and the same average size. Therefore, not only the amount of the free volume but also its distribution over the hole sizes are important factors that influence the diffusion coefficient.

The incorporation of nanoparticles in a polymeric matrix can cause redistribution of the free volume hole sizes. Changes in the free volume hole size distribution will affect both rubbery and glassy polymers. Even when the total FFV is identical between two polymers the differences in their hole sizes distribution may be able to alter their diffusivities [Jean et al., 1995]. This distribution may strongly affect the diffusion process as very small holes, where the gas molecules cannot enter, do not contribute to the diffusion. The solubility, which is connected to the overall free volume, remains unaffected by the hole size distribution.

This was the case in an acrylic resin/laponite nanocomposite where the particles did not influence the FFV but the diffusion coefficient was increased as a function of laponite loading [Choudalakis et al., 2011]. This enhancement was ascribed to changes in hole size distribution. Another example is the polymethyl methacrylate (PMMA)/MMT system [Manninen et al., 2005]. While the solubility of CO_2 in the PMMA/MMT is approximately the same as that for the pure PMMA, the diffusion coefficient is much greater than that for pure PMMA. This has been attributed to changes in the free volume size distribution towards a relatively greater number of larger holes.

4.5 Permeability and Free Volume

The permeability coefficient is the product of the solubility coefficient and the diffusion coefficient. Thus, the permeability coefficient of clay polymer nanocomposites will be equal to:

$$P = \frac{A'S}{\tau} \exp(-B/FFV). \quad (4.12)$$

This equation shows that the permeability depends on the diffusion coefficient, the solubility and the tortuosity. As described above the first two depend on the free volume in the system. However, the permeability coefficient seems to be less sensitive to the FFV than these two coefficients.

In polymer clay nanocomposites where the tortuosity factor dominates the fractional free volume variations, the percentage reduction on gas permeability is 20% – 90% [Choudalakis and Gotsis, 2012]. Priolo et al. [2010] managed to fabricate a super barrier polymer-clay thin film using layer-by-layer assembly technique. This method is

based on the alternating exposure of a substrate to aqueous cationic and anionic mixtures. Negatively charged clay nanoparticles seem to form highly structured layer-by-layer films when combined with a positively charged polymer. The oxygen barrier performance of the resulting polymer nanocomposite thin films was reported to be below $10^{-5} \text{ cm}^3 \text{ m}^{-2} \text{ day}^{-1} \text{ bar}^{-1}$ at a thickness of just 51 nm.

Recently, Moller et al. [2012] demonstrated a high charge coarse-grained Li-hectorites that they produced by melt synthesis. The clay is delaminated spontaneously yielding platelets with aspect ratios typically larger than 1000. Completely delaminated clay show $800 \text{ m}^2/\text{g}$ surface which is transformed into interface when perfectly dispersed into the polymer matrix. The authors managed to disperse the high aspect ratio Li-hectorite particles into a UV-curable polyurethane and to produce a flexible and transparent nanocomposite coating with remarkable oxygen barrier properties.

An effective aspect ratio of the hectorite filler of 410 was deduced from the permeability measurement but, since the aspect ratio of the hectorite-precursor is 1000 or more, the oxygen transmission rate (OTR) improvement can potentially be another two orders of magnitude better than what has actually been observed experimentally. The OTR for the hectorite composite may either be impaired by coating defects or by an increase of the diffusion coefficient through the matrix, which is related to an enlargement of free volume by solvent trapped in the film [Moller et al., 2012].

In polymer clay nanocomposites, where the tortuosity dominates the fractional free volume variations, the percentage reduction on gas permeability is 20% – 90%. In polyimide/MMT nanocomposites a reduction of 83% in oxygen permeability is observed for only 1 wt% MMT [Min et al., 2011], while for polyamide 6/MMT a reduction in the order of 77% was reported [Fasihi and Abolghasemi, 2012] for 2 vol% of MMT. A 76% reduction of the He permeability was measured for 8 wt% MMT in polyurethane/MMT nanocomposites [Maji et al., 2010], while the presence of 5 wt% MMT in polyacrylate decreased the permeability by up to 85% [Herrera-Alonso et al., 2010]. The addition of 4 wt% of MMT in Nylon-6 reduced the oxygen permeability by 50% [Sadeghi et al., 2011] and in Epoxy/MMT the reduction is of the order of 86% for 7 wt% MMT [Dai et al., 2008]. An appreciable reduction in gas permeability compared to the unfilled polymer film was reported in PP/MMT nanocomposites [Villaluenga et al., 2007], where both the diffusivity and the solubility were reduced by the presence of the filler.

There are also cases, where the permeability is affected appreciably by free volume changes. The nitrogen permeability of SBR containing 40 phr rectorite decreased by a 69% compared to the pure rubber [Wang et al., 2005]. This reduction, however, cannot be attributed solely to the tortuosity, since the fractional f.v. of the nanocomposite was also reduced by 27%. The two factors that affect f.v. and permeation properties may be competitive and the gas permeability can in some cases show a small decrease or remain constant. Such a case was reported in PE/HDPE-g-MA20/MMT nanocomposite [Jacquelot et al., 2006], where the diffusion coefficient was reduced by 44% when 18.42 wt% of MMT was added, while the solubility increased by 36% and the permeability decreased by 24%. The poor compatibility between the polymer and the inorganic particles creates interfacial regions, which enhance the f.v. This was the case in polyurethane/vermiculite nanocomposites [Qian et al., 2011], where the permeability of CO_2 and N_2 , was reduced only by 20 and 30%, although the high aspect ratio

particles were expected to be more effective barriers.

The overall transport properties of the nanocomposites are affected by the presence of interfacial regions. In their multi-scale hierarchical numerical model, [Xiao et al. \[2010\]](#) defined a polymer-nanoparticle interaction strength parameter to quantify this effect. For high values of this parameter, they showed that the polymer density next to the interface increases, indicating that the enhancement of the barrier properties are due also to the decrease of the free volume there. For large gas molecules, however, [Pryamitsyn et al. \[2011\]](#) showed that the polymer-particle interactions are less important than the tortuosity effect. The mass transport properties, therefore, can be determined by the segmental dynamics of the matrix.

While the total amount of free volume affects the permeability of a material as described above, the distribution of the free volume hole sizes may also influence the permeation process. This distribution can strongly affect the diffusion process because the very small holes, where the gas molecules cannot enter, do not contribute significantly to the diffusion. The solubility, which is connected to the overall free volume, remains unaffected by the hole size distribution. An example is the PMMA/MMT system [[Manninen et al., 2005](#)]: While the solubility of CO_2 in the PMMA/MMT is approximately the same as that for pure PMMA, the diffusion coefficient is much greater. This has been attributed to changes in the free volume size distribution towards a relatively greater number of larger holes.

Summarising the effect of nanoparticles on the mass transport properties of the nanocomposites, one could state that when exfoliated nano-clay is added to the polymer, then the permeability is expected to be reduced significantly. The resulting tortuosity of the diffusion path is the major cause for this enhancement. The free volume may increase somewhat, due to the presence of the expansive interfacial regions, but this is a minor effect and, in most cases, cannot overrule that of the tortuosity. Of course, this is the case when the clay particles are well exfoliated and properly oriented. At lower degrees of exfoliation the situation can point towards that of the isometric nano-fillers.

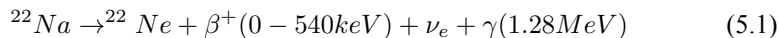
Chapter 5

Direct measurement of the free volume using PALS

One of the most accurate ways to measure the free volume in polymers is Positron Annihilation Lifetime Spectroscopy. A good review of this method and its applications has been given by Pethrick [1997]. In the present work PALS was utilised to measure possible changes in the free volume of the matrix in the nanocomposites due to the presence of the nanoparticles.

5.1 Positron annihilation lifetime spectroscopy

In the method used in the present work the positrons are created by radioactive isotopes, such as the ^{22}Na , which decays to ^{22}Ne with the simultaneous emission of a positron, e^+ with energy up to 540 keV, and a γ photon with 1.28 MeV energy, through the reaction:



The positrons emitted from such sources have a wide energy distribution (0–540 keV) and are usually called “fast positrons”. Fast positrons can be used for bulk measurements as they can penetrate a few tenths of a mm inside the sample. The energy of the injected positrons decreases within a few picoseconds due to inelastic collisions with the surrounding media. On reaching thermal energies (~ 0.027 eV), the positron diffuses in the material (diffusion length ~ 100 nm) before it is trapped in a lattice defect or a free volume hole.

The positron is the anti-particle of the electron and it will be annihilated upon collision with an electron to generate photons of a specific energy as determined by the mass-energy conversion law of Einstein, $E = m_0c^2$. When the two particles are annihilated in vacuum, the annihilation occurs via three different processes. The first is the direct annihilation which results in the creation of two γ photons of 511 keV energies that are emitted in opposite directions, around the centre of mass of the system.

The other two processes employ the formation of a temporary pair between the two particles that is called a positronium, Ps . A Ps is similar to a hydrogen atom with a binding energy ~ 6.8 eV and a radius of 1.06 \AA . Depending on the spin state of the two particles, there are two possible Ps atoms: The $p - Ps$ positronium corresponds to the antiparallel, while the $o-Ps$ positronium to the parallel spin configuration. In vacuum the annihilation of these positronium atoms occurs within lifetimes of 0.125 ns for the $p - Ps$ (2γ -annihilation) and 140 ns for the $o-Ps$ (3γ -annihilation) respectively.

When the positrons are injected in the material, similar processes of annihilation occur as above. In this case the Ps formation can be achieved only in low electron density regions like in voids or in the free volume of the polymers. If no such areas are present, then the positrons will be annihilated via the direct annihilation process. The lifetimes of the free and the $p - Ps$ positrons remain the same as in the case of vacuum but the $o-Ps$ lifetime is very much reduced now.

The reduction of the lifetime of the $o-Ps$ is due to the “pick off” reaction, in which the electron with the parallel spin is exchanged with an electron with antiparallel spin from the cavity wall. This reduction depends on the overlap of the wave-functions between the $o-Ps$ and the surrounding electrons. In materials with small voids, such as in polymers, the overlap is strong and, thus, the reduction is large, from 140 ns to $2 - 5$ ns.

The whole process, from the time of generation of the positron until its annihilation, can be divided into four stages: The first stage is the generation of the positrons, according, e.g., to the reaction 5.1. This generation is accompanied by the emission of a γ photon at 1.28 MeV. The detection of this photon marks the starting point for the measurement of the lifetime. The second stage is the implantation of the positrons in the material and their acceleration through inelastic collisions. The third stage is the diffusion process of the positrons through the polymer, which leads to their trapping and the formation of Ps . The final stage is the annihilation of the positrons and the detection of the $\gamma 511 \text{ keV}$ photons.

The measured lifetime of the positron is the time difference between the detection of the 1.28 MeV γ photon and the detection of the 511 KeV photon. The lifetime spectrum can be resolved into N Debye decaying processes by fitting the curve by a sum of N exponentials:

$$F(t) = \sum_{i=1}^N \frac{I_i}{\tau_i} \exp\left(-\frac{t}{\tau_i}\right). \quad (5.2)$$

Here I_i is the relative intensity and τ_i is the lifetime of the i -th Debye process. In polymers the lifetime spectrum (eq. 5.2) is usually resolved into three terms. The first term (I_1, τ_1) has a relaxation time (lifetime) $\tau_1 \sim 0.125$ ns and is related to the fast annihilation of the $p-Ps$ and the free positrons. The second process (I_2, τ_2) with a relaxation time $\tau_2 \sim 0.4$ ns corresponds to the direct annihilation of the free positrons. The third process (I_3, τ_3) is the “pick-off” annihilation process of the $o-Ps$ and has a relaxation time τ_3 in the range of 1 to 5 ns.

In some rare cases of high free volume polymers there is a fourth significant lifetime component, (I_4, τ_4), with τ_4 greater than 10 ns [Winberg et al., 2005a, etc.]. Lifetime,

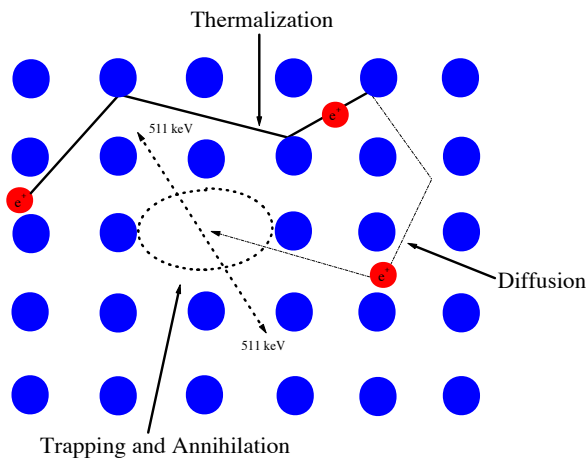


Figure 5.1: The process from the time of positron implantation to the time of Ps annihilation.

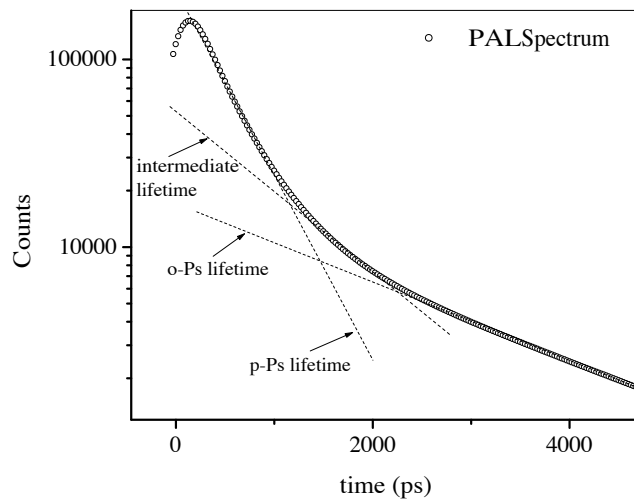


Figure 5.2: Positron Annihilation Lifetime Spectrum and the extrapolation of the lifetimes for the three processes.

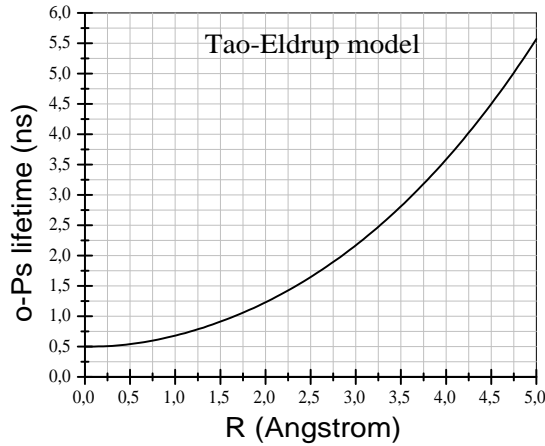


Figure 5.3: Tao-Eldrup model.

τ_4 , was ascribed to the bimodal distribution of possibly non spherical free volume elements.

To *o-Ps* lifetime is related to the size, R , of the free volume hole where it is trapped by the Tao-Eldrup model:

$$\tau_3 = \frac{1}{2} \left[1 - \frac{R}{R + \Delta R} + \frac{\sin \frac{2\pi R}{R + \Delta R}}{2\pi} \right]^{-1}, \quad (5.3)$$

where ΔR is the electron layer thickness around the hole, usually assumed to be uniform and ~ 0.1656 nm.

This model is sufficient for characterising small voids with cavity diameter smaller than the thermal de Broglie wavelength of *Ps* (~ 6 nm). There is also a low threshold for detecting free volume holes by PALS, equal to the minimum for *o-Ps* localisation, R_c :

$$R_c = \frac{\pi}{2} \left(\frac{\hbar^2}{2m\tilde{V}_0} \right)^{1/2}. \quad (5.4)$$

\hbar is Planck's constant, m is the electron mass and \tilde{V}_0 is the potential barrier (~ 1.4 eV). Typically $R_c \approx 2$ Å.

The intensity I_3 is related to the formation probability of *o-Ps* in the free volume holes and is connected to their number. The fractional free volume in polymers is $FFV \sim V_h I_3$, where $V_h = (4/3)\pi R^3$, in Å³, is the volume of the average spherical hole. The total fractional free volume cannot be estimated, since I_3 originates only from

the holes, where the *o-Ps* can be formed, which are not the total free volume. Thus, a proportionality parameter, C , is used:

$$FFV = CV_h I_3 , \quad (5.5)$$

where C depends on the polymer and can be deduced by comparing the values of FFV from PALS measurements with values of FFV from P-V-T data. Indicative values are 0.325 nm^{-3} for poly(vinyl acetate) [Kobayashi et al., 1989] and 1.8 nm^{-3} for amine-cured epoxy polymers [Wang et al., 1990].

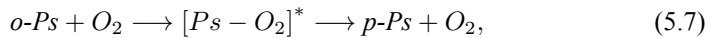
When a fourth mode (I_4, τ_4) is found, the size can be estimated by an extended Tao-Eldrup model [Ito et al., 1999]:

$$\tau_4 = 0.0626 \left[1 - \left(\frac{R - R_a}{R + \Delta R} \right)^b + \frac{1}{140} \right]^{-1}, \quad (5.6)$$

where $R_a \approx 8 \text{ \AA}$ and $b \approx 0.55$ are fitted parameters.

In molecular solids, a decrease in I_3 can be due either to a decrease in the number of *o-Ps* annihilation sites or to a decrease in the probability of *Ps* formation. Negatively charged polar groups, M^- (nitro, halogen, hydroxyl), can suppress *Ps* formation considerably by arresting the positrons. This competing mechanism, which reduces the *o-Ps* formation and results in a decrease of I_3 , is often observed upon addition of salts. The latter increase the dipole moment of the polymer molecules enhancing localisation of the negative charges. This decrease in I_3 is approximately exponential with anion concentration, approaching a saturation value [Zhang et al., 2011].

Besides its effect on I_3 , the chemistry of the material also affects τ_3 . A stronger polarity effectively quenches the *Ps* atoms and, thus, shortens the *Ps* lifetimes. The size of the cavities may remain constant, but the *o-Ps* lifetimes can be quenched by various oxidisers, including paramagnetic ions and chlorides. Oxygen is particularly efficient in promoting the conversion of *o-Ps* to *p-Ps* [Consolati et al., 1996]:



At high temperatures, well above T_g , the *o-Ps* lifetime may reflect the formation of so-called *o-Ps* bubbles. When the surface tension is small enough, the repulsive forces between the *Ps* and the surrounding polymer chains are sufficient to form a “bubble” around the *o-Ps* atom. This bubble formation is only possible if the segmental relaxation times are in the order of, or shorter than the *o-Ps* lifetime [Winberg et al., 2004]. Obviously, when bubbles are present, the *o-Ps* lifetime does not reflect the actual size of a free volume hole.

5.1.1 Doppler broadening of the annihilation line

The annihilation of a thermal positron and an electron occurs with the emission of two γ photons. In a co-ordinate system following the centre of mass of the two particles of the positronium the photons are emitted in opposite directions and the available energy of the pair is divided equally into two quanta. In the laboratory co-ordinate system,

however, this energy is not split equally among the two gamma rays. The frequency of one of them is up-shifted, while the other is downshifted by an amount given by $\Delta E = p_L c/2$ according to the Doppler effect, where p_L is the longitudinal component of the momentum of the pair along the direction of the gamma ray emission. This energy shift results in a Doppler broadening of the spectral line by a few KeV around the 511 KeV line (Fig. 5.4) and is measurable with a solid state detector.

In general, the energy distribution of positron annihilation in polymers can be separated in three intrinsic energy distributions (e^+ , $o\text{-}Ps$, $p\text{-}Ps$) profiles. The e^+ and $p\text{-}Ps$ depend on the chemical elements that constitute the polymer while the $o\text{-}Ps$ is identical for all polymer groups [Sato et al., 2005].

The energy spectrum of Fig. 5.4 can be used to extract information about the spatial source of the electrons that cause the annihilation. This source could give a clue for the number of the free volume holes and whether their position is in the bulk or near an interface in the nanocomposite. The basic difference between these two is the sort of atoms that make the inorganic and the organic phases. The clay includes metallic atoms with nuclei of high proton density, which will tend to repel the positrons, while the polymer consists mostly of carbon with much fewer protons.

Two portions of the Doppler broadening line are of interest for this: The area under the curve immediately around the peak, and the area under the tails of the curve in Fig. 5.4. Because of their positive charge, positrons are repelled from the atomic nuclei. Thus, they are located mainly in intrinsically empty lattice sites (defects) and their rate of annihilation is determined by the low momentum covalent electrons. Thus they contribute to the central part (peak) of the curve. The edges of the profile have lower intensities due to the fact that annihilation occurs there with the high momentum core electrons. Thus, the narrower and higher the peak of the profile, the higher the number of the defects.

The description of the curve in Fig. 5.4 can be quantified by using two shape parameters: parameter S_1 is defined as the ratio of the area under the curve around the 511 keV peak (e.g. ± 0.77 keV, [Mohamed and Abd El-Aziz, 2001]), normalised over the total area; parameter W is the normalised area under the tails (e.g. the ranges W_1 between 508.44 and 509.72 keV, and W_2 between 512.28 and 513.56 keV, in Fig. 5.4). Obviously, the higher the value of the ratio S_1/W , the higher the number of the free volume holes (defects) inside the polymer and far from the inorganic phase, where the positrons are repelled more strongly than in the bulk of the polymer.

5.2 Free volume measurements in polymer clay nano-composites

The influence of the clay on the polymer free volume is different from that of the isometric nanoparticles. Most experimental results show a reduction of the amount of the free volume as a function of clay loading. This reduction concerns mainly the $o\text{-}Ps$ intensity, I_3 , and not the lifetime, τ_3 , which remains mostly unaffected: While the mean hole size remains constant, the number of the free volume holes seems to decrease. This is a clear evidence that the clays inhibit the polymer chain motions resulting in a reduction

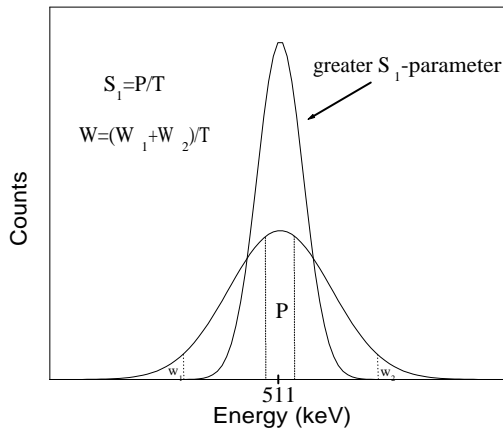


Figure 5.4: Doppler broadening of the 511 keV annihilation line. The S_1 -parameter is defined as the ratio of the central peak area P to the total area T , while the W -parameter is defined as the ratio of the tails ($W_1 + W_2$) area to the total peak area.

of the dynamic free volume relative to the neat polymer. However, if the interaction between the two phases is very weak, then the contribution of interfacial layers on free volume can overwhelm the immobilisation effect resulting in an increased free volume.

In elastomers, such as styrene-butadiene rubber/MMT [Wang et al., 2004], SBR / Rectorite [Wang et al., 2005] etc., a decrease in FFV is observed as a function of clay loading, mainly due to the o-Ps intensity reduction. The hole radius in these elastomers is about 3 Å and does not vary with the addition of filler. The reduction of the FFV is stronger (27%) in nanocomposites of SBR with 40 phr rectorite, while the other materials present a slight reduction of the order of 5–6% for filler contents of 2.5–10 wt%.

Similar trends for I_3 have been observed for rectorite in epoxy [Wang et al., 2007a] and ethylene-co-(vinyl acetate) [Fang et al., 2006a] nanocomposites. The o-Ps lifetime is unaffected or slightly reduced, due to the increasing fraction of positrons that annihilate in the interfacial layers between silicate platelets and polymer matrix. This reduction is accompanied by a small increase in I_2 . In EVA/rectorite systems the 1% reduction in FFV is due to the chain immobilisation effect. Adding MMT to an epoxy/polyurethane (EP/PU) blend has no significant effect on FFV for clay loadings in the area 0–5 wt% [Jia et al., 2007]; for laponite particles added to an acrylic resin [Choudalakis et al., 2011]; and in HDPE/PA6 blend/clay nanocomposites [Fang et al., 2006b].

These results indicate that the incorporation of clay in the polymer matrix does not alter the free volume properties significantly, especially at relatively low clay volume fractions. Higher clay loadings have been found to have a stronger effect on free volume. The exfoliation of the particles and the successful formation of the nanocomposite

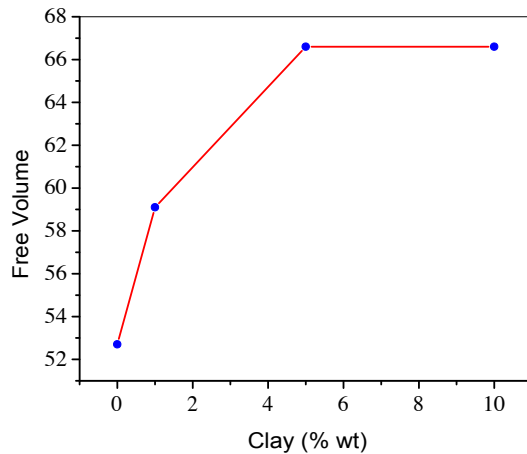


Figure 5.5: Free volume as a function of clay mass fraction for a PVA/MMT nanocomposite.

become particularly difficult in these cases. In polyamide-6/MMT an enhancement in *o-Ps* lifetime has been reported [Winberg et al., 2004], especially when the clay loading exceeds 19 wt%. At these loadings the samples are rather microcomposites with large particle aggregates. Since the clay on its own shows an *o-Ps* lifetime in the order of 2.17 ns and the neat polyamide shows a lifetime of 1.67 ns, it is expected that addition of clay above 10 wt% will lead to an increase in τ_3 , simply by applying the rule of mixtures.

Some reports mention that clay loadings lower than 10% may enhance significantly the polymer free volume. Paranchos et al. [2007] reported a 26% increase of the mean volume of the holes when 5 wt% of MMT was added in PVA-PES hydrogels. This behaviour is attributed to the free volume in the interfacial layers between the organic and inorganic components.

Both the *o-Ps* lifetime and intensity increased in cyanate/ bentonite systems [Yu et al., 2006]. The enhancement of free volume was about 4.5% for the sample containing 2.5 wt% of particles. This increasing trend is ascribed to the insufficient chain packing that the particles cause in the polymer.

Summarising, the free volume in the polymer matrix remains mostly unaffected by the addition of clay at low volume fractions or even decreases slightly. This small reduction is seen mainly as a decrease of the number of the free volume holes, while their average size remains the same. Exceptions to this involve systems with large interfacial regions, where extra free volume may develop. Further, at high clay volume fractions exfoliation/deagglomeration is incomplete. The free volume, then, is enhanced by the presence of interstitial empty space inside the aggregates, which is inaccessible to the polymer.

Chapter 6

Acrylic resin/laponite nanocomposite coatings

*Part of this chapter has been published in the European Polymer Journal, **47** (2011) 264–272, under the title “The free volume in acrylic resin/laponite nanocomposite coatings” (G. Choudalakis, A.D. Gotsis, H. Schut, and S.J. Picken).*

The aim of the chapter is to examine the permeability characteristics of nanocomposite coatings consisting of exfoliated laponite nano-disks dispersed in an acrylic matrix. The effects on the free volume in the polymeric matrix was studied by a combination of positron annihilation lifetime spectroscopy (PALS) and gas transport measurements in the permeation cell.

6.1 Experimental

6.1.1 Sample preparation

The primary particles of laponite are disk-shaped with sizes of 20–30 nm across and 1 nm thick. The clay was supplied by Rockwood Additives® as powder agglomerates ($\rho_L = 2.65 \text{ g/cm}^3$). The agglomerates are dispersible in water upon applying high shear. A small amount of phosphonic ester (PNP9®, Akzo Nobel surfactants) was used in order to improve the compatibility between the laponite disks and the acrylic resin. Nuplex Resins provided Setalux 6768® ($\rho_{resin} = 1.04 \text{ g/cm}^3$) a speciality acrylic emulsion in water. This resin is self-crosslinkable: The crosslinking mechanism is triggered upon drying and results in a fully cured coating. The acrylic based nanocomposites dispersions were prepared by mixing of aqueous laponite nanoparticles dispersions with acrylic resin dispersions. Four samples in the form of cured films were prepared with concentrations 0, 0.5, 2 and 4.5 % w/w of laponite disks respectively. The fractions were verified by TGA measurements. More details on the material preparation can be found at [Nobel, 2007; Nobel et al., 2007a].

Table 6.1: Particle mass and volume fractions, nanocomposite density, membrane thickness and standard deviation values for the tested samples.

code	w/w%	v/v%	ρ_{comp} (g/cm ³)	d (mm)
L0	0	0	1.04	0.73 ± 0.15
L1	0.5	0.2	1.045	0.43 ± 0.03
L2	2	0.8	1.053	0.74 ± 0.11
L3	4.5	1.8	1.07	0.84 ± 0.10

The volume fraction of the samples was deduced by the formula:

$$\phi = \frac{\rho_{comp}}{\rho_L} w \quad (6.1)$$

where w is the particles mass fraction and ρ_{comp} is the nanocomposite density:

$$\rho_{comp} = \frac{\rho_L \rho_{resin}}{w \rho_L + (1-w) \rho_{resin}} \quad (6.2)$$

In order to prepare samples for the permeation experiments, the nanocomposite dispersions were smeared on sparse glass fibre filters. After hardening, this produced a compact (non-porous) membrane reinforced by the glass fibres of the filter of total thickness between 0.5 and 1.5 mm. The average thickness, d , of the membranes were estimated a posteriori from the mass of the sample (including the reinforcing filter), m_s , the mass of the filter, m_{flt} and ρ_{comp} :

$$d = \frac{m_s - m_{flt}}{\rho_{comp} A}, \quad (6.3)$$

where the area of the sample was $A = 23.76$ cm². The samples characteristics are shown in Table 6.1.

6.1.2 Measurements

The morphological features of the samples were investigated using X-ray diffraction. The XRD measurements were performed at the Technical University of Crete for angles $2^\circ < 2\theta < 10^\circ$ using a Siemens diffractometer with CuK_α radiation of wavelength $\lambda = 1.5406$ Å. The degree of exfoliation and the free volume properties were studied as a function of laponite particles loading.

PAL spectra were recorded at the Interfaculty Reactor Institute (IRI) of Delft University of Technology, in the Netherlands, at room temperature using ^{22}Na as radioactive positron source. The minimum thickness of the sample can be estimated by evaluating the mean implantation depth Z_0 (Å) in a material of density ρ :

$$Z_0 = \frac{400}{\rho} E^{1.6}, \quad (6.4)$$

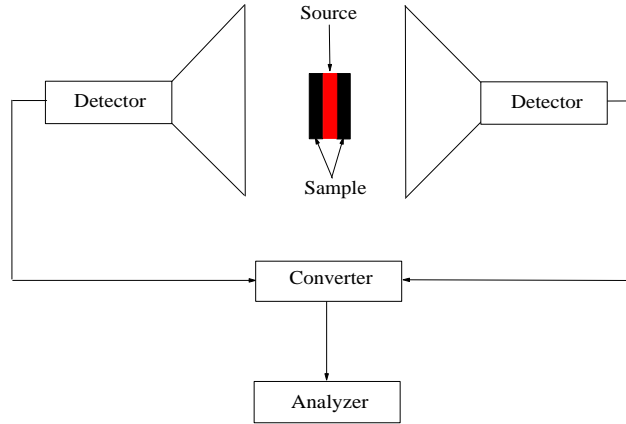


Figure 6.1: Experimental PALS set-up. The source is located between two pieces of the sample.

where E is the energy of the beam (keV). The source was located between two flat pieces of the sample with an appropriate thickness of 2 mm so that the positrons would be stopped in the bulk.

Each spectrum contained approximately 10^6 counts and was analysed by the POSITRONFIT computer program [Kirkegaard et al., 1989] into three Debye relaxation modes. Doppler broadening spectra were also measured and the parameters S_1 and W were deduced.

Gas permeability measurements were performed in a permeation cell that was designed at T.U.C. for the present work (Fig. 2.1). The cell was divided by the membrane in two compartments. The right compartment contained a CO_2 gas sensor supplied by Vaisala® of Finland. The measuring range of the sensor was 0–5000 ppm.

Both chambers of the cell were filled initially with He gas at 1 atm for 24 h. This procedure removed any possible residue of CO_2 that might have been absorbed by the membrane. Then the left chamber was filled with CO_2 at 1 atm and the CO_2 concentration in the right chamber was recorded as a function of time. Using Fick's first law the concentration of the gas that permeates the membrane at steady state is given there by the following relations [Choudalakis and Gotsis, 2009]:

$$c = \frac{ADSP_0}{Vd}(t - t_L) \quad \text{with} \quad t_L = \frac{d^2}{6D}, \quad (6.5)$$

where D is the diffusion coefficient, S is the solubility coefficient, p_0 is the initial pressure (= 1 atm), V is the volume of the chamber that contains the sensor, t_L is the time lag to reach steady state and d is the membrane thickness. The time lag is determined by extrapolation of the steady state straight portion of the $c(t)$ curve to zero concentration (Fig. 6.2). The slope of the curve at steady state gives the permeability

coefficient $P = D \cdot S$. Thus, the diffusion coefficient, D can be determined directly from measuring t_L and, then, the solubility, S , can be extracted from the value of P .

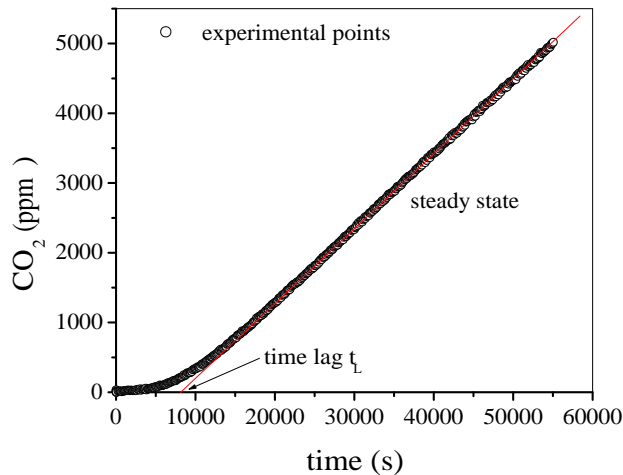


Figure 6.2: Time evolution of the gas concentration in the chamber of the cell where the sensor is present. The time lag, t_L , and the place where the slope is taken are shown. The measurement corresponds to the sample 0.2 v/v%.

6.2 Results and Discussion

6.2.1 X-ray diffraction patterns

The use of the X-ray diffraction pattern in the case of nanocomposites can reveal the degree of exfoliation of the clay nanoparticles. The characteristic distance inside the stacks of silicate layers can be calculated using Bragg's law, $2d \sin \theta = n\lambda$, where λ is the wavelength of the X-ray, 2θ is the angular position of the (001) basal reflection and $n = 1$ for the first order reflection. In intercalated structures the (001) reflection is present but it is shifted to lower angles. This shift indicates that the d -spacing increases due to the partial intrusion of the polymer chains in the galleries. Decreasing the mean stack size and increasing the fraction of individual layers broadens the basal reflection and lowers the magnitude of the intensity, which is proportional to the mean stack size. Thus, if such a reflection is not present, then the nanoparticles are fully dispersed in the amorphous matrix.

Fig. 6.3 presents XRD patterns for various concentrations of laponite nanoparticles. The absence of any Bragg peak verifies the amorphous state of the resin and the good exfoliation of the laponite disks. The form of the scattering curves for the filled samples are similar. The similarity indicates that the addition of the clay particles has no

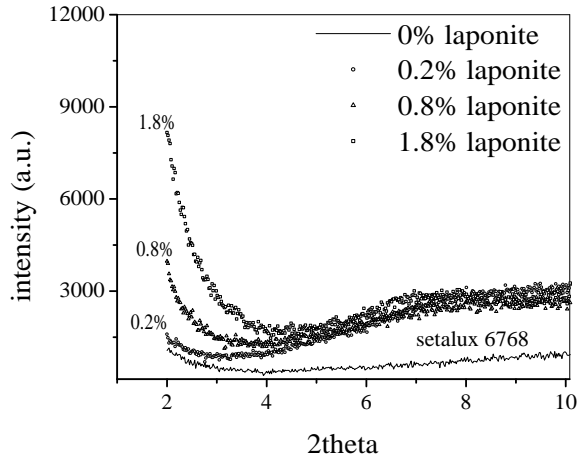


Figure 6.3: X ray diffraction patterns for the samples containing 0, 0.2, 0.8 and 1.8 % v/v laponite particles.

significant structural effects in the nanocomposite.

The scattering intensity increases with increasing clay content for all 2θ values. Its magnitude at low angles is connected to the mean size of the stacks. Generally, the scattered intensity at low angles follows a power-law behaviour, $I \sim q^m$, where $q = 4\pi \sin \theta / \lambda$ is the wave-vector and m is the mean stack size of the scattering object. For highly dispersed systems m reaches the value -2 [Nobel et al., 2007a; Vaia et al., 2003]. Fig. 6.4 shows the plot of $\log I$ versus $\log q$ at low angles for three filled samples, where the amorphous scattering of the unfilled resin has been subtracted. The exponent m can be calculated from the slopes of the lines. As the fraction of the particles increases the values of m at $2\theta \rightarrow 0^\circ$ decrease, indicating an increase in stacking order.

6.2.2 PALS results

Fig. 6.5 shows the positronium lifetimes in the nanocomposites and the related intensities as functions of laponite particles volume fraction. The measured lifetime for the unfilled sample, τ_3 , is about 2.175 ns . This corresponds to free volume holes with sizes of 3 \AA , according to eq. 5.3. The intensity, I_3 , is 25.24% , giving a fractional free volume of 5.16% according to eq. 5.5. These values are close enough with those for other systems like polystyrene at temperatures below their T_g ($R = 2.88 \text{ \AA}$, $V_f = 5.7 \%$, [Liu et al., 1993]).

Lifetime measurements in polymer systems like styrene-butadiene rubber (SBR) [Wang et al., 2003] and epoxy-rectorite nanocomposite [Wang et al., 2007b] reported similar values for τ_3 but lower values for I_3 , i.e., holes of the same average size but at lower numbers. Small differences in the value of I_3 have been observed by different

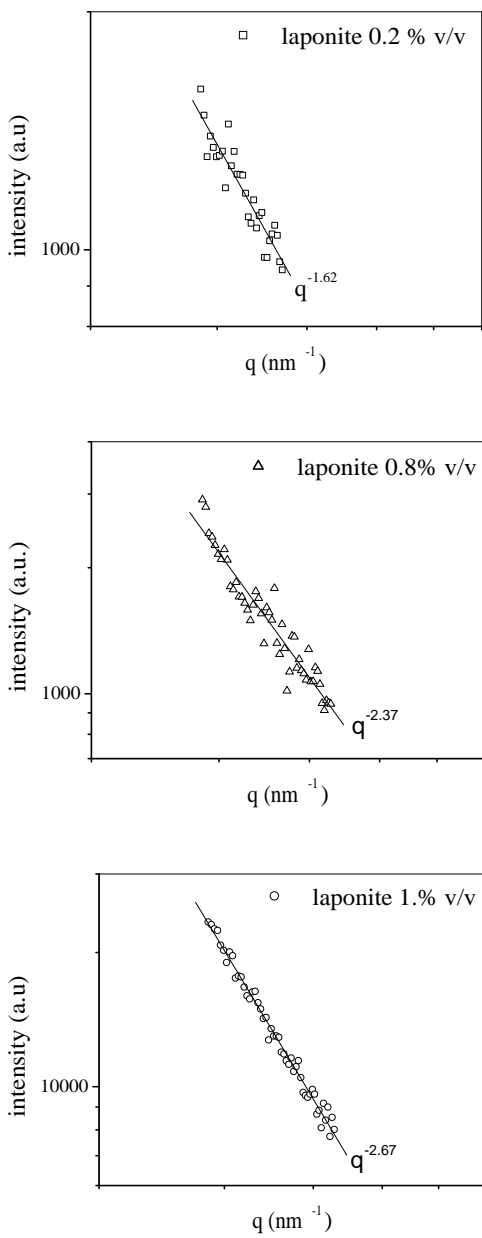


Figure 6.4: Power law behaviour at low angles for the samples 0.2, 0.8 and 1.8 % v/v.

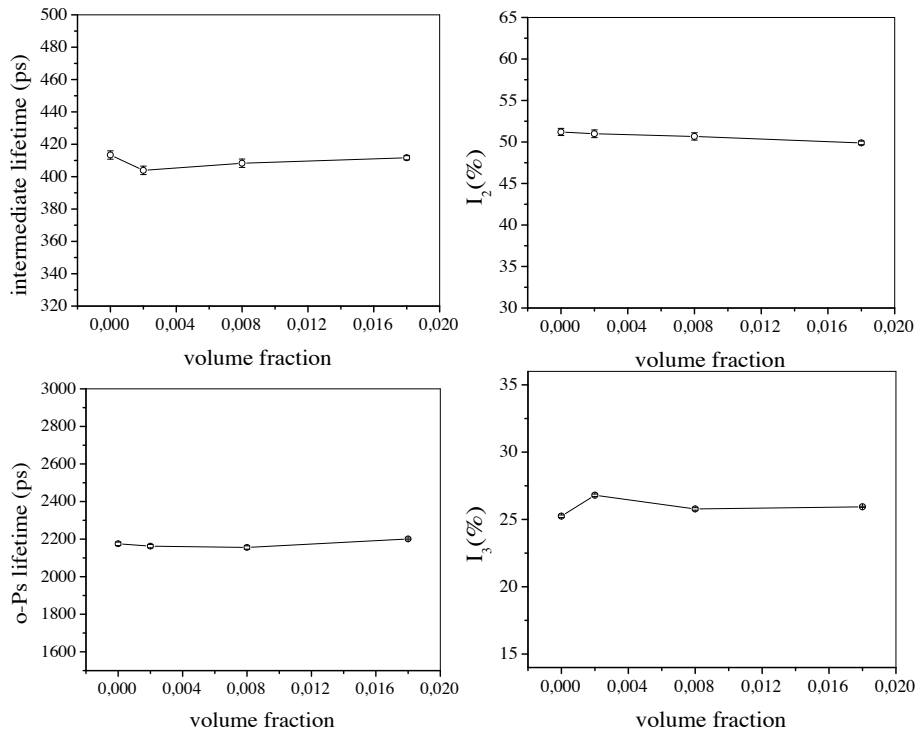


Figure 6.5: Intermediate lifetime τ_2 , o - P_s lifetime τ_3 , and the relative intensities I_2 and I_3 , as functions of laponite particle volume fraction.

authors for Polyamide-6. Winberg et al. [2005b] give the value 1.67 ns for τ_3 and 22.9% for I_3 , while Garcia et al. [2007] give $\tau_3 = 1.7$ ns and $I_3 = 19.52\%$ respectively. It seems that the fractional free volume in different systems depends on the details of their structure.

The o - P_s lifetime, that reflects the average size of the free volume holes, remains almost unchanged as the laponite content is increased (Fig. 6.5). The intensity I_3 , which is related to the number of the free volume holes, also does not change with particle content. Therefore, it seems that the overall free volume properties of the matrix are not affected by the addition of nanoparticles or by increasing their concentration. The same behaviour is followed by the lifetime τ_2 , its intensity, I_2 , and the parameters S_1 and W , Fig. 6.5 and Fig. 6.6. Similar results have been reported for NBR/MMT and poly(dimethylsiloxane)/polysilicate nanoparticles by other authors [Dreiss et al., 2007; Kim and Lee, 2001].

6.2.3 Effect of particle content on the free volume

In most cases, where free volume variations due to the presence of particles were reported to be large and detectable [Wang et al., 2003; Garcia et al., 2007; Zhang et al.,

2003], the clay loading was higher than what was used in the present work. It is possible, therefore, that the variations of the free volume caused by the addition of particles are too small to be detected by the present method and the experimental set-up, as it has been reported, e.g., by Winberg et al. [2005b]. The variations concerned the intensities (I_3 and I_2) and not the lifetimes, which remained almost constant.

Another reason for the absence of measurable change due to particle loading is the presence of two opposite mechanisms which contribute to the free volume. In principle, the particles could immobilise the chain segmental motions in the vicinity of their surfaces and their presence could reduce, thus, the free volume. This could be enhanced by the modification process that is used to compatibilise the clay and the matrix. On the other hand, the interfacial regions between matrix and clay should enhance the free volume because of the repulsive forces between polymer and particles or the difference in the thermal expansion coefficients of the organic matrix and the inorganic fillers. If these two free volume affecting processes are mutually balanced, then the total variation of the free volume could become zero.

This compensation seems to be common to all nanocomposites but it is not complete in all cases. The interfacial area depends on the compatibility between the matrix and the particles and on the aspect ratio of the particles. Clays with high aspect ratio create larger interfacial areas that could overwhelm the effect of chain immobilisation, resulting in larger total free volume. Such are the results of Wang et al. [2007b], which could be explained on the basis of the higher aspect ratio of the rectorite nanoparticles. More research is needed here to verify the effect of the particle aspect ratio on the free volume in nanocomposites.

It is interesting to notice that the o - Ps intensity of the 0.2 % v/v sample is slightly higher than the others. This feature is also observed at the estimation of the free volume using measurements of gas solubility as it will be discussed below. The X-ray results confirmed that this sample is well exfoliated and, consequently, it is expected to present larger interfacial regions. These regions contribute to the average free volume and the I_3 intensity seems to be affected even though these contributions are relatively small.

Because the o - Ps intensity does not always reflect the actual number of the free volume holes, as there is the possibility of radiation damage or complicated positron chemistry, it is useful to examine also the Doppler broadening of the annihilation line. These measurements are not appropriate for quantitative results but they can give a qualitative picture for the effects of the inorganic particles on the free volume.

The Doppler broadening parameter S_1 shows similar behaviour as the intensity I_3 (Fig. 6.5). The total variation of S_1 and W with particle fraction is almost negligible. The S_1 parameter is influenced mostly by the annihilation processes that involve low momentum covalent electrons. The origins of these electrons are the free volume holes or/and the interfacial regions. On the other hand, the W parameter involves annihilations with the high momentum core electrons which are located in the bulk sites. The lack of influence of the laponite particles on the ratio S_1/W indicates that the number of the open volume sites remains unchanged. Even though the degree of stacking is increased and the amount of interfacial region is decreased, the free volume is not decreased because it is located mostly in the bulk of the polymeric matrix.

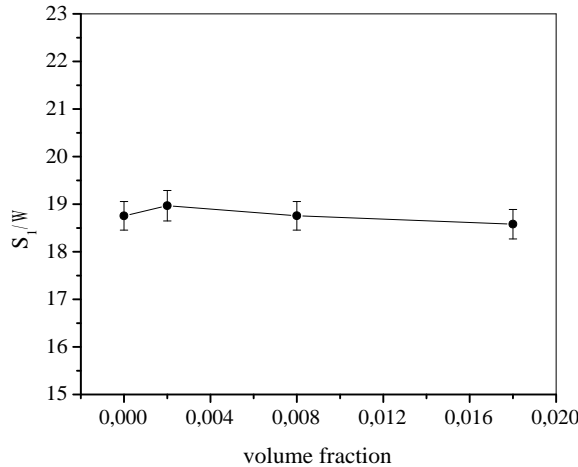


Figure 6.6: The ratio of the Doppler broadening parameters S_1/W as function of the laponite particle volume fraction.

6.2.4 Permeability measurements

In the CO_2 permeability measurements, the diffusion, D , solubility, S , and permeability, K , coefficients of the nanocomposites were extracted from curves as in Fig. 6.2 and are summarised in Table 6.2. The diffusion coefficient is correlated with the fractional free volume via the relation:

$$D = Ae^{-\frac{B}{V_f}}, \quad (6.6)$$

where the parameter A is related to the size and the shape of the diffusion molecule while the parameter B is related to the minimal hole size available for diffusional jumping. Jean et al. [1995] calculated the above coefficients for CO_2 as $A = 39 \cdot 10^{-8} \text{ cm}^2/\text{s}$ and $B = 0.297$. Using these values and the fractional free volume extracted from the PALS data, eq. 6.6 gives for the diffusion coefficient of the unfilled sample $D = 1.23 \cdot 10^{-9} \text{ cm}^2/\text{s}$. This is one order of magnitude lower than that extracted from the time lag in the permeability measurement. Similar order of magnitude differences were obtained in the results of Jean et al. [1995]: The CO_2 diffusion coefficient in polycarbonate was measured to be $D = 3.2 \cdot 10^{-8} \text{ cm}^2/\text{s}$, while eq. 6.6 for the fractional free volume of PC (measured by PALS) gave $D = 3.3 \cdot 10^{-9} \text{ cm}^2/\text{s}$.

The volume of a CO_2 molecule is 70.9 \AA^3 [Yu et al., 2006], while the average hole volume for the unfilled sample is 113.5 \AA^3 . That is, only one molecule of gas can fit in a hole of average size. If all the holes were of this size, the mobility of the gas molecules would be severely restricted, and the actual diffusion coefficient should be in the order of $\sim 10^{-9}$ rather than $\sim 10^{-8}$. The larger values of D measured above, then, are probably the result of the free volume size distribution: The small holes cannot contribute to the diffusion of the gas molecules and the diffusion is biased towards the

Table 6.2: The coefficients D , S and K from the permeability measurements and the fractional free volume V_f as it was calculated from PALS data, for nanocomposite samples.

v/v %	D $10^{-8} \text{ cm}^2/\text{s}$	S $10^{-5} \text{ mol}/\text{m}^3 \text{ Pa}$	K $10^{-16} \text{ mol}/\text{m s Pa}$	f_V %
0	6.1 ± 2.5	4.92 ± 2.24	3.0 ± 0.6	5.16
0.2	3.8 ± 0.5	7.89 ± 1.16	3.0 ± 0.2	5.44
0.8	7.3 ± 2.2	5.49 ± 1.85	4.0 ± 0.6	5.12
1.8	11.7 ± 2.8	7.63 ± 2.04	8.93 ± 1.06	5.41

larger holes. The broader the free volume hole size distribution, especially at the higher tail, the larger the gas diffusion coefficient for the same average hole size.

The addition of the filler should decrease the diffusion coefficient of the material according to the tortuous path model. A consistent decrease, though, is not seen in Table 6.2. The PALS measurements did not show any significant variation of the average free volume for these samples, that could explain the inconsistency. However, even though the total fractional free volume remains constant, its distribution may vary and this may influence the diffusion and permeation processes as indicated in the previous paragraph. Further, possible uncertainty in measuring the time-lag and incomplete orientation of the clay nanoplatelets will also affect the diffusion coefficient measurements in permeability experiments.

The fractional free volume, V_f , in an amorphous polymer above T_g is related to the solubility, S , and the density of the adsorbed gas, ρ_g :

$$V_f \sim S/\rho_g. \quad (6.7)$$

The solubility coefficient is shown in Fig. 6.7 as function of the clay volume fraction. It is remarkable that this curve, which was extracted solely from the permeability measurements, is very similar to those of the intensity I_3 and the S_1 -parameter, which were determined from the PALS measurements, and also define the free volume as a function of the clay content in the system. Since the solubility depends on the average free volume rather than its distribution, this agreement coming from an independent measurement confirms the accuracy of the free volume results of the PALS experiments. The agreement also shows that even small changes on the average free volume are detectable by the Positron Annihilation Lifetime Spectroscopy method, mainly through the measurement of the o - Ps annihilation intensity.

6.3 Conclusions

The amount of free volume in the acrylic resin/laponite nanocomposites remains unaffected by the addition of exfoliated laponite particles at low volume fractions, as indicated by the o - Ps lifetimes and annihilation intensities. The same behaviour is shown

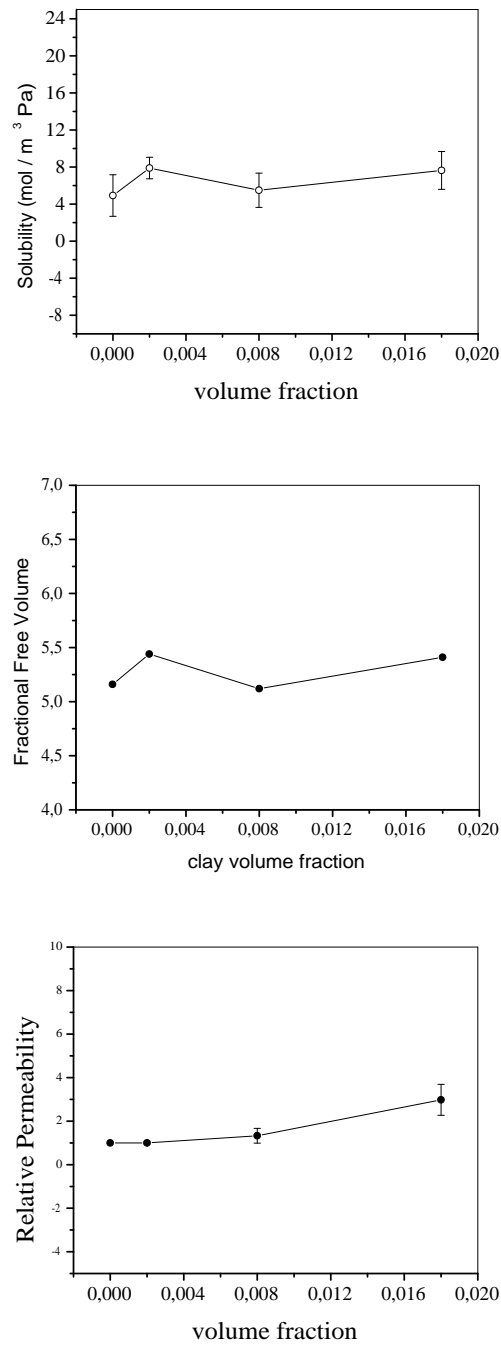


Figure 6.7: The solubility coefficient, measured by the permeability measurements, as a function of the clay volume fraction.

by the S_1/W ratio of the Doppler broadening of the annihilation line, indicating that the clay-polymer interfaces are not sources of extra free volume in the composite material. The distribution of the size of the free volume holes, on the other hand, seems to become broader with higher clay loading. Measuring the *o-Ps* annihilation intensity in PALS is a good method to estimate the free volume in a material and it is sensitive even in small changes of the free volume. This was verified by independent measurements of the solubility coefficient of CO_2 gas in the composite.

Chapter 7

Acrylic resin/bentonite nanocomposite coatings

Part of this chapter has been submitted for publication in Progress in Organic Coatings under the title "Morphology and gas transport properties in acrylic resin/bentonite nanocomposite coatings", October, 2012 (G. Choudalakis and A.D. Gotsis).

In this chapter hydrophilic bentonite nanoparticles are incorporated in an aqueous acrylic resin emulsion, which is then polymerised to make the nanocomposite coating. The purpose of these experiments is to explore methods to prepare nanocoatings with improved gas barrier properties. The formation mechanism of the nanocoating film is analysed and the entrapping of the nanolayers at the resin droplets boundaries during the solvent evaporation is explained. The resulting gas permeation properties are, then, discussed.

7.1 Experimental

7.1.1 Sample preparation

An amount of 0.5g of untreated Bentonite (Nanocor[®]) was added to 50 mL de-ionised water and the suspension was stirred for 30 min at 4000 rpm with a high shear mixer. The suspension was left to equilibrate for 24 h and then was sonicated for 30 min with an ultrasonic Sonotrode 400W (Hielscher[®]) operating at 35 kHz. The sedimentation that could be observed before ultra-sonication, disappeared completely after the sonication, indicating high exfoliation and adequate wetting of the bentonite particulates. The suspension was stable and no obvious sedimentation appeared, even after a period of months.

Nuplex Resins[®] provided Setalux 6768[®] ($\rho_{resin} = 1.04 \text{ g/cm}^3$) a speciality acrylic coating polymer emulsion in water with 40% resin content. The droplets of the emulsion are 60–70 nm in diameter and have a core shell structure consisting of a hydrophobic acrylate core and a stabilising hydrophilic acrylic shell. This resin is self-crosslinkable.

Table 7.1: Characteristics of the samples. In order to estimate the error on the membranes thickness, a micrometer was used and measurements of the thickness of each membrane were performed at ten random points.

sample	wt %	vol %	density (g/cc)	membr. thickness (mm)
BT	-	-	2.6	-
B0	0	0	1.04	1.03±0.06
B1	0.75	0.3	1.045	0.83± 0.04
B2	0.875	0.35	1.046	0.78± 0.07
B3	1.5	0.61	1.05	0.75± 0.05
B4	2.25	0.91	1.054	0.95± 0.08
B5	3.125	1.3	1.06	0.59± 0.05
B6	5	2.1	1.072	0.51± 0.08

The crosslinking mechanism is triggered upon drying at room temperature and results in a fully cured coating. Details on the colloidal structure of this emulsion are given in [Nobel et al., 2007b]. The glass transition temperature of the cured resin was measured by DMA [Nobel, 2007] to be around 100 °C. The acrylic based nanocomposite dispersions were prepared by mixing the aqueous bentonite nanoparticle dispersions with the aqueous acrylic resin emulsions and letting them dry at room temperature. Several samples in the form of cured films were prepared with various concentrations of nanoparticles.

The clay mass fraction, w , was verified by TGA measurements. The volume fraction was estimated from the mass fraction and the nanocomposite density, ρ_{comp} :

$$\rho_{comp} = \frac{\rho_{particles}\rho_{resin}}{w\rho_{resin} + (1-w)\rho_{particles}} \quad (7.1)$$

$$\phi = \frac{\rho_{comp}}{\rho_{particles}} w . \quad (7.2)$$

In order to prepare samples for permeation experiments, the nanocomposite dispersions were smeared on sparse glass fibre filters. After hardening, this produced a compact (non-porous) membrane (the nano-composite sample) reinforced by the sparse glass fibres of the filter, of total thickness between 0.5 and 1 mm. The average thickness, d , of the membranes (the cured coating itself, excluding the substrate) were calculated from the mass of the sample (including the reinforcing filter), m_s , the mass of the substrate (filter), m_{flt} and ρ_{comp} :

$$d = \frac{m_s - m_{flt}}{\rho_{comp} A}, \quad (7.3)$$

where A , the nominal area of the sample (directly exposed to the gas), was 23.76 cm². The sample characteristics are shown in Table 7.1.

7.1.2 Measurements

The morphological features of the samples were investigated using X-ray diffraction. The XRD patterns were collected for angles 2θ between 2 and 15° using a Siemens[®] diffractometer with a CuK_α radiation source of wavelength $\lambda = 1.5406 \text{ \AA}$. The degree of exfoliation was studied as a function of bentonite particles loading.

Gas permeability measurements were performed in a permeation cell as it was described in the previous chapter.

7.2 Results

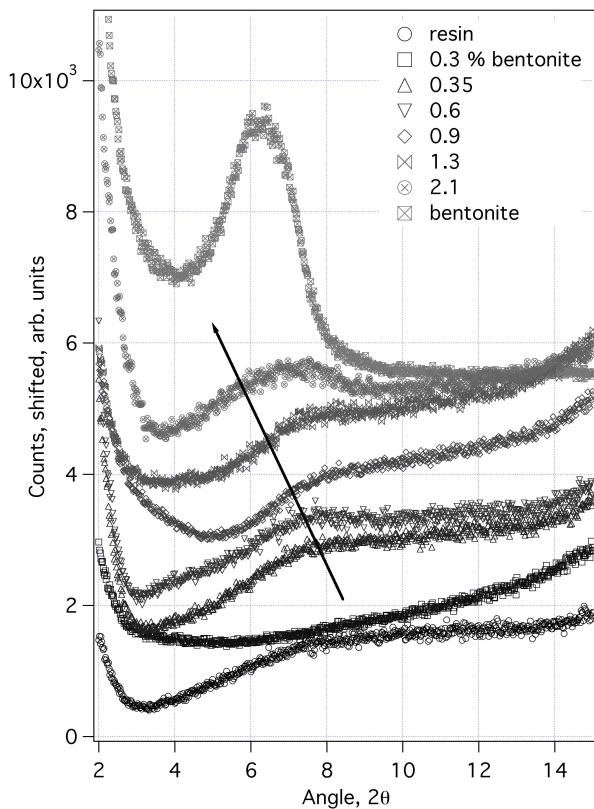


Figure 7.1: X-ray results for acrylic resin nanocomposite samples containing different volume fractions of untreated bentonite, increasing in the direction of the arrow. The curves are shifted vertically for clarity and to facilitate the comparison.

7.2.1 X-ray Diffraction

The XRD results for five acrylic resin (AR)/untreated bentonite (BT) nanocomposite samples are shown in Fig. 7.1. The bentonite powder shows a primary, (001), peak at $2\theta \approx 6.5^\circ$. For low mass fractions of BT this peak has disappeared in the composites. This indicates that the nanoclay particles are well dispersed and exfoliated in the AR matrix. However, a peak reappears at around $2\theta = 7^\circ$ for the sample with 1.3 vol % clay. This peak is more obvious and better formed in the sample of 2.1 vol% and shifted to angles closer to those of the untreated BT particles. It is clear that beyond 2 vol% an efficient nanocomposite cannot be made.

The scattering intensity, $I(q)$, per unit volume for a two phase dilute system is given in the low angle region by Negrete-Herrera et al. [2006]:

$$I(q) = \Delta\rho^2\phi P(q)S(q), \quad (7.4)$$

where q is the scattering vector, $q = 4\pi \sin \theta / \lambda$, $\Delta\rho$ is the electron density difference between the particle and the surrounding medium, $P(q)$ is the particle form factor and $S(q)$ is the structure factor. For small angles ($2\theta \rightarrow 0$), $S(q) \sim 1$ and the form factor for randomly oriented flat particles of thickness W is proportional to q^{-2} :

$$P(q) = \frac{I_0}{q^2} \exp\left(-\frac{W^2 q^2}{12}\right), \quad (7.5)$$

with I_0 the proportionality constant. Thus, for small angles we can write:

$$I(q)q^2 \sim \exp\left(-\frac{W^2 q^2}{12}\right). \quad (7.6)$$

The plot of $\log[I(q)q^2]$ versus q^2 is a straight line. From its slope, m (in nm^2), one can estimate the thickness of the scattering object:

$$W = \sqrt{-27.6 m} \quad (7.7)$$

In order to make an estimation of the actual aspect ratio of the bentonite particles, we plot $\log[I(q)q^2]$ vs. q^2 for the sample containing 0.35 vol% of bentonite (Fig. 7.2), which is well within the dilute region. The slope of the straight line in Fig. 7.2 is $m = -0.29 \text{ nm}^2$. Thus, eq. 7.7 gives 2.83 nm for the thickness of the scattering object. Since the width of the bentonite particles according to the supplier is in the range of 300-500 nm, the particles aspect ratio, $\alpha = L/W$, is in the area of 105-177. That is, there are on the average two to three individual nano-platelets in the stacks in the final composite.

In order to study the effects of the curing temperature of the film on the morphology of the nanocomposite, two samples, containing 1.3 and 2.1 vol% BT, respectively, were cured at 80°C , and their XRD patterns were compared to those that had been cured at 20°C . As it is shown in Fig. 7.3, the higher curing temperature affects negatively the degree of exfoliation. This is ascribed later in this work to the faster evaporation of the solvent. Note that both temperatures are below the glass transition temperature of the cured polymer.

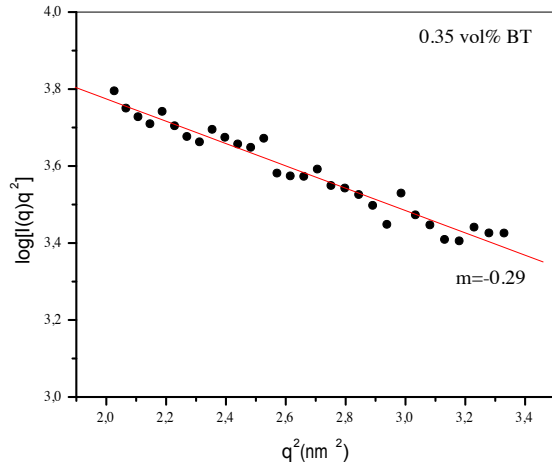


Figure 7.2: Low angles plot of $\log[I(q)q^2]$ versus q^2 for the sample containing 0.35 vol% of bentonite particles. The slope, m , of the straight line is -0.29 nm^2 .

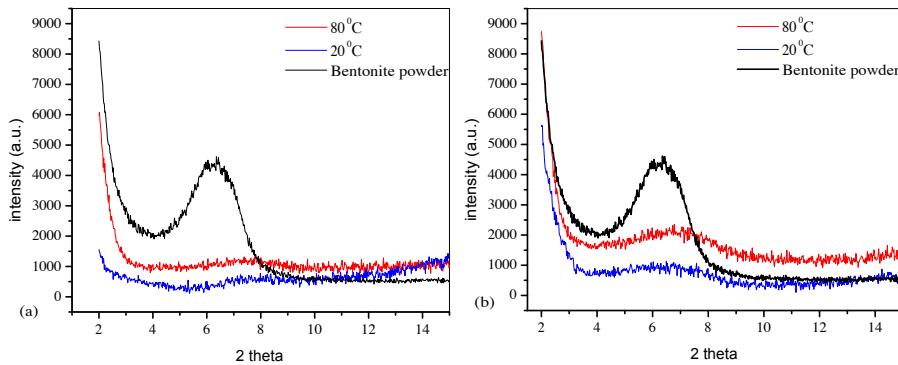


Figure 7.3: X-ray diffraction patterns (vertically shifted) for two samples (1.3 and 2.1 vol% BT) hardened at different temperatures.

Table 7.2: CO_2 gas transport coefficients of the samples at 14^0C and 50 % rel. humidity measured in the permeability cell.

vol %	Diffusion coefficient $10^{-12}(m^2/s)$	Solubility $10^{-5}(mol/m^3 Pa)$	Permeability $10^{-16}(mol/m s Pa)$
0	4.51 ± 0.52	6.72 ± 0.87	3.03 ± 0.18
0.3	3.90 ± 0.38	7.03 ± 0.76	2.74 ± 0.13
0.35	3.25 ± 0.58	8.22 ± 1.64	2.67 ± 0.24
0.61	2.91 ± 0.39	8.56 ± 1.29	2.49 ± 0.17
0.91	3.33 ± 0.56	7.00 ± 1.32	2.33 ± 0.20
1.3	2.80 ± 0.48	8.25 ± 1.58	2.31 ± 0.20
2.1	3.67 ± 1.16	7.41 ± 2.62	2.72 ± 0.43

7.2.2 Transport Coefficients

The transport coefficients of the samples that were measured are listed in Table 7.2. The measurements took place at a temperature of 14^0C and relative humidity of 50%. As the particle volume fraction increases, the diffusion coefficient decreases, e.g. by about 40% for the sample containing 1.3 vol% BT. However, the permeability coefficient decreases only by about 25%, as the solubility increases by 15% for this sample. Beyond 2 vol% bentonite, the decrease of the transport coefficients stops. As we argue in the next section, this is due to the reduction of the degree of exfoliation of the particles.

7.3 Discussion

7.3.1 The stability of the aqueous suspensions

The van der Waals forces (permanent dipoles, induced dipoles, dispersion forces) between the particles are attractive. Thus, the delaminated nano-layers of the aqueous suspension should tend to re-aggregate through collisions, due to Brownian motions, and finally precipitate out of the suspension [Grillet et al., 2004]. However, the suspension of clay in water seems to remain stable over a long time period.

Aggregation is prevented by the presence of electric long range repulsive forces, which oppose the attractive van der Waals forces. The force between two charged surfaces interacting through a liquid medium is due to the electrical double layer (EDL) formed around the particles [Liang et al., 2007]. When two colloidal particles approach each other, their EDL's begin to overlap and a significant repulsive electrostatic force develops preventing their further approach and stabilising the dispersion.

When polymer modification of the surfaces has been used and the suspension medium is not polar, then steric interactions keep the suspension from collapsing. The flocculation forces are due to the polymer chain conformations caused by the differences between the compatibilities of the clay, the matrix and the compatibiliser.

In the case of aqueous suspensions the total energy for the interaction of the two surfaces is the sum of the van der Waals attraction energy U_A and the EDL repulsion

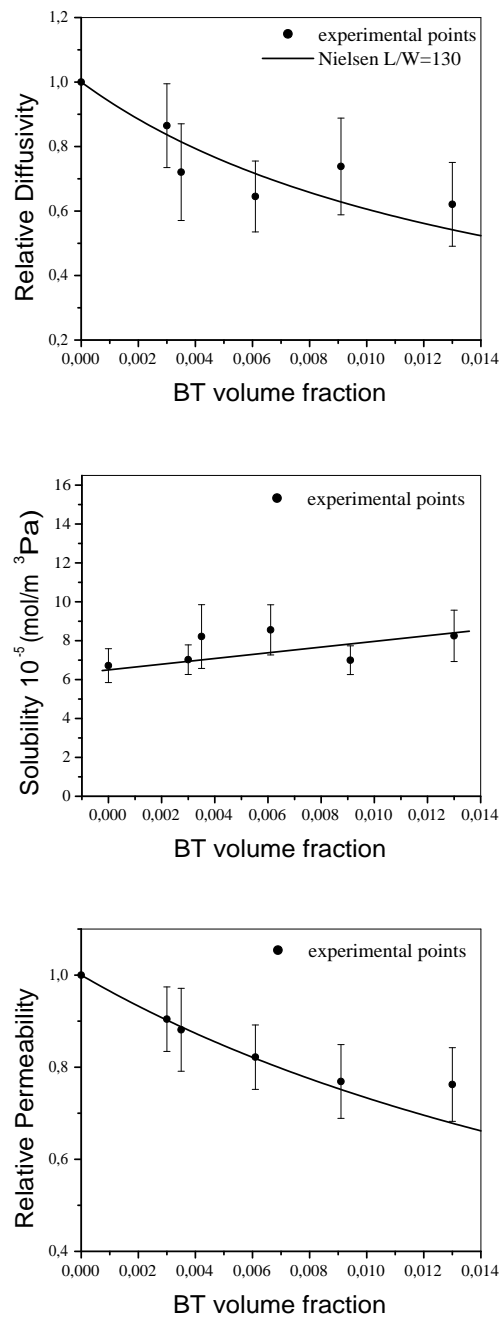


Figure 7.4: Gas transport coefficients of the acrylic resin/bentonite nanocomposite as a function of clay volume fraction.

energy U_R . In the presence of highly hydrophilic particles, however, another energy, U_H , due to the polarity of the medium, needs to be added to the interaction energy [Liang et al., 2007]:

$$U = U_R + U_A + U_H \quad (7.8)$$

The hydration or solvation forces that result from U_H are strong short distance forces and decay exponentially. They are attractive for hydrophobic and repulsive for hydrophilic particles in water.

The curve of the interaction energy as a function of the distance between the plates shows two minima [McBride, 1997; Smith and Zukoski, 2006]: A primary at short distances, which corresponds to aggregation, and a secondary at larger distances, which corresponds to flocculation [Tadros, 2011]. The maximum between the minima gives the energy barrier that the particles must overcome in order to be exfoliated. The height of the energy barrier or, alternatively, the balance between the attractive and the repulsive forces will finally determine the stability or instability of the suspension.

When the clay powder is added to the suspension medium under mechanical stirring, the hydration forces overcome the attractive interactions and the system passes the energy barrier and ends up into the secondary energy minimum which corresponds to a flocculation state. This, however, is not the stable exfoliated state and the particles may settle when the stirring of the suspension stops. The flocculation state is reversible: when stirring resumes the sediment re-flocculates. In order to achieve permanent colloidal suspension the system requires more energy, so that the particles will be able to escape the energy minimum by passing a second barrier. This energy is supplied by the ultra-sonication process, which leads to full exfoliation. In physical terms, the stability of the suspension is due to the long range repulsive forces, which dominate over the attractive van der Waals forces.

The nanocomposites are made by adding the aqueous bentonite suspension to the polymer emulsion that will form the matrix. The waterborne colloidal polymer emulsion used in this work consists of droplets of an acrylic resin that contains hydrophilic groups and is not yet cured. The non-polar segments of the monomers associate with each other to form colloidal aggregates (droplets). The non-polar parts of the monomers are in the interior of the droplets, while the polar groups reside on their periphery. These droplets are dispersed in the continuous phase (water) and form the resin emulsion. Repulsive forces, similar to the ones described above, exist also between the monomer droplets, preventing them from coalescence and stabilising this suspension. When the clay dispersion is mixed with the acrylic one, also the resulting suspension is stable, i.e. repulsive forces still exist not only between the bentonite particles and the resin monomer droplets by themselves but also between droplets and particles.

7.3.2 Coating film formation

During the drying and curing of the nanocomposite, various overlapping processes take place [Wicks et al., 2007]:

1. The water evaporates leading to close-packed layers of droplets and bentonite particles.

2. Droplets deform due to capillary pressure and particles may aggregate.
3. Monomers inter-diffuse across the droplet boundaries leading to coalescence.
4. The cross-linking reaction takes place.

The monomers in the droplets are generally hydrophobic and cannot easily encapsulate the hydrophilic inorganic clay layers. At the first stages of the formation of the coating, as the water evaporates, an ordered structure can be formed in which the dispersed inorganic particles are situated at the boundaries between the colloidal (not yet cured) resin droplets. Further evaporation of the solvent results in entrapping the nanolayers at these contact surfaces. During the final stages of the crosslinking reaction the two different phases are united into the fully coalesced nanocomposite coating [Strawhecker and Manias, 2000; Valadares et al., 2008].

The kinetics of the film formation is determined by the rates of the four processes taking place. The water evaporation rate depends on the temperature and the humidity of the surroundings. The particles aggregation rate depends mainly on the particle volume fraction, since it is determined by the face-to-face distance of the nano-layers. The cross-linking reaction rate depends on the temperature and the chemical nature of the reactants. The rate of diffusion of the reactants is determined by the thermodynamics and the free volume.

The kinetics and the thermodynamic state of the system are governed by the Brownian motions of the constituents. The mean transfer distance for this motion is $\ell = \sqrt{6D_B t}$ and the Brownian diffusion coefficient is:

$$D_B = \frac{kT}{3\pi\eta d_p}, \quad (7.9)$$

η is the viscosity of the medium and d_p is the particle size. The bigger the size of the diffusants and the higher the viscosity, the lower the mobility of the particles.

As the water evaporates, η and T_g increase and the free volume decreases. For the reactions to proceed, the reacting groups must diffuse into the reaction volume and form stable bonds of sufficient energy. When the diffusion rate is greater than the reaction rate, the reaction will be controlled by the chemistry kinetics. When the diffusion rate is slow compared to the chemical reaction rate, the rate of curing will be controlled by the mobility of the constituents. The major factor controlling the diffusion rate is the availability of free volume. Since the hardening process of the film takes place at temperature below the T_g of the cured resin, it is expected that the curing rate will be determined by the mobility of the reactants, at least at the final stages.

The attractive forces between the platelets vary as d^{-3} (eq. 1.1), i.e. they are effective at short distances but they have limited range. On the other hand, the attractive forces between the spherical polymer droplets vary as d^{-2} [Tadros, 2011; Behrens et al., 2000] and they are more effective at relatively larger distances. During the evaporation of the solvent the polymer droplets coalesce encapsulating the inorganic particles. Further, the reduction of the free volume during solvent evaporation hinders the diffusion of the inorganic platelets, reducing the possibility of their re-aggregation.

When the volume fraction of the nanoparticles increases, the rate of aggregation of the particles also increases. Further, by increasing the solvent evaporation rate, the

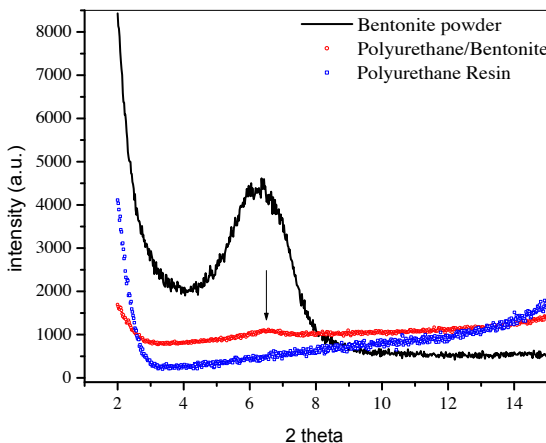


Figure 7.5: X-ray diffraction pattern for a polyurethane/bentonite nanocomposite sample containing 0.6 vol% particles.

repulsive forces, which stabilise the suspensions, disappear quickly and the aggregation accelerates. This was the case when the curing of the film took place at higher temperatures (but still lower than T_g). The XRD patterns of the samples cured at 80 °C indicate that they are less exfoliated than those cured at 20 °C (Fig. 7.3). Since both temperatures are below T_g , the crosslinking reactions are diffusion controlled and the curing rate is not expected to be affected. Thus the faster evaporation of water at 80 °C results in faster aggregation rates and worse exfoliation.

The above arguments are compatible with the results observed when the reaction takes place at temperatures above T_g . An attempt was made to disperse the aqueous bentonite suspension in an aqueous polyurethane monomer suspension and prepare films in a similar way as in the acrylic resin case. The polyurethane was crosslinked with a melamine hardener and the curing took place at 120 °C. Fig. 7.5, shows that exfoliation of the inorganic particles was not achieved: a peak can be seen at $2\theta = 6.5^\circ$ even for very low volume fractions. Since the curing temperature was well above T_g , the water molecules diffusion and evaporation rates were high and there was enough free volume to help the nanoparticles to diffuse and re-aggregate.

It can be concluded, therefore, that successful formation of a nanocomposite film requires low solvent evaporation rates, as well as curing temperatures below the T_g of the final resin. This combination seems to give a good chance to entrap the delaminated inorganic nano-objects between the contact surfaces of the polymer droplets and hinder their re-aggregation during the coalescence stage.

It should also be noted that the fast evaporation of the solvent (often due to unnecessary heating) brings about the formation of various defects, such as bubbles or pores, which are detrimental for the quality of the film and the measurement of the gas transport properties in the permeation cell. Because the viscosity increases faster at the outer surface of the film compared to the bulk, the evaporation of the solvent molecules that originate from the inner layers of the film, creates more defects on the film surface than

in the bulk.

7.3.3 Transport properties

Since the diffusion of the gas molecules through the dispersed crystalline inorganic particles is orders of magnitude lower than the diffusion through the continuous amorphous polymer phase, it is expected that the particles act as obstacles, around which the permeating gas molecules must detour in order to penetrate the membrane. Therefore, the diffusion path is prolonged. This is accounted for by the tortuosity factor, τ , defined as $\tau = \ell'/\ell$, where ℓ is the length of the diffusion path in the neat polymer and ℓ' the prolonged diffusion path due to the presence of the crystalline nano-layers. Obviously, this factor will depend on the clay volume fraction, the aspect ratio and the orientation of the basal planes of the particles.

In an ideal case, the particles are uniform rectangular platelets located in a periodical arrangement and their basal plane is perpendicular to the diffusion direction. This configuration corresponds to the maximisation of the tortuosity and is given, as proposed by Nielsen [Choudalakis and Gotsis, 2009; Nielsen, 1967], by the relation:

$$\tau = 1 + \frac{\alpha\phi}{2}, \quad (7.10)$$

where $\alpha = L/W$ is the aspect ratio of the particles and ϕ is their volume fraction. Thus, the relative diffusivity varies as:

$$\frac{D_{comp}}{D_{polym}} = \frac{1}{1 + \frac{\alpha\phi}{2}}. \quad (7.11)$$

This equation fits well the experimental data for $\alpha = 130$, as is shown in Fig. 7.4. Note that the selected value for the clay aspect ratio is in accordance with the estimation made from the low angle scattering data (Fig. 7.2). This agreement indicates that the actual orientation of the platelets is indeed as assumed in the model. It seems that, even in these low volume fractions, the self organisation tendency of the highly anisometric particles in combination with the kinetics of film formation/coalescence lead easily to the appropriate orientation of the platelets parallel to the film.

The total reduction of the diffusion coefficient due to the bentonite nanoparticles is about 40% when 1.3 vol% bentonite is added to the resin. On the other hand, the solubility coefficient increases under the same conditions. This enhancement compromises the gas barrier properties of the nanocomposite and the overall reduction of the relative permeability is limited to 25%.

The incorporation of the particles in the polymer matrix influences the free volume characteristics and this is reflected on the solubility trend. As the volume fraction of the particles increases, the solubility increases almost linearly, up to 23% for the sample with 1.3 vol% BT. A possible cause for this effect is the presence of the interfacial regions between the two components, which are larger when the degree of exfoliation and the volume fraction of the particles are higher. Since the measurement temperature is well below T_g , the free volume of the polymer can be considered frozen. Thus, the effect of the particles on the mobility of the chain segments is negligible. Changes in the

free volume hole size distribution should also affect the diffusion coefficient but not the solubility, because the latter depends on the total free volume, where the gas molecules can locate, and not on their mobility [Choudalakis and Gotsis, 2012]. Therefore, the solubility trend seems to be determined by the contribution of the interfacial regions, which create extra free volume at the organic-inorganic contact layers.

The entrapment of the nanoparticles at the boundaries of the resin particles may prevent their agglomeration but it creates low density interfacial regions, due to their incompatibility. These regions will contribute positively to the adsorption of diffusing gas molecules around the platelets, increasing the solubility. The 2.1 vol% BT sample presents a lower solubility than the exfoliated samples, but still higher than the neat resin, probably because its stacks of platelets have lower total interfacial area and, thus, lower free volume. However, even in this less exfoliated sample, the tortuosity still has an appreciable value and lowers the diffusion coefficient by about 18%. This indicates that a portion of the particles in the composite can be in the exfoliated state, while the rest remain in the agglomerated state.

7.4 Conclusions

Acrylic resin/bentonite nanocomposite coatings with improved barrier properties can be prepared for dispersed particles content less than 2 vol%. By mixing an aqueous suspension of exfoliated nanoparticles with one of colloidal acrylic resin monomer droplets, a stable nanocomposite suspension is produced, which, upon slow drying, results in uniform, non-porous, bubble-free coatings/films. The presence of the dispersed inorganic nano-platelets improves the barrier properties of the film, e.g. the gas permeability can be reduced by 25% for 1.3 vol% added nanoparticles. The extensive interfacial regions between the two components limit this reduction by increasing the solubility of the gas in the system. This is due to the enhanced adsorption of the gas molecules in the free volume created around the interfaces. Thus, although the reduction in the diffusion coefficient is significant due to the tortuosity imposed by the large aspect ratio particles, the possibility of solubility enhancement due to the interfacial free volume may compromise the final gas permeation characteristics of the material.

Chapter 8

Acrylic resin/hectorite nanocomposite coatings

Part of this chapter has been submitted for publication in the Journal of Membrane Science under the title "Significant improvement of the gas barrier properties in polymer nanocomposite coatings containing Li-hectorite clays", January, 2013 (G. Choudalakis, J. Breu and A.D. Gotsis).

It has repeatedly been mentioned that the aspect ratio of the nano-layers is one of the most important factors that contributes to the tortuosity of the diffusion paths in the nanocoating. To explore this idea to its limit, we utilised synthetic hectorite nanoparticles with a very high aspect ratio (> 1000), that were produced at the University of Bayreuth by the group of professor Breu [Moller et al., 2010], and studied their effect on the barrier properties of the final composite. Various preparation procedures were tested and compared, the free volume in the matrix was measured and the gas transport coefficients were calculated. The applicability of the various permeability models was tested on the basis of the dilute and semi-dilute regions.

8.1 Li-Hectorites

Since the thickness of the single clay layers is around 1 nm, in order to increase the particle aspect ratio L/W only the lateral dimension can be extended. The achievement of this extension is determined by the appropriate synthesis conditions, such as the crystallisation temperature, the nature of the interlayer cations, the layer surface charge and the composition. Moller et al. [2010] managed to synthesise such a Li-Hectorite clay with a very high L dimension by a fast and facile high temperature melt synthesis technique. Huge aspect ratios were achieved, of the order of 10000 or more. The authors claim that the clay is spontaneously exfoliated as soon as it is immersed in water, with no need for additional shearing or ultrasonic treatment, due to the large hydration enthalpy of the interlayer cation (Li).

Table 8.1: Characteristics of the samples containing hectorite nanoparticles. The letter U in the code denotes samples treated with ultrasound, W denotes samples without any treatment and B denotes samples treated in an ultrasound bath. The volume fractions, the densities and the membrane thicknesses were calculated in the same way as reported in the previous chapters.

Sample	wt%	vol%	Density (g/cc)	d (mm)
Resin	0	0	1.040	0.88
Hectorite	0	0	2.600	-
1U	0.84	0.34	1.0453	0.71
2U	1.67	0.67	1.0505	0.69
3U	2.86	1.16	1.0582	0.70
4U	7.85	3.70	1.100	0.375
1W	0.84	0.34	1.0453	0.914
2W	1.25	0.50	1.0478	0.79
3W	2.10	0.88	1.0537	0.75
4W	3.25	1.33	1.061	0.56
5W	4.3	1.77	1.068	0.633
1B	0.84	0.34	1.0453	0.91
2B	1.25	0.50	1.0478	1.02
3B	2.17	0.88	1.0537	1.00

8.2 X-ray results

The primary Bragg peak of the Li-hectorite powder appears at $2\theta = 7.3^0$. This angle corresponds to an interlayer distance of about 12 Å. When added to the polymeric resin, this peak, if present, is shifted to lower angles for the samples treated in the ultrasound bath, indicating that there is a swelling of the hectorite particulates ($d_{001} = 12.8$ Å, Fig. 8.1a). For the sample with the lowest hectorite volume fraction, the peak is broad, which indicates that the main part of the particulates is in exfoliated state, while the rest remains in stacks. The peak becomes more obvious and narrower as the volume fraction of the nanoparticles increases. The addition of the inorganic particles results in an enhancement of the particulate portion and in a reduction of the delaminated layers.

The nanocomposite samples that had not received any ultrasound treatment presented a more complicated picture. The sample with the lowest volume fraction (0.35 %) shows an obvious, quite sharp peak at $2\theta = 6.7^0$. This is at a lower angle than the one of the original particulates ($d_{001} = 13.2$ Å), indicating a swelling (intercalation) in the composite. For the other two volume fractions (0.5 and 0.67 %), the shift at lower angles is smaller than that of the former, indicating a lower degree of intercalation. The sharper peaks in this case show that the portion of delaminated layers is significantly less than that when the ultrasound bath was used.

The above observations verify the suggestion of Moller et al. [2010] that the swelling of the primary particulates of *Li*-hectorite is a spontaneous process. The effect of the ultrasound bath on the degree of exfoliation of the nano-layers is relatively weak and

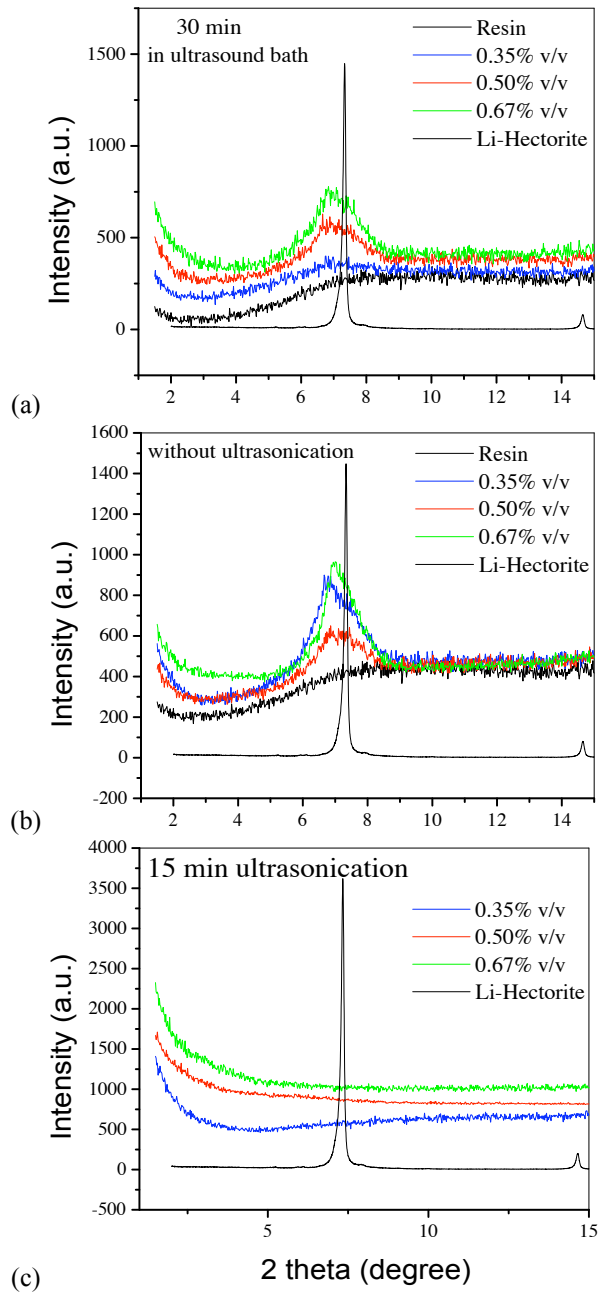


Figure 8.1: X-ray diffractograms of 0, 0.35, 0.5, 0.67 and 100 wt% acrylic resin / hectorite nanocomposite samples treated with and without ultrasonication.

the energy transferred thus to the suspension of the particles is small relative to the large hydration enthalpy of the interlayer cation (Li). This is also evident in the case of the samples that were treated using an ultrasound immersion probe, which is much more energy intensive than that of the ultrasound bath. As it is seen in Fig. 8.1c, the peaks have completely disappeared. This is an indication of complete exfoliation in these samples.

8.3 Transport properties

8.3.1 Low-energy or no ultrasonication treatment

Although the degree of exfoliation of the samples treated in ultrasound bath is relatively low, there is a small effect of the tortuosity on the diffusion coefficient, as it can be seen in Fig. 8.2a. The fitting of Nielsen's equation predicts an aspect ratio in the order of 140, which is very low compared to the layer nominal lateral dimension, L , of about 10000. Obviously, the tortuosity effect is caused by the huge lateral dimension of the particles, rather than by their aspect ratio. The reduction of the diffusion coefficient by the addition of less than 1 vol% nanoparticles is about 35%.

The solubility coefficient on the other hand, shows a slight increase of 10% (Fig. 8.2b), probably due to the large interfacial regions between the two components. Thus, the permeability coefficient presents an overall reduction of only about 30% in the sample with the highest volume fraction, due to the negative contribution of the solubility coefficient. However, the tortuosity effect seems to dominate over the possible free volume enhancement, and Nielsen's equation can be fitted for the relative permeability with a lower value of the aspect ratio. This shows that the extrapolation of the aspect ratio by fitting of only the permeability coefficient is not always accurate, even if this is possible as in our case. Accurate predictions can be made only if all three transport coefficients are known.

In the case of the samples that have not been treated by ultrasound (Fig. 8.3) the degree of delamination of the particles is lower, the tortuosity effect exists but the solubility is enhanced significantly. However, an almost linear reduction of the relative permeability is obtained. With less than 1 vol% of reinforcement the diffusion coefficient is reduced by about 45%, the solubility coefficient is increased by 25% and the permeability is reduced again by about 30%. Nielsen's equation can be fitted for this region (dilute region) with a value of the aspect ratio equal to 200. For higher volume fractions (semi-dilute region), the Nielsen model fails to predict the reduction of the relative diffusivity, while Cussler's equation seems to be fitted sufficiently.

The aspect ratio value of the Cussler model is lower (114) than that of the Nielsen model. The total reduction of the diffusion coefficient is of the order of 70% with 1.3 vol% hectorite, while the permeability coefficient is reduced by 60% due to the negative impact of the solubility coefficient.

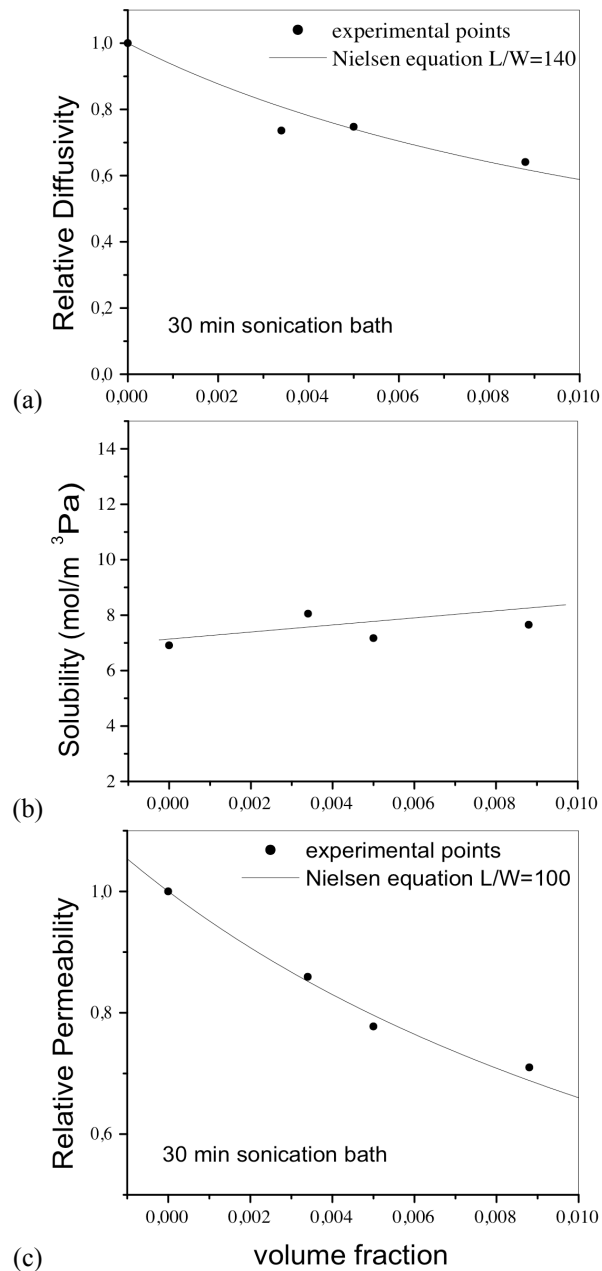


Figure 8.2: Transport coefficients for the acrylic resin/hectorite nanocomposite samples treated for 30 min in an ultrasound bath, as a function of clay particles loading at 23 °C. The permeation curves are given in the Appendix.

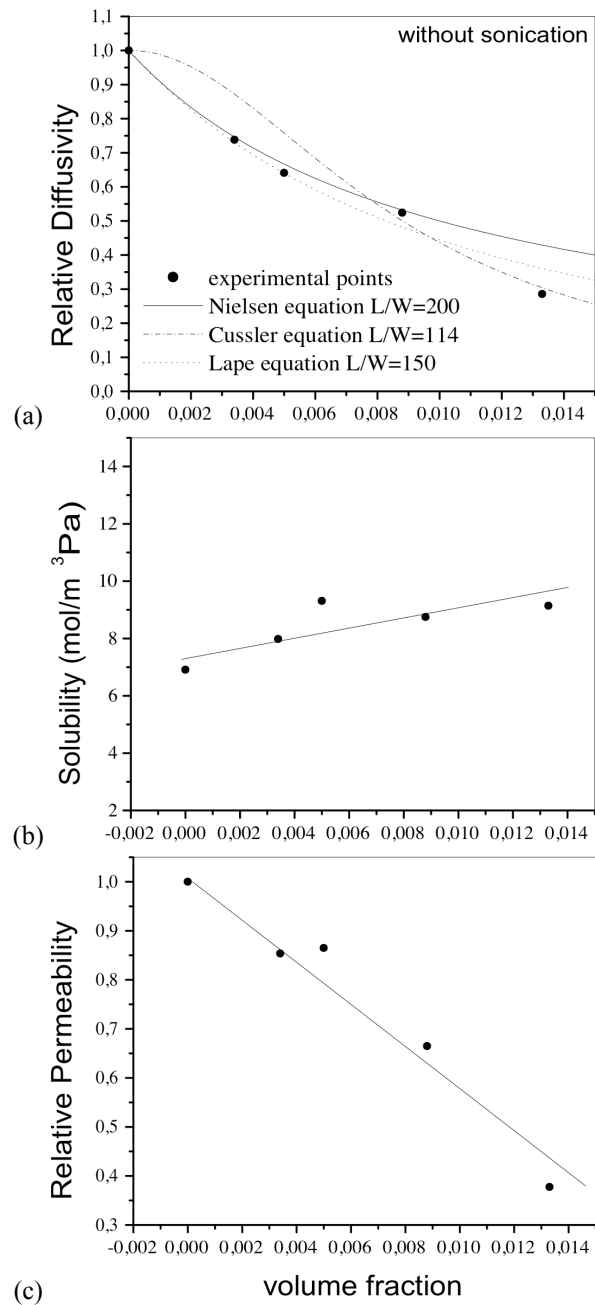


Figure 8.3: Transport coefficients at 23 °C, for the acrylic resin/hectorite nanocomposite samples without any ultrasonic treatment, as a function of clay particles loading. The permeation curves are given in the Appendix.

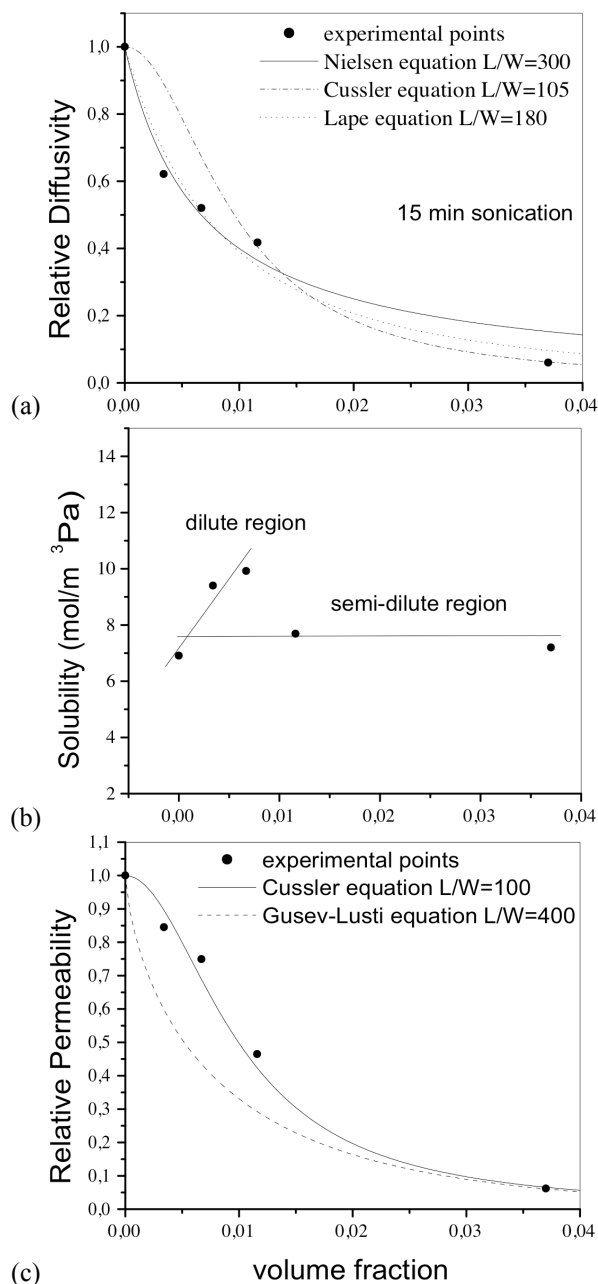


Figure 8.4: Transport coefficients at 23°C for the acrylic resin/hectorite nanocomposite samples treated with a high energy ultrasonication probe, as a function of clay particles loading. The permeation curves are given in the Appendix.

8.3.2 High-energy ultrasonication treatment

Fig. 8.4 shows the results of the high-energy ultrasonicated samples. In the dilute region (below 1 vol% clay) Nielsen's equation is adequate and the predicted value of the aspect ratio is 300, significantly higher than that of the previous samples, due to the better exfoliation of the particles. In the semi-dilute region (above 1 vol%) Cussler's equation is more suitable and the aspect ratio is predicted to be only 100.

The solubility behaviour of these samples follows a bimodal trend: In the dilute region it is significantly enhanced, while in the semi-dilute region it remains almost constant. Finally, the relative permeability fits well the Cussler equation for a value of the aspect ratio equal to 100. The overall reduction of the relative permeability approaches an order of magnitude for the sample with 3.7 vol % hectorite, which results in a significant improvement of the gas barrier properties of the membrane.

8.4 Discussion

As it was described in the previous chapter, the success of the nanocoating formation is based on the entrapping of the nano-layers between the droplets of the resin during the evaporation of the solvent. Since the hectorite particles are significantly larger than those of bentonite, this entrapping mechanism is expected to be more effective now. Thus, it is possible to exfoliate higher volume fractions of nano-layers, compared to the bentonite case in which the highest volume fraction was about 1.5 vol% before re-agglomeration began.

While the huge surface of the hectorite particles seems to be a remarkable advantage for their entrapping, as well as (mainly) for the exceptional improvement of the gas barrier properties, there are also some serious limitations. For coating applications the volume fraction of the hectorite cannot be higher than 4 vol%, otherwise the viscosity of the suspension becomes unmanageable. On the other hand, the drying process of the film becomes much slower because the wide hectorite particles hinder the water evaporation. Also, it is expected that there will be a significant amount of water molecules trapped inside the membrane between the clay layers, even after the apparent completion of the drying process.

In order to check the influence of the trapped water molecules on the transport properties, two membranes were heated above the glass transition temperature ($T_g = 100^{\circ}\text{C}$) for 24h and they were measured again in the permeation cell at 23°C . When the temperature increases above T_g the free volume may be significantly expanded, giving the chance to the trapped water molecules to escape from the membrane. Depending on the chain dynamics and the crosslink density, the free volume created by the escaping water molecules may either be filled by a macromolecular rearrangement or remain empty, increasing the total amount of the polymer free volume. In any case, it is expected that this procedure will affect the gas transport coefficients.

As it can be seen in Fig. 8.5, both membranes show worse barrier properties when heated at 120°C for 24h. The weight loss of the membranes after heating was about 3%, while the gas barrier loss is about 40%. This reduction concerns the diffusion coefficient and not the solubility, which remains constant. Since membranes and films have lateral

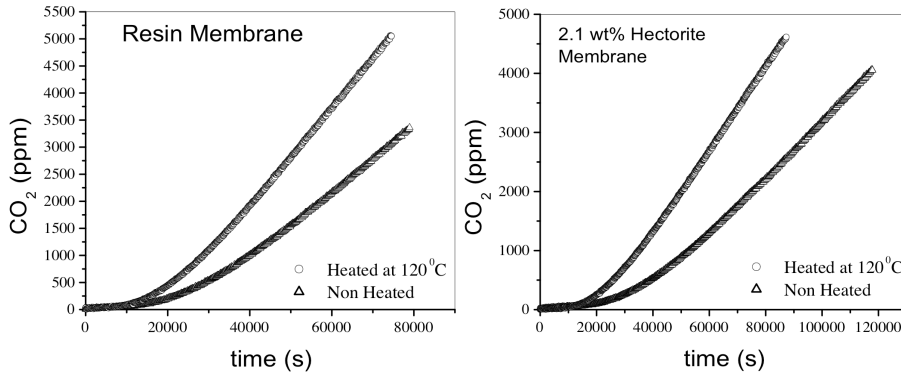


Figure 8.5: Permeation curves for two samples before and after heating at 120°C .

dimensions much larger than their thickness, most of the free volume is located near the surface and the amount of the free volume in the bulk is only a small part of the overall. However, the trapped water molecules are mainly located at the inner part of the membrane. Thus, when they are removed (after re-heating), the generated new free volume will be in the bulk. So, it is expected that the solubility coefficient will remain unchanged, while the diffusion coefficient will depend strongly on the removal of the water molecules. Even though the resulting change of the diffusion coefficient values seems not to be as severe as [Moller et al. \[2012\]](#) expected, the permeation properties can be improved by almost an order of magnitude if the solvent/suspension medium is completely removed during the film formation process.

[Moller et al. \[2012\]](#) managed to disperse 11 vol% of hectorite in UV-curable polyurethane and observed a more than two orders of magnitude reduction of the relative permeability. The authors estimated the effective aspect ratio of the hectorite based on the Gusev-Lusti model to be about 410. Since the reduction is about one order of magnitude in our sample of 3.7 vol%, it seems logical that, at high volume fraction of hectorite, two orders of magnitude reduction of the permeability should be expected, even in the water based coatings.

The models of Nielsen and Cussler are based on the assumption of the parallel and periodic arrangement of nano-platelets, while the models of Lape and Gusev-Lusti assume random positioning of the parallel nano-layers. The latter is the most realistic assumption. Due to their high degree of anisometry, the clay-platelets are forced to align parallel, even in a sparse suspension. Free rotation of clay platelets is hampered, due to their large hydrodynamic radii. Large excluded volumes are generated between the platelets, resulting in possible liquid-crystalline ordering and birefringence [[Moller et al., 2012](#)]. In the same line, the continuously increasing concentration of the suspension as the solvent evaporates forces the alignment of the platelets. As might be anticipated, the degree of alignment depends strongly on the aspect ratio. The larger the lateral dimensions of the thin platelets, the better the alignment will be in the film.

As it can be seen from the Fig. 8.3 and 8.4, Nielsen's model underestimates the effectiveness of the tortuosity on the reduction of the diffusion coefficient in the semi-

dilute region, while Cussler's model deviates from the experimental results in the dilute region below 1 vol%. On the other hand, Lape's model seems to be fitted well in both the dilute and the semi-dilute regions and gives averaged values for the aspect ratio of 150 and 180 correspondingly.

The behaviour of the relative permeability is described adequately by the Cussler equation for $L/W = 100$. The Gusev-Lusti model overestimates the barrier properties in the dilute region but coincides with the Cussler model at higher volume fractions (>3 vol %). Fitting the Gusev-Lusti equation gives exactly the same value of the aspect ratio ($L/W=400$) as it was estimated by Moller et al. [2012].

We conclude, therefore, that the Cussler and Gusev-Lusti models are adequate to predict the relative permeability of the polymer/clay nanocomposites at high clay loadings but they are insufficient to be used in the low volume fraction region. The differences in the values of the aspect ratio predicted by the two models arise from the fact that Cussler's model assumes periodic arrangement, while the Gusev-Lusti model assumes random positioning of the platelets. Thus, the aspect ratio should be higher in the latter case in order to give similar results.

On the other hand, Nielsen's model describes very well the behaviour of the relative diffusivity in the dilute region, while Lape's model approaches the Nielsen model in the dilute region, and approximates the Cussler model in the semi-dilute region. Therefore, Lape's model can be considered as an average between the other two, resulting in a reliable approximation of the overall diffusion behaviour.

It should be noted here, that the estimations of the aspect ratio are more reliable if they are based on the relative diffusivity and not on the relative permeability, since the impact of the solubility coefficient on the later may significantly alter the tortuosity effect and, consequently, the estimated aspect ratio. Usually, the aspect ratio extracted from the relative permeability is underestimated, as it is seen in the results of Fig. 8.1, 8.3, 8.4.

As it is reported in chapter 3, most permeability models are based on the assumption that the physical properties of the matrix (e.g. the free volume) do not change by the addition of the particles. Also, the solubility coefficient should remain constant or slightly reduced by the incorporation of the particles. However, the experimental results of Fig. 8.1, 8.3, 8.4, show that the solubility coefficient increases mainly in the dilute region. This enhancement can be attributed to the adsorption of the gas molecules in the huge interfacial regions developed between the organic matrix and the inorganic crystalline layers.

The interfacial regions contain empty sites which may contribute to the free volume in the system, adding to the existing free volume in the matrix. In order to detect this extra free volume, positron annihilation lifetime measurements were performed for the *Li*-hectorite samples. However, both the lifetime and the intensity of the o-Ps remain constant as a function of clay loading, Fig. 8.6. It seems that PALS may not be able to measure the additional free volume, if it is generated in these interfacial regions. This failure may be attributed to the fact that the surfaces of the hectorite particles are highly charged, as there is no modifier to compensate their surface charge. The interfacial free volume is a strongly repulsive region for the positrons, which cannot be localised and annihilate in its holes. Therefore, the PALS parameters may reflect only the contribution of the free volume inside the amorphous matrix, which remains almost unchanged since

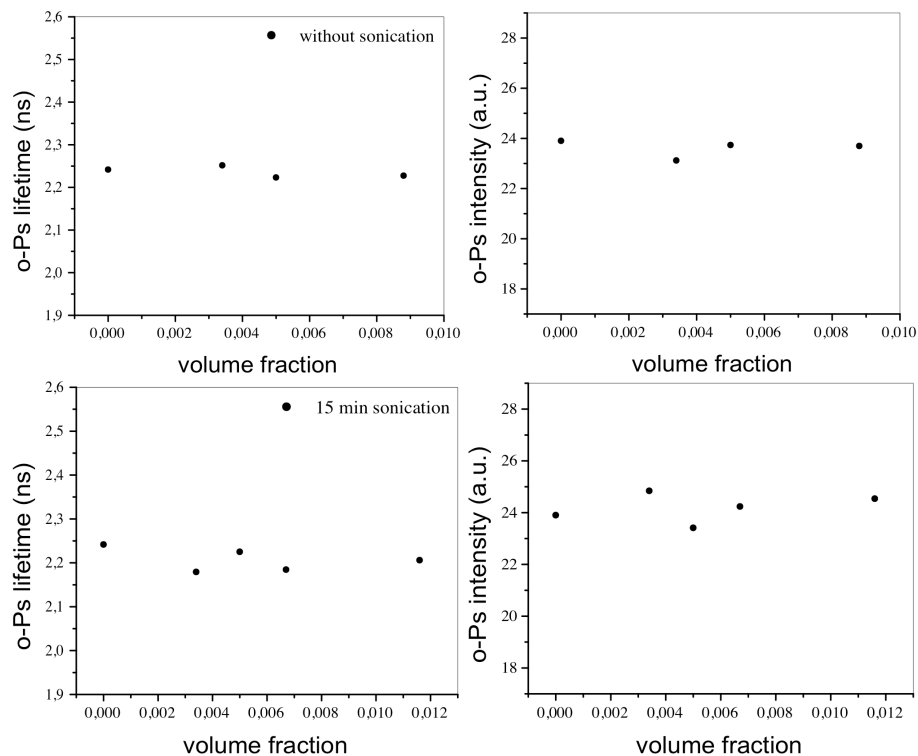


Figure 8.6: o-Ps lifetime and relative intensity for the acrylic resin/hectorite nanocomposite samples with (15 min) and without ultrasonication treatment as a function of hectorite volume fraction.

the particle volume fraction is very low.

There are still two questions to be answered with regard to the mass transport through the nanocomposite: Why does the solubility significantly increases in the dilute region? And why is the predicted aspect ratio so low, even for the exfoliated samples, when the surface of the hectorite particles is so large?

A potential answer to the above questions can be that the hectorite particles are flexible and get bent upon incorporation in the polymer matrix. The entrapping of the hydrophilic particles among the mainly hydrophobic polymer chains results in the development of capillary forces between the two components, which deform the flexible crystalline layers. The higher the exfoliation, the higher the flexibility and the stronger the curvature. Under these circumstances, the effective aspect ratio of the particles which contribute to the tortuosity would be significantly lower than their actual aspect ratio.

The degree of curvature of the particles, will inevitably affect the area and the shape of the interfacial regions between the two components and, consequently, the solubility coefficient. It seems that the higher the curvature and degree of exfoliation of the particles, the higher the increase of the solubility.

8.5 Conclusions

The incorporation of the hydrophilic Li-Hectorite nanoparticles in the acrylic resin matrix produces nanocomposites membranes with enhanced gas barrier properties. Due to their huge surface area, the hectorite particles create tortuous routes for the gas molecules increasing their diffusion length even if they are not completely exfoliated. The overall reduction of the relative permeability approaches an order of magnitude for the sample with the highest volume fraction of 3.7 vol%.

As it was confirmed by the experimental results, Nielsen's model describes adequately the behaviour of the relative diffusivity in the dilute region, while Cussler's model is more appropriate to be used in the semi-dilute region. Lape's model seems to give intermediate predictions between the two previous and predicts an averaged value for the aspect ratio in both the dilute and the semi-dilute regions.

Due to the impact of the solubility coefficient, the relative permeability behaviour is inadequate to offer reliable values of the aspect ratio especially in the dilute region. In the semi-dilute region however, where the solubility effect is less important, the Cussler or the Gusev-Lusti models for the relative permeability can be applied.

During the film formation process, a significant amount of the solvent molecules can be trapped in the free volume sites of the polymer matrix, generating additional free space when removed, which would not have existed if the solvent had fully evaporated during the curing stage. The removal of the residual solvent after the curing stage by the re-heating above the glass transition temperature, will leave their previously occupied space free, if the macromolecular rearrangements are not able to fill it. In fact, this free space can be considered as an excess free volume. The excess free volume could affect the gas diffusion and permeability coefficients by as much as 50%.

The gas barrier performance of the *Li*-hectorite filled polymer coating would be even higher if the exfoliated crystalline layers remain flat, maintaining, thus, their huge

lateral dimensions. This would lead to the maximisation of the tortuosity and improve the gas barrier properties by an order of magnitude. Unfortunately, it seems that their flexibility often leads to their bending, which drastically reduces their effective aspect ratio, limiting the final gas barrier performance of the coating.

Chapter 9

Acrylic resin with surface modified montmorillonite

Part of this chapter has been submitted for publication in Progress in Organic Coatings under the title "Influence of some thermodynamic parameters on the morphology and gas transport properties in polymer nanocomposite coatings containing organically modified clays", January, 2013 (G. Choudalakis, M. Stratigaki and A.D. Gotsis).

In this chapter, various types of organo-modified montmorillonites are dispersed in some organic solvents and then mixed with the aqueous acrylic resin emulsion in order to prepare the nanocomposite coatings. An effort is made to clarify the influence of the various interactions among the ingredients of the final composite, both on the structural characteristics and on the transport properties of the final composite.

In order to improve the compatibility between the hydrophobic polymer and the hydrophilic inorganic component, a surface modification of the clay is needed to compensate its surface charge. The modification lowers the interfacial energy. The lower interfacial energy leads to weaker forces between the basal planes. This results in an expansion of the d -spacing of the crystalline layers as compared to the case of the hydrophilic clay. The organic cations used for this purpose have one polar end that becomes attached to the surface of the clay, while its other ends (alkyl chains) are hydrophobic and, thus, compatible with the polymer matrix (Fig. 9.2).

9.1 Sample preparation and characteristics

Various types of organo-modified montmorillonites (OMMT) were tested in this work. Their characteristics are listed in Table 9.1.

The long-chains of the surfactants used for the modification of montmorillonites can become oriented more or less parallel to the surface and usually cover the platelets with a single layer. This effect can be further enhanced by using surfactants with two long aliphatic chains, one of which orients vertically to the surface, leading to larger gallery distance. This explains why the C93A, C25A and C20A modifiers, which have

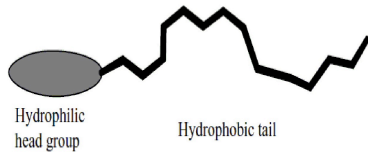


Figure 9.1: The concept of clay/organic matrix compatibilisation

Table 9.1: Modifier content, cation exchange capacity (CEC), density and d-spacing of various types of organo-modified and hydrophilic montmorillonites. BE denotes hydrophilic bentonite while OMBE is the modified bentonite with octadecylamine.

Type	Modifier (wt%)	CEC (meq/100g)	Density (g/cc)	d(001) Å Manuf.	d(001) Å Measur.
C10A	39	125	1.90	19.2	19.3
C20A	38	95	1.77	24.2	23.7
C25A	34	95	1.87	18.6	24.7
C93A	37.5	90	1.88	23.6	26.1
C30B	30	90	1.98	18.5	18.5
OMBE	35		1.71	-	21.7
BE	0	-	2.6	-	14.1
Na-MMT	0	-	-	-	12.4

at least two long tallow chains attached to the ammonium cation (Table 9.2), present the highest *d*-spacing among the several types of organo-modified montmorillonites tried in this work.

The OMMTs are not as readily dispersible in water as the unmodified clays. Since water-borne acrylic resin is used to prepare the matrix, dispersions of the particles are needed that can be mixed with the aqueous resin dispersion. To achieve this a suitable dispersion medium (solvent) is required. This solvent must be soluble in water to complete the final aqueous dispersion of the acrylic resin and the particles. This final dispersion is then dried, the resin is polymerised and the final nano-composite coating film is formed.

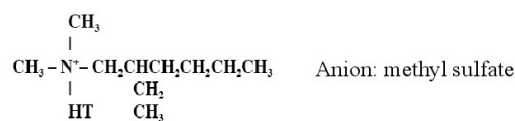
The solvents selected for the dispersions were acetone and ethanol. These are both soluble in water. To prepare the initial particle dispersions certain amount of OMMT was added to these solvents under high shear flow stresses and ultrasonication. Then, this suspension was mixed under high shear flow with the aqueous acrylic resin dispersion. After the drying and the polymerisation reaction, X-ray and permeation film samples were prepared using the standard procedure described in the previous chapters. The density and geometrical characteristics of the samples are shown in Tables 9.3, 9.4, 9.5. The clay mass fractions of the samples were verified by TGA. The clay volume fraction, the sample density and the membrane thickness were calculated as described in chapters 7 and 8.



C10A: dimethyl, benzyl, hydrogenated tallow, quaternary ammonium



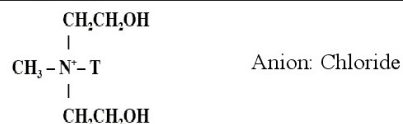
C20A: dimethyl, dehydrogenated tallow, quaternary ammonium



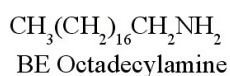
C25A: dimethyl, dehydrogenated tallow, 2-ethylhexyl quaternary ammonium



C93A: methyl, dehydrogenated tallow ammonium



C30B: methyl, tallow, bis-2-hydroxyethyl, quaternary ammonium



Where T is Tallow (~65% C18; ~30% C16; ~5% C14)

Where HT is Hydrogenated Tallow (~65% C18; ~30% C16; ~5% C14)

Table 9.2: Various surfactants used in organo-modified montmorillonites.

Table 9.3: Characteristics of the nanocomposite samples containing organo-modified bentonite (OMBE) that was initially dispersed in ethanol.

sample	vol %	density (g/cc)	membr. thickness (mm)
resin	0.00	1.040	0.88±0.05
1	0.50	1.043	0.964± 0.042
2	0.75	1.045	0.713± 0.047
3	1.00	1.047	0.71± 0.04
4	1.23	1.048	0.75± 0.08
5	1.50	1.050	0.654± 0.046

Table 9.4: Characteristics of the nanocomposite samples containing organo-modified montmorillonite (C25A) that was initially dispersed in ethanol.

sample	vol %	density (g/cc)	membr. thickness (mm)
resin	0.00	1.040	0.723± 0.045
1	0.16	1.041	0.778±0.039
2	0.32	1.043	0.716± 0.52
3	0.48	1.044	0.656± 0.049
4	0.63	1.045	0.567± 0.046
5	0.74	1.046	0.615± 0.051

Table 9.5: Characteristics of the nanocomposite samples containing organo-modified montmorillonite (C93A) that was initially dispersed in ethanol.

sample	vol %	density (g/cc)	membr. thickness (mm)
resin	0.00	1.040	0.723±0.045
1	0.10	1.040	0.80±0.05
2	0.25	1.042	0.70± 0.04
3	0.39	1.043	0.67± 0.05
4	0.60	1.045	0.64± 0.06
5	0.80	1.047	0.557±0.047

9.2 Solubility parameters and surface tensions

The Hildebrand solubility parameter, δ (MPa^{1/2}), is often used to obtain estimates for the mutual miscibility between substances, especially solvents. It is defined as the square root of the cohesive energy density (CED) per volume of the substance:

$$\delta = \sqrt{CED} . \quad (9.1)$$

The CED is, in fact, the energy required to convert a liquid to a gas. In other words, the energy of evaporation is a direct measure of the total cohesive energy holding the molecules in the liquid together. In more complex compounds (like polymers), where evaporation is not possible, the solubility parameter can be calculated from the swelling factor of the polymer in a certain solvent or by the Group Contribution Method [Fedors, 1974]. The latter method was used in order to calculate the solubility parameters of the various clay types with different organic modifiers in Table 9.6 in the present work. A detailed description of the method is given in the Appendix.

Thermodynamics requires that the change of free energy of mixing ΔG^M must be zero or negative for the solution process to occur spontaneously:

$$\Delta G^M = \Delta H^M - T\Delta S^M \quad (9.2)$$

The enthalpy of mixing is

$$\Delta H^M = \varphi_1 \varphi_2 V_M (\delta_1 - \delta_2)^2 , \quad (9.3)$$

where φ_1, φ_2 is the solvent and polymer volume fractions and V_M is the volume of the mixture. Since the entropy of mixing is $\Delta S^M > 0$, when $\delta_1 \approx \delta_2$ the above equation gives $\Delta G^M < 0$.

The existence of (interfacial) surfaces is associated with the (interfacial) surface energy. The specific surface energy (J/m²) is often called surface tension γ (N/m). Since the surface tension is a manifestation of intermolecular forces, it is expected to be related to other properties derived from intermolecular forces such as cohesion energy and, consequently, the solubility parameter. The following expression is frequently used:

$$\gamma = \kappa V_m^{1/3} \delta^2 , \quad (9.4)$$

where V_m is the molar volume (mol/m³) of the solvent and κ (mol^{1/3}) is a parameter which depends on the chemical structure/composition of the solvent [Beerbower, 1971].

Another approach that is used for the calculation of the interfacial tension involves the molecular parameter “parachor”, P' , that can be calculated by the group contribution method [Quayle, 1953]. The surface tension, then, is extracted by the relation:

$$\gamma = \left(\frac{P'}{V_m} \right)^4 , \quad (9.5)$$

where P' is in (m³/mol)×(mJ/m²)^{1/4}. A detailed description of the calculation of the surface tension via this contribution method is given in the Appendix.

Table 9.6: Solubility parameters and surface tensions of some solvents and the organic modifiers of the clay particles. Values were taken from Burgentzle et al. [2004]; Heinz et al. [2006]; Ho and Glinka [2003]; Krikorian and Pochan [2003]. δ_{lit} , γ_{lit} is referred to values from the literature while δ_{calc} , γ_{calc} values are based on calculation via the group contribution method proposed by Fedors [1974] and Quayle [1953].

sample	δ_{lit} (MPa ^{1/2})	δ_{calc} (MPa ^{1/2})	γ_{lit} (mN/m)	γ_{calc} (mN/m)
Water	48	-	59	-
Ethanol	26.2	25.7	22.3	23.2
Acetone	19.7	20.7	23.7	22.4
C30B	19.5	20.8	34.5	32.8
OMBE	19.0	17.6	38	33.3
C10A	-	17.1	30	28.8
C93A	-	17.1	-	31.9
C20A	19.2	16.8	-	28.7
C25A	16.5	16.5	-	26.3
Na-MMT	-	-	44	-

The good dispersion of the organo-modified clays in a solvent requires two main conditions: The first is the miscibility between the solvent and the organic modifier; and the second is the matching of the surface tensions of the solvent and the clay. If there is not enough miscibility, then the addition of the clay in the solvent will cause the gelation of the clay and, consequently, the suspension cannot be treated ultrasonically nor mixed with the resin aqueous emulsion.

However, the miscibility criterion alone does not guarantee the inter-layer swelling of the clay in the solvent. If such a swelling does not occur, then the exfoliation of the clay in the final dispersion is very difficult or incomplete, even under ultrasonication. The requirement to achieve inter-layer swelling by the wetting of the clay surface by the solvent and its insertion between the galleries of the nano-layers is that the surface tension of the solvent be equal or higher than that of the clay.

Therefore, the swelling factor (miscibility) and the inter-layer swelling are two independent parameters. The first is determined by the solubility parameters between the solvent and the modifier, while the second depends on the polar character of the solvent and the swelling capacity of the clay and is determined by the surface tension.

The solubility parameter of acetone is almost equal to those of the organic modifiers of the clays used here. Therefore, acetone is expected to be compatible with all these clay types. On the other hand, the solubility parameter of ethanol is higher but this difference does not create observable effects on the miscibility between the two components. The surface tension of both solvents are very close and lower than that of the clays. This means that the exfoliation of the inorganic crystalline layers is expected to be incomplete in both solvents.

Because C25A and C93A have the highest *d*-spacing among the other types of clays

and, consequently, the lowest attractive forces between their basal planes, it is expected that the ultrasonication process should have the highest impact on these clay types. The strong polar nature of acetone (stronger than ethanol) is expected to have a stronger influence on the more polar clays, such as the C30B, OMBE and C93A. On the other hand, ethanol is more compatible with water, due to the formation of hydrogen bonding. The final suspension (after the addition of the aqueous resin dispersion), therefore, is expected to be more stable and the film formation process will occur sufficiently.

9.3 The state of particle deagglomeration

Fig. 9.2 shows the X-ray results for 5 nanocomposites made from different organo-modified montmorillonites, initially dispersed in acetone.

Only the samples containing C93A and C30B do not show any diffraction peak. This is an indication of a high degree of exfoliation in these samples. The samples that contain C10A and C25A show a diffraction peak at angles higher than those of the pristine modified clay powders. This means that the acetone reacts with the organic modifiers, partially removing them from the clay surfaces. Thus, the layer spacing decreases, leading to a shift of the corresponding peak to higher angles in the diffraction pattern.

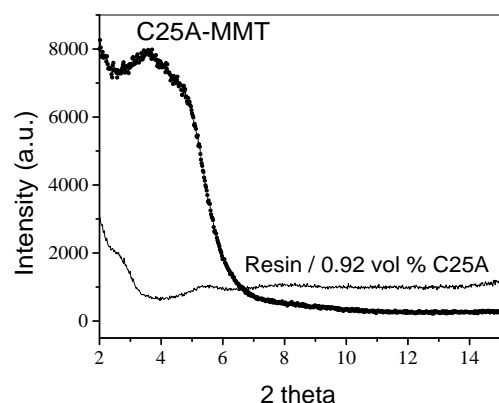
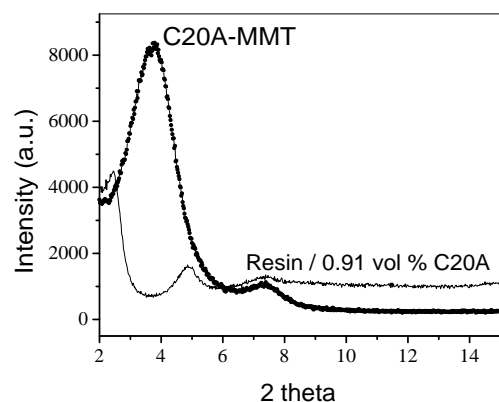
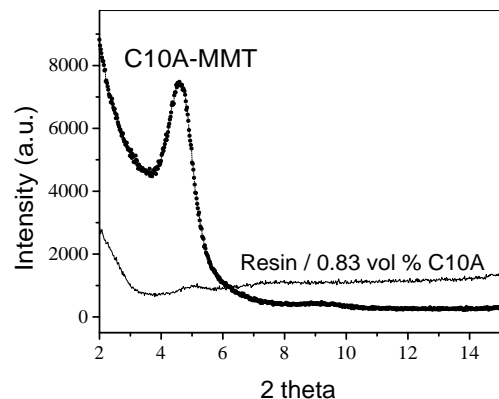
The sample containing C20A shows a more complicate behaviour. There are three peaks in the diffraction curve. The peak at the lowest angle indicates that a portion of the crystalline layers has been expanded, probably due to the insertion of the resin chains inside the galleries of the clay. The second peak indicates that another portion has been further aggregated, due to the reduction of the quantity of the organic modifier, while the third peak at higher angles, which corresponds to the second order diffraction, indicates that another portion of the clay particles remains unaffected.

This can be explained assuming that, on the one hand, acetone is not an appropriate solvent for the dispersion of the C20A particles and, on the other hand, the C20A particles are compatible with the acrylic resin. Therefore, the lowest angle peak is due to the interactions between the C20A and the resin, the second is due to the modifier destruction by the acetone and the third is due to the insufficient dispersion of the C20A in acetone.

In the case of ethanol, Fig. 9.3, there are three clays that seem to become exfoliated: C25A, C93A and OMBE. The other three clay types show a diffraction peak at angles equal to (C30B) or a little higher (C10A, C20A) than those of the clay powder. These angle shifts are not as strong as in the case of acetone indicating that the interaction of ethanol with the organic modifiers is relatively weak. Overall, it seems that ethanol is a more suitable solvent for the dispersion of the modified clays, at least in comparison with acetone.

It should be noted that in the case of C20A, it is not clear whether the peak originates from the shift to higher angles of the primary clay peak or whether it originates from the shift to lower angles of the secondary clay peak.

Following the encouraging X-ray results of the above three clay types, they were used to prepare nanocomposite samples at different volume fractions. It should be noted that even though the use of acetone lead to two samples that showed good X-



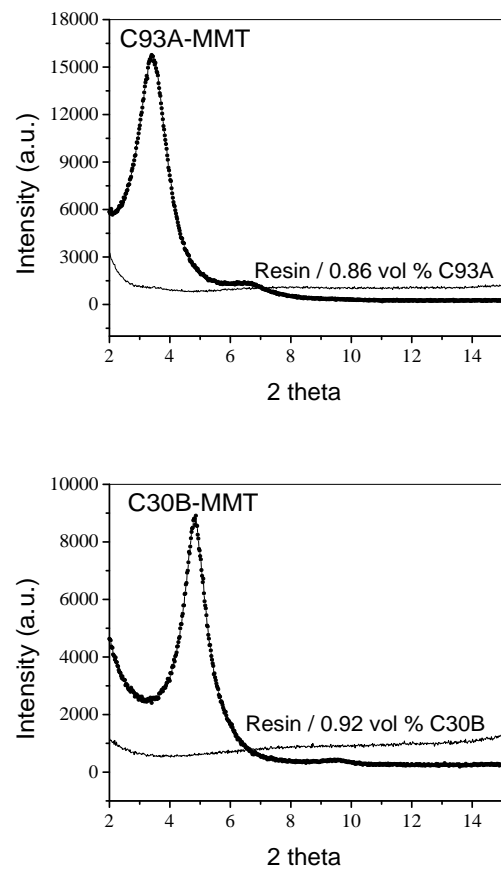
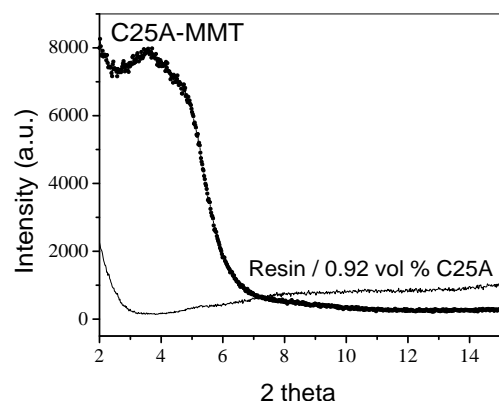
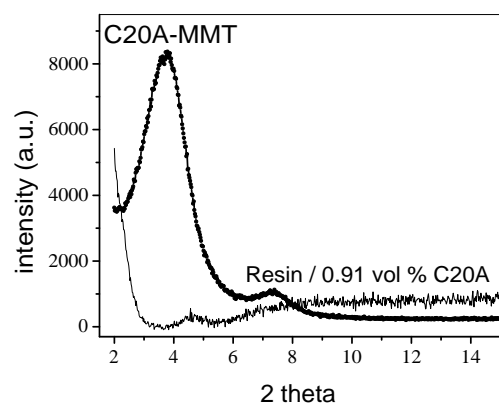
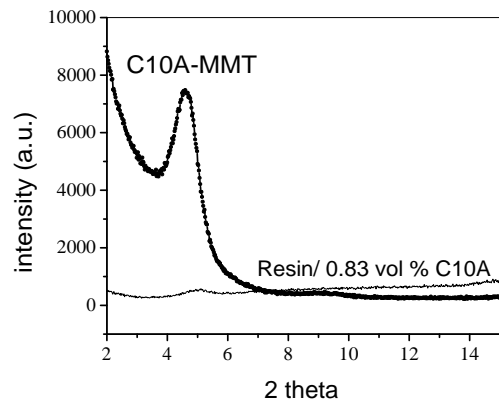


Figure 9.2: X-ray results for different organo-modified montmorillonites dispersed in acetone and then mixed with the acrylic resin aqueous dispersion to make the coatings. The line corresponds to the nanocomposite and the symbols to the OMMT powder.



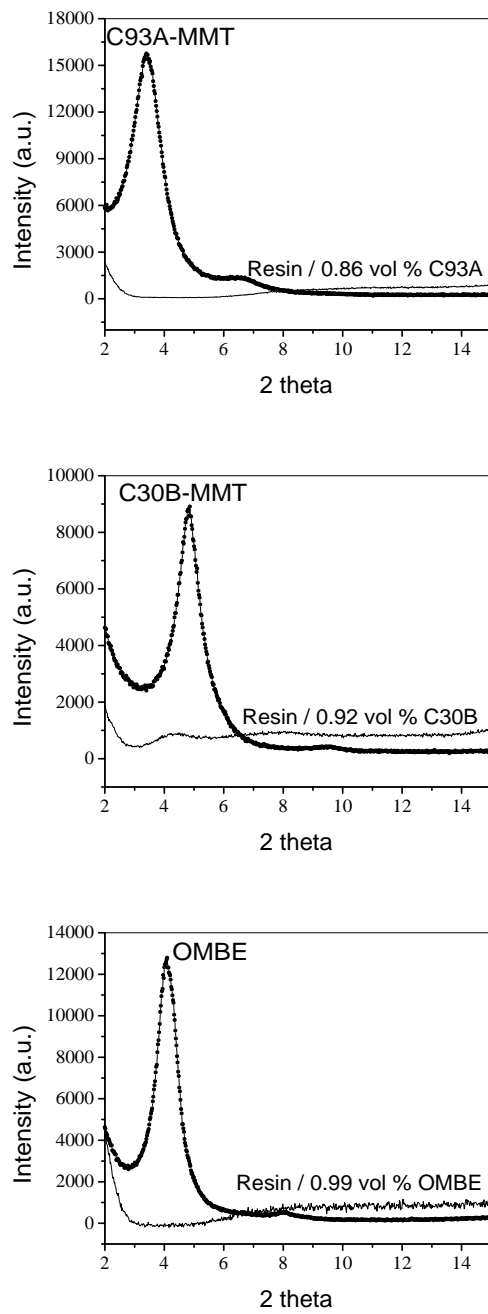


Figure 9.3: X-ray results for different organo-modified montmorillonites dispersed in ethanol and then mixed with the acrylic resin aqueous dispersion. The line corresponds to the nanocomposite and the symbols to the OMMT powder.

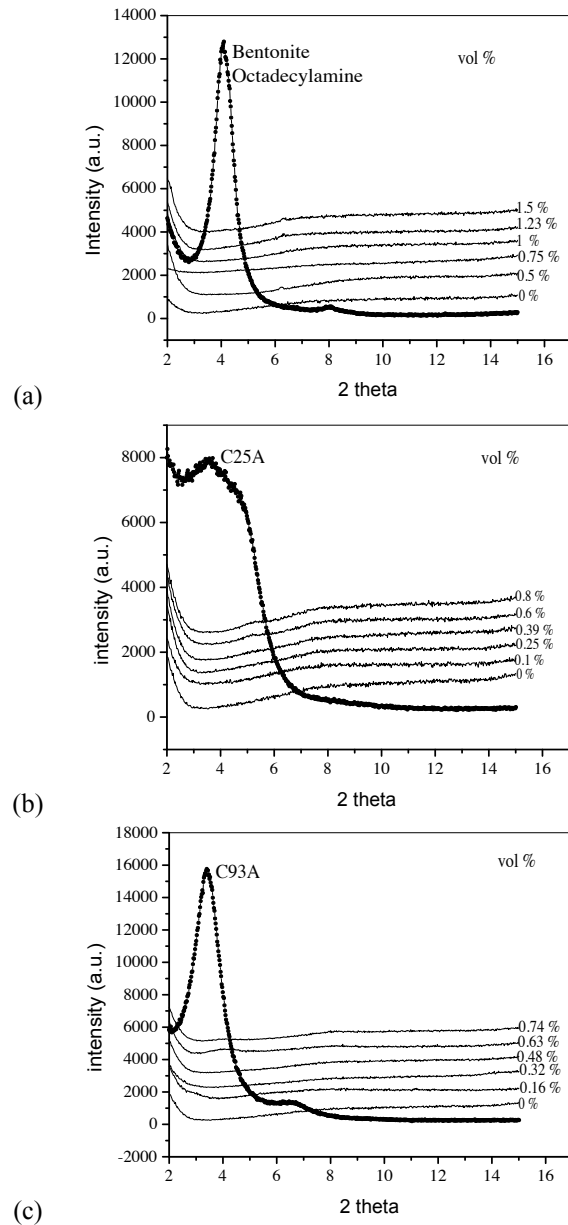


Figure 9.4: X-ray results for different volume fractions of organo-modified montmorillonites (a) OMME, (b) C25A and (c) C93B, dispersed in ethanol and then mixed with the acrylic resin aqueous dispersion.

ray results, acetone is a very volatile substance (boiling point at 57°C) and it is difficult to produce films adequate for permeation measurements, as bubbles or pores are often generated in the film. For this reason we did not proceed further with these samples.

Fig. 9.4a shows the X-ray results for five different volume fractions of organo-modified bentonite (OMBE). All samples seem to be well exfoliated, since no obvious diffraction peak is detected. However, after careful observation, a small peak can be discerned at an angle around 6.2°, especially for the samples with 1.23 vol% and 1.5 vol%. This peak corresponds to that of the unmodified clay and means that the ethanol reacts with the octadecylamine causing reaggregation of the particles at distances equal to those of the unmodified clay. Of course this effect is very weak and hardly detectable by XRD.

In Fig. 9.4b the X-ray results for 5 different volume fractions of organo-modified montmorillonite (C25A) are shown. For low volume fractions the diffraction peak has completely disappeared but another weak and broad peak is starting to form at higher volume fractions (0.6 vol % and 0.8 vol %) at around 5°. This seems to be an indication of incomplete exfoliation. Since this peak appears at angles higher than those of the clay powder, it seems that these crystalline layers begin to aggregate due to the influence of ethanol on the surfactant.

Similar results are shown in Fig. 9.4c for five different volume fractions of organo-modified montmorillonite (C93A). Again, there is no diffraction peak in the low volume fraction area, while at higher volume fractions a broad peak appears at around 4°, indicating incomplete exfoliation. This time the peak is located very close to that of the pristine modified clay and this means that there is no reaggregation of the particles, as in the case of C25A, but just incomplete exfoliation. Probably, this is due to the incomplete initial dispersion of the modified clay in ethanol. Therefore, the ethanol does not influence the modifier, as it does in the cases of OMBE and C25A.

From the above results it seems that there are three main parameters affecting the final state of dispersion in the nanocomposite: The initial dispersion level of the clay in the solvent; the degree of interaction between the solvent and the modifier of the particles; and the compatibility between the modified particles and the resin. Obviously, it is very difficult to satisfy all these requirements.

9.4 Transport Properties

Gas transport measurements were performed in the permeation cell using the standard procedure described in chapters 7 and 8. The results are tabulated in Tables A.1 to A.2.

Figure 9.5 shows the three transport coefficients as a function of clay volume fraction for the case of organo-modified bentonite (OMBE). There is an almost linear reduction of the diffusion coefficient down to about 60% of the value of the pure resin. This behaviour does not follow the tortuous path model and may be an indication that there is another significant contribution on the diffusion process, probably due to the free volume.

On the other hand, the solubility coefficient has an increasing trend, up to about 40% of the initial value, which can be attributed to the interfacial regions developed between the two components (extra free volume) and to the affinity between the or-

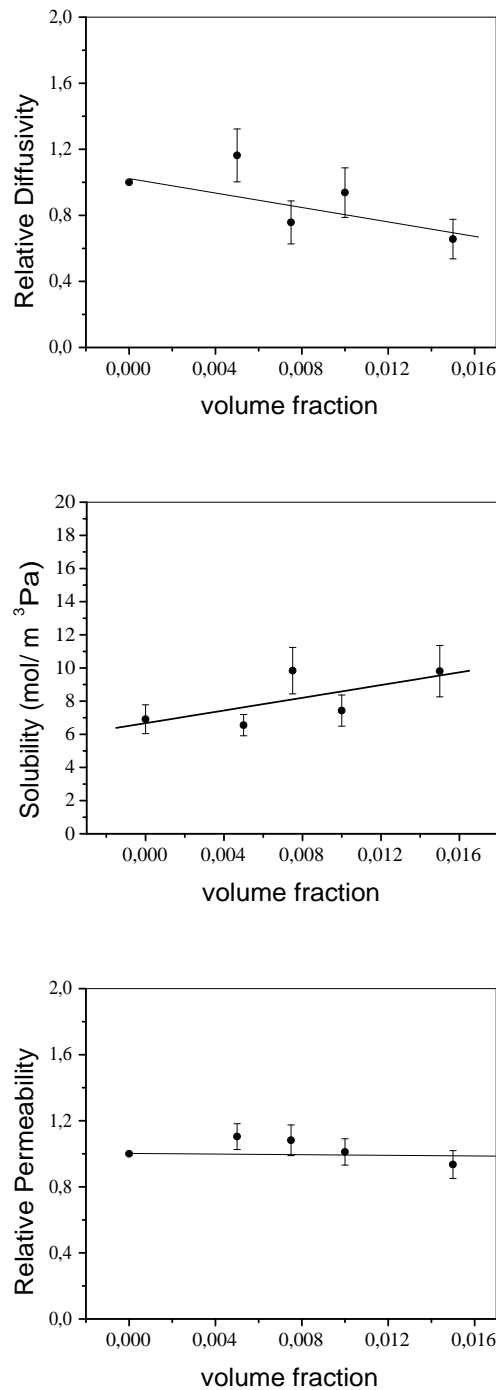


Figure 9.5: Carbon dioxide transport coefficients as a function of OMME clay volume fraction. The measurements were performed in the permeation cell at 23°C.

Table 9.7: CO_2 gas transport coefficients at 23 °C and 50 % rel. humidity of the samples containing OMBE, measured in the permeation cell.

vol %	Diffusion coefficient $10^{-12} (m^2/s)$	Solubility $10^{-5} mol/m^3 Pa$	Permeability $10^{-16} (mol/m s Pa)$
0.00	5.15 ± 0.58	6.91 ± 0.87	3.55 ± 0.20
0.50	5.99 ± 0.52	6.55 ± 0.64	3.92 ± 0.17
0.75	3.90 ± 0.51	10.0 ± 1.4	3.84 ± 0.25
1.00	4.83 ± 0.55	7.43 ± 0.94	3.59 ± 0.20
1.50	3.38 ± 0.48	9.81 ± 1.55	3.32 ± 0.23

Table 9.8: CO_2 gas transport coefficients of the samples containing (C25A) at 13 °C and 50 % rel. humidity measured in the permeability cell.

vol %	Diffusion coefficient $10^{-12}(m^2/s)$	Solubility $10^{-5} (mol/m^3 Pa)$	Permeability $10^{-16} (mol/m s Pa)$
0.00	3.96 ± 0.49	7.25 ± 1.00	2.87 ± 0.18
0.16	2.75 ± 0.28	8.58 ± 0.98	2.36 ± 0.12
0.32	3.03 ± 0.44	8.2 ± 1.3	2.49 ± 0.18
0.48	2.80 ± 0.42	8.8 ± 1.5	2.47 ± 0.18
0.63	2.56 ± 0.41	9.4 ± 1.7	2.41 ± 0.20
0.74	2.37 ± 0.45	8.7 ± 1.6	2.37 ± 0.20

ganic modifier (octadecylamine) and the carbon dioxide gas. As a consequence, the permeability coefficient remains almost constant (actually there is a slight reduction of 10%).

By comparing these results with those of hydrophilic bentonite of the previous chapter, Fig. 7.4, we can see that, while the solubility is enhanced by only 15% in the case of hydrophilic bentonite, the enhancement in the case of modified particles is 40%. This is an evidence that there is a interaction between the carbon dioxide gas molecules and the organic modifier. Therefore, it seems that the compatibiliser may have two opposite effects: it may improve the interactions between the two components of the nano-composite but it may also enhance the adsorption of the gas molecules in the interfacial regions between the organic matrix and the inorganic crystalline layers.

In the case of organo-modified montmorillonite C25A (Fig. 9.6), the diffusion coefficient can be described by the tortuous path model and the Nielsen equation predicts a value of the aspect ratio (L/W) of 200. This is relatively high and implies that there is a high degree of exfoliation of the inorganic particles. At higher volume fractions the degree of exfoliation is lower, as it is confirmed by the X-ray results, and the tortuous path becomes less effective. The overall reduction of the diffusion coefficient for 0.63 vol % C25A particles is about 30%.

The solubility coefficient on the other hand, increases by about 30% for similar reasons, as in the case of OMBE, limiting the final barrier properties improvement to

Table 9.9: CO_2 gas transport coefficients at $13^{\circ}C$ and 50 % rel. humidity of the samples containing C93A, measured in the permeability cell.

vol %	Diffusion coefficient 10^{-12} (m ² /s)	Solubility 10^{-5} (mol/m ³ Pa)	Permeability 10^{-16} (mol/m s Pa)
0.00	3.96 ± 0.49	7.25 ± 1.00	2.87 ± 0.18
0.10	3.10 ± 0.38	7.9 ± 1.1	2.45 ± 0.15
0.25	2.94 ± 0.34	8.2 ± 1.1	2.40 ± 0.14
0.39	2.90 ± 0.44	8.0 ± 1.3	2.30 ± 0.17
0.60	2.53 ± 0.47	9.1 ± 1.9	2.30 ± 0.22
0.80	2.46 ± 0.42	10.0 ± 1.9	2.48 ± 0.21

only 15%. It should be noted that in this case the free volume that originates from the interfacial regions has less impact on the diffusion and the solubility coefficients compared to the case of OMBE. The affinity of the carbon dioxide gas with the organic modifier of C25A seems to be the dominant factor affecting the solubility enhancement.

Similar results were obtained for the case of C93A (Fig. 9.7). The reduction in the diffusion coefficient is about 30% for 0.6 vol% of C93A particles and is dominated by the tortuous path that the crystalline layers create in the polymer matrix. The aspect ratio value is again 200, as in the case of C25A, based on fitting Nielsen's equation. In this case the solubility coefficient presents an enhancement of about 40%, limiting the improvement of the final barrier properties to 20% for 0.4 vol% C93A. Above this volume fraction the barrier properties worsen, due to the strong increase of the solubility and the weakening of the tortuosity. The latter is due to the lower degree of the particle exfoliation at higher volume fractions.

9.5 Conclusions

In order to achieve the dispersion of the organo-modified montmorillonites in an aqueous acrylic resin dispersion and the formation of a well exfoliated nano-coating various parameters must be taken into account:

- The miscibility between the solvent and the modified clays
- The surface tension between the solvent and the modified clays
- The d -spacing of the modified clays
- The miscibility between the solvent and water
- The compatibility between the polymer and the modified particles

The solubility parameters between the solvent and the modifier must be as close as possible while the surface tension of the solvent must be equal or higher than that of the modified particles in order to completely wet their surfaces helping to their delamination. The higher the d -spacing of the primary modified particles the easier their

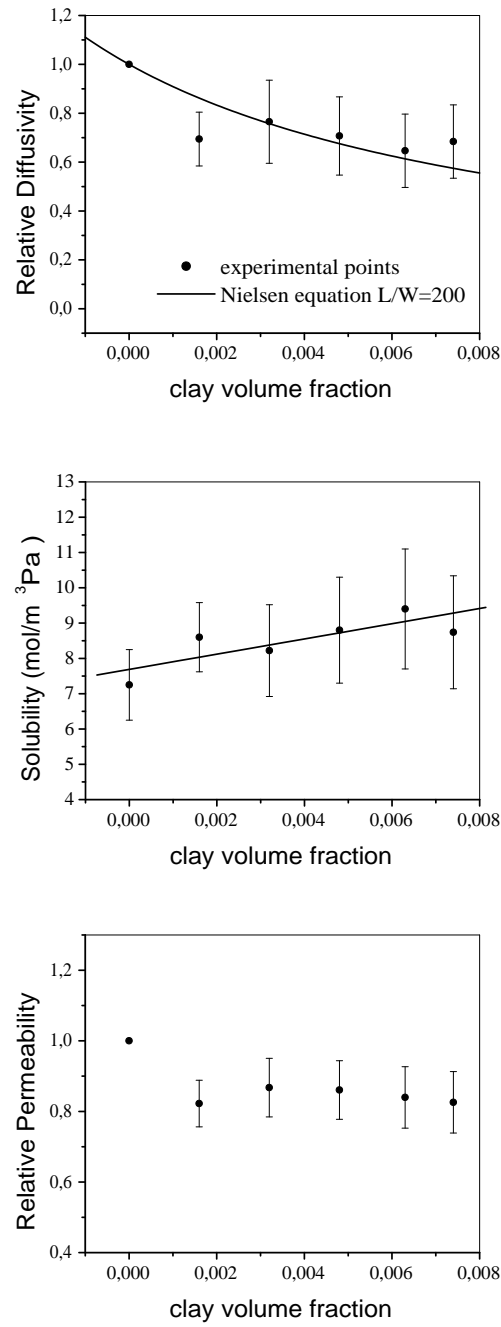


Figure 9.6: Carbon dioxide transport coefficients as a function of clay (C25A) volume fraction. The measurements were performed in the permeation cell at 13°C.

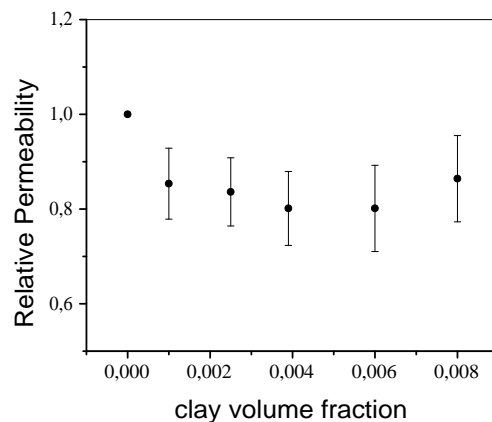
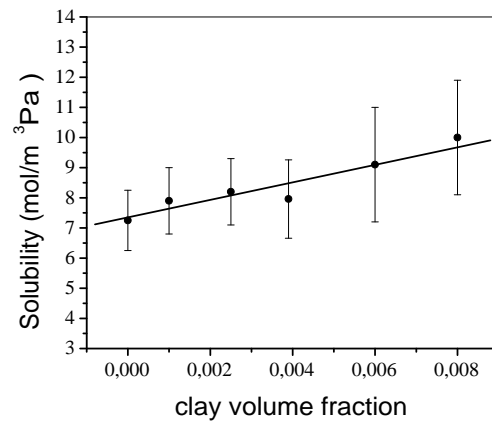
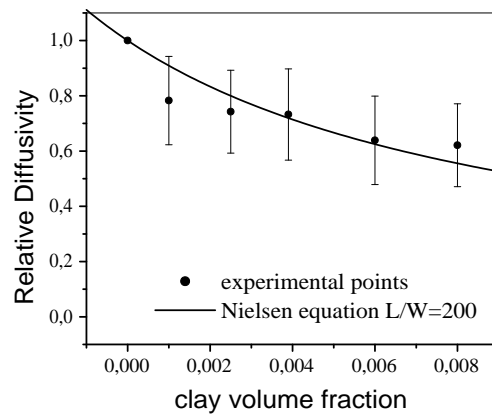


Figure 9.7: Carbon dioxide transport coefficients as a function of clay (C93A) volume fraction. The measurements were performed in the permeation cell at 13°C.

exfoliation in the solvent under ultrasonication and the more sufficient the polymer chains insertion between the galleries of the crystalline layers. The latter will be more efficient if the compatibility between the organic modifier and the polymer is as high as possible. Also, the solvent must not be volatile enough to avoid defects on the film surface during the curing process.

Obviously, an *a priori* knowledge of all these factors may not be always possible. Thus, although this chapter offers a general guidance, the trial and error method cannot be completely avoided. The complexity of the various interactions (polar, dispersive, hydrogen bonds) among the various components of the system render the selection of the appropriate ingredients rather tricky and limits the choices.

Even if the exfoliation of the particles is achieved to some extend, this does not mean that the desired barrier properties will be obtained. This is because the organic modifier, located at the interfaces between the two components, may act as an adsorption center, increasing the gas solubility significantly. If the affinity of the gas to the modifier is large, then the barrier properties of the film may be limited or even eliminated, even though the aspect ratio and the tortuosity of the exfoliated nano-layers present an opposite trend.

Chapter 10

General Conclusions and Recommendations

This PhD thesis studied the results of the incorporation of various types of inorganic clays in an acrylic resin matrix. The influence of the fillers on the morphological, free volume and gas transport properties of the final nano-coating was revealed and discussed. The nature, the shape, the size, the volume fraction and the type of the organic modifier of the inorganic nanoparticles, as well as the effect of the several solvents used and the thermodynamic interactions between the organic component and the inorganic reinforcement were checked and analysed. Mainly three experimental techniques were utilised: X-ray diffraction, positron annihilation lifetime spectroscopy and gas permeation measurements.

The goal of the research project was to produce coatings with good barrier properties against the permeation of gasses. The basic initial hypothesis of the work was that the nanoparticles would create tortuous paths in the resin for the diffusion of the gas molecules and hinder, thus, their mass transfer through the coating. This hypothesis was proved valid in most cases but the situation was found to be more complicated, as more parameters of the nanocomposite composition and structure should also be taken into consideration.

In the case of the acrylic resin filled with disks of around 1 nm thickness and 30nm diameter, i.e., particles with relatively low aspect ration, L/D , an enhancement of diffusion and permeability coefficients is observed, while the solubility remains almost constant as a function of the fraction of laponite particles. While the o-Ps lifetime and intensity measured by PALS do not indicate any significant change in the factional free volume in the resin, the changes of the gas transport coefficients can be explained on the basis of the changes of the free volume hole size distribution caused by the nano-disks of the clay. Even if the total free volume, as well as the average hole size remain unaffected by the presence of the particles, the hole size distribution can be altered (broadened), influencing mainly the mobility of the gas molecules, which is reflected in the diffusion coefficient.

On the other hand, the solubility coefficient is related to the total amount of the

free volume. In the case of membranes and thin films this can be assumed to be located mainly near the surface of the sample. By increasing the nanoclay loading the solubility coefficient presents a trend identical to that of the fractional free volume. When the disks aspect ratio and volume fraction are low, the tortuosity factor on the diffusion coefficient is also very low. The free volume variations, then, overwhelm the effect on the barrier properties. Thus, the gas transmission rate (permeability) may be higher than that of the neat resin. Therefore, the addition of low lateral dimensions (low aspect ratio) particles may act destructively on the gas barrier performance of the final nanocoating.

In order to avoid such effects on the barrier properties, particles with larger lateral dimensions should be used. Due to their hydrophilic character, most clays are compatible only with polar polymers. Dispersing them in the generally hydrophobic polymers to form a nanocomposite can be a difficult matter that depends on several factors. Often exfoliation may be impossible. There are mainly two methods to achieve the dispersion: The first (and most conventional) is the chemical process. This takes place through the organic modification of the clay platelet surfaces by substituting the sodium cations in the galleries with (multi-alkyl)ammonium cations consisting of aliphatic tails with, at least, 12 carbon atoms. The second method is based on physical processes and can be applied to disperse the clay in thermosetting coatings by exploiting the use of certain solvents, as it was utilised in the present work.

For example, in thermoplastic polymers the polymer melt is mixed with the nanoparticles in a mixer flow under high shear stresses. The interactions between the clay and the organic component is direct and, if there is no inter-miscibility, the nanocomposite will not be formed. In a thermosetting coating, however, as long as the solvent is in place, there is no direct interaction between these two ingredients. The interactions will start during the evaporation of the solvent and during the curing process. By controlling the temperature and the solvent evaporation rate it is possible to entrap the exfoliated crystalline layers between the resin droplets, prevent their re-agglomeration and create, thus, a well dispersed exfoliated clay-polymer nanocomposite coating.

This procedure was followed for the hydrophilic bentonite and Li-Hectorite nanoclays, the crystalline layers of which have large aspect ratios. After their exfoliation in water under ultrasonication and high shear stresses, these clays were dispersed in the aqueous acrylic resin emulsion and formed a coherent nanocomposite film upon drying and curing at 23°C and 50% relative humidity. The entrapping procedure is more successful when the particles loading is low and their lateral dimensions are as large as possible, in order to have the maximum face-to-face distance and to prevent their precipitation, which will lead to their re-aggregation at that stage.

The bentonite clay layers have an aspect ratio of 100 - 300. Acrylic resin/bentonite nanocomposite coatings with improved barrier properties were prepared for dispersed particles content of less than 2 vol%. The presence of the dispersed inorganic nano-platelets improves the gas barrier properties of the film by 25% for 1.3 vol% added nanoparticles. However, the extensive interfacial regions between the two components limit this reduction by increasing the solubility of the gas molecules in the system. This is due to the enhanced adsorption of the molecules in the free volume created around the interfaces. Thus, although the reduction in the diffusion coefficient is significant due to the tortuosity imposed by the large aspect ratio particles, the possibility of solubility enhancement due to the interfacial free volume may compromise the final gas

permeation characteristics of the material.

The Li-Hectorite single platelets have aspect ratios of more than 1000. The incorporation of the hydrophilic Li-Hectorite nanoparticles in the acrylic resin matrix produces nanocomposite membranes with enhanced gas barrier properties at all particle volume fractions. Due to their huge surface area, the hectorite particles create tortuous routes for the gas molecules increasing their diffusion length to a great degree, even if they are not completely exfoliated. The overall reduction of the relative permeability approaches one order of magnitude for the sample with a volume fraction of just 3.7 vol%.

The barrier performance of the polymer coating filled with high aspect ratio platelets would be even higher if the exfoliated crystalline layers were rigid and maintained their huge lateral dimensions to the end. This would lead to the maximisation of the tortuosity and improve the gas barrier properties by several orders of magnitude. Unfortunately, their large lateral dimension and thinness gives them enough flexibility, which leads to their bending and a drastic reduction of the effective aspect ratio, limiting the final gas barrier coating performance.

Organic-modification on the clays may also be used to improve their compatibility with the resin and enhance their chances for exfoliation. When such organomodified clays are used in an aqueous acrylic resin emulsion, the successful formation of a well exfoliated nano-coating depends on the following parameters:

- The solubility parameters between the solvent used to disperse/exfoliate the clay and the organic-modifier used on the clay should be close enough
- The interfacial tensions between the solvent and the modified clays should be as close as possible
- The initial *d*-spacing of the modified clay layers in the powder should be as high as possible
- The miscibility between the solvent and the water should be as high as possible
- The compatibility between the polymer (resin) and the modified particles should be as high as possible

However, even if the exfoliation of the particles is achieved in some extend, this does not mean that the desired barrier properties will always be fulfilled. This is because the organic modifier located at the interfaces between the two components may act as an adsorption area for the gas molecules, increasing the gas solubility significantly. Therefore, the improvement of the barrier properties of the film may be limited or even reversed, even though the aspect ratio and the tortuosity of the exfoliated nano-layers present an opposite trend.

A few things we must avoid in order to optimise the gas barrier properties of a polymer nanocoating, beyond the obvious, i.e., a low degree of exfoliation, a low aspect ratio and volume fraction of the inorganic reinforcement, are:

1. The bending of the crystalline nano-layers.
2. The affinity between the test gas and the organic modifier.

3. The extended interfacial area between the two components. It must be as dense as possible.
4. The excess free volume resulting from solvent molecules trapped during the curing process.

The avoiding of the bending of the layers probably requires another coating formation technique. If the interactions between the polymer and the organic modifier are strong enough, they will create high density interfacial regions, occupying and covering the empty space, and reducing the contribution of the interfaces on the free volume. The interfacial tension between the resin and the modifier should be as low as possible, to ensure a complete wetting of the particle surfaces by the polymer chains. On the other hand, a sufficient chemical bonding between the two components is required to create interfaces as dense as possible.

The above, in combination with a low affinity between the gas and the modifier, will reverse the negative contribution of the solubility coefficient improving the gas barrier properties significantly. The elimination of the excess free volume requires that the curing must be done above the glass transition temperature of the resin, if this is technically feasible. For example, the T_g of the resins in the present work was about 100^0C , which is the boiling point of water. Curing above 100^0C in this case, will produce steam bubbles and incoherent coatings, inappropriate for gas barrier properties.

Future work

Beyond gas barrier properties, it would be interesting and technologically desired to study the effects of hydrophilic clay particles on the water vapour transmission rate of the nanocoatings. The water vapour permeation mechanism is quite different from that of the gas, since the water molecules are polar and can interact more effectively with the also polar clay particles. Thus, on one hand the interactions between the mainly hydrophobic polymer matrix with the polar penetrant are expected to be unfavourable; on the other hand the dispersed polar nanoclays are able to develop strong interactions and facilitate the water transport through the coating. It seems that the interfacial regions will determine the mass transport characteristics in this case, since the contribution of the matrix can be ignored. Therefore, the study of water vapour permeation is an efficient route to examine the interfacial properties of the material.

The gas barrier performance can be further improved through the incorporation in the polymer matrix of an active ingredient which reacts with the test gas. This will further delay the diffusion process, at least for a time period until the exhaustion of the reactants. The combination of a reactive barrier with a passive barrier may improve the barrier performance of the coating by several orders of magnitude, which is the final objective for the development of alternative protective coating materials.

Gas, vapour and liquid permeation processes through hybrid materials are of great scientific interest since their potential uses are numerous. Except barrier properties, other properties can be desirable for specific applications, such as enhanced permeability (e.g. for breathable coatings), gas separation ability for membranes (e.g. for

reverse osmosis) and controlled permeability of coatings for controlled release applications (e.g. drug release). All these cases rely on a similar background with those of the barrier coatings examined in the present work and are parts of a desired field of activity in the near future for the author.

BIBLIOGRAPHY

REFERENCES

- R. Aris. On a problem in hindered diffusion. *Arch.Ration.Mech.Anal.*, 12:83–91, 1986.
- J. Arnold. A free-volume hole-filling model for the solubility of liquid molecules in glassy polymers 1: Model derivation. *Eur. Polym. J.*, 46:1131–1140, 2010.
- C. Ballik. On the extraction of diffusion coefficients from gravimetric data for sorption of small molecules by polymer thin films. *Macromolecules*, 29:3025–3029, 1996.
- R. Barbee and C. Matayabas. Nanocomposites for high barrier applications, 2000. United States Patent WO0078855, 28.12.2000, European Patent EP 0 670 058 B1, 08.07.1998, Canadian Patent CA 2,149,891, 15.02.2000, Finnish Patent FI 952480, 13.12.2002.
- R. Barrer and J. Petropoulos. Diffusion in heterogeneous media: lattice and parallelepipeds in a continuous phase. *Br.J.Appl.Phys.*, 12:691–697, 1961.
- O. Becker, Y. B. Cheng, R. J. Varley, and G. P. Simon. Layered silicate nanocomposites based on various high-functionality epoxy resins: The influence of cure temperature on morphology, mechanical properties and free volume. *Macromolecules*, 36:1616–1625, 2003.
- A. Beerbower. Surface free energy: A new relationship to bulk energies. *J. Colloid. Inter. Sci.*, 35:126–132, 1971.
- S. Behrens, D. Christl, R. Emmerzael, P. Schurtenberger, and M. Borkovec. Charging and aggregation properties of carboxyl latex particles: Experiments versus dlvo theory. *Langmuir*, 16:2566–2575, 2000.
- R. Bharadwaj. Modeling the barrier properties of polymer-layered silicate nanocomposites. *Macromolecules*, 34:9189–9192, 2001.
- M. Bhattacharya, S. Biswas, and A. Bhowmick. Permeation characteristics and modeling of barrier properties of multifunctional rubber nanocomposites. *Polymer*, 52:1562–1576, 2011.

- M. Bohning, H. Goering, N. Hao, R. Mach, and A. Schonhals. Polycarbonate/*SiC* nanocomposites-influence of nanoparticle dispersion on molecular mobility and gas transport. *Polym. Adv. Technol.*, 16:262–268, 2005.
- A. Bondi. Van der waals volumes and radii. *J.Phys.Chem.*, 68:441, 1964.
- D. Burgentzle, J. Duchet, J. Gerard, A. Jupin, and B. Fillon. Solvent-based nanocomposite coatings. dispersion of organophilic montmorillonite in organic solvents. *J. Colloid. Inter. Sci.*, 278:26–39, 2004.
- C. Chen, B. Han, J. Li, T. Shang, J. Zou, and W. Jiang. A new model on the diffusion of small molecule penetrants in dense polymer membranes. *J. Membr. Sci.*, 187: 109–118, 2001.
- M. Choi, Y. Kim, and C. Ha. Polymers for flexible displays: From material selection to device applications. *Prog. Polym. Sci.*, 33:581–630, 2008.
- G. Choudalakis and A. Gotsis. Permeability of polymer/clay nanocomposites: A review. *Eur. Polym. J.*, 45:967–984, 2009.
- G. Choudalakis and A. Gotsis. Free volume and mass transport in polymer nanocomposites. *Curr. Opin. Coll. Inter. Sci.*, 17:132–140, 2012.
- G. Choudalakis, A. Gotsis, H. Schut, and S. Picken. The free volume in an acrylic resin/laponite nanocomposite coatings. *Eur. Polym. J.*, 47:264–272, 2011.
- L. Y. Chul and K. M. Jun. Organo clay containing anticorrosive coating composition and preparation method, 2007. WO2007055498, 18.05.2007.
- G. Consolati, I. Genco, M. Pegoraro, and L. Zanderighi. Positron annihilation lifetime (PAL) in poly[1-(trimethyl-silyl)propine](PTMSP): Free volume determination and time dependence of permeability. *J. Polym. Sci. Part B: Polym. Phys.*, 34:357–367, 1996.
- L. Cui, J. T. Yeh, K. Wang, F. C. Tsai, and Q. Fu. Relation of free volume and barrier properties in the miscible blends of poly(vinyl alcohol) and nylon 6-clay nanocomposites film. *J. Membr. Sci.*, 327:226–233, 2009.
- E. Cussler, S. Hughes, W. Ward, and R. Aris. Barrier membranes. *J.Membr.Sci.*, 38: 161–174, 1988.
- C. Dai, P. Li, and J. Yeh. Comparative studies for the effect of intercalating agent on the physical properties of epoxy resin-clay based nanocomposite materials. *Eur. Polym. J.*, 44:2439–2447, 2008.
- C. Dreiss, T. Cosgrove, N. Benton, D. Kilburn, M. Alam, R. Schmidt, and G. Gordon. Effect of crosslinking on the mobility of PDMS filled with polysilicate nanoparticles: Positron lifetime, rheology and NMR relaxation studies. *Polymer*, 48:4419–4428, 2007.

- J. Duran, M. Ramos-Tejada, F. Arroyo, and F. Gonzalez-Caballero. Rheological and electrokinetic properties of sodium montmorillonite suspensions. *J. Colloid Inter. Sci.*, 229:107–117, 2000.
- A. Esfandiari, H. Nazokdast, A. Rashidi, and M. Yazdanshenas. Review of polymer - organoclay nanocomposites. *J. Appl. Sci.*, 8:545–561, 2008.
- W. Falla, M. Mulski, and E. Cussler. Estimating diffusion through flake-filled membranes. *J. Membr. Sci.*, 119:129–138, 1996.
- P. Fang, Z. Chen, S. Zhang, S. Wang, L. Wang, and J. Feng. Microstructure and thermal properties of ethylene-(vinyl acetate) copolymer/montmorillonite nanocomposites. *Polym. Int.*, 55:312–318, 2006a.
- Z. Fang, Y. Xu, and L. Tong. Free-volume hole properties of two kinds thermoplastic nanocomposites based on polymer blends probed by positron annihilation lifetime spectroscopy. *J. Appl. Polym. Sci.*, 102:2463–2469, 2006b.
- M. Fasihi and M. Abolghasemi. Oxygen barrier and mechanical properties of masterbatch-based PA-6/nanoclay composite films. *J. Appl. Polym. Sci.*, 125:E2–E8, 2012.
- R. Fedors. A method for estimating both the solubility parameters and molar volumes of liquids. *Polym. Eng. Sci.*, 14:147–154, 1974.
- B. Flaconneche, J. Martin, and M. Klopffer. Permeability, diffusion and solubility of gases in polyethylene, polyamide11, and poly(vinylidene fluoride). *Oil and Science Technology-Rev. IFP*, 56:261–278, 2001.
- G. Fredrickson and J. Bicerano. Barrier properties of oriented disk composites. *J. Chem. Phys.*, 110:4, 1999.
- M. Frounchi, S. Dadbin, Z. Salehpour, and M. Noferesti. Gas barrier properties of PP/EPDM blend nanocomposites. *J. Membr. Sci.*, 282:142–148, 2006.
- Y. Fu, C. Hu, K. Lee, H. Tsai, R. Ruaan, and J. Lai. The correlation between free volume and gas separation properties in high molecular weight poly(methyl methacrylate) membranes. *Eur. Polym. J.*, 43:959–967, 2007.
- H. Fujita and A. Kishimoto. Diffusion-controlled stress relaxation in polymers. stress relaxation in swollen polymers. *J. Polym. Sci.*, XXVIII:547–567, 1958.
- A. Garcia, M. Iriarte, C. Uriarte, and A. Etxeberria. Study of the relationship between transport properties and free volume based in polyamide blends. *J. Membr. Sci.*, 284: 173–179, 2006.
- A. Garcia, S. Eceolaza, M. Iriarte, C. Uriarte, and A. Etxeberria. Barrier character improvement of an amorphous polyamide (trogamid) by the addition of a nanoclay. *J. Membr. Sci.*, 301:190–199, 2007.
- M. Greenfield and D. Theodorou. Geometric analysis of diffusion pathways in glassy and melt atactic polypropylene. *Macromolecules*, 26:5461–5472, 1993.

- C. Grillet, A. S. Brunel, Y. Chevalier, S. Usoni, V. Ansanay-Alex, and J. Allemand. Control of the morphology of waterborne nanocomposite films. *Polym. Int.*, 53: 569–575, 2004.
- A. Gusev and H. Lusti. Rational design of nanocomposites for barrier applications. *Adv. Mater.*, 13:21, 2001.
- M. Hanika, H. Langowski, U. Moosheimer, and W. Peukert. Inorganic layers on polymeric films - influence of defects and morphology on barrier properties. *Chem. Eng. Technol.*, 26:605–614, 2003.
- N. Hatzigrigoriou and C. Papaspyrides. Nanotechnology in plastic food-contact materials. *J. Appl. Polym. Sci.*, 122:3720–3739, 2011.
- H. Heinz, R. Vaia, and B. Farmer. Interaction energy and surface reconstruction between sheets of layered silicates. *J. Chem. Phys.*, 124:224713, 2006.
- E. Hensema, M. Mulder, and C. Smolders. On the mechanism of gas transport in rigid polymer membranes. *J. Appl. Polym. Sci.*, 49:2081–2090, 1993.
- J. Herrera-Alonso, Z. Sedlakova, and E. Marand. Gas transport properties of polyacrylate/clay nanocomposites prepared via emulsion polymerization. *J. Membr. Sci.*, 363: 48–56, 2010.
- M. Heuchel, D. Hofmann, and P. Pullumbi. Molecular modeling of small-molecule permeation in polyimides and its correlation to free-volume distributions. *Macromolecules*, 37:201–214, 2004.
- A. Hiltner, R. Liu, Y. Hu, and E. Baer. Oxygen transport as a solid state structure probe for polymeric materials: a review. *J. Polym. Sci. Part B: Polym. Phys.*, 43:1047–1063, 2005.
- D. L. Ho and C. Glinka. Effects of solvent solubility parameters on organoclay dispersions. *Chem. Mater.*, 15:1309–1312, 2003.
- K. Holmberg, B. Jonsson, B. Kronberg, and B. Lindman. *Surfactants and polymers in aqueous solution*. John Wiley & Sons, Ltd., 2002.
- K. Ito, H. Nakanishi, and Y. Ujihira. Extension of the equation for the annihilation lifetime of ortho-positronium at a cavity larger than 1 nm in radius. *J. Phys. Chem.*, 103:4555–4558, 1999.
- A. Jacob, P. Kurian, and A. Aprem. Transport properties of natural rubber latex layered clay nanocomposites. *J. Appl. Polym. Sci.*, 108:2623–2629, 2008.
- E. Jacquemet, E. Espuche, J. Gerard, J. Duchet, and P. Mazabraud. Morphology and gas barrier properties of polyethylene-based nanocomposites. *J. Polym. Sci. Part B: Polym. Phys.*, 44:431–440, 2006.
- Z. Jang Bor. Nanocomposite compositions for hydrogen storage and methods for supplying hydrogen to fuel cells, 2006. US2006030483, 09.02.2006.

- Y. Jean. Positron annihilation spectroscopy for chemical analysis: A novel probe for microstructural analysis of polymers. *Microchem. J.*, 42:72–102, 1990.
- Y. Jean, J. Yuan, J. Liu, Q. Deng, and H. Yang. Correlations between gas permeation and free-volume hole properties probed by positron annihilation spectroscopy. *J. Polym. Sci.: Part B: Polym. Phys.*, 33:2365–2371, 1995.
- Q. Jia, M. Zheng, Y. Zhu, J. Li, and C. Xu. Effects of organophilic montmorillonite on hydrogen bonding, free volume and glass transition temperature of epoxy resin/polyurethane interpenetrating polymer networks. *Eur. Polym. J.*, 43:35–42, 2007.
- J. Jordan, K. Jacob, R. Tannenbaum, M. Sharaf, and I. Jasiuk. Experimental trends in polymer nanocomposites-a review. *Mat.Sci..Eng. A*, 393:1–11, 2005.
- J. Kim and Y. Lee. Gas permeation properties of poly(amide-6-ethylene oxide)-silica hybrid membrane. *J. Membr. Sci.*, 193:209–225, 2001.
- P. Kirkegaard, N. Pedersen, and M. Eldrup. POSITRONFIT. *Riso National Laboratory, Denmark*, 1989.
- Y. Kobayashi, W. Zheng, E. Meyer, J. McGervey, A. Jamieson, and R. Simha. Free volume and physical aging of poly(vinyl acetate) studied by positron annihilation. *Macromolecules*, 22:2302–2306, 1989.
- V. Krikorian and D. Pochan. Poly (l-lactic acid)/layered silicate nanocomposite: Fabrication, characterization, and properties. *J.Chem. Phys.*, 15:4317–4324, 2003.
- G. Lagaly. Interaction of alkylamines with different types of layered compounds. *Solid State Ionics*, 22:43–51, 1986.
- J. Lange and Y. Wyser. Recent innovations in barrier technologies for plastic packaging - a review. *Packag. Technol. Sci.*, 16:149–158, 2003.
- N. Lape, E. Nuxoll, and E. Cussler. Polydisperse flakes in barrier films. *J.Membr.Sci.*, 236:29–37, 2004.
- P. LeBaron, Z. Wang, and T. Pinnavaia. Polymer-layered silicate nanocomposites:an overview. *Appl.Clay Sci.*, 15:11–29, 1999.
- Y. Liang, N. Hilal, P. Langston, and V. Starov. Interaction forces between colloidal particles in liquid: Theory and experiment. *Adv. Colloid Inter. Sci.*, 134-135:151–166, 2007.
- J. Liu, Q. Deng, and Y. Jean. Free-volume distributions of polystyrene probed by positron annihilation: Comparison with free volume theories. *Macromolecules*, 26: 7149–7155, 1993.
- P. Maji, N. Das, and A. Bhowmick. Preparation and properties of polyurethane nanocomposites of novel architecture as advanced barrier materials. *Polymer*, 51: 1100–1110, 2010.

- R. D. Maksimov, S. Gaidukov, J. Zicans, and J. Jansons. Moisture permeability of a polymer nanocomposite containing unmodified clay. *Mech.Comp.Mat.*, 44(5):505–514, 2008.
- A. Manninen, H. Naguib, A. Nawaby, and M. Day. CO_2 sorption and diffusion in polymethyl methacrylate-clay nanocomposites. *Polym.Eng.Sci.*, 45:904–914, 2005.
- M. McBride. A critique of diffuse double layer models applied to colloid and surface chemistry. *Clays and Clay Minerals*, 45:598–608, 1997.
- T. Merkel, B. Freeman, R. Spontak, Z. He, I. Pinna, P. Meakin, and A. Hill. Sorption, transport, and structural evidence for enhanced free volume in poly(4-methyl-2-pentyne)/fumed silica nanocomposite membranes. *Chem. Mater.*, 15:109–123, 2003.
- A. Michaels and H. Bixler. Flow of gases through polyethylene. *J.Polym.Sci.L.*, pages 413–439, 1961.
- U. Min, J. Kim, and J. Chang. Transparent polyimide nanocomposite films: Thermo-optical properties, morphology, and gas permeability. *Polym. Eng. Sci.*, 51:2143–2150, 2011.
- G. Moggridge, N. Lape, C. Yang, and E. Cussler. Barrier films using flakes and reactive additives. *Prog.Org.Coat.*, 46:231–240, 2003.
- H. Mohamed and N. Abd El-Aziz. Study on polystyrene via positron annihilation lifetime and doppler broadened techniques. *Polymer*, 42:8013–8017, 2001.
- M. Moller, T. Lunkenbein, H. Kalo, M. Schieder, D. Kunz, and J. Breu. Barrier properties of synthetic clay with a kilo-aspect ratio. *Adv. Mater.*, 22:5245–5249, 2010.
- M. Moller, D. Kunz, T. Lunkenbein, S. Sommer, A. Nennemann, and J. Breu. Uv-cured, flexible, and transparent nanocomposite coating with remarkable oxygen barrier. *Adv. Mater.*, 24:2142–2147, 2012.
- A. Morgan. *Long-term durability of polymeric matrix composites*. Springer, 2012.
- K. Myung-Ho and L. S. Ho. Nanocomposite blend composition having excellent barrier property, 2006. JP2006328426, 07.12.2006.
- S. Nazarenko, P. Meneghetti, B. Julmon, and S. Qutubuddin. Gas barrier of polystyrene montmorillonite clay nanocomposites: Effect of mineral layer aggregation. *J.Polym.Sci. Part B: Polym.Phys.*, 45:1733–1753, 2007.
- N. Negrete-Herrera, J. Putaux, L. David, and E. Lami. Polymer/laponite composite colloids through emulsion polymerization: Influence of the clay modification level on particle morphology. *Macromolecules*, 39:9177–9184, 2006.
- P. Neogi. *Diffusion in Polymers*. Marcel Dekker, Inc., 1996.
- Q. Nguyen and D. Baird. Preparation of polymer-clay nanocomposites and their properties. *Adv.Polym.Tech.*, 25:270–285, 2006.

- L. Nielsen. Models for the permeability of filled polymer systems. *J.Macromol.Sci. A*, 1:929–942, 1967.
- L. Nobel. *Water-born Nanocomposite Coatings*. PhD thesis, Delft University of Technology, Delft, the Netherlands, 2007.
- M. L. Nobel, E. Mendes, and S. J. Picken. Enhanced properties of innovative laponite-filled waterborne acrylic resin dispersions. *J.Appl.Polym.Sci.*, 103(2):687–697, 2007a.
- M. L. Nobel, S. J. Picken, and E. Mendes. Waterborne nanocomposite resins for automotive coating applications. *Prog. Org. Coat.*, 58(2-3):96–104, 2007b.
- C. Paranchos, B. Soares, J. Machado, D. Windmoller, and L. Pessan. Microstructure and free volume evaluation of poly(vinyl alcohol) nanocomposite hydrogels. *Eur. Polym. J.*, 43:4882–4890, 2007.
- R. Pethrick. Positron annihilation – a probe for nanoscale voids and free volume? *Prog.Polym.Sci.*, 22:1–47, 1997.
- E. Picard, A. Vermogen, J. Gerard, and E. Espuche. Barrier properties of nylon-6 montmorillonite nanocomposite membranes prepared by melt blending: influence of the clay content and dispersion state: consequences of modelling. *J.Membr. Sci.*, 292: 133–144, 2007.
- C. Powell and G. Beall. Physical properties of polymer/clay nanocomposites. *Curr. Opin. Sol. State Mater. Sci.*, 10:73–80, 2006.
- M. Priolo, D. Gamboa, K. Holder, and G. J.C. Super gas barrier of transparent polymer-clay multilayer ultrathin films. *Nano Lett.*, 10:4970–4974, 2010.
- V. Pryamitsyn, B. Hanson, and V. Ganesan. Coarse-grained simulations of penetrant transport in polymer nanocomposites. *Macromolecules*, 44:9839–9851, 2011.
- Y. Qian, C. Lindsay, C. Macosko, and A. Stein. Synthesis and properties of vermiculite-reinforced polyurethane nanocomposites. *Appl.Mater.Interf.*, 3:3709–3717, 2011.
- O. Quayle. The parachors of organic compounds. *Chem. Rev.*, 53:439, 1953.
- S. S. Ray and M. Okamoto. Polymer/layered silicate nanocomposites: a review from preparation to processing. *Prog.Polym.Sci.*, 28:1539–1641, 2003.
- W. A. Rogers, R. S. Buritz, and D. Alpert. Diffusion coefficient, solubility and permeability for helium in glass. *J.Appl.Phys.*, 25:7, 1954.
- M. Sadat-Shojaei and A. Ershad-Langroudi. Polymeric coatings for protection of historic monuments: Opportunities and challenges. *J. Appl. Polym. Sci.*, 112:2535–2551, 2009.
- F. Sadeghi, M. Fereydoon, and A. Ajji. Rheological, mechanical and barrier properties of multilayer nylon/clay nanocomposite film. *Adv. Polym. Tech.*, in press, 2011. doi: 10.1002/adv.20270.

- M. Salame and S. Steingiser. Barrier polymers. *Polym. Plast. Technol. Eng.*, 8:155–175, 1977.
- K. Sato, K. Ito, R. S. Yu, and Y. Kobayashi. Intrinsic momentum distributions of positron and positronium annihilation in polymers. *Phys. Rev. B*, 71:012201, 2005.
- A. Shishatskii, Y. Yampolskii, and K. Peinemann. Effects of film thickness on density and gas permeation parameters of glassy polymers. *J. Membr. Sci.*, 112:275–285, 1996.
- W. Smith and C. Zukoski. Role of solvation forces in the gelation of fumed silica-alcohol suspensions. *J. Colloid Inter. Sci.*, 304:348–358, 2006.
- A. Sorrentino, M. Tortora, and V. Vittoria. Diffusion behavior in polymer-clay nanocomposites. *J. Polym. Sci. Part B: Polym. Phys.*, 44:265–274, 2006.
- A. Sorrentino, G. Gorraso, and V. V. Potential perspectives of bio-nanocomposites for food packaging applications. *Trends in Food Science and Technology*, 18:84–95, 2007.
- V. Sridhar and D. K. Tripathy. Barrier properties of chlorobutyl nanoclay composites. *J. Appl. Polym. Sci.*, 101:3630–3637, 2006.
- R. Stephen, C. Ranganathaiah, S. Varghese, J. Kuruvilla, and T. Sabu. Gas transport through nano and micro composites of natural rubber (NR) and their blends with carboxylated styrene butadiene rubber (XSBR) latex membranes. *Polymer*, 47:858–870, 2006.
- K. Strawhecker and E. Manias. Structure and properties of poly(vinyl alcohol)/Na montmorillonite nanocomposites. *Chem. Mater.*, 12:2943–2949, 2000.
- C. Swannack, C. Cox, A. Liakos, and H. D. A three-dimensional simulation of barrier properties of nanocomposite films. *J. Membr. Sci.*, 263:47–56, 2005.
- T. Tadros. Interparticle interactions in concentrated suspensions and their bulk (theoretical) properties. *Adv. Colloid Inter. Sci.*, 168:263–277, 2011.
- S. Takashi, H. A. Goldberg, C. A. Feeney, D. P. Karim, M. Farrel, K. O’Leary, and D. R. Paul. Gas properties of butyl rubber/vermiculite nanocomposite coatings. *Polymer*, 47:3083–3093, 2006.
- P. Thomas, P. Sreekumar, A. Aprem, and S. Thomas. Poly(ethylene-co-vinyl acetate)/calcium phosphate nanocomposites: Mechanical, gas permeability, and molecular transport properties. *J. Appl. Polym. Sci.*, 120:1974–1983, 2011.
- A. Thornton, K. Nairn, A. Hill, and J. Hill. New relation between diffusion and free volume: Predicting gas diffusion. *J. Membr. Sci.*, 338:29–37, 2009.
- A. Thran and G. Faupel. Correlation between fractional free volume and diffusivity of gas molecules in glassy polymers. *J. Polym. Sci. Part B: Polym. Phys.*, 37:3344–3358, 1999.

- M. Tortora, V. Vittoria, G. Galli, S. Ritrovati, and E. Chiellini. Transport properties of modified montmorillonite-poly(ϵ -caprolactone) nanocomposites. *Macromol.Mater.Eng.*, 287:243–249, 2002.
- Y. Tsujita. Gas sorption and permeation of glassy polymers with microvoids. *Prog. Polym. Sci.*, 28:1377–1401, 2003.
- A. Usuki, N. Hasegawa, and M. Kato. Polymer-clay nanocomposites. *Adv.Polym.Sci.*, 179:135–195, 2005.
- R. Vaia, W. Liu, and H. Koerner. Analysis os small-angle scattering of suspensions of organically modified montmorillonite: implications to phase behavior of polymer nanocomposites. *J. Polym. Sci.: Part B: Polym. Phys.*, 41:3214–3236, 2003.
- L. Valadares, E. Linares, F. Braganca, and F. Galembeck. Electrostatic adhesion of nanosized particles: The cohesive role of water. *J. Phys. Chem. C*, 112:8534–8544, 2008.
- R. K. Venkata and S. Kattimuttathu. Oxygen barrier material for packaging, 2005. US2005145138, 07.07.2005.
- J. Villaluenga, M. Khayet, M. Lopez-Manchado, J. Valentin, B. Seoane, and J. Mengual. Gas transport properties of polypropylene/clay composite membrane. *Eur. Polym. J.*, 43:1132–1143, 2007.
- M. Vinay and K. Brian. Asphalt nanocomposite-based roofing products, 2007. WO2007109314, 27.09.2007.
- W. Wakeham and E. Mason. Diffusion through multiperforate lamninae. *Ind.Eng.Chem.Fundam.*, 18(4):301–305, 1979.
- S. Wang, L. Liu, P. Fang, Z. Chen, H. Wang, and S. Zhang. Microstructure of polymer-clay nanocomposites studied by positrons. *Radiation Physics and Chemistry*, 76: 106–111, 2007a.
- S. Wang, L. Liu, P. Fang, Z. Chen, H. Wang, and S. Zhang. Microstructure of polymer-clay nanocomposites studied by positrons. *Rad. Phys. Chem.*, 76:106–111, 2007b.
- X. Wang, Y. Du, J. Yang, X. Wang, and Y. H. Xiaowen Shi. Preparation, characterization and antimicrobial activity of chitosan/layered silicate nanocomposites. *Polymer*, 47 (19):6738–6744, 2006.
- Y. Wang, H. Nakanishi, and Y. Jean. Positron annihilation in amine-cured epoxy polymers-pressure dependence. *J.Polym.Sci.: PartB: Polym.Phys.*, 28:1431–1441, 1990.
- Y. Wang, Y. Wu, H. Zhang, B. Wang, and Z. Wang. Free volume of montmorillonite/styrene-butadiene rubber nanocomposites estimated by positron annihilation lifetime spectroscopy. *Macromol. Rapid Commun.*, 25:1973–1978, 2004.

- Z. Wang, B. Wang, Y. Yang, and C. Hu. Correlations between gas permeation and free-volume hole properties of polyurethane membranes. *Eur. Polym. J.*, 39:2345–2349, 2003.
- Z. Wang, B. Wang, N. Qi, H. Zhang, and L. Zhang. Influence of fillers on free volume and gas barrier properties in styrene-butadiene rubber studied by positrons. *Polymer*, 46:719–724, 2005.
- Z. Wicks, F. Jones, S. Pappas, and D. Wicks. *Organic Coatings: Science and Technology*. Wiley-Interscience, 2007.
- P. Winberg, M. Eldrup, and F. Maurer. Nanoscopic properties of silica filled poly-dimethylsiloxane by means of positron annihilation lifetime spectroscopy. *Polymer*, 45:8253–8264, 2004.
- P. Winberg, K. DeSitter, C. Dotremont, S. Mullens, I. Vankelecom, and F. Maurer. Free volume and interstitial mesopores in silica filled poly(1-trimethylsilyl-1-propyne) nanocomposites. *Macromolecules*, 38:3776–3782, 2005a.
- P. Winberg, M. Eldrup, N. Pedersen, M. Van Es, and F. Maurer. Free volume sizes in intercalated polyamide 6/clay nanocomposites. *Polymer*, 46:8239–8249, 2005b.
- B. Wong, Z. Zhang, and P. Handa. High precision gravimetric technique for determining the solubility and diffusivity of gases in polymers. *J. Polym. Sci. B: Polym. Phys.*, 36:2025–2032, 1998.
- J. Xiao, Y. Huang, and C. Manke. Computational design of polymer nanocomposite coatings: A multiscale hierarchical approach for barrier property prediction. *Ind. Eng. Chem. Res.*, 49:7718–7727, 2010.
- L. Xie, D. Gidley, H. Hristov, and A. Yee. Evolution of nanometer voids in polycarbonate under mechanical stress and thermal expansion using spectroscopy. *J. Polym. Sci. Part B: Polym. Phys.*, 33:77–84, 1995.
- A. Yano, A. Usuki, A. Okada, T. Karauchi, and O. Kamigaito. Synthesis and properties of polyimide-clay hybrid. *J. Polym. Sci. Part A: Polym. Chem.*, 31:2493–2499, 1993.
- J. Yeh, H. Huang, C. Chen, W. Su, and Y. Yu. Siloxane modified epoxy resin-clay nanocomposite coatings with advanced anticorrosive properties prepared by a solution dispersion approach. *Surf. Coat. Tech.*, 200:2753–2763, 2006.
- K. Yoon, H. Sung, Y. Hwang, S. Noh, and D. Lee. Modification of montmorillonite with oligomeric amine derivatives for polymer nanocomposite preparation. *Appl. Clay Sci.*, 2007.
- D. Yu, B. Wang, Y. Feng, and Z. Fang. Investigation of free volume, interfacial, and toughening behavior for cyanate ester/bentonite nanocomposites by positron annihilation. *J. Appl. Polym. Sci.*, 102:1509–1515, 2006.
- J. Zhang, M. Yang, and F. Maurer. Effect of TiO_2 formation on the free volume properties of electrospun PMMA nanohybrids. *Macromolecules*, 44:5711–5721, 2011.

- M. Zhang, P. Fang, S. Zhang, B. Wang, and S. Wang. Study of structural characteristics of HDPE/ $CaCO_3$ nanocomposites by positrons. *Rad. Phys. Chem.*, 68:565–567, 2003.
- Y. Zhong, D. Janes, Y. Zheng, M. Hetzer, and D. De Kee. Mechanical and oxygen barrier properties of organoclay-polyethylene nanocomposite film. *Polym. Eng. Sci.*, 47:1101–1107, 2007.

Appendix A

Solubility Parameter and Surface Tension Calculations

A.1 Solubility Parameter

The cohesive energy density (CED) of a substance is the ratio of the energy of vapourisation (E_{vap}) to its molar volume (V_m):

$$CED = \frac{E_{vap}}{V_m} . \quad (\text{A.1})$$

Thus, the solubility parameter (δ) can be written as

$$\delta = \left(\frac{\sum E_i}{\sum V_i} \right)^{1/2} , \quad (\text{A.2})$$

where E_i and V_i are the additive atomic and group contribution for the energy of vapourisation and molar volume respectively. These values are given in Table A.1, p. 156. The units of δ in this table are $(\text{cal}/\text{cm}^3)^{1/2}$ but can be converted to $(\text{MPa})^{1/2}$ by multiplying by the factor 2.0455.

- Example for the calculation of the solubility parameter of ethanol (CH_3CH_2OH)

Group	E_i (cal/mol)	V_i (cm ³ /mol)
1 CH_3	1125	33.5
1 CH_2	1180	16.1
1 OH	7120	10
Total	9425	59.6

$$\delta = \left(\frac{9425}{59.6} \right)^{1/2} = 12.6 \text{ cal/cm}^3 = 25.7 \text{ MPa}^{1/2}$$

- Calculation Example 2: Toluene, $C_6H_5CH_3$

Group	E_i (cal/mol)	V_i (cm^3/mol)
1 CH_3	1125	33.5
5 - CH =	5·1030	5·13.5
1 - C =	1030	-5.5
1 ring closure 5 or more atoms	250	16
3 for each double bond in ring	3·400	3·(-2.2)
Total	8755	104.9

$$\delta = \left(\frac{8755}{104.9} \right)^{1/2} = 9.14 \text{ cal/cm}^3 = 18.7 \text{ MPa}^{1/2}$$

In the literature, Hansen's solubility parameter is often used instead of Hildebrand's. This parameter is based on the fact that the total energy of vaporisation of a liquid consists of several individual contributions. These arise from dipole-dipole forces, dispersion forces, and hydrogen bonding. Thus, the Hansen solubility parameter is defined as:

$$\delta = \sqrt{\delta_P^2 + \delta_D^2 + \delta_H^2}, \quad (\text{A.3})$$

where δ_P , δ_D , δ_H are the polar, dispersive and hydrogen bonding contributions, respectively. Although, the two above solubility parameters should coincide, this is not always the case and there may be some discordance between the above calculated values with those from the literature.

A.2 Surface Tension

The relation between the surface tension and the density of a liquid was found to be

$$\gamma = C(D - d)^4, \quad (\text{A.4})$$

where D and d are the densities of the liquid and its vapour while C is a constant characteristic of the liquid. This equation was revised to express the equivalence of the constant in molar proportions and called the parachor. The revised equation has the form

$$P' = \gamma^{1/4} \frac{M}{D - d}, \quad (\text{A.5})$$

where M is the molecular weight. When the vapour density is small in comparison with that of the liquid, the above relation becomes

$$P' = V_m \gamma^{1/4}, \quad (\text{A.6})$$

The molecular parachor, P' , depends on the chemical composition and it is an additive function. It has been found that:

- P' can be reproduced by adding together two sets of constants: one for the atoms in the molecule; and another for the unsaturated bonds or ring closure.
- The values for a particular atom is independent of the manner in which it is situated.
- The values for an individual element are the same from compound to compound.

The surface tension γ can be then calculated by a group contribution method using the values of tables A.1, A.2 and the relation [Quayle, 1953]:

$$\gamma = \left(\frac{P'}{V_m} \right)^4 , \quad (\text{A.7})$$

where P' can be calculated from the values of table A.2 and V_m is the molar volume which is calculated from the values of table A.1 or by the relation $V_m = M/\rho$, with M the molecular mass (g/mol) and ρ the density (g/cm³).

- Calculation Example of the surface tension of o-Xylene, $C_6H_4(CH_3)_2$

Group	V_i (cm ³ /mol)
2 CH_3	2 · 33.5
4 $-CH =$	4 · 13.5
2 $-C =$	2 · (-5.5)
1 ring closure 5 or more atoms	16
3 for each double bond in ring	3 · (-2.2)
Total	119.4

Group	P_s (cm ³ /mol) × (mJ/m ²) ^{1/4}
8 C	8 · 9.0
10 H	10 · 15.5
six-membered ring	0.8
3 double bonds	3 · 17.5
Total	280.3

$$\gamma = \left(\frac{280.3}{119.4} \right)^4 = 30.4 \text{ mN/m}$$

Table A.1: Atomic and group contributions to the energy of vaporization and the molar volume at 25°C [Fedors, 1974].

Atom or group	E_i (cal/mol)	V_i (cm ³ /mol)
CH_3	1125	33.5
CH_2	1180	16.1
CH	820	-1.0
C	350	-19.2
$H_2C =$	1030	28.5
$-CH =$	1030	13.5
$C =$	1030	-5.5
$HC \equiv$	920	27.4
$-C \equiv$	1690	6.5
$COOH$	6600	28.5
COO	4300	18.0
CO	4150	10.8
CHO	5100	22.3
$CONH_2$	10000	17.5
NH_2	3000	19.2
NH	2000	4.5
N	1000	-9.0
$-N =$	2800	5.0
O	800	3.8
OH	7120	10.0
Ring closure 3 or 4 atoms	750	18
Ring cl. 5 or more atoms	250	16
conjug. in ring for each dbl bond	400	-2.2

Table A.2: Atomic and structural contributions to the Parachor [Quayle, 1953].

Unit	Value $(cm^3/mol) \times (mJ/m^2)^{1/4}$
C	9.0
$-(CH_2)_n$ for $n < 12$	40.0
$-(CH_2)_n$ for $n > 12$	40.3
H	15.5
H in OH	10.0
H in NH	12.5
O	19.8
O_2 (in esters)	54.8
N	17.5
S	49.1
F	26.1
Cl	55.2
Br	68.0
I	90.3
Carbonyl bond (acetone)	20.0
Double bond	16.3-19.1
Triple bond	40.6
Four-membered ring	6.0
Five-membered ring	3.0
Six-membered	0.8

Appendix B

Sample codes and solvent characteristics

Table B.1: Clays and resins used in this work

sample	density g/cm ³	d-spacing Å	characteristics
Acrylic Rsn.	1.040	-	resin
PU Rsn.	1.100	-	resin
Laponite	2.600	-	powder
Bentonite	2.600	14.1	powder
Hectorite	2.600	12.0	powder
mod. bentonite	1.710	21.7	powder
MMT, C25A	1.870	24.7	powder
MMT, C93A	1.880	26.1	powder
MMT, C20A	1.770	24.2	powder
MMT, C10A	1.900	19.3	powder
MMT, C30B	1.980	18.5	powder

Table B.2: Solvents characteristics

solvent	density g/cm ³	δ MPa ^{1/2}	γ mN/m	B.P. °C
Water	1.000	48	59	100
Acetone	0.791	20.7	22.4	57
Ethanol	0.789	25.7 -	23.2	78

Table B.3: Nano-composites sample codes used throughout this work.

sample	composition vol%	density g/cm ³	membr. thickns. mm	characteristics
Acrylic resin/laponite nanocomposites				
L0	0.00	1.040	0.73 ± 0.15	pure acr. resin
L1	0.5	1.045	0.43 ± 0.03	in water
L2	2	1.053	0.74 ± 0.11	in water
L3	4.5	1.07	0.84 ± 0.10	in water
Acrylic resin/bentonite nanocomposites				
B0	0	1.040	1.03 ± 0.06	pure acr. resin
B1	0.75	1.045	0.83 ± 0.04	in water
B2	0.875	1.046	0.78 ± 0.07	in water
B3	1.5	1.05	0.75 ± 0.05	in water
B 4	2.25	1.054	0.95 ± 0.08	in water
B5	3.125	1.06	0.59 ± 0.05	in water
B 6	5	1.072	0.51 ± 0.08	in water
Acrylic resin/hectorite nanocomposites				
1U	0.34	1.0453	0.71	ultrasonic trtmnt.
2U	0.67	1.0505	0.69	ultrasonic trtmnt.
3U	1.16	1.0582	0.70	ultrasonic trtmnt.
4U	3.70	1.100	0.375	ultrasonic trtmnt.
1W	0.34	1.0453	0.914	no ultrasonic trtmnt.
2W	0.50	1.0478	0.79	no ultrasonic trtmnt.
3W	0.88	1.0537	0.75	no ultrasonic trtmnt.
4W	1.33	1.061	0.56	no ultrasonic trtmnt.
5W	1.77	1.068	0.633	no ultrasonic trtmnt.
1B	0.34	1.0453	0.91	ultrasound bath
2B	0.50	1.0478	1.02	ultrasound bath
3B	0.88	1.0537	1.00	ultrasound bath
Acrylic resin/modified montmorillonite nanocomposites				
OMBE0	0	1.040		pure acr. resin
OMBE1	0.50	1.043	0.964 ± 0.042	OMBE in <i>EtOH</i>
OMBE2	0.75	1.045	0.713 ± 0.047	OMBE in <i>EtOH</i>
OMBE 3	1.00	1.047	0.71 ± 0.04	OMBE in <i>EtOH</i>
OMBE 4	1.23	1.048	0.75 ± 0.08	OMBE in <i>EtOH</i>
OMBE 5	1.50	1.050	0.654 ± 0.046	OMBE in <i>EtOH</i>
C25A1	0.16	1.041	0.778 ± 0.039	C25A in <i>EtOH</i>
C25A2	0.32	1.043	0.716 ± 0.52	C25A in <i>EtOH</i>
C25A3	0.48	1.044	0.656 ± 0.049	C25A in <i>EtOH</i>
C25A4	0.63	1.045	0.567 ± 0.046	C25A in <i>EtOH</i>
C25A5	0.74	1.046	0.615 ± 0.051	C25A in <i>EtOH</i>
C93A1	0.10	1.040	0.80 ± 0.05	C93A in <i>EtOH</i>
C93A2	0.25	1.042	0.70 ± 0.04	C93A in <i>EtOH</i>
C93A3	0.39	1.043	0.67 ± 0.05	C93A in <i>EtOH</i>
C93A4	0.60	1.045	0.64 ± 0.06	C93A in <i>EtOH</i>
C93A 5	0.80	1.047	0.557 ± 0.047	C93A in <i>EtOH</i>

Appendix C

Permeation Measurements

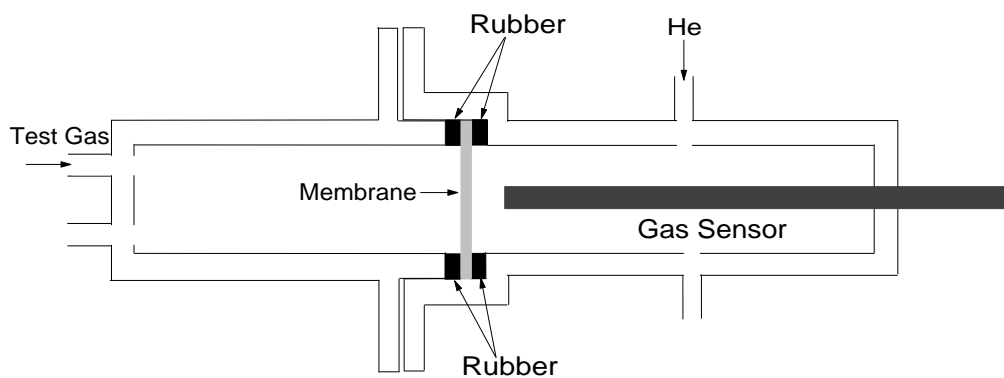


Figure C.1: The experimental permeation cell used in this work.

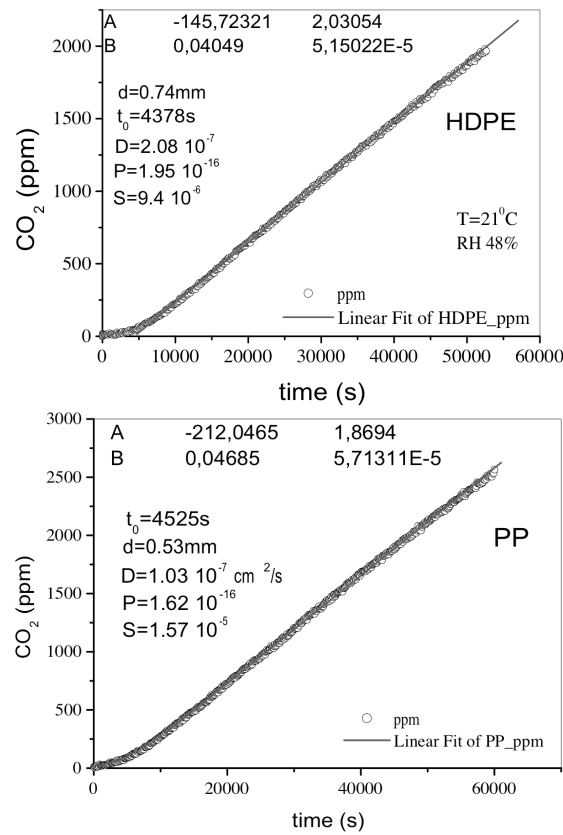
C.1 Test measurements

In order to ensure the accuracy of the permeation device various known samples were tested like high density polyethylene (HDPE), low density polyethylene (LDPE), polypropylene (PP) and polyimide (PI). The polyolefins samples were prepared on a hydraulic heated press while the LDPEclay sample was prepared in the single screw extruder using organo-modified bentonite clay at 1 wt%. Some values of the carbon dioxide transport coefficients from the literature for HDPE are $D = 4 \cdot 10^{-7} \text{ cm}^2/\text{s}$, $P = 2.46 \cdot 10^{-15} \text{ mol/m s Pa}$, $S = 6.25 \cdot 10^{-5} \text{ mol/m Pa}$ at 40°C and for LDPE $D = 6.7 \cdot 10^{-7} \text{ cm}^2/\text{s}$, $P = 9.82 \cdot 10^{-15} \text{ mol/m s Pa}$, $S = 1.47 \cdot 10^{-4} \text{ mol/m Pa}$ at 40°C [Flaconneche et al.,

2001]. These values are somewhat higher than what we measured in our permeation cell but this is mainly due to the higher temperature of measurement. For the PI the carbon dioxide diffusion coefficient is in the range of $2.1 \cdot 10^{-9} - 4 \cdot 10^{-11} \text{ cm}^2/\text{s}$ [Tsujita, 2003] which is in agreement with those extracted from the permeation cell at 17°C .

The significant lower values of the solubility coefficients of these polymers compared to the acrylic resin samples are due to the influence of crystallinity. The acrylic resin is an amorphous polymer while HDPE, LDPE and PP are semi-crystalline polymers with a crystallinity degree of the order of 50% or above. The crystalline phase does not contribute to the gas solubility as the amorphous phase does. From the other hand, the crystalline phase acts as a gas barrier affecting the diffusion coefficient. However, the diffusion coefficient of the polyolefins is higher than that of the amorphous acrylic resin. This is due to the influence of the free volume: The glassy acrylic resin has significant lower free volume than that of the amorphous part of the polyolefins.

C.2 Nanocomposites



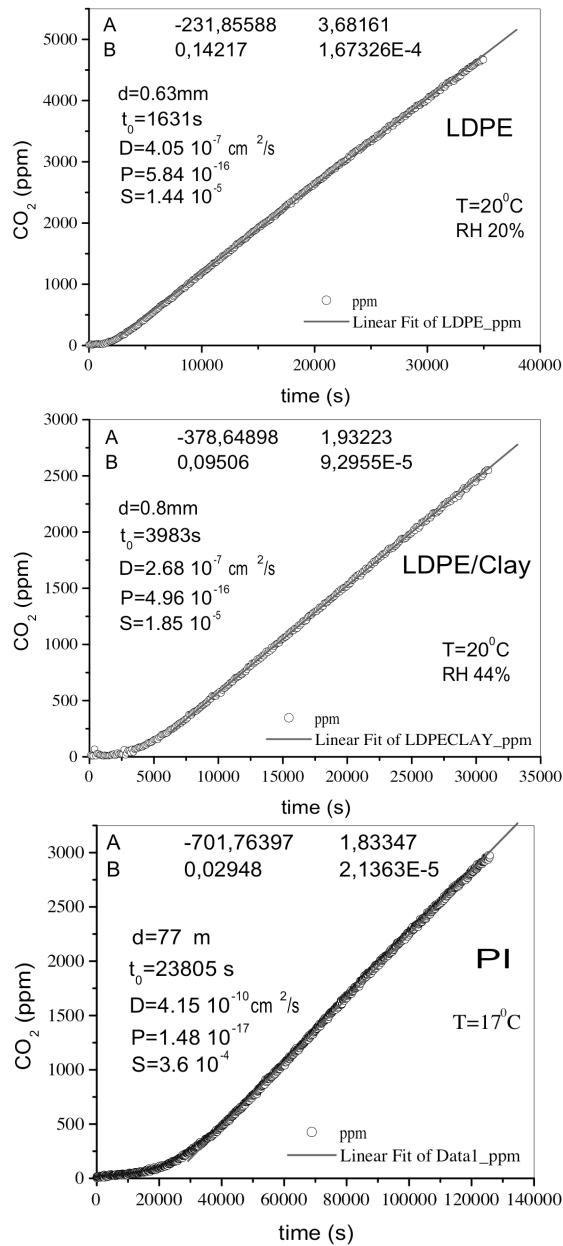
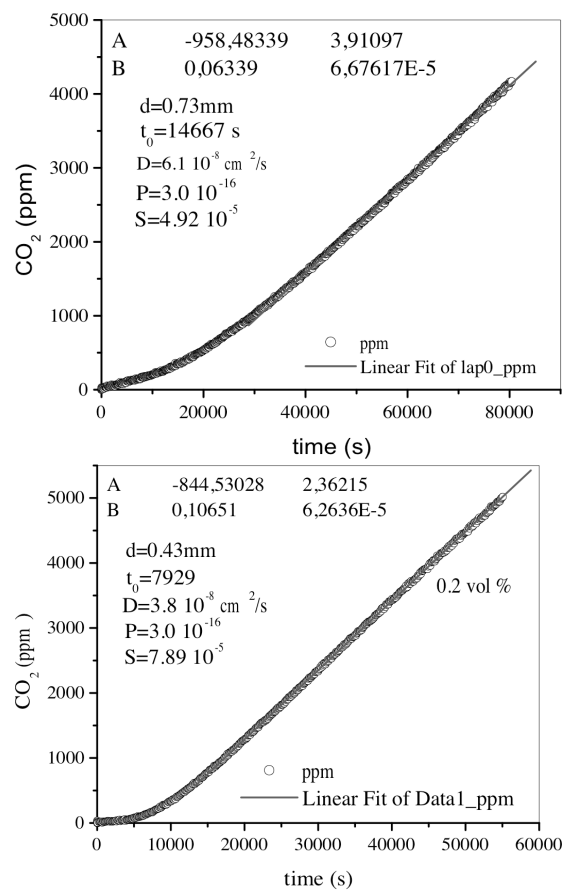


Figure C.2: Carbon dioxide permeation curves for various common polyolefins and polyimide. The coefficients A and B from the linear fitting of the steady state line ($y = -A + Bx$) are shown. The membrane thickness d , the time lag $t_0 = A/B$, and the values of the three transport coefficients are also shown. The diffusion coefficient was calculated by the relation $D = d^2/6t_0$, the permeability coefficient by the slope B of the line as $P = 6.52 \cdot 10^{-12} \cdot B \cdot d$ and the solubility coefficient by the relation $S = P/D$. The units of the diffusion coefficient is cm^2s^{-1} of the solubility coefficient are $\text{mol m}^{-3} \text{Pa}^{-1}$ and of the permeability coefficient are $\text{mol m}^{-1} \text{s}^{-1} \text{Pa}^{-1}$.



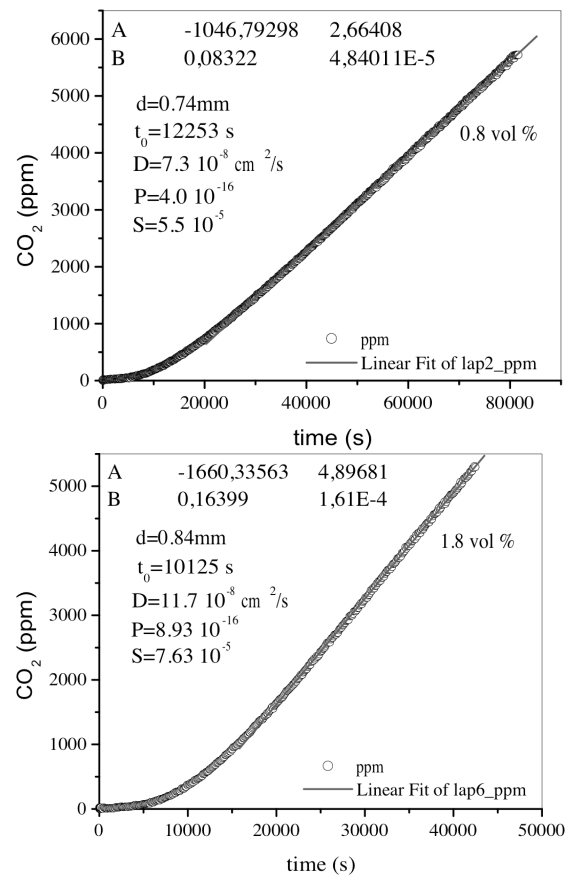
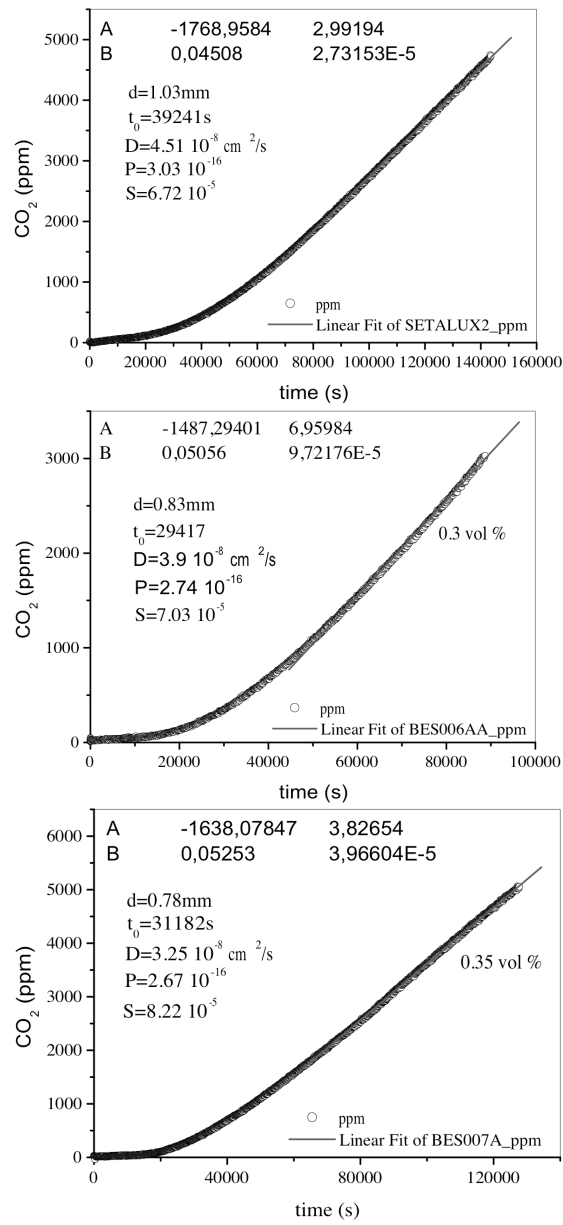


Figure C.3: Carbon dioxide permeation curves for the Acrylic resin/Laponite nanocomposites coatings. The diffusion, solubility and permeability coefficients are estimated as in Fig. C.2.



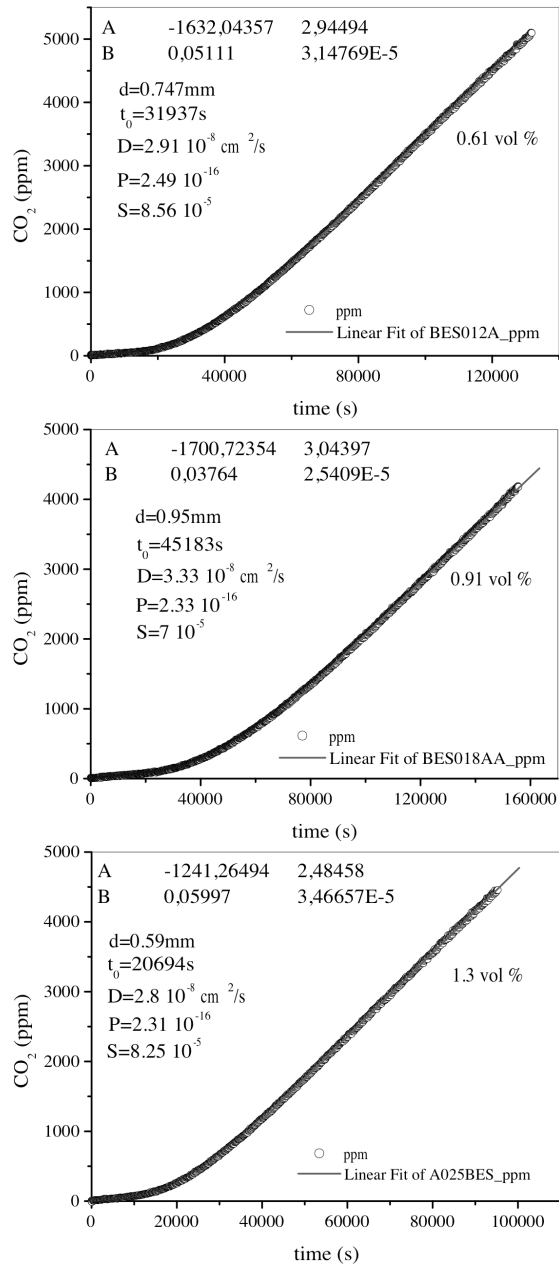
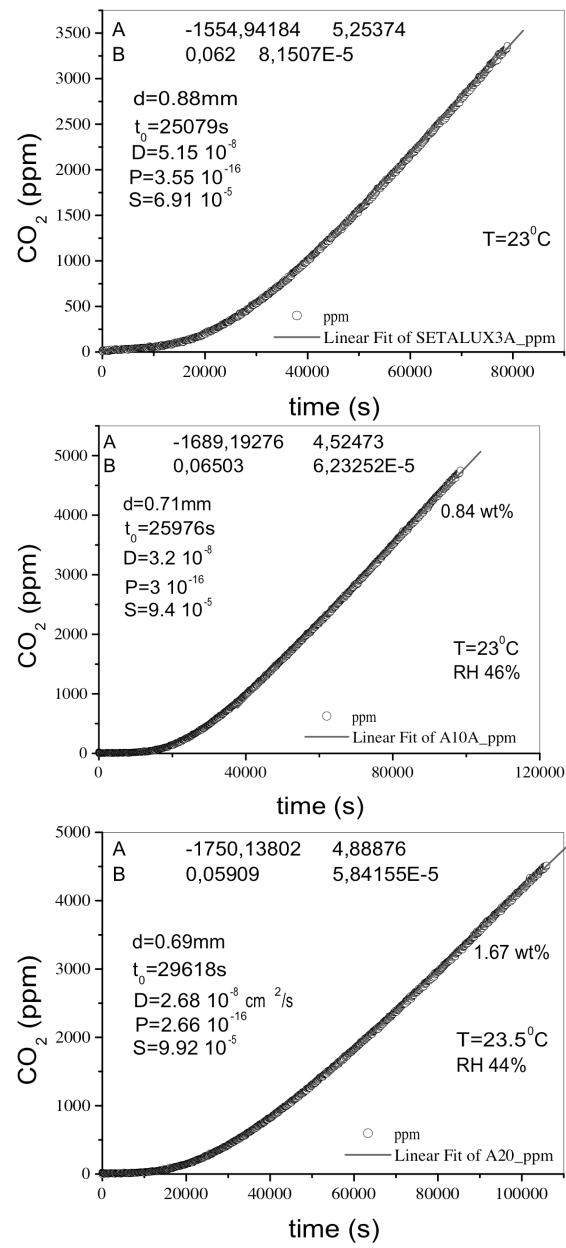


Figure C.4: Carbon dioxide permeation curves for the Acrylic resin/Bentonite nanocomposites coatings. The diffusion, solubility and permeability coefficients are estimated as in Fig. C.2.



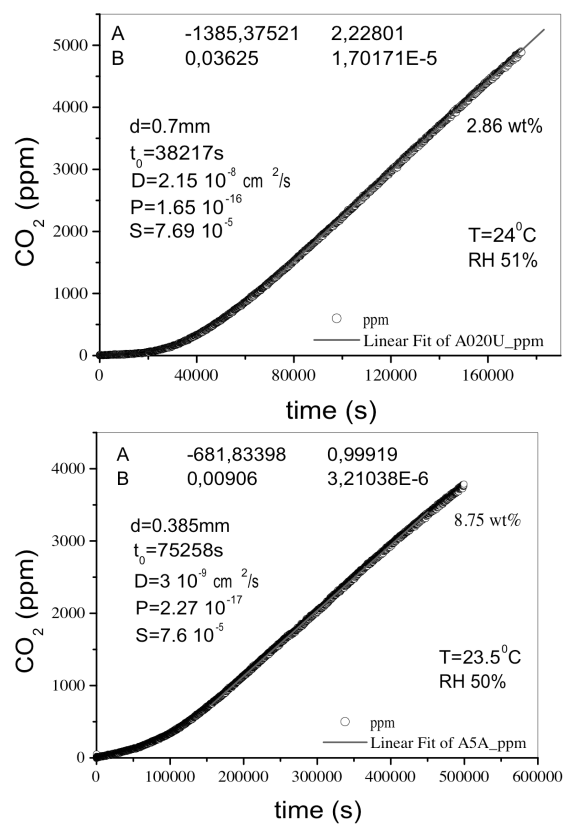
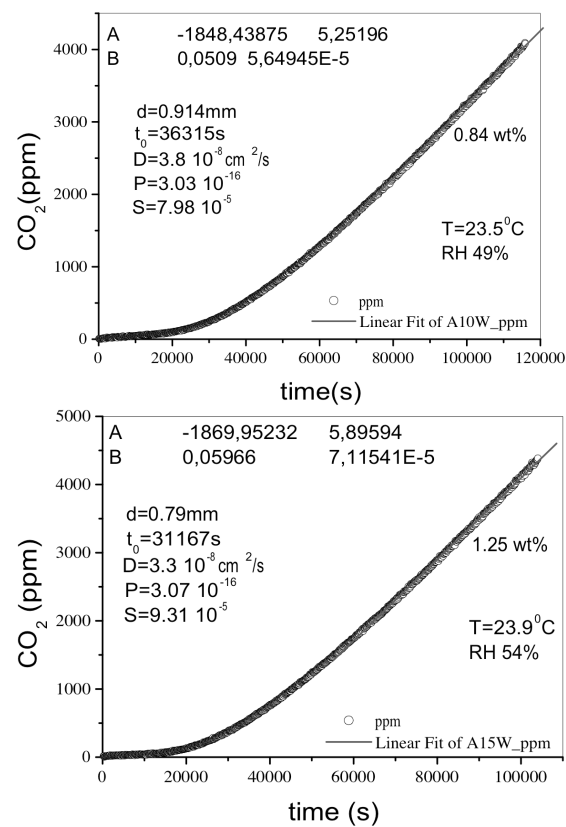


Figure C.5: Carbon dioxide permeation curves for the Acrylic resin/Hectorite nanocomposites coatings that were treated by ultrasonication. The diffusion, solubility and permeability coefficients are estimated as in Fig. C.2.



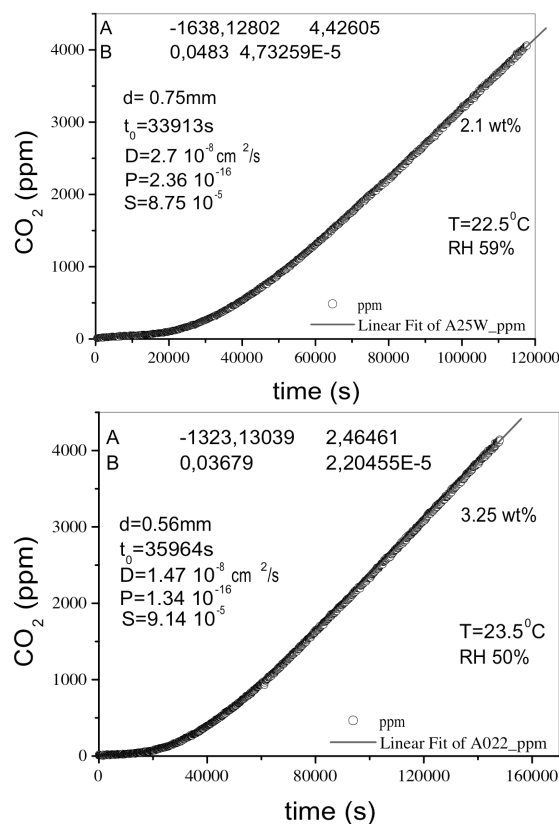


Figure C.6: Carbon dioxide permeation curves for the Acrylic resin/Hectorite nanocomposites coatings that were not ultrasonicated. The diffusion, solubility and permeability coefficients are estimated as in Fig. C.2.

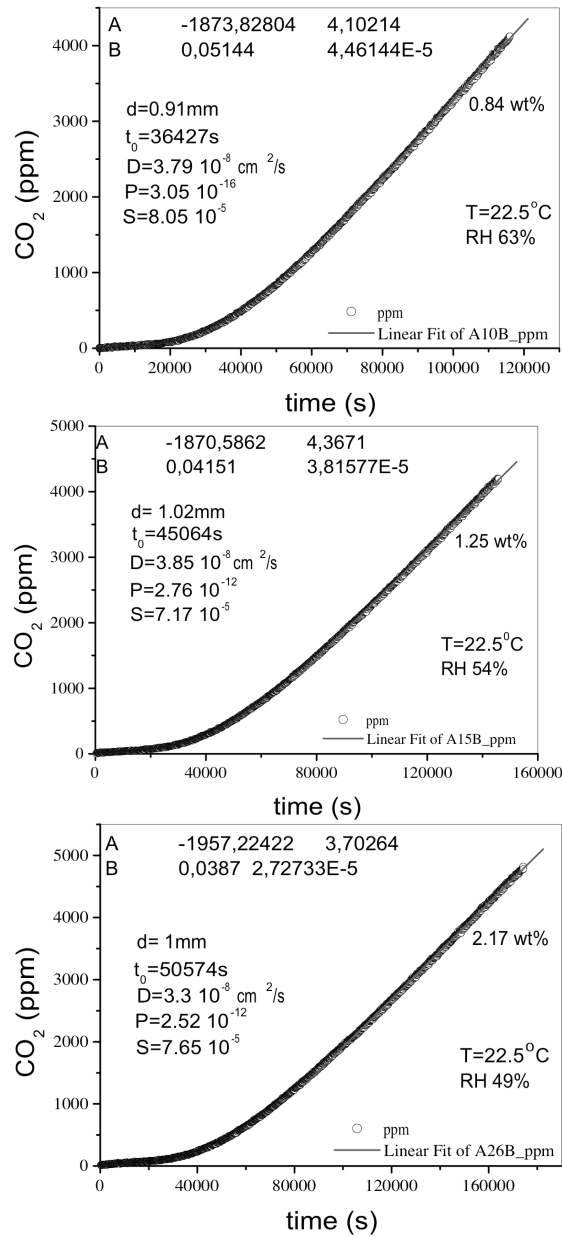
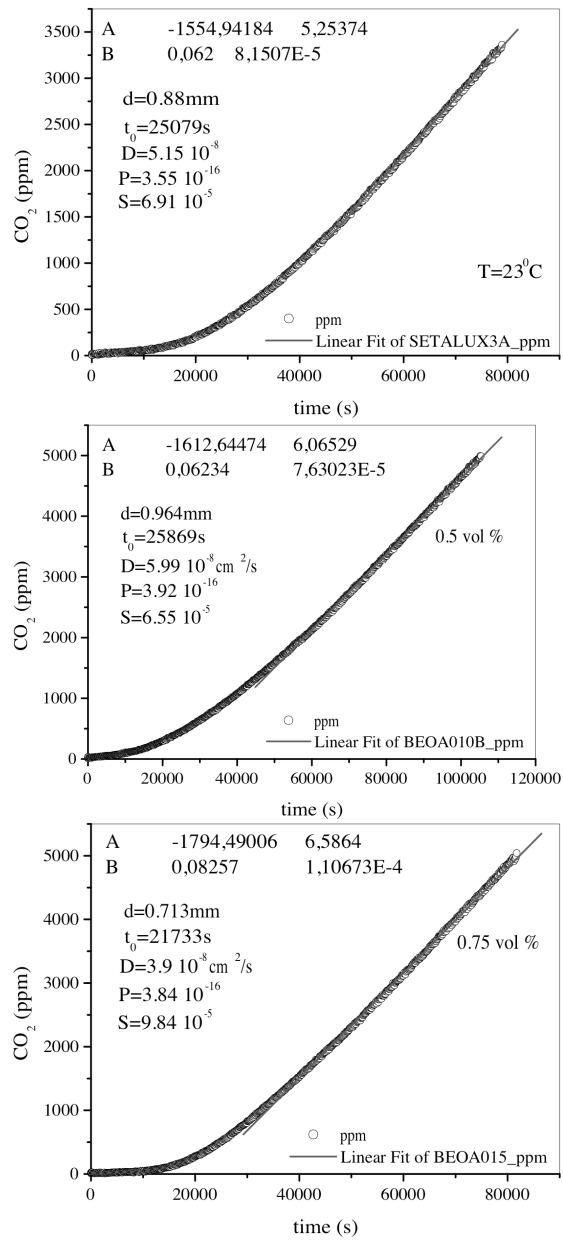


Figure C.7: Carbon dioxide permeation curves for the Acrylic resin/Hectorite nanocomposites coatings that were treated in an ultrsonication bath at the University of Bayreuth. The diffusion, solubility and permeability coefficients are estimated as in Fig. C.2.



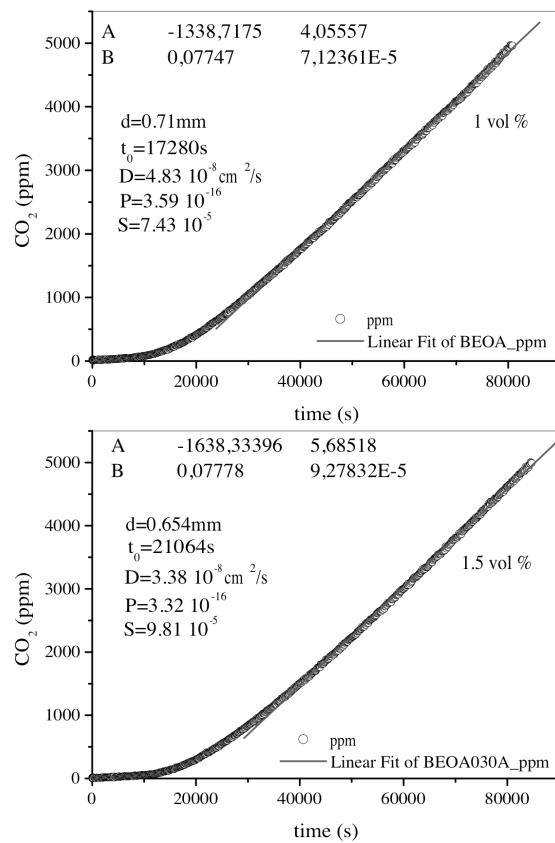
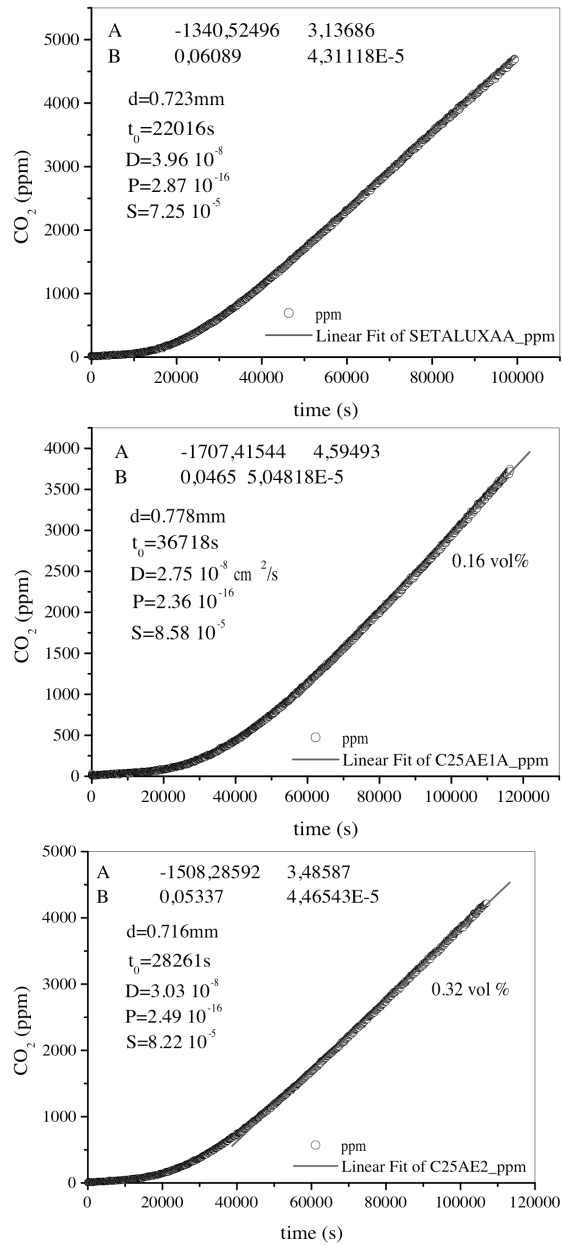


Figure C.8: Carbon dioxide permeation curves for the Acrylic resin/organo-modified Bentonite nanocomposites coatings. The diffusion, solubility and permeability coefficients are estimated as in Fig. C.2.



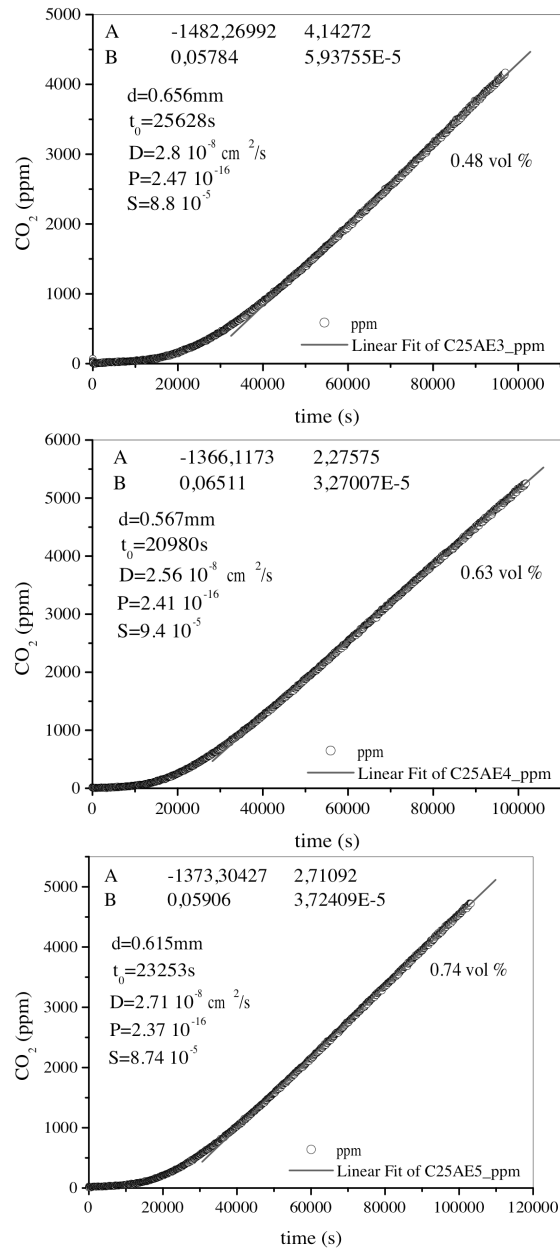
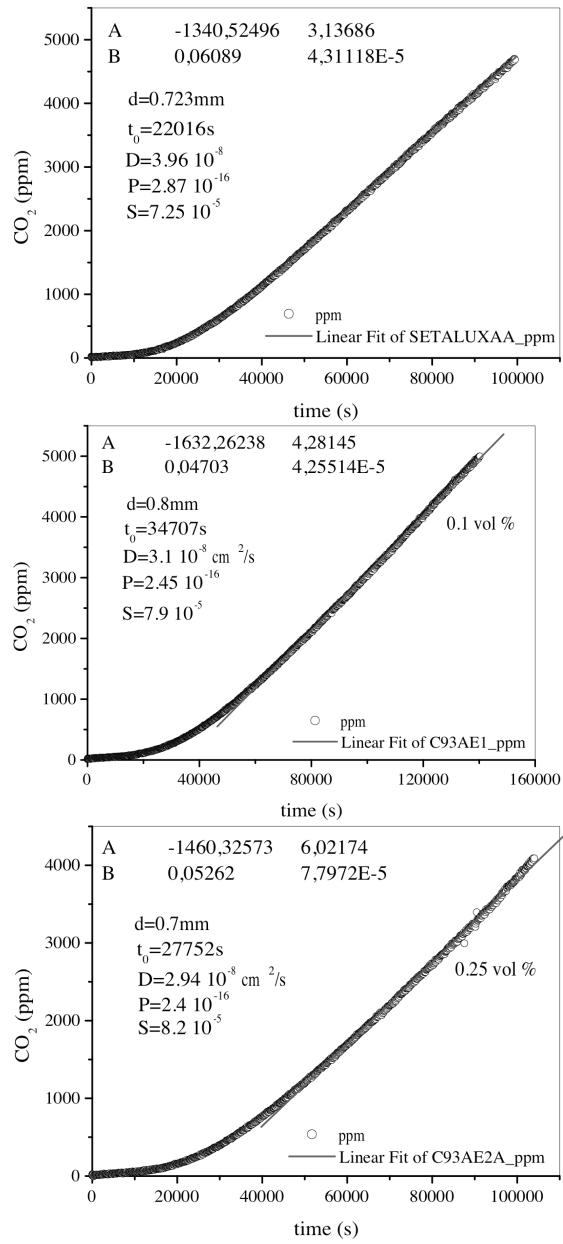


Figure C.9: Carbon dioxide permeation curves for the Acrylic resin/organo-modified montmorillonite C25A nanocomposites coatings. The diffusion, solubility and permeability coefficients are estimated as in Fig. C.2.



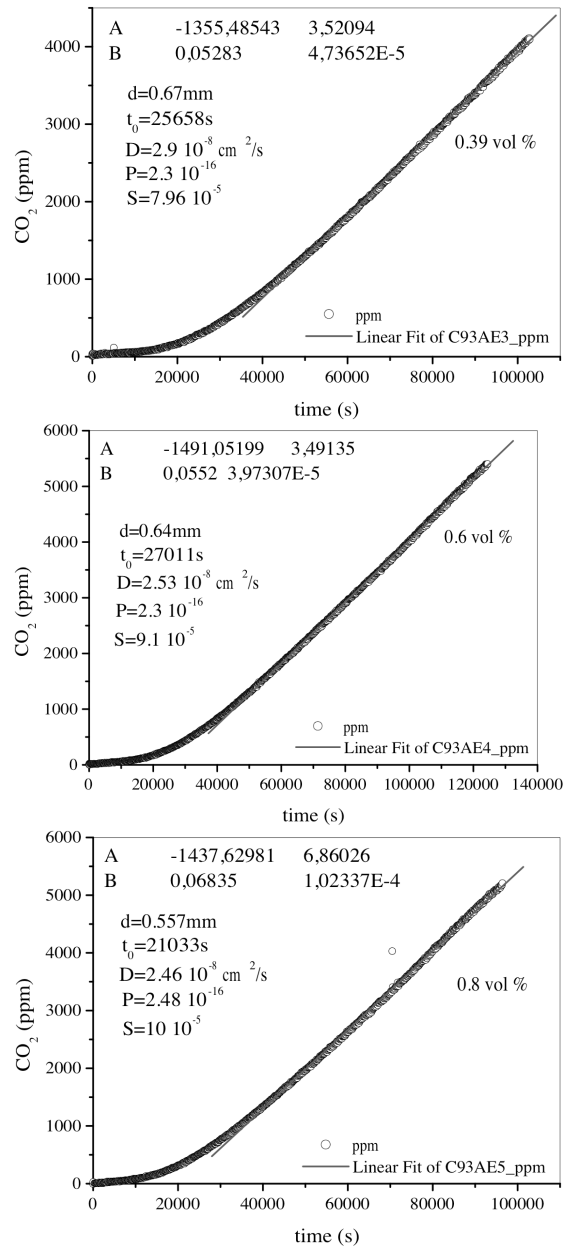


Figure C.10: Carbon dioxide permeation curves for the Acrylic resin/organo-modified montmorillonite C93A nanocomposites coatings. The diffusion, solubility and permeability coefficients are estimated as in Fig. C.2.

List of Tables

6.1	Particle mass and volume fractions, nanocomposite density, membrane thickness and standard deviation values for the tested samples.	78
6.2	The coefficients D , S and K from the permeability measurements and the fractional free volume V_f as it was calculated from PALS data, for nanocomposite samples.	86
7.1	Characteristics of the samples. In order to estimate the error on the membranes thickness, a micrometer was used and measurements of the thickness of each membrane were performed at ten random points.	90
7.2	CO_2 gas transport coefficients of the samples at $14^{\circ}C$ and 50 % rel. humidity measured in the permeability cell.	94
8.1	Characteristics of the samples containing hectorite nanoparticles. The letter U in the code denotes samples treated with ultrasound, W denotes samples without any treatment and B denotes samples treated in an ultrasound bath. The volume fractions, the densities and the membrane thicknesses were calculated in the same way as reported in the previous chapters.	102
9.1	Modifier content, cation exchange capacity (CEC), density and d-spacing of various types of organo-modified and hydrophilic montmorillonites. BE denotes hydrophilic bentonite while OMBE is the modified bentonite with octadecylamine.	116
9.2	Various surfactants used in organo-modified montmorillonites.	117
9.3	Characteristics of the nanocomposite samples containing organo-modified bentonite (OMBE) that was initially dispersed in ethanol.	118
9.4	Characteristics of the nanocomposite samples containing organo-modified montmorillonite (C25A) that was initially dispersed in ethanol.	118
9.5	Characteristics of the nanocomposite samples containing organo-modified montmorillonite (C93A) that was initially dispersed in ethanol.	118

9.6	Solubility parameters and surface tensions of some solvents and the organic modifiers of the clay particles. Values were taken from Burgentzle et al. [2004]; Heinz et al. [2006]; Ho and Glinka [2003]; Krikorian and Pochan [2003]. δ_{lit} , γ_{lit} is referred to values from the literature while δ_{calc} , γ_{calc} values are based on calculation via the group contribution method proposed by Fedors [1974] and Quayle [1953].	120
9.7	CO_2 gas transport coefficients at 23 °C and 50 % rel. humidity of the samples containing OMBE, measured in the permeation cell.	129
9.8	CO_2 gas transport coefficients of the samples containing (C25A) at 13 °C and 50 % rel. humidity measured in the permeability cell.	129
9.9	CO_2 gas transport coefficients at 13 °C and 50 % rel. humidity of the samples containing C93A, measured in the permeability cell.	130
A.1	Atomic and group contributions to the energy of vaporization and the molar volume at 25°C [Fedors, 1974].	156
A.2	Atomic and structural contributions to the Parachor [Quayle, 1953].	157
B.1	Clays and resins used in this work	160
B.2	Solvents characteristics	160
B.3	Nano-composites sample codes used throughout this work.	161

List of Figures

1	Διαχωρισμός των κρυσταλλικών επιπέδων του αρχικού συστοματώματος.	3
2	Σχηματική αναπαράσταση του κελιού διαπερατότητας. Η μεμβράνη πάχους d και επιφάνειας A χωρίζει το κελί σε δύο τμήματα. Το αέριο εισάγεται στο αριστερό τμήμα, όγκου V_0 , υπό πίεση 1 atm. Η συγκέντρωση του αερίου που διαπερνά τη μεμβράνη $c_d(t)$ καταγράφεται (στο δεξιό τμήμα) σαν συνάρτηση του χρόνου.	6
3	(a) Θεωρητική καμπύλη της συγκέντρωσης του αερίου που διαπερνά τη μεμβράνη συναρτήσει του χρόνου ϵ . 6. Το γραμμικό τμήμα είναι η ευθεία σταθερής κατάστασης. (b) Πειραματική καμπύλη μεμβράνης από νανοσύνθετο πολυμερές μετρημένο στο κελί διαπερατότητας.	7
4	Η ιδανική περίπτωση ορθογωνίων διεσπαρμένων πλακιδίων σε περιοδική διάταξη με τις επιφάνειες τους κάθετες στη διεύθυνση διάχυσης.	8
5	Τιμές της παραμέτρου τάξης S' για τρεις διαφορετικούς προσανατολισμούς των νανοσωματιδίων.	9
6	Συντελεστής διαλυτότητας (S), κλασματικός ελεύθερος όγκος (FFV), σχετική διαπερατότητα (P_{comp}/P_{matrix}) και σχετική διαχυτότητα (D_{comp}/D_{matrix}) συναρτήσει του κλάσματος όγκου των νανοσωματιδίων.	15
7	Συντελεστές μεταφοράς μάζας για το νανοσύνθετο ακρυλική ρητίνη/μπεντονίτης συναρτήσει του κλάσματος όγκου των νανοσωματιδίων.	17
8	Συντελεστές μεταφοράς μάζας για το νανοσύνθετο ακρυλική ρητίνη/εκτορίτης συναρτήσει του κλάσματος όγκου των νανοσωματιδίων.	20
1.1	The crystal structure of the phyllosilicates [Ray and Okamoto, 2003].	28
1.2	Delamination of the primary mineral particles into individual nanolayers. The layers are located on top of each other like the pages of a book. The Van der Waals gaps between the layers, are called galleries.	28
1.3	Schematic of an alkylammonium cation [Holmberg et al., 2002].	29
1.4	Schematic representation of three types of polymer/clay nanocomposites [Ray and Okamoto, 2003].	30
1.5	Schematic representation of a stabilised colloidal droplet [Holmberg et al., 2002].	32
2.1	Schematic representation of the permeation cell. The gas diffuses through the membrane separating the two chambers [Rogers et al., 1954; Choudalakis and Gotsis, 2009].	35

2.2	The three sorption isotherms.	36
2.3	(a) The theoretical curve of the concentration of the gas that permeates the membrane as a function of time based on eq. 2.17. The linear part is the steady state line. (b) Experimental curve for a nanocomposite membrane measured by the permeation cell procedure.	38
2.4	Plot of M_t/M_{eq} as a function of \sqrt{t}/d . The characteristic time $t_{1/2}$ is the half time for sorption and corresponds to the initial linear part of the curve.	40
3.1	The ideal case of rectangular nano-platelets dispersed in a periodical arrangement perpendicular to the diffusion direction.	44
3.2	The 2D diffusion case. Rectangular dispersed nano-platelets in a periodical arrangement perpendicular to the diffusion direction. Some characteristic dimensions are shown.	46
3.3	The dilute regime where the distances of the disks exceed R . The semi-dilute regime where the disks are overlapped.	48
3.4	Values of the order parameter S' for three orientations of the particles [Bharadwaj, 2001].	50
3.5	Degrees of delamination of clay layers [Bharadwaj, 2001].	51
3.6	(a) Relative permeability as a function of clay mass fraction for an epoxy resin/MMT system for two different gases [Yeh et al., 2006]. (b) Oxygen relative permeability as a function of clay mass fraction for the same particles dispersed in different matrices [Zhong et al., 2007].	54
3.7	(a) Oxygen relative permeability as a function of clay volume fraction for an Ethylene Vinyl Acetate/MMT and Polypropylene/EPDM/MMT nanocomposites and the fitted model of Nielsen.(b) Carbon dioxide relative permeability as a function of clay volume fraction for a Polyethylene/MMT and Butyl Rubber/Vermiculite nanocomposite. The curves are the Nielsen equation fittings for the selected values of aspect ratio.	55
4.1	Definition of the excess free volume [Hiltner et al., 2005].	59
4.2	Schematic representation of the diffusion process of a gas molecule through a polymer.	63
4.3	Schematic representation of the diffusion process of a gas molecule through a polymer/clay nanocomposite.	65
5.1	The process from the time of positron implantation to the time of Ps annihilation.	71
5.2	Positron Annihilation Lifetime Spectrum and the extrapolation of the lifetimes for the three processes.	71
5.3	Tao-Eldrup model.	72
5.4	Doppler broadening of the 511 keV annihilation line. The S_1 -parameter is defined as the ratio of the central peak area P to the total area T , while the W -parameter is defined as the ratio of the tails ($W_1 + W_2$) area to the total peak area.	75

5.5	Free volume as a function of clay mass fraction for a PVA/MMT nanocomposite	76
6.1	Experimental PALS set-up. The source is located between two pieces of the sample.	79
6.2	Time evolution of the gas concentration in the chamber of the cell where the sensor is present. The time lag, t_L , and the place where the slope is taken are shown. The measurement corresponds to the sample 0.2 v/v%.	80
6.3	X ray diffraction patterns for the samples containing 0, 0.2, 0.8 and 1.8 % v/v laponite particles.	81
6.4	Power law behaviour at low angles for the samples 0.2, 0.8 and 1.8 % v/v.	82
6.5	Intermediate lifetime τ_2 , o-Ps lifetime τ_3 , and the relative intensities I_2 and I_3 , as functions of laponite particle volume fraction.	83
6.6	The ratio of the Doppler broadening parameters S_1/W as function of the laponite particle volume fraction.	85
6.7	The solubility coefficient, measured by the permeability measurements, as a function of the clay volume fraction.	87
7.1	X-ray results for acrylic resin nanocomposite samples containing different volume fractions of untreated bentonite, increasing in the direction of the arrow. The curves are shifted vertically for clarity and to facilitate the comparison.	91
7.2	Low angles plot of $\log[I(q)q^2]$ versus q^2 for the sample containing 0.35 vol% of bentonite particles. The slope, m , of the straight line is -0.29 nm ²	93
7.3	X-ray diffraction patterns (vertically shifted) for two samples (1.3 and 2.1 vol% BT) hardened at different temperatures.	93
7.4	Gas transport coefficients of the acrylic resin/bentonite nanocomposite as a function of clay volume fraction.	95
7.5	X-ray diffraction pattern for a polyurethane/bentonite nanocomposite sample containing 0.6 vol% particles.	98
8.1	X-ray diffractograms of 0, 0.35, 0.5, 0.67 and 100 wt% acrylic resin / hectorite nanocomposite samples treated with an without ultrasonication.	103
8.2	Transport coefficients for the acrylic resin/hectorite nanocomposite samples treated for 30 min in an ultrasound bath, as a function of clay particles loading at 23 °C. The permeation curves are given in the Appendix.	105
8.3	Transport coefficients at 23 °C, for the acrylic resin/hectorite nanocomposite samples without any ultrasonic treatment, as a function of clay particles loading. The permeation curves are given in the Appendix.	106
8.4	Transport coefficients at 23°C for the acrylic resin/hectorite nanocomposite samples treated with a high energy ultrasonication probe, as a function of clay particles loading. The permeation curves are given in the Appendix.	107

8.5	Permeation curves for two samples before and after heating at 120°C.	109
8.6	o-Ps lifetime and relative intensity for the acrylic resin/hectorite nano-composite samples with (15 min) and without ultrasonication treatment as a function of hectorite volume fraction.	111
9.1	The concept of clay/organic matrix compatibilisation	116
9.2	X-ray results for different organo-modified montmorillonites dispersed in acetone and then mixed with the acrylic resin aqueous dispersion to make the coatings. The line corresponds to the nanocomposite and the symbols to the OMMT powder.	123
9.3	X-ray results for different organo-modified montmorillonites dispersed in ethanol and then mixed with the acrylic resin aqueous dispersion. The line corresponds to the nanocomposite and the symbols to the OMMT powder.	125
9.4	X-ray results for different volume fractions of organo-modified montmorillonites (a) OMBE, (b) C25A and (c) C93B, dispersed in ethanol and then mixed with the acrylic resin aqueous dispersion.	126
9.5	Carbon dioxide transport coefficients as a function of OMBE clay volume fraction. The measurements were performed in the permeation cell at 23°C.	128
9.6	Carbon dioxide transport coefficients as a function of clay (C25A) volume fraction. The measurements were performed in the permeation cell at 13°C.	131
9.7	Carbon dioxide transport coefficients as a function of clay (C93A) volume fraction. The measurements were performed in the permeation cell at 13°C.	132
C.1	The experimental permeation cell used in this work.	163
C.2	Carbon dioxide permeation curves for various common polyolefins and polyimide. The coefficients A and B from the linear fitting of the steady state line ($y = -A + Bx$) are shown. The membrane thickness d , the time lag $t_0 = A/B$, and the values of the three transport coefficients are also shown. The diffusion coefficient was calculated by the relation $D = d^2/6t_0$, the permeability coefficient by the slope B of the line as $P = 6.52 \cdot 10^{-12} \cdot B \cdot d$ and the solubility coefficient by the relation $S = P/D$. The units of the diffusion coefficient is cm^2s^{-1} of the solubility coefficient are $\text{mol m}^{-3} \text{Pa}^{-1}$ and of the permeability coefficient are $\text{mol m}^{-1} \text{s}^{-1} \text{Pa}^{-1}$	165
C.3	Carbon dioxide permeation curves for the Acrylic resin/Laponite nano-composites coatings. The diffusion, solubility and permeability coefficients are estimated as in Fig. C.2.	167
C.4	Carbon dioxide permeation curves for the Acrylic resin/Bentonite nano-composites coatings. The diffusion, solubility and permeability coefficients are estimated as in Fig. C.2.	169

C.5	Carbon dioxide permeation curves for the Acrylic resin/Hectorite nano-composites coatings that were treated by ultrasonication. The diffusion, solubility and permeability coefficients are estimated as in Fig. C.2.	171
C.6	Carbon dioxide permeation curves for the Acrylic resin/Hectorite nano-composites coatings that were not ultrasonicated. The diffusion, solubility and permeability coefficients are estimated as in Fig. C.2.	173
C.7	Carbon dioxide permeation curves for the Acrylic resin/Hectorite nano-composites coatings that were treated in an ultrsonication bath at the University of Bayreuth. The diffusion, solubility and permeability coefficients are estimated as in Fig. C.2.	174
C.8	Carbon dioxide permeation curves for the Acrylic resin/organo-modified Bentonite nanocomposites coatings. The diffusion, solubility and permeability coefficients are estimated as in Fig. C.2.	176
C.9	Carbon dioxide permeation curves for the Acrylic resin/organo-modified montmorillonite C25A nanocomposites coatings. The diffusion, solubility and permeability coefficients are estimated as in Fig. C.2.	178
C.10	Carbon dioxide permeation curves for the Acrylic resin/organo-modified montmorillonite C93A nanocomposites coatings. The diffusion, solubility and permeability coefficients are estimated as in Fig. C.2.	180

INDEX

- γ photon, 73
d-spacing, 115, 120
2:1 phyllosilicates, 27

acetone, 116, 120, 121
acrylic, 31
acrylic resin, 31, 77, 89, 98
activation energy, 64
additives, 31
aggregation, 51, 52
alkaline earth cations, 27
alkylammonium cations, 29
aluminium hydroxide, 27
amorphous, 60
amorphous polymer, 39
aqueous acrylic resin emulsion, 115
Arrhenius, 38
aspect ratio, 45–47, 67, 84, 92, 99, 101, 109, 110, 112, 129, 130

barrier properties, 31, 49, 53, 100
bending, 112
bentonite, 89
binder, 31
birefringence, 109
Bragg, 102
bubble effect, 73

capillary forces, 112
cation exchange capacity, 27
cationic surfactants, 29
CEC, 27
chain immobilisation, 84
chain packing, 61
coating, 31
cohesive energy density, 119
colloidal droplets, 31

colloidal polymer suspension, 31
compatibilisation, 29
concentration, 37
concentration gradient, 33
core-shell structure, 89
crosslink density, 108
crosslinking, 60
 density, 62
 reaction, 62
crosslinking reaction, 97
crystallinity, 62
curing temperature, 92, 98
Cussler's model, 53, 104, 109, 110

degree of wettability, 29
Derjaguin-Landau-Verwey-Overbeek, 27
desorption, 34, 39
diffusion, 31, 33, 34, 63, 70
diffusion coefficient, 33, 37, 39, 43–45, 52, 57, 64, 65, 79, 85, 94, 99, 104, 108, 109, 112, 127, 129
diffusion selectivity, 37
diffusivity, 34
dispersion, 27, 44
dispersion medium, 116
DLVO, 27
DMA, 90
Doppler broadening, 74, 79, 83, 84
drying, 32
dynamic free volume, 57

electrical double layer, 94
electrostatic forces, 29
emulsion, 90
enthalpy of mixing, 119
entropy of mixing, 29, 119
ethanol, 116, 120

- exfoliated, 29, 43
exfoliation, 30, 43, 44, 68, 75, 89, 92, 102, 112, 121, 129
- Fick's first law, 33
Fick's second law, 34
film, 32
film formation, 97
kinetics, 97
flocculated, 29
fractional free volume, 64–66, 72, 86
free energy of mixing, 119
free volume, 31, 39, 53, 57, 59, 62, 67, 72, 74, 75, 84, 97, 99, 110, 130
accessible, 64
configurational, 58
excess, 58
fluctuations, 58
hole, 58, 60
hole size distribution, 62, 66, 68
holes, 35, 72, 81
- galleries, 27
Gaussian, 59
glass transition temperature, 59
glassy polymer, 35, 39, 65
glassy state, 60
Group Contribution Method, 119
Gusev's model, 53
Gusev-Lusti model, 109
- Hamaker constant, 27
Henry, 35, 36, 62
Henry's coefficient, 34
Henry's solubility, 34
Hildebrand, 119
hole affinity constant, 36
hydrogen bonding, 121
hydrogen bridges, 29
hydrophilic, 29, 31, 89, 115
hydrophobic, 89, 115
- inorganic particles, 27
inter-layer distance, 29
inter-layer spacing, 29
interaction energy, 96
- interactions, 29
intercalated, 29, 44
intercalation, 30, 44
interface, 30
interface entropy, 30
interfacial energy, 30, 115
interfacial region, 68, 84
interfacial regions, 52, 61
interstitial cavities, 61
isomorphic substitution, 27
- kinetics, 29
- Langmuir, 35, 36, 63
capacity, 35
- laponite, 77, 80
layer thickness, 27
layered silicates, 29
Li-hectorite, 67, 101
liquid-crystalline ordering, 109
- magnesium hydroxide, 27
- mass flux, 33
mass transfer, 44
mass transport, 33
mechanical properties, 31
miscibility, 120
Monte Carlo calculations, 55
montmorillonite, 55, 115
- nanocoating, 108
nanocomposite, 29, 43, 62, 75, 90, 115
nanocomposites, 27, 67, 84, 96
nanometer scale, 27
nanoplatelets, 43
Nielsen's model, 44, 50, 53, 104, 109, 110, 129, 130
nucleating agents, 62
- order parameter, 50
organo-modified bentonite, 127
organo-modified montmorillonites, 115, 116
organophilic, 29
orientation, 45, 50, 99
ortho-positronium, 70
oxygen transmission rate, 67

- para-positronium, 70
 parachor, 119
 partial pressure, 34
 particle-particle attractions, 29
 percolation threshold, 64
 permeability, 31, 36, 39, 43, 44, 47, 51, 54, 66, 67, 79, 86, 91, 94, 99, 104, 110, 112, 129
 permeability coefficient, 37, 49
 permeability models, 44
 permeation, 33
 permeation cell, 91
 Permeation Cell Method, 37
 phosphonium cations, 29
 phyllosilicate, 27, 29
 pick off reaction, 70
 polarity, 73
 polymer matrix, 27, 43
 polyurethane, 67, 98
 positron, 69
 - annihilation, 70
 - intensity, 70, 83
 - lifetime, 70, 83
 Positron Annihilation Life Time Spectroscopy, 63
 Positron Annihilation Lifetime Spectroscopy, 69, 78, 86, 110
 positronium, 70, 73
 - lifetime, 70, 81
 radioactive isotopes, 69
 radius of gyration, 29
 resin, 31
 rubbery polymer, 34, 62
 rubbery state, 60
 scattering
 - intensity, 81, 92
 - vector, 92
 segmental motion immobilisation, 61
 silicon oxide, 27
 solubility, 37, 39, 41, 43, 57, 62, 79, 84, 86, 94, 99, 104, 108, 110, 112, 127, 129
 solubility coefficient, 36
 solubility parameter, 119
 Solubility selectivity, 37
 solvent, 31, 67, 115
 - evaporation, 108
 solvent evaporation rate, 98
 sonication, 89
 sorption, 33, 36, 62
 sorption coefficient, 37
 static free volume, 57
 surface charge, 115
 surface energy, 119
 surface modification, 115
 surface tension, 119
 surfactants, 117
 suspension medium, 96
 swelling, 102
 Tao-Eldrup model, 73
 thermal expansion coefficient, 84
 thermogravimetric analysis, 90, 116
 tortuosity, 43, 45, 50, 53, 65–68, 99, 104, 109, 113, 130
 tortuous path, 31, 129
 transport coefficients, 37, 94, 108, 127
 transport properties, 57
 ultrasonic, 29
 ultrasonic treatment, 101
 ultrasonication, 108, 116
 ultrasound bath, 102, 104
 Van der Waals, 27, 29
 van der Waals, 94
 volatile component, 31
 water-borne acrylic resin, 116
 waterborne acrylic resin coatings, 31
 X-ray diffraction, 78, 80, 91, 102, 121

Epilogue

In 1996-1997 I started my studies at the Department of Physics of the University of Athens. My graduation research project was in the area of solid state physics and, specifically, on electron transport and low temperature physics. I used polycrystalline ceramic samples (manganites) doped with cobalt of various contents. These materials are known as colossal magneto-resistance materials because their electron transport properties are directly correlated with their magnetic state through the double exchange mechanism. On September of 2001 I presented part of the results at the Panhellenic Solid State Conference in Xanthi.

I graduated with a degree in Physics in the academic year 2001-2002 and I started immediately the MSc. program on solid state physics (condensed matter) at the same Department. In the summer of 2002, I visited the Physics Department of the University of Bayreuth, Germany twice in order to perform DC magnetisation measurements in a superconductive magnetometer (SQUID) and presented these measurements at the Panhellenic Solid State Conference at F.O.R.T.H. in Heraclion, in September, 2002. The results were published at the Journal of Physics: Condensed Matter (Em. Syskakis, G. Choudalakis, C. Papastaikoudis, 15(45):7735-7749, 2003).

My MSc research project involved also AC magnetic susceptibility measurements in a cryostat with the appropriate coil geometry, a system which I had to design and make at the Material Science Institute of the National Research Center Democritos (Fall 2002-end of 2003). I fulfilled my master thesis at the beginning of 2004 and a few months later I fulfilled my military service at the Greek Army Special Forces until the summer of 2005. I started to search for a Phd project and finally ended up in the Technical University of Crete, where, through the recommendation/prompting of prof. Dionisios Hristopoulos, I came into contact with prof. Alexandros D. Gotsis.

The project that I decided to do aimed at the improvement of the gas barrier properties of polymeric coatings with the use of nanoparticles. I chose this project basically for two reasons: The first was my decision to distance myself somewhat from the basic physics, in order to deal with a more directly applicable subject. The second was that I would not have to abandon the scientific approach that I had already developed and deal with a purely engineering project. The specific subject was in fact a bridge between those two, namely an applied sciences project.

The research started in the summer of 2006 with a bibliographic search on polymer clay nanocomposites, gas permeability models and experimental studies, and free volume. In the summer of 2007, I visited Delft University of Technology, in the Nether-

lands, to perform free volume measurements via Positron Annihilation Lifetime Spectroscopy in the acrylic resin/laponite nanocomposite samples.

I presented the PALS results in the Panhellenic Polymer Conference at Ioannina in September of 2008. A review article prepared on the permeability of polymer clay nanocomposites and published in the European Polymer Journal in 2009 has received more than 150 citations until now (10/1/2013). In 2009 I designed and built a gas permeation cell device able to measure gas transmission rate through a membrane and each one of the three transport coefficients.

In the fall of 2010, I gave an invited talk at the Materials Research Society Fall Meeting in Boston, USA. An article combining the PALS results and the gas transport coefficients measured in the permeation cell for the acrylic resin/laponite nanocomposite coatings was written and published in the European Polymer Journal in 2011. Another review article on free volume and mass transport in polymer nanocomposites has been published in the Current Opinion of Colloid and Interface Science Journal in 2012. A chapter on the Recent Developments in the Permeability of Polymer Clay Nanocomposites for the book entitled Technological Advancement in Polymer Nanocomposites of Layered Silicates, to be published by Springer in 2013, was written after the editors invitation.

In the spring of 2012 I gave a talk at the Chemistry Department of the University of Bayreuth in Germany, after the invitation of prof. Josef Breu. I also prepared there samples of acrylic resin reinforced with Li-hectorite clay that the group of prof. Breu have produced with aspect ratios of more than 1000. A manuscript was submitted for publication in Progress in Organic Coatings Journal about the morphological and gas transport properties of acrylic resin/bentonite nanocomposite coatings.

Two more manuscripts are being prepared to be submitted in January 2013 for publication: One for the acrylic resin/hectorite nanocomposite coatings and another for the acrylic resin/organo-modified montmorillonites nanocomposite coatings.

Curiculum Vitae

Giorgos Choudalakis was born in Chania-Crete of Greece in 1975. He graduated from the 1st Lyceum of Chania in 1993. He entered the Physics Department of the University of Athens after national examinations in 1996 and graduated in 2001. He entered immediately in the post graduate programme of the Condensed Mater Physics and Material Science in the Physics Department of the University of Athens and he graduated in 2004. He fulfilled his military obligations during 2004-2005 and started his doctorate studies in 2006 in the Department of Sciences of the Technical University of Crete.